NOTE TO USERS

This reproduction is the best copy available.

FLIGHT STABILITY ANALYSIS OF A FLEXIBLE ROCKET USING FINITE ELEMENTS AND REDUCED-ORDER MODELING

by

Kyle Davidson
BEng, Ryerson University, 2002

A thesis

presented to Ryerson University

in partial fulfillment of the

requirements for the degree of

Master of Applied Science

in the Program of

Mechanical Engineering

Toronto, Ontario, Canada, 2005

Author's Declaration Page

I hereby declare that I am the sole author of this thesis.

I authorize Ryerson University to lend this thesis to other institutions or individuals for the purpose of scholarly research.

Kyle Davidson

I further authorize Ryerson University to reproduce this thesis by photocopying or by other means, in total or in part, at the request of other institutions or individuals for the purpose of scholarly research.

Kyle Davidson

Borrower's Page

Ryerson University requires the signatures of all persons using or photocopying this thesis. Please sign below, and give address and date.

Flight Stability Analysis of a Flexible Rocket using Finite Elements and Reduced Order Modeling

Master of Applied Science, Mechanical Engineering, 2005
Kyle Davidson
Ryerson Univeristy

The coupling of advanced structural and aerodynamic methods is a complex and computationally demanding task. In many cases, simplifications must be made. For the flight simulation of flexible aerospace vehicles, it is common to reduce the overall structure down to a series of linked degenerate structures such as Euler-Bernoulli beams in order to expedite the structural portion of the solution process.

The current study employs the sophistication and generality of finite-element based modeling with the concepts of reduced-order modeling to create a general flexible-body flight simulation program. The program was created for use with the MATLAB-Simulink programming package. A parametric analysis on the stability of flexible rockets is performed and results are presented for a variety of rocket configurations based on the SPHADS-1 vehicle under development at Ryerson University. The primary instability mode under study is that associated with the flapping and twist motions of the tailfins under aerodynamic loading. By varying the average fin thickness, both stable and unstable behaviour is recorded for a variety of flight conditions.

Acknowledgements

I would like to take this opportunity to extend my greatest and most sincere thanks to all those who have supported me throughout the duration of my thesis work.

First and foremost, I would like to thank my thesis supervisors, Dr. Don McTavish and Dr. David Greatrix, whose support, guidance, and confidence have been invaluable to me. Their patience and determination helped me to overcome the obstacles and hurdles that periodically sprang onto my path. For that, I am truly grateful.

I would also like to thank all of the PRF staff, Jerry Karpynczyk, who has always been extremely helpful, upbeat, encouraging and entertaining. To Primoz Cresnik, Harman Chopra, Sarah Hardacre, I wish to thank for keeping me sane during those long hours of programming turmoil in the PRF.

I must thank my family and friends for their never-ending confidence in me, no matter how frustrated (and irritable) I became. To my little cousins, Kassandra, Mackenzie, Nicholas and Parker, thanks for brightening my day whenever you came to visit, and for forcing me to take a much needed break.

Thanks of course to Nadia Rachiele, who let me ramble on about things like Coriolis matrices and faulty programming despite being hopelessly lost in jargon. Thanks for all the love and support *amore*.

Lastly, humble thanks be to God, who has supported me in all things.

This work was supported by the Natural Sciences and Engineering Research Council (NSERC) of Canada.

Table of Contents

List of Tables

List of Figures

Nomenclature

Convention	Description
$\mathbf{A}, \mathbf{B}, \mathbf{c}, \mathbf{d}$	Matrix or vector (line or column)
a, b, c, d	Scalar or element of matrix/vector
$\mathbf{A}^T$	Matrix transpose
$\mathbf{A}^{-1}$	Matrix inverse
$\mathbf{a}^\times$	Skew symmetric matrix of a 3 element array. Where, $\mathbf{a}^\times = \begin{bmatrix} 0 & -a_3 & a_2 \\ a_3 & 0 & -a_1 \\ -a_2 & a_1 & 0 \end{bmatrix}$
$\mathbf{A}_B$	Subscripts indicate properties relative to certain frame or component reference (e.g. the body frame)
$\overline{\mathbf{A}}, \overline{\mathbf{a}}$	Overbar indicates a reduced order quantity (unless otherwise specified)
$\underline{\mathbf{A}}, \underline{\mathbf{a}}$	Vector-space notation
$\dot{\mathbf{a}}, \dot{a}$	Rate of change with respect to time, $\dot{a} = \frac{da}{dt}$

Variable	Description
A_n	Fourier coefficient
b	fin span
cc_l	load distribution
c_i , c_j	local fin chord
c_l	local lift coefficient
c_r	root chord
c_t	tip chord
$\mathbf{c}$	first moment of inertia (rigid)
$\mathbf{c}_{tot}$	total first moment of inertia
$\overline{\mathbf{c}}_{tot}$	reduced total first moment of inertia
$\mathbf{c}_u$	first moment of inertia (flexible)
C_A	axial force coefficient
C_{Ao}	nominal axial force coefficient
C_{Af_i}	axial force coefficient for *i*-th fin
$C_{A\alpha}$	axial force coefficient with respect to α, $\left(C_{A\alpha} = \frac{\partial C_A}{\partial \alpha}\right)$
$\mathbf{C}_{ba,bn}$	rotation matrix from ($\mathcal{F}_{bn}$) to ($\mathcal{F}_{ba}$)
$\mathbf{C}_{bn,B}$	rotation matrix from ($\mathcal{F}_{B}$) to ($\mathcal{F}_{bn}$)
$\mathbf{C}_{co,ba}$	rotation matrix from ($\mathcal{F}_{ba}$) to ($\mathcal{F}_{co}$)

$\mathbf{C}_{f_i}$	rotation matrix from ($\mathcal{F}_B$) to ($\mathcal{F}_{fi}$)
$\mathbf{C}_{f\delta_i}$	rotation matrix for angular orientation of *i*-th fin
$\mathbf{C}_{f\theta_i}$	rotation matrix for flexible deformation of *i*-th fin
C_M	pitch moment coefficient
C_{Mo}	nominal pitch moment coefficient
$C_{M\alpha}$	pitch moment coefficient with respect to α, $\left(C_{M\alpha} = \frac{\partial C_M}{\partial \alpha}\right)$
C_N	normal force coefficient
$C_{N_{f_i}}$	normal force coefficient for *i*-th fin
$C_{N\alpha}$	normal force coefficient with respect to α, $\left(C_{N\alpha} = \frac{\partial C_N}{\partial \alpha}\right)$
$C_{N\alpha_{f_i}}$	normal force coefficient with respect to α for *i*-th fin
$C_{N\dot{\alpha}}$	normal force coefficient with respect to $\dot{\alpha}$, $\left(C_{N\dot{\alpha}} = \frac{\partial C_N}{\partial \dot{\alpha}}\right)$
$\mathbf{C}_T$	deformed thrust rotation matrix
E	complete elliptic integral of the second kind
$\mathcal{F}$	inertial reference frame
$\mathcal{F}_{ba}$	body aerodynamics frame
$\mathcal{F}_{bn}$	body key-node reference frame
$\mathcal{F}_B$	body reference frame
$\mathcal{F}_{fi}$	*i*-th fin reference frame
f_{f_j}	fin nodal force corresponding to node *j*
f_{tip}	fin load distribution correction factor
$\mathbf{f}$	nodal force vector
$\bar{\mathbf{f}}$	reduced nodal force vector
$\mathbf{f}_\sigma$	internal nodal force vector
$\bar{\mathbf{f}}_\sigma$	reduced internal nodal force vector
$\mathbf{F}$	external force vector
$\mathbf{F}_{f_i}$	fin aerodynamic force vector for *i*-th fin
$\mathbf{F}_T$	thrust force vector
$\mathbf{g}$	inertial gravitational acceleration vector
$\mathbf{G}$	external torque vector
$\mathbf{G}_T$	thrust torque/moment vector
$\mathbf{h}$	angular momentum vector
$\mathbf{h}_{\dot{u}}$	flexible component of angular momentum
$\dot{\mathbf{h}}$	rate of change of angular momentum vector
$\mathbf{H}_{tot}$	total angular momentum matrix

$\overline{\mathbf{H}}_{tot}$	reduced total angular momentum matrix
$\mathbf{H}_u$	flexible angular momentum component
$\mathbf{H}'_i$	flexible angular momentum coefficient
$\mathbf{H}_\omega$	rotational Coriolis matrix (rigid component)
$\mathbf{H}_{\omega u}$	rotational Coriolis matrix (flexible component)
$\mathbf{H}_{\omega,tot}$	total rotational Coriolis matrix
$\overline{\mathbf{H}}_{\omega,tot}$	reduced total rotational Coriolis matrix
$\mathbf{J}$	second moment of inertia (rigid component)
$\mathbf{J}_{ru}$	second moment of inertia (rigid-flexible component)
$\mathbf{J}_{tot}$	total second moment of inertia
$\overline{\mathbf{J}}_{tot}$	reduced total second moment of inertia
$\mathbf{J}_{uu}$	second moment of inertia (flexible-flexible component)
$\mathbf{J}'_{ru,i}$	rigid-flexible second moment coefficient
$\widetilde{\mathbf{J}}'_{ru,i}$	approximate rigid-flexible second moment coefficient
$\overline{\mathbf{J}}'_{ru,m}$	reduced rigid-flexible second moment coefficient
$\mathbf{J}''_{uu,ij}$	flexible-flexible second moment coefficient
$\widetilde{\mathbf{J}}''_{uu,ij}$	approximate flexible-flexible second moment coefficient
$\overline{\mathbf{J}}''_{uu,mp}$	reduced flexible-flexible second moment coefficient
K_b	fin nodal spanwise load factor
K_c	fin nodal chordwise load factor
K_t	total nodal fin load factor
$\mathbf{K}$	finite element stiffness matrix
m	total mass
M_∞	Mach number
$\mathbf{M}$	finite element mass matrix
$\mathbf{M}_{kl}$	mass nodal block
$\mathbf{M}_\omega$	flexible Coriolis matrix
$\overline{\mathbf{M}}_\omega$	reduced flexible Coriolis matrix
n_{fins}	number of fins
N	Normal force
ΔP	pressure distribution over upper and lower fin surfaces
$\mathbf{p}$	translational momentum vector
$\mathbf{p}_{\dot{u}}$	flexible component of translational momentum
$\dot{\mathbf{p}}$	rate of change of translational momentum vector
$\mathbf{P}$	translational momentum coefficient matrix
$\overline{\mathbf{P}}$	reduced translational momentum coefficient matrix

$\mathbf{P}_{\omega}$	translational Coriolis matrix term
$\overline{\mathbf{P}}_{\omega}$	reduced translational Coriolis matrix term
$\mathbf{q}$	flexible coordinate deformation vector
$\dot{\mathbf{q}}$	flexible coordinate velocity vector
$\ddot{\mathbf{q}}$	flexible coordinate acceleration vector
q_{∞}	dynamic pressure
$\mathbf{r}$	rigid location of a material point in ($\mathcal{F}_B$)
$\mathbf{r}_{bn}$	location of body key-node in ($\mathcal{F}_B$)
$\mathbf{r}_{f_i}$	location of *i*-th fin key-node in ($\mathcal{F}_B$)
$\mathbf{r}_T$	location of thrust key-point in ($\mathcal{F}_B$)
$\mathbf{R}$	position vector in inertial frame ($\mathcal{F}$)
$\mathbf{R}_B$	position of body frame ($\mathcal{F}_B$) origin in inertial frame ($\mathcal{F}$)
$s_{m,i}$	scalar component of *m*-th shape vector for *i*-th row
S	body aerodynamic reference area
S_f	fin aerodynamic reference area
$\mathbf{S}$	matrix of coordinate mode vectors
t	time
T	thrust magnitude
$\mathbf{u}$	flexible displacement of a material point
$\overset{\circ}{\mathbf{u}}$	deformation velocity in body frame ($\mathcal{F}_B$)
$\dot{\mathbf{u}}_{bn}$	deformation velocity of body key-node
$\dot{\mathbf{u}}_{f_i}$	deformation velocity of fin key-node
$\overset{\circ\circ}{\mathbf{u}}$	deformation acceleration in body frame ($\mathcal{F}_B$)
$\mathbf{V}$	velocity vector in inertial frame ($\mathcal{F}$)
$\mathbf{V}_{bn}$	velocity vector in body key-node frame ($\mathcal{F}_{bn}$)
$\mathbf{V}_B$	velocity of body frame ($\mathcal{F}_B$) origin
$\mathbf{V}_w$	wind velocity vector
$\dot{\mathbf{V}}$	acceleration vector in inertial frame ($\mathcal{F}$)
$\dot{\mathbf{V}}_B$, $\dot{\mathbf{v}}_B$	acceleration of body frame ($\mathcal{F}_B$) origin
x_c	non-dimensional fin node chordwise position
x_{c_jLE}	location of local chord leading edge
x_j	chordwise position of node j
y_b	non-dimensional fin node spanwise position
y_{cr}	spanwise location of the root chord from ($\mathcal{F}_B$) x-axis
y_j	spanwise location of node j
α	vehicle angle of attack

α_b	body key-node angle of attack
α_{fi}	*i*-th fin key-node angle of attack
$\dot{\alpha}$	rate of change of angle of attack
$\boldsymbol{\alpha}_T$	angular misalignments of thrust vector (fixed)
β	sideslip angle
$\dot{\beta}$	rate of change of sideslip angle
δ_i	angular location of *i*-th fin about body frame x-axis
$\boldsymbol{\delta}_T$	translational misalignment of thrust vector (fixed)
ϕ	roll angle
Γ	circulation
$\boldsymbol{\eta}$	reduced order flexible displacement vector
$\dot{\boldsymbol{\eta}}$	reduced order flexible velocity vector
$\boldsymbol{\Phi}$	matrix of reduced order shape function
μ	Mach angle
ν	radial angle used in supersonic wing theory
ψ	shape function
$\boldsymbol{\Psi}$	shape vector matrix
θ	pitch angle
$\boldsymbol{\theta}_{bn}$	angular deformation of body key-node (variable)
$\boldsymbol{\theta}_{fi}$	angular deformation of *i*-th fin key-node (variable)
$\boldsymbol{\theta}_T$	angular deformation of thrust vector (variable)
$\dot{\boldsymbol{\theta}}_{f_i}$	angular deformation rate of i-th fin key-node
ρ_∞	air density
$\boldsymbol{\omega}_{bn}$	angular velocity of body key-node
$\boldsymbol{\omega}_B$	angular velocity of body frame ($\mathcal{F}_B$)
$\boldsymbol{\omega}_{f_i}$	angular velocity of *i*-th fin
$\mathring{\boldsymbol{\omega}}_B$, $\dot{\boldsymbol{\omega}}_B$	angular acceleration of body frame ($\mathcal{F}_B$)
ψ	yaw angle

Chapter 1: Introduction

The problem of simulating the flight of a flexible aerial vehicle is a complex one. It involves the coupling of the fields of advanced aerodynamics and structural analysis. The addition of flexibility to a given structural model can significantly increase the number of system degrees of freedom, depending on the level of complexity and sophistication involved.[1,2] Consequently, this may often become a stumbling block for the simulation of complicated structures due to the increased computational time required to establish the system response. However, obtaining a realistic flexible flight model is of great benefit to the designers of any flight vehicle whether it be rocket, aircraft, spacecraft, or seacraft.

The ability to predict vehicle performance under certain loadings or flight conditions is critical for identifying and eliminating any aeroelastic or dynamic instabilities, which may threaten the overall integrity of the vehicle. These instabilities may yield undesirable performance characteristics that may hamper the vehicle's ability to achieve its mission goals, or in more extreme circumstances, may result in structural failure.

With the aid of an accurate flexible flight model, design engineers can optimize the structure by strengthening critical components so as to limit any undesired characteristics, while reducing and trimming other less critical regions to improve overall performance. The knowledge of the vehicle response envelope is also critical for vehicles with autonomous navigation systems. The navigation control systems must be carefully designed to ensure the vehicle remains stable and, ideally, within its optimal flight envelope.

Individually, the disciplines of aerodynamics and structures are both highly developed. Computational fluid dynamics (CFD) represents the state of the art of aerodynamics work. It is essentially the numerical solution of the equations that describe fluid flow, the Navier Stokes equations.[1,2,3] Commercial CFD packages such as FLUENT™, CFD-ACE™, TASCFlow™ and FASTRAN™ are commonly

employed in industry and academia for determining solutions to flows around or within complex structures.

On the structural side, finite element analysis (FEA) has similarly become the industry standard. A complicated structure may be represented as a grid of points and the material behavior under various loading conditions can be determined using a variety of advanced techniques.[4,5,6,7] Commercially available software such as ANSYS™ and IDEAS™ are some examples of commonly employed FEA software packages that are utilized worldwide.[8]

Addressing the problem of a flexible flight vehicle in its most complete and complex formulation would include state-of-the-art methods from both CFD and FEA, in combination with a flight dynamics engine for tracking gross motion relative to a specified location. There lies the heart of the problem. The full solution of complicated aeroelastic configurations may take weeks to solve on a high-speed computer, in attempting to solve the model behavior over a small fraction of simulated flight time.

In response to this complication, a series of simplifications are often made to the problem to expedite the large motion flexible structure analysis. A common technique used in the simulation of flexible structures is to reduce the structural components down to a series of simplified interconnected blocks. One often employed modeling procedure is to represent the main components of a body as a series of Euler Bernouilli beams. Beams are commonly chosen due to the fact that their shape functions are known and are readily available. [9,10,11]

The aerodynamic modeling procedure may be as simple or as complicated as desired, and as is deemed computationally acceptable. An aircraft (generally a very complex-shaped structure) would then be reduced to a series of four or five interconnected flexible beams to represent the fuselage, wings and empennage structures. While this model reduction may allow for tracking of flexible motions as the vehicle encounters different flight stimuli (such as wind gusts) the overall accuracy of the method may be questioned. The simple fact is that aircraft are not beams, so it should not be expected for them to behave entirely so.

This project undertakes a different analysis route. Instead of reducing the structure down to a series of degenerate elements, the flight vehicle will be modeled using a finite element (FE) grid. The FE grid will allow for more accurate deflection shapes of the structure under various loading conditions. However, an obvious drawback to employing a finite element model (FEM) is the drastic increase in the number of nodes and corresponding degrees of freedom. Therefore, to aid the solution process, the model will undergo a transformation to convert it into a reduced order model (ROM). The ROM effectively selects key deformation shapes that will combine to create the range of flexible motion for the vehicle.[12,13,14] These selected deformation shapes become the new degrees of freedom of the model. As a result, the size of the system being analyzed may be drastically reduced to something much more manageable. For example, a model comprised of 200 nodes, and 1200 degrees of freedom could be condensed to a ROM with 10-15 degrees of freedom.

The scope of this project is predominantly limited to the flexible flight of a rocket vehicle, using a reduced order FE derived structural model for various flight conditions. A parametric study is to be performed for determining stability boundaries for rocket models of varying configurations. With respect to the aerodynamic modeling, the level of complexity employed is generally allowed to be as simple or complex as desired and as is computationally feasible. However, the aim of this project is not to focus on the utilization of the latest state-of-the-art CFD techniques, as the development (and computation) time is prohibitory under the time frame of this study. As a result, with regard to the aerodynamic modeling, simpler relations are employed in combination with empirical relations (when available) for obtaining relevant aerodynamic details.

The current study will integrate the previously discussed reduced order FE rocket model, with a rocket flight dynamics simulation program. The program computes all the pertinent gross (rigid-body) motions and structural deformations for the vehicle in response to the net forces and torques acting upon the vehicle (thrust, gravity, aerodynamic, etc.).[15] This program has been developed in the MATLAB/Simulink programming environment.

The rigid body motions are relative to a predefined body reference frame. When referring to flexible bodies, the body reference frame generally conforms to one of two classifications. The first category is to select the body reference frame as fixed relative to some point on the undeformed vehicle. The second is to select the reference axes so as to eliminate the contributions to the linear and angular momentum vectors due to the flexible motions. This type of reference is commonly referred to as the selection of 'mean' axes. Mean axes have the benefit of having inertially decoupled translations, rotations and deformations. However, the drawback to choosing such a method is that the constraints for evoking it are difficult to establish.[3] Thus, for this study the reference frame is chosen to coincide with a location on the undeformed vehicle structure.

The parametric rocket study will be presented from two perspectives. The more comprehensive detailed evaluation requires the full flight simulation of the flexible reduced order rocket model through various flight conditions to directly simulate and capture unstable flight behaviour. A second, less-detailed approach will employ a simplified planar representation of the flexible rocket problem, which will be formatted so as to provide a state space eigen-analysis stability description. It is not expected that the two methods of evaluation should perfectly coincide given the difference in model complexity; however, the state-space stability analysis will serve to qualitatively validate the integrity of the simulation results.

Chapter 2: Theory and Background

The following sections provide some basic derivations used for establishing the general framework for the flexible and rigid body dynamics employed within this project. The equations of motion are established and all relevant coefficients are defined.

2.1 Derivation of the Flexible Body Equations of Motion

A vehicle structural model is typically considered to be a continuous system, defined as a collection of infinitesimal differential mass particles (dm). Each of these mass elements has a position that is defined with respect to a given reference frame. In the current context, the frame will either be the body frame ($\mathcal{F}_B$) defined with respect to a given point within the body or some arbitrarily defined inertial frame ($\mathcal{F}$).[13] The position of a given point in the inertial frame for a flexible structure is defined by the following equation and shown in **Figure 2.1.**

$$\underrightarrow{\mathbf{R}} = \underrightarrow{\mathbf{R}_B} + \underrightarrow{\mathbf{r}} + \underrightarrow{\mathbf{u}} \tag{2.1.1}$$

where $\underrightarrow{\mathbf{R}}$ is the location of a given material point (dm) in the inertial frame, $\underrightarrow{\mathbf{R}_B}$ is the location of the body frame ($\mathcal{F}_B$) origin in the inertial frame, $\underrightarrow{\mathbf{r}}$ is the rigid location of the material point in the body frame ($\mathcal{F}_B$), and $\underrightarrow{\mathbf{u}}$ is the flexible displacement of the given material point.

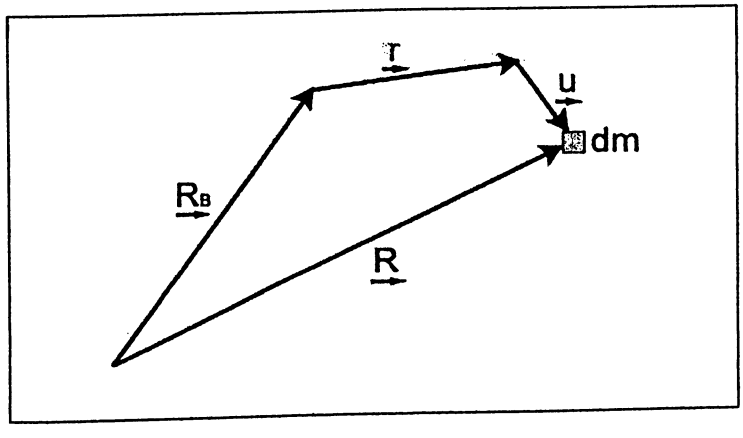

Figure 2.1: Position of a Material Point

The velocity of this same point with respect to the body frame can then be defined as

$$\underset{\rightarrow}{\mathbf{V}} = \underset{\rightarrow}{\mathbf{V}_B} + \dot{\underset{\sim}{\mathbf{u}}} + \underset{\rightarrow}{\boldsymbol{\omega}_B} \times (\underset{\sim}{\mathbf{r}} + \underset{\sim}{\mathbf{u}}) \qquad (2.1.2)$$

where $\underset{\rightarrow}{\mathbf{V}_B}$ is the velocity vector of the body frame origin, $\dot{\underset{\sim}{\mathbf{u}}}$ is the deformation velocity of any given material point, and $\underset{\rightarrow}{\boldsymbol{\omega}_B}$ is the angular velocity vector.

Note that the overcircle "o" corresponds to a rate of change with respect to ($\mathcal{F}_B$).

Similarly the inertial acceleration can be found via the expression

$$\dot{\underset{\rightarrow}{\mathbf{V}}} = \dot{\underset{\rightarrow}{\mathbf{V}_B}} + \dot{\underset{\rightarrow}{\boldsymbol{\omega}_B}} \times (\underset{\sim}{\mathbf{r}} + \underset{\sim}{\mathbf{u}}) + \underset{\rightarrow}{\boldsymbol{\omega}_B} \times \left(\dot{\underset{\sim}{\mathbf{r}}} + \dot{\underset{\sim}{\mathbf{u}}} \right) + \ddot{\underset{\sim}{\mathbf{u}}} + \underset{\rightarrow}{\boldsymbol{\omega}_B} \times \left(\underset{\rightarrow}{\mathbf{V}_B} + \underset{\rightarrow}{\boldsymbol{\omega}_B} \times (\underset{\sim}{\mathbf{r}} + \underset{\sim}{\mathbf{u}}) + \dot{\underset{\sim}{\mathbf{u}}} \right) \qquad (2.1.3\ a)$$

which can be expanded into

$$\dot{\underset{\rightarrow}{\mathbf{V}}} = \dot{\underset{\rightarrow}{\mathbf{V}_B}} + \underset{\rightarrow}{\boldsymbol{\omega}_B} \times \underset{\rightarrow}{\mathbf{V}_B} + \ddot{\underset{\sim}{\mathbf{u}}} + 2\underset{\rightarrow}{\boldsymbol{\omega}_B} \times \dot{\underset{\sim}{\mathbf{u}}} + \dot{\underset{\rightarrow}{\boldsymbol{\omega}_B}} \times (\underset{\sim}{\mathbf{r}} + \underset{\sim}{\mathbf{u}}) + \underset{\rightarrow}{\boldsymbol{\omega}_B} \times \underset{\rightarrow}{\boldsymbol{\omega}_B} \times (\underset{\sim}{\mathbf{r}} + \underset{\sim}{\mathbf{u}}) \qquad (2.1.3\ b)$$

Note that the rate of change of the rigid body position vector is known to be equivalent to $\dot{\underset{\sim}{\mathbf{r}}} \equiv 0$ by definition. If applicable, simplifications to the above equations may be made to accommodate situations that may be subject to small deformations or deformation rates.

2.2 Newton's 2nd Law of Motion

Newton originally stated the second law of motion in his treatise "The Principia" as follows:

"*Change of motion is proportional to the moving force impressed, and takes place in the direction of the straight line in which such force is impressed.*"

More directly it defines the force acting on an object to be equivalent to the differential change in momentum per unit of time.[16] Note that in the sections that follow, terms are now expressed in matrix form, with all rate of change terms

being denoted by solid 'overdots'. The rate of change of translational momentum is then,

$$\frac{d\mathbf{p}}{dt} = \dot{\mathbf{p}} = \mathbf{f} \tag{2.2.1}$$

where $\mathbf{f}$ is the resultant force vector. The translational momentum ($\mathbf{p}$) is given by the following definition

$$\mathbf{p} = \int \mathbf{V} dm \tag{2.2.2}$$

where the flexible velocity of a given mass element ($\mathbf{V}$) was defined previously.

Similarly, Newton's law is again used to define the rate of change of angular momentum and its relation to the moments acting upon a body:

$$\frac{d\mathbf{h}}{dt} = \dot{\mathbf{h}} = \mathbf{g} \tag{2.2.3}$$

The angular momentum ($\mathbf{h}$) is given by

$$\mathbf{h} = \int (\mathbf{r} + \mathbf{u}) \mathbf{V} dm \tag{2.2.4}$$

Substituting in the velocities into **Equations (2.2.2)** and **(2.2.4)** and simplifying gives the following equations for the respective momenta:

$$\mathbf{p} = m\mathbf{v}_B - \mathbf{c}_{tot}^{\times} \boldsymbol{\omega}_B + \mathbf{p}_{\dot{u}} \tag{2.2.5}$$

$$\mathbf{h} = \mathbf{c}_{tot}^{\times} \mathbf{v}_B + \mathbf{J}_{tot} \boldsymbol{\omega}_B + \mathbf{h}_{\dot{u}} \tag{2.2.6}$$

The variables presented in **Equations (2.2.5)** and **(2.2.6)** are discussed and presented below. The total first moment of inertia ($\mathbf{c}_{tot}$) is given as

$$\mathbf{c}_{tot} = \int (\mathbf{r} + \mathbf{u}) dm \tag{2.2.7}$$

Equation (2.2.7) may be alternately expressed in terms of its rigid and flexible components. Thus,

$$\mathbf{c}_{tot} = \mathbf{c} + \mathbf{c}_u \tag{2.2.8}$$

where the rigid component is

$$\mathbf{c} = \int \mathbf{r} dm \tag{2.2.9}$$

and the flexible component is

$$\mathbf{c}_u = \int \mathbf{u} dm \tag{2.2.10}$$

The second moment comprised of several sub-matrices dependent upon the rigid and flexible positions of each mass element, that is,

$$\mathbf{J}_{tot} = \mathbf{J}_{rr} + \mathbf{J}_{ru} + \mathbf{J}_{ur} + \mathbf{J}_{uu} \tag{2.2.11}$$

where the rigid component is

$$\mathbf{J} = -\int \mathbf{r}^{\times}\mathbf{r}^{\times} dm\,, \tag{2.2.12}$$

the rigid-flexible component is

$$\mathbf{J}_{ru} = -\int \mathbf{r}^{\times}\mathbf{u}^{\times} dm\,, \tag{2.2.13}$$

the flexible-rigid component is

$$\mathbf{J}_{ur} = -\int \mathbf{u}^{\times}\mathbf{r}^{\times} dm\,, \tag{2.2.14}$$

and the flexible-flexible component is

$$\mathbf{J}_{uu} = -\int \mathbf{u}^{\times}\mathbf{u}^{\times} dm \tag{2.2.15}$$

The flexible momentum coefficient terms are given by

$$\mathbf{p}_{\dot{u}} = \int \dot{\mathbf{u}} dm \tag{2.2.16}$$

and

$$\mathbf{h}_{\dot{u}} = \mathbf{h}_{r\dot{u}} + \mathbf{h}_{u\dot{u}} \tag{2.2.17}$$

where the rigid-flexible component is

$$\mathbf{h}_{r\dot{u}} = \int \mathbf{r}^{\times}\dot{\mathbf{u}} dm \tag{2.2.18}$$

and the flexible-flexible component is

$$\mathbf{h}_{u\dot{u}} = \int \mathbf{u}^{\times}\dot{\mathbf{u}} dm \tag{2.2.19}$$

These components will be discussed and presented in further detail with respect to the finite element context in the sections that are to follow.

2.3 Assumed-Modes Method

The deformation of a flexible structural model may be represented by a series of linearly independent shape functions ψ. These shape functions may be selected judiciously at the discretion of the user. Ideally, the shape functions (ψ) chosen will include the exact elemental deformation shape vectors; however, these are not always readily available for complex structures. The selected shape functions may be relative to the full structural model or specific components and may be a combination of free vibration modes, finite element shape functions, forced deformation shapes, or any other conceivable and justifiable profile.

In terms of the assumed-modes method, the flexible deformations take on the following form.

$$\mathbf{u}(\mathbf{r},t)=\sum_i q_i(t)\psi_i(\mathbf{r}) \tag{2.3.1}$$

where $\mathbf{u}$ is the vector containing the flexible deformations of the structure, q_i corresponds to the *i*-th flexible coordinate, and ψ_i is the *i*-th shape vector

The shape vector matrix given as the set of deformation shape vectors is of the form,

$$\Psi=[\psi_1 \quad \psi_2 \quad \cdots \quad \psi_N]$$

2.4 Newton-Euler Equations of Motion

The general equations of motion are defined using a Newton-Euler approach. Recalling **Equations (2.2.1)** and **(2.2.3)**, the equations of motion in their simplest form can be presented as:

$$\dot{\mathbf{p}}+\boldsymbol{\omega}_B^{\times}\mathbf{p}=\mathbf{F} \tag{2.4.1}$$

$$\dot{\mathbf{h}}+\boldsymbol{\omega}_B^{\times}\mathbf{h}+\mathbf{v}_B^{\times}\mathbf{p}=\mathbf{G} \tag{2.4.2}$$

Substituting the expressions for translational and angular momentum into the above expressions and following some simplifications yield the full flexible-body equations of motion, which are presented and explained in detail below. For additional derivation details the reader may refer to dynamics texts or papers by McTavish[13].

2.5 Full Flexible-Body Equations of Motion

Substituting the definitions for the translational and angular momenta into **Equations (2.4.1)** and **(2.4.2)**, and following some considerable algebraic manipulation generates a simplified matrix based set of equations of motion in terms of the model degrees of freedom. The nomenclature for the various coefficients presented below is that used by McTavish.[13] Thus, the full flexible-body equations of motion for the system becomes,

$$\begin{bmatrix} m\mathbf{1} & -\mathbf{c}_{tot}^{\times} & \mathbf{P} \\ \mathbf{c}_{tot}^{\times} & \mathbf{J}_{tot} & \mathbf{H}_{tot} \\ \mathbf{P}^{T} & \mathbf{H}_{tot}^{T} & \mathbf{M} \end{bmatrix} \begin{bmatrix} \dot{\mathbf{v}}_B \\ \dot{\boldsymbol{\omega}}_B \\ \ddot{\mathbf{q}} \end{bmatrix} = \begin{bmatrix} \mathbf{F} \\ \mathbf{G} \\ \mathbf{f} \end{bmatrix} - \begin{bmatrix} \mathbf{0} \\ \mathbf{0} \\ \mathbf{f}_{\sigma} \end{bmatrix} - \begin{bmatrix} m\boldsymbol{\omega}_B^{\times} & -\boldsymbol{\omega}_B^{\times}\mathbf{c}_{tot}^{\times} & 2\mathbf{P}_{\omega} \\ \mathbf{c}_{tot}^{\times}\boldsymbol{\omega}_B^{\times} & \boldsymbol{\omega}_B^{\times}\mathbf{J}_{tot} & 2\mathbf{H}_{\omega,tot}(\boldsymbol{\omega}_B) \\ -\mathbf{P}_{\omega}^{T} & -\mathbf{H}_{\omega,tot}^{T}(\boldsymbol{\omega}_B) & -2\mathbf{M}_{\omega}(\boldsymbol{\omega}_B) \end{bmatrix} \begin{bmatrix} \mathbf{v}_B \\ \boldsymbol{\omega}_B \\ \dot{\mathbf{q}} \end{bmatrix} \tag{2.5.1}$$

There are several variables within **Equation (2.5.1)** that must be defined and explained. The term $\mathbf{M}$ corresponds to the distributed mass matrix. In terms of the cases examined within this project, $\mathbf{M}$ corresponds to the finite element mass matrix. This finite element mass matrix $\mathbf{M}$ is cropped to allocate a single body node with the total rigid body properties (i.e. the selected node is the origin location of the body frame). More explicitly, the mass matrix is divided into a series of 'nodal blocks', as seen below.

$$\mathbf{M}_{full} = \left[\begin{array}{c|cccc} \mathbf{M}_{00} & \mathbf{M}_{01} & \mathbf{M}_{02} & \cdots & \mathbf{M}_{0N} \\ \hline \mathbf{M}_{10} & \mathbf{M}_{11} & \mathbf{M}_{12} & \cdots & \mathbf{M}_{1N} \\ \mathbf{M}_{20} & \mathbf{M}_{21} & \mathbf{M}_{22} & \cdots & \mathbf{M}_{2N} \\ \vdots & \vdots & \vdots & \ddots & \vdots \\ \mathbf{M}_{N0} & \mathbf{M}_{N1} & \mathbf{M}_{N2} & \cdots & \mathbf{M}_{NN} \end{array}\right] \tag{2.5.2}$$

The terms with zero ('0') subscripts correspond to blocks associated with the body frame origin. The node blocks are generally of the form ($\mathbf{M}_{kl}$) and effectively represent the effect of node-k on node-l. These mass nodal blocks are typically 6 x 6 matrices, assuming full order 3D motion for all nodes. The blocks may be further broken down into a collection of four 3x3 sub-blocks, which relate the translational and rotational coupling between the individual nodes.

$$\mathbf{M}_{kl} = \begin{bmatrix} \mathbf{M}_{\underline{u}_k \underline{u}_l} & \mathbf{M}_{\underline{u}_k \underline{\theta}_l} \\ \mathbf{M}_{\underline{\theta}_k \underline{u}_l} & \mathbf{M}_{\underline{\theta}_k \underline{\theta}_l} \end{bmatrix} \tag{2.5.3}$$

Here, the subscripts u and θ correspond to the translational and rotational degrees of freedom of node-k or node-l respectively. These nodal blocks will be used as the basis to define the majority of terms and coefficients in **Equation (2.5.1)**.

The total mass is a scalar quantity, and is obtained through the summation of all the differential masses within the model. i.e.

$$m = \int dm \tag{2.5.4}$$

The total first moment of mass includes consideration for both rigid and flexible inertia values that may alter the characteristics of the model as it deforms. Recall from **Equation (2.2.8)**,

$$\mathbf{c}_{tot} = \mathbf{c} + \mathbf{c}_u(\mathbf{q}) \tag{2.5.5}$$

where the rigid part of the first moment $\mathbf{c}$ is

$$\mathbf{c} = \int \mathbf{r} dm \tag{2.5.6}$$

This may also be derived from node blocks using the expression

$$\mathbf{c}^{\times} = \sum_{k=0}^{N} \sum_{l=0}^{N} \left(\mathbf{r}_k^{\times} \mathbf{M}_{u_k, u_l} + \mathbf{M}_{\theta_k, u_l} \right) \tag{2.5.7}$$

The flexible part of the first moment, denoted as $\mathbf{c}_u$ is calculated via

$$\mathbf{c}_u = \int \mathbf{u} dm = \mathbf{P}\mathbf{q} \tag{2.5.8}$$

where $\mathbf{P}$ is a 3 x N translational momentum coefficient matrix, where each *i*-th column corresponds to the translational momentum for the *i*-th node.

$$\mathbf{P} = [\mathbf{p}_1 \quad \mathbf{p}_2 \quad \cdots \quad \mathbf{p}_N]$$

A similar matrix is defined for the angular momentum.

$$\mathbf{H} = [\mathbf{h}_1 \quad \mathbf{h}_2 \quad \cdots \quad \mathbf{h}_N]$$

The second moment ($\mathbf{J}_{tot}$) is now dealt with in more detail, specifically with focus upon the case of a model derived from finite elements.

Recall from **Equation (2.2.11)** that the total second moment of inertia is given by

$$\mathbf{J}_{tot} = \mathbf{J}_{rr} + \mathbf{J}_{ru} + \mathbf{J}_{ur} + \mathbf{J}_{uu}$$

Note also that due to symmetry $\mathbf{J}_{ur} = \mathbf{J}_{ru}^T$.

The flexible components of the second moment of inertia are dependent upon the individual flexible coordinates and as yet to be determined flexible second moment coefficients. The inertia components are given by the *rigid-flexible part of the second moment*

$$\mathbf{J}_{ru} = -\int \mathbf{r}^{\times}\mathbf{u}^{\times} dm = \sum_{i=1}^{n} q_i \mathbf{J}'_{ru,i} \tag{2.5.9}$$

and the *flexible-flexible part of the second moment*

$$\mathbf{J}_{uu} = -\int \mathbf{u}^{\times}\mathbf{u}^{\times} dm = \sum_{i=1}^{n}\sum_{j=1}^{n} q_i q_j \mathbf{J}''_{uu,ij} \tag{2.5.10}$$

The second moment coefficients ($\mathbf{J}'_{ru,i}$) and ($\mathbf{J}''_{uu,ij}$) given in **Equations (2.5.9)** and **(2.5.10)** are constant and are defined with respect to the deformation shape functions. That is, the *rigid-flexible second moment coefficients* ($\mathbf{J}'_{ru,i}$) are given by

$$\mathbf{J}'_{ru,i} = -\int \mathbf{r}^{\times}\psi_i^{\times} dm \tag{2.5.11}$$

The *flexible-flexible second moment coefficients* ($\mathbf{J}''_{uu,ij}$) are given by

$$\mathbf{J}''_{uu,ij} = -\int \psi_i^{\times}\psi_j^{\times} dm \tag{2.5.12}$$

However, it is often the case that these shape functions are not readily available for a general finite element model. Therefore, it becomes necessary to utilize some approximate expressions for these coefficient terms. The approximations presented below are derived from the components of the finite-element mass matrix.

2.5.1 New Coefficient Methodology

The preceding equations represent a set of generally accepted coefficient terms and equations. This section presents a new theory for developing further equation of motion coefficient approximations.[12,13] Before presenting these approximations it is important to re-examine the nodal block structure. Each of the four (3x3) sub-blocks of $\mathbf{M}_{kl}$ may be further discretized into a set of three (3x1) $\mathbf{m}_{k,i}$ vectors. These $\mathbf{m}_{k,i}$ components serve to isolate the effect of each degree of freedom from node-l on the translational and rotation degrees of freedom of node-k. For node-k, the translational degrees of freedom are given as u_k, v_k, w_k with the rotational degrees of freedom being defined by $\alpha_k, \beta_k, \gamma_k$. That is,

$$\mathbf{M}_{kl} = \begin{bmatrix} \mathbf{M}_{\underline{u}_k,\underline{u}_l} & \mathbf{M}_{\underline{u}_k,\underline{\theta}_l} \\ \mathbf{M}_{\underline{\theta}_k,\underline{u}_l} & \mathbf{M}_{\underline{\theta}_k,\underline{\theta}_l} \end{bmatrix} = \left[\begin{array}{ccc|ccc} \mathbf{m}_{\underline{u}_k,u_l} & \mathbf{m}_{\underline{u}_k,v_l} & \mathbf{m}_{\underline{u}_k,w_l} & \mathbf{m}_{\underline{u}_k,\alpha_l} & \mathbf{m}_{\underline{u}_k,\beta_l} & \mathbf{m}_{\underline{u}_k,\gamma_l} \\ \mathbf{m}_{\underline{\theta}_k,u_l} & \mathbf{m}_{\underline{\theta}_k,v_l} & \mathbf{m}_{\underline{\theta}_k,w_l} & \mathbf{m}_{\underline{\theta}_k,\alpha_l} & \mathbf{m}_{\underline{\theta}_k,\beta_l} & \mathbf{m}_{\underline{\theta}_k,\gamma_l} \end{array}\right] \tag{2.5.13}$$

The approximation for the *rigid-flexible second moment coefficient* is

$$\mathbf{J}'_{ru,i} \approx \tilde{\mathbf{J}}'_{ru,i} = -\sum_{l=0}^{N} \mathbf{r}_l^{\times} \mathbf{m}_{u_l,i}^{\times} \tag{2.5.14}$$

The process for determining the flexible-flexible second moment coefficients ($\mathbf{J}''_{uu,ij}$) is a bit more involved. It is important to introduce a few terms before proceeding. Prior to being used in the $\mathbf{J}''_{uu,ij}$ computation, the $\mathbf{M}_{kl}$ nodal block sub-components in **Equation (2.5.3)** are averaged using the following expressions. Translation-translation mass sub-blocks are defined by

$$\overline{\mathbf{M}}_{\underline{u}_k,\underline{u}_l} = \tfrac{1}{3} trace\left(\mathbf{M}_{\underline{u}_k,\underline{u}_l}\right)\mathbf{1} \tag{2.5.15}$$

Translation-rotation mass sub-blocks are defined by

$$\overline{\mathbf{M}}_{\underline{u}_k,\underline{\theta}_l} = \tfrac{1}{2}\left(\mathbf{M}_{\underline{u}_k,\underline{\theta}_l} - \mathbf{M}^T_{\underline{u}_k,\underline{\theta}_l}\right) \tag{2.5.16}$$

Rotation-translation mass sub-blocks are defined by

$$\overline{\mathbf{M}}_{\underline{\theta}_k,\underline{u}_l} = \tfrac{1}{2}\left(\mathbf{M}_{\underline{\theta}_k,\underline{u}_l} - \mathbf{M}^T_{\underline{\theta}_k,\underline{u}_l}\right) \tag{2.5.17}$$

Rotation-rotation mass sub-blocks are defined by

$$\overline{\mathbf{M}}_{\underline{\theta}_k,\underline{\theta}_l} = \mathbf{M}_{\underline{\theta}_k,\underline{\theta}_l} \tag{2.5.18}$$

Additional pertinent quantities are as follows:

$$\overline{\mathbf{Q}}_{kl} = \tfrac{1}{2} trace\left(\mathbf{M}_{\underline{\theta}_k,\underline{\theta}_l}\right)\mathbf{1} - \mathbf{M}_{\underline{\theta}_k,\underline{\theta}_l} \tag{2.5.19}$$

$$\overline{\mathbf{h}}^{\times}_{kl} = \mathbf{M}^T_{\underline{\theta}_k,\underline{\theta}_l} - \mathbf{M}_{\underline{\theta}_k,\underline{\theta}_l} \tag{2.5.20}$$

Note that the overbar "—" is used to denote an average value. The body frame unit vectors are given as

$$\hat{\mathbf{x}} = [1 \quad 0 \quad 0]^T$$

$$\hat{\mathbf{y}} = [0 \quad 1 \quad 0]^T$$

$$\hat{\mathbf{z}} = [0 \quad 0 \quad 1]^T \tag{2.5.21}$$

The $\mathbf{J}''_{uu,ij}$ approximations are now presented in the following four tables:

Node-k (translation) + node-l (translation)

$\tilde{\mathbf{J}}''_{uu,ij}$	u_l	v_l	w_l
u_k	$-\hat{\mathbf{x}}^{\times}\overline{\mathbf{M}}_{\underline{u}_k,\underline{u}_l}\hat{\mathbf{x}}^{\times}$	$-\hat{\mathbf{x}}^{\times}\overline{\mathbf{M}}_{\underline{u}_k,\underline{u}_l}\hat{\mathbf{y}}^{\times}$	$-\hat{\mathbf{x}}^{\times}\overline{\mathbf{M}}_{\underline{u}_k,\underline{u}_l}\hat{\mathbf{z}}^{\times}$
v_k	$-\hat{\mathbf{y}}^{\times}\overline{\mathbf{M}}_{\underline{u}_k,\underline{u}_l}\hat{\mathbf{x}}^{\times}$	$-\hat{\mathbf{y}}^{\times}\overline{\mathbf{M}}_{\underline{u}_k,\underline{u}_l}\hat{\mathbf{y}}^{\times}$	$-\hat{\mathbf{y}}^{\times}\overline{\mathbf{M}}_{\underline{u}_k,\underline{u}_l}\hat{\mathbf{z}}^{\times}$
w_k	$-\hat{\mathbf{z}}^{\times}\overline{\mathbf{M}}_{\underline{u}_k,\underline{u}_l}\hat{\mathbf{x}}^{\times}$	$-\hat{\mathbf{z}}^{\times}\overline{\mathbf{M}}_{\underline{u}_k,\underline{u}_l}\hat{\mathbf{y}}^{\times}$	$-\hat{\mathbf{z}}^{\times}\overline{\mathbf{M}}_{\underline{u}_k,\underline{u}_l}\hat{\mathbf{z}}^{\times}$

Table 2.1: $\tilde{\mathbf{J}}''_{uu,ij}$ Translation-Translation Approximations

Node-k (translation) + node-l (rotation)

$\tilde{\mathbf{J}}''_{uu,ij}$	α_l	β_l	γ_l
u_k	$\left(\hat{\mathbf{x}}^T\overline{\mathbf{M}}_{\underline{u}_k,\underline{\theta}_l}\hat{\mathbf{x}}\right)\mathbf{1}-\overline{\mathbf{M}}_{\underline{u}_k,\underline{\theta}_l}\hat{\mathbf{x}}\hat{\mathbf{x}}^T$	$\left(\hat{\mathbf{x}}^T\overline{\mathbf{M}}_{\underline{u}_k,\underline{\theta}_l}\hat{\mathbf{y}}\right)\mathbf{1}-\overline{\mathbf{M}}_{\underline{u}_k,\underline{\theta}_l}\hat{\mathbf{y}}\hat{\mathbf{x}}^T$	$\left(\hat{\mathbf{x}}^T\overline{\mathbf{M}}_{\underline{u}_k,\underline{\theta}_l}\hat{\mathbf{z}}\right)\mathbf{1}-\overline{\mathbf{M}}_{\underline{u}_k,\underline{\theta}_l}\hat{\mathbf{z}}\hat{\mathbf{x}}^T$
v_k	$\left(\hat{\mathbf{y}}^T\overline{\mathbf{M}}_{\underline{u}_k,\underline{\theta}_l}\hat{\mathbf{x}}\right)\mathbf{1}-\overline{\mathbf{M}}_{\underline{u}_k,\underline{\theta}_l}\hat{\mathbf{x}}\hat{\mathbf{y}}^T$	$\left(\hat{\mathbf{y}}^T\overline{\mathbf{M}}_{\underline{u}_k,\underline{\theta}_l}\hat{\mathbf{y}}\right)\mathbf{1}-\overline{\mathbf{M}}_{\underline{u}_k,\underline{\theta}_l}\hat{\mathbf{y}}\hat{\mathbf{y}}^T$	$\left(\hat{\mathbf{y}}^T\overline{\mathbf{M}}_{\underline{u}_k,\underline{\theta}_l}\hat{\mathbf{z}}\right)\mathbf{1}-\overline{\mathbf{M}}_{\underline{u}_k,\underline{\theta}_l}\hat{\mathbf{z}}\hat{\mathbf{y}}^T$
w_k	$\left(\hat{\mathbf{z}}^T\overline{\mathbf{M}}_{\underline{u}_k,\underline{\theta}_l}\hat{\mathbf{x}}\right)\mathbf{1}-\overline{\mathbf{M}}_{\underline{u}_k,\underline{\theta}_l}\hat{\mathbf{x}}\hat{\mathbf{z}}^T$	$\left(\hat{\mathbf{z}}^T\overline{\mathbf{M}}_{\underline{u}_k,\underline{\theta}_l}\hat{\mathbf{y}}\right)\mathbf{1}-\overline{\mathbf{M}}_{\underline{u}_k,\underline{\theta}_l}\hat{\mathbf{y}}\hat{\mathbf{z}}^T$	$\left(\hat{\mathbf{z}}^T\overline{\mathbf{M}}_{\underline{u}_k,\underline{\theta}_l}\hat{\mathbf{z}}\right)\mathbf{1}-\overline{\mathbf{M}}_{\underline{u}_k,\underline{\theta}_l}\hat{\mathbf{z}}\hat{\mathbf{z}}^T$

Table 2.2: $\tilde{\mathbf{J}}''_{uu,ij}$ Translation-Rotation Approximations

Node-k (rotation) + Node-l (translation)

$\tilde{\mathbf{J}}''_{uu,ij}$	u_l	v_l	w_l
α_k	$\left(\hat{\mathbf{x}}^T\overline{\mathbf{M}}_{\underline{\theta}_k,\underline{u}_l}\hat{\mathbf{x}}\right)\mathbf{1}-\hat{\mathbf{x}}\hat{\mathbf{x}}^T\overline{\mathbf{M}}_{\underline{\theta}_k,\underline{u}_l}$	$\left(\hat{\mathbf{x}}^T\overline{\mathbf{M}}_{\underline{\theta}_k,\underline{u}_l}\hat{\mathbf{y}}\right)\mathbf{1}-\hat{\mathbf{y}}\hat{\mathbf{x}}^T\overline{\mathbf{M}}_{\underline{\theta}_k,\underline{u}_l}$	$\left(\hat{\mathbf{x}}^T\overline{\mathbf{M}}_{\underline{\theta}_k,\underline{u}_l}\hat{\mathbf{z}}\right)\mathbf{1}-\hat{\mathbf{z}}\hat{\mathbf{x}}^T\overline{\mathbf{M}}_{\underline{\theta}_k,\underline{u}_l}$
β_k	$\left(\hat{\mathbf{y}}^T\overline{\mathbf{M}}_{\underline{\theta}_k,\underline{u}_l}\hat{\mathbf{x}}\right)\mathbf{1}-\hat{\mathbf{x}}\hat{\mathbf{y}}^T\overline{\mathbf{M}}_{\underline{\theta}_k,\underline{u}_l}$	$\left(\hat{\mathbf{y}}^T\overline{\mathbf{M}}_{\underline{\theta}_k,\underline{u}_l}\hat{\mathbf{y}}\right)\mathbf{1}-\hat{\mathbf{y}}\hat{\mathbf{y}}^T\overline{\mathbf{M}}_{\underline{\theta}_k,\underline{u}_l}$	$\left(\hat{\mathbf{y}}^T\overline{\mathbf{M}}_{\underline{\theta}_k,\underline{u}_l}\hat{\mathbf{z}}\right)\mathbf{1}-\hat{\mathbf{z}}\hat{\mathbf{y}}^T\overline{\mathbf{M}}_{\underline{\theta}_k,\underline{u}_l}$
γ_k	$\left(\hat{\mathbf{z}}^T\overline{\mathbf{M}}_{\underline{\theta}_k,\underline{u}_l}\hat{\mathbf{x}}\right)\mathbf{1}-\hat{\mathbf{x}}\hat{\mathbf{z}}^T\overline{\mathbf{M}}_{\underline{\theta}_k,\underline{u}_l}$	$\left(\hat{\mathbf{z}}^T\overline{\mathbf{M}}_{\underline{\theta}_k,\underline{u}_l}\hat{\mathbf{y}}\right)\mathbf{1}-\hat{\mathbf{y}}\hat{\mathbf{z}}^T\overline{\mathbf{M}}_{\underline{\theta}_k,\underline{u}_l}$	$\left(\hat{\mathbf{z}}^T\overline{\mathbf{M}}_{\underline{\theta}_k,\underline{u}_l}\hat{\mathbf{z}}\right)\mathbf{1}-\hat{\mathbf{z}}\hat{\mathbf{z}}^T\overline{\mathbf{M}}_{\underline{\theta}_k,\underline{u}_l}$

Table 2.3: $\tilde{\mathbf{J}}''_{uu,ij}$ Rotation-Translation Approximations

Node-k (rotation) + Node-l (rotation)

$\tilde{\mathbf{J}}''_{uu,ij}$	α_l	β_l	γ_l
α_k	$\left(\hat{\mathbf{x}}^T\overline{\mathbf{M}}_{\underline{\theta}_k,\underline{\theta}_l}\hat{\mathbf{x}}\right)\mathbf{1}-\hat{\mathbf{x}}^\times\overline{\mathbf{Q}}_{kl}\hat{\mathbf{x}}^\times$	$\left(\hat{\mathbf{x}}^T\overline{\mathbf{M}}_{\underline{\theta}_k,\underline{\theta}_l}\hat{\mathbf{y}}\right)\mathbf{1}-\hat{\mathbf{y}}^\times\overline{\mathbf{Q}}_{kl}\hat{\mathbf{x}}^\times$	$\left(\hat{\mathbf{x}}^T\overline{\mathbf{M}}_{\underline{\theta}_k,\underline{\theta}_l}\hat{\mathbf{z}}\right)\mathbf{1}-\hat{\mathbf{z}}^\times\overline{\mathbf{Q}}_{kl}\hat{\mathbf{x}}^\times$
β_k	$\left(\hat{\mathbf{y}}^T\overline{\mathbf{M}}_{\underline{\theta}_k,\underline{\theta}_l}\hat{\mathbf{x}}\right)\mathbf{1}-\hat{\mathbf{x}}^\times\overline{\mathbf{Q}}_{kl}\hat{\mathbf{y}}^\times$	$\left(\hat{\mathbf{y}}^T\overline{\mathbf{M}}_{\underline{\theta}_k,\underline{\theta}_l}\hat{\mathbf{y}}\right)\mathbf{1}-\hat{\mathbf{y}}^\times\overline{\mathbf{Q}}_{kl}\hat{\mathbf{y}}^\times$	$\left(\hat{\mathbf{y}}^T\overline{\mathbf{M}}_{\underline{\theta}_k,\underline{\theta}_l}\hat{\mathbf{z}}\right)\mathbf{1}-\hat{\mathbf{z}}^\times\overline{\mathbf{Q}}_{kl}\hat{\mathbf{y}}^\times$
γ_k	$\left(\hat{\mathbf{z}}^T\overline{\mathbf{M}}_{\underline{\theta}_k,\underline{\theta}_l}\hat{\mathbf{x}}\right)\mathbf{1}-\hat{\mathbf{x}}^\times\overline{\mathbf{Q}}_{kl}\hat{\mathbf{z}}^\times$	$\left(\hat{\mathbf{z}}^T\overline{\mathbf{M}}_{\underline{\theta}_k,\underline{\theta}_l}\hat{\mathbf{y}}\right)\mathbf{1}-\hat{\mathbf{y}}^\times\overline{\mathbf{Q}}_{kl}\hat{\mathbf{z}}^\times$	$\left(\hat{\mathbf{z}}^T\overline{\mathbf{M}}_{\underline{\theta}_k,\underline{\theta}_l}\hat{\mathbf{z}}\right)\mathbf{1}-\hat{\mathbf{z}}^\times\overline{\mathbf{Q}}_{kl}\hat{\mathbf{z}}^\times$

Table 2.4: $\tilde{\mathbf{J}}''_{uu,ij}$ Rotation-Rotation Approximations

The development and approximation of these second moment of inertia terms is discussed and presented in greater detail in the papers by McTavish et al.[12,13,15]

The total angular momentum coefficient is comprised of a rigid and flexible part, as seen by the equation,

$$\mathbf{H}_{tot} = \mathbf{H} + \mathbf{H}_u(\mathbf{q}) \tag{2.5.22}$$

The rigid translational and angular momentum coefficients (as mentioned previously) can be calculated utilizing the full order mass matrix and the mass nodal blocks by performing the following operation:

$$\begin{bmatrix} \mathbf{P}_k \\ \mathbf{H}_k \end{bmatrix} = \sum_{l=0}^{N} \mathbf{R}_l^T \mathbf{M}_{lk} \tag{2.5.23}$$

where $\mathbf{R}_k$ is a matrix which relates the position of node-k. $\mathbf{R}_k$ is defined as,

$$\mathbf{R}_k = \begin{bmatrix} \mathbf{1} & -\mathbf{r}_k^{\times} \\ \mathbf{0} & \mathbf{1} \end{bmatrix} \tag{2.5.24}$$

The rigid-body mass properties may also be extracted directly from the finite element mass matrix via the following relation.

$$\begin{bmatrix} m\mathbf{1} & -\mathbf{c}^{\times} \\ \mathbf{c}^{\times} & \mathbf{J} \end{bmatrix} = \sum_{k=0}^{N} \sum_{l=0}^{N} \mathbf{R}_k^T \mathbf{M}_{kl} \mathbf{R}_l \tag{2.5.25}$$

Note that **Equation (2.5.25)** only calculates the fixed (constant) inertia mass matrix, and does not include the determination of flexible inertia terms. This computation may be useful as a reference check to verify the accuracy of the finite element model versus any manual calculations or previously known mass properties.

The flexible angular momentum component is defined via

$$\mathbf{H}_u = \sum_{i=1}^{n} q_i \mathbf{H}'_i \tag{2.5.26}$$

where $\mathbf{H}'_i$ is the flexible angular momentum coefficient and is of the form,

$$\mathbf{H}'_i = \left[\mathbf{H}'_{i,\underline{u}_1} \quad \mathbf{H}'_{i,\underline{\theta}_1} \mid \mathbf{H}'_{i,\underline{u}_1} \quad \mathbf{H}'_{i,\underline{\theta}_2} \mid \cdots \mid \mathbf{H}'_{i,\underline{u}_N} \quad \mathbf{H}'_{i,\underline{\theta}_N} \right]$$

A $\mathbf{H}'_i$ coefficient will exist for each degree of freedom in the model (i = 1,2...N). The coefficients are separated into translational and rotational components of node-k, as seen in the following tables.

Node-k (translation) – Node-l

i	$\mathbf{H}'_{i,\underline{u}_l}$	$\mathbf{H}'_{i,\underline{\theta}_l}$
u_k	$\hat{\mathbf{x}}^{\times}\overline{\mathbf{M}}_{\underline{u}_k,\underline{u}_l}$	$\hat{\mathbf{x}}^{\times}\overline{\mathbf{M}}_{\underline{u}_k,\underline{\theta}_l}$
v_k	$\hat{\mathbf{y}}^{\times}\overline{\mathbf{M}}_{\underline{u}_k,\underline{u}_l}$	$\hat{\mathbf{y}}^{\times}\overline{\mathbf{M}}_{\underline{u}_k,\underline{\theta}_l}$
w_k	$\hat{\mathbf{z}}^{\times}\overline{\mathbf{M}}_{\underline{u}_k,\underline{u}_l}$	$\hat{\mathbf{z}}^{\times}\overline{\mathbf{M}}_{\underline{u}_k,\underline{\theta}_l}$

Table 2.5: $\mathbf{H}'_i$ Translation Approximations

Node-k (rotation) – Node-l

i	$\mathbf{H}'_{i,\underline{u}_l}$	$\mathbf{H}'_{i,\underline{\theta}_l}$
α_k	$-\left(\overline{\mathbf{M}}_{\underline{\theta}_k,\underline{u}_l}\hat{\mathbf{x}}\right)^{\times}$	$\left(\hat{\mathbf{x}}^T\overline{\mathbf{h}}_{kl}\right)\mathbf{1}+\overline{\mathbf{Q}}_{kl}\hat{\mathbf{x}}^{\times}$
β_k	$-\left(\overline{\mathbf{M}}_{\underline{\theta}_k,\underline{u}_l}\hat{\mathbf{y}}\right)^{\times}$	$\left(\hat{\mathbf{y}}^T\overline{\mathbf{h}}_{kl}\right)\mathbf{1}+\overline{\mathbf{Q}}_{kl}\hat{\mathbf{y}}^{\times}$
γ_k	$-\left(\overline{\mathbf{M}}_{\underline{\theta}_k,\underline{u}_l}\hat{\mathbf{z}}\right)^{\times}$	$\left(\hat{\mathbf{z}}^T\overline{\mathbf{h}}_{kl}\right)\mathbf{1}+\overline{\mathbf{Q}}_{kl}\hat{\mathbf{z}}^{\times}$

Table 2.6: $\mathbf{H}'_i$ Rotation Approximations

Next, the Coriolis terms from the equations of motion are discussed and presented. The translational Coriolis matrix term ($\mathbf{P}_{\omega}$) is found by

$$\mathbf{P}_{\omega} = \boldsymbol{\omega}_B^{\times}\mathbf{P} \tag{2.5.27}$$

The total rotational Coriolis matrix ($\mathbf{H}_{\omega,tot}$) is comprised of a rigid and flexible component, and is given via

$$\mathbf{H}_{\omega,tot} = \mathbf{H}_{\omega}(\omega_B)+\mathbf{H}_{\omega u}(\omega_B,\mathbf{q}) \tag{2.5.28}$$

The rigid component is defined with the following format:

$$\mathbf{H}_{\omega}(\boldsymbol{\omega}_B)=\begin{bmatrix}\mathbf{h}_{\omega,1} & \mathbf{h}_{\omega,2} & \cdots & \mathbf{h}_{\omega,N}\end{bmatrix}$$

The respective elements of $\mathbf{H}_{\omega}$ are

$$\mathbf{h}_{\omega,i} = \mathbf{J}'_{ru,i}\,\boldsymbol{\omega}_B \tag{2.5.29}$$

The flexible component is defined as

$$\mathbf{H}_{\omega u}(\boldsymbol{\omega}_B, \mathbf{q}) = \begin{bmatrix} \mathbf{h}_{\omega u,1} & \mathbf{h}_{\omega u,2} & \cdots & \mathbf{h}_{\omega u,N} \end{bmatrix}$$

with the respective elements being

$$\mathbf{h}_{\omega u,i} = \sum_{j=1}^{n} q_j \mathbf{J}''_{uu,ji}\, \boldsymbol{\omega}_B \tag{2.5.30}$$

The final Coriolis term is the flexible Coriolis matrix ($\mathbf{M}_\omega$), and is defined by

$$\mathbf{M}_\omega = \begin{bmatrix} \boldsymbol{\omega}_B^T \mathbf{H}'_1 \\ \boldsymbol{\omega}_B^T \mathbf{H}'_2 \\ \vdots \\ \boldsymbol{\omega}_B^T \mathbf{H}'_4 \end{bmatrix} \tag{2.5.31}$$

The force vector in **Equation (2.5.1)** is given by $\begin{bmatrix} \mathbf{F} & \mathbf{G} & \mathbf{f} \end{bmatrix}^T$ where $\mathbf{F}$ and $\mathbf{G}$ are the net external force and torques acting upon the body.

The term $\mathbf{f}$ corresponds to the external forces acting upon the flexible coordinates through body and surface loadings. The term $\mathbf{f}_\sigma$ corresponds to the internal forces developed by the structural model. For simple cases, it may be assumed that the model exhibit linear elastic behaviour. The internal force vector is then strictly a function of elemental stiffness and flexible deformation. Thus,

$$\mathbf{f}_\sigma = \mathbf{K}\mathbf{q} \tag{2.5.32}$$

where $\mathbf{K}$ is the stiffness matrix associated with the model.

Other behavioral models are acceptable, including the cases that consider the effects of viscous damping.

Chapter 3: Reduced-Order Model (ROM)

The focus of this chapter is to elaborate on the nature of reduced-order modeling. The following sections address the concepts required to adequately model a sophisticated structure while maintaining a manageable number of degrees of freedom.[13]

3.1 Reduced-Order Model Basics

As mentioned previously, the reduced order model decreases the numerical order of the original structure by considering a series of user selected shape functions to represent the overall flexibility modes of the system. The shape functions can be taken as the deflections of the structure as a whole and/or with consideration as to the flexibility of individual components. The displacement vector corresponding to the reduced set is presented in a form similar to that of **Equation (2.3.1)**, with full order quantities q and ψ being replaced with the reduced order quantities η, and φ.

$$\mathbf{u}(\mathbf{r},t)=\sum_{m=1}^{M}\eta_m(t)\varphi_m(\mathbf{r}) \tag{3.1.1}$$

or expressed in matrix form,

$$\mathbf{u}(\mathbf{r},t)=\Phi(\mathbf{r})\eta(t) \tag{3.1.2}$$

where η is the vector of generalized reduced order coordinates, and Φ is the matrix of reduced order shape functions, that is,

$$\Phi=[\Phi_1 \quad \Phi_2 \quad \cdots \quad \Phi_M] \qquad \eta=[\eta_1 \quad \eta_2 \quad \cdots \quad \eta_M]^T$$

The reduced order shape function set Φ is related to the full order shape function set Ψ via the following relation:

$$\Phi(\mathbf{r})=\Psi(\mathbf{r})\mathbf{S}^T \tag{3.1.3}$$

where S is an (N x M) matrix of M (N x 1) coordinate vectors, which define the reduced order mode shapes from the full order set that is,

$$\mathbf{S} = [\mathbf{s}_1 \quad \mathbf{s}_2 \quad \cdots \quad \mathbf{s}_M]$$

3.2 Reduced Order Property Adjustment

Having established the chosen set of shape functions that will adequately capture the flexibility of a structure under study, the structural model parameters must be similarly reduced. This reduction is a relatively simple transformation involving the matrix of coordinate mode vectors $\mathbf{S}$ as defined in the previous section. An overbar '—' will now be employed to signify a reduced property within the nomenclature.

$$\begin{bmatrix} m\mathbf{1} & -\bar{\mathbf{c}}^{\times}_{tot} & \bar{\mathbf{P}} \\ \bar{\mathbf{c}}^{\times}_{tot} & \bar{\mathbf{J}}_{tot} & \bar{\mathbf{H}}_{tot} \\ \bar{\mathbf{P}}^{T} & \bar{\mathbf{H}}^{T}_{tot} & \bar{\mathbf{M}} \end{bmatrix} \begin{bmatrix} \dot{\mathbf{v}}_B \\ \dot{\boldsymbol{\omega}}_B \\ \ddot{\boldsymbol{\eta}} \end{bmatrix} = \begin{bmatrix} \mathbf{F} \\ \mathbf{G} \\ \bar{\mathbf{f}} \end{bmatrix} - \begin{bmatrix} \mathbf{0} \\ \mathbf{0} \\ \bar{\mathbf{f}}_{\sigma} \end{bmatrix} - \begin{bmatrix} m\boldsymbol{\omega}^{\times}_B & -\boldsymbol{\omega}^{\times}_B \bar{\mathbf{c}}^{\times}_{tot} & 2\bar{\mathbf{P}}_{\omega} \\ \bar{\mathbf{c}}^{\times}_{tot}\boldsymbol{\omega}^{\times}_B & \boldsymbol{\omega}^{\times}_B \bar{\mathbf{J}}_{tot} & 2\bar{\mathbf{H}}_{\omega,tot}(\boldsymbol{\omega}_B) \\ -\bar{\mathbf{P}}^{T}_{\omega} & -\bar{\mathbf{H}}^{T}_{\omega,tot}(\boldsymbol{\omega}_B) & -2\bar{\mathbf{M}}_{\omega}(\boldsymbol{\omega}_B) \end{bmatrix} \begin{bmatrix} \mathbf{v}_B \\ \boldsymbol{\omega}_B \\ \dot{\boldsymbol{\eta}} \end{bmatrix} \tag{3.2.1}$$

Thus, the mass and momentum coefficients may be reduced as follows. For the flexible mass matrix,

$$\bar{\mathbf{M}} = \mathbf{S}^T \mathbf{M} \mathbf{S} \tag{3.2.2}$$

For the translational momentum coefficient

$$\bar{\mathbf{P}} = \mathbf{P}\mathbf{S} \tag{3.2.3}$$

For the 'total' angular momentum coefficient

$$\bar{\mathbf{H}}_{tot} = \bar{\mathbf{H}} + \bar{\mathbf{H}}_u \tag{3.2.4}$$

where the rigid component is

$$\bar{\mathbf{H}} = \mathbf{H}\mathbf{S} \tag{3.2.5}$$

and the flexible component is given as

$$\bar{\mathbf{H}}_u = \sum_{m=1}^{M} \eta_m \mathbf{H}'_m \tag{3.2.6}$$

The reduced angular momentum coefficient ($\mathbf{H}'_m$) is defined as

$$\mathbf{H'}_m = \sum_{i=1}^{n} s_{m,i}(\mathbf{H'}_i \mathbf{S}) \tag{3.2.7}$$

The reduced model inertias are now given by their reduced components

$$\bar{\mathbf{c}}_{tot} = \mathbf{c} + \bar{\mathbf{c}}_u \tag{3.2.8}$$

$$\bar{\mathbf{J}}_{tot} = \mathbf{J} + \bar{\mathbf{J}}_{ru} + \bar{\mathbf{J}}_{ru}^T + \bar{\mathbf{J}}_{uu} \tag{3.2.9}$$

The respective reduced components of these two equations are summarized below. The flexible component of the first moment is

$$\bar{\mathbf{c}}_u = \bar{\mathbf{P}}\boldsymbol{\eta} \tag{3.2.10}$$

The rigid/flexible component of the second moment is

$$\bar{\mathbf{J}}_{ru} = \sum_{m=1}^{M} \eta_m \bar{\mathbf{J}}'_{ru,m} \tag{3.2.11}$$

The flexible/flexible component of the second moment is

$$\bar{\mathbf{J}}_{uu} = \sum_{m=1}^{M}\sum_{p=1}^{M} \eta_m \eta_p \bar{\mathbf{J}}''_{uu,mp} \tag{3.2.12}$$

Equations (3.2.11) and **(3.2.12)** have constant components $\bar{\mathbf{J}}'_{ru,m}$ and $\bar{\mathbf{J}}''_{uu,mp}$ that are named and defined below. The *constant second moment coefficient* (rigid-flexible component) is

$$\bar{\mathbf{J}}'_{ru,m} = \sum_{i=1}^{n} s_{m,i} \mathbf{J}'_{ru,i} \tag{3.2.13}$$

The *constant second moment coefficient* (flexible-flexible component) is

$$\bar{\mathbf{J}}''_{uu,mp} = \sum_{i=1}^{n}\sum_{j=1}^{n} s_{m,i} s_{p,j} \mathbf{J}''_{uu,ij} \tag{3.2.14}$$

The Coriolis terms are reduced as follows. The *translational Coriolis matrix* is given by

$$\bar{\mathbf{P}}_\omega = \boldsymbol{\omega}_B^{\times} \bar{\mathbf{P}} \tag{3.2.15}$$

The rotational Coriolis *matrix* is given by

$$\overline{\mathbf{H}}_{\omega,tot} = \overline{\mathbf{H}}_{\omega} + \overline{\mathbf{H}}_{\omega u} \tag{3.2.16}$$

The rigid part of the rotational Coriolis matrix is of the form

$$\overline{\mathbf{H}}_{\omega} = \left[\overline{\mathbf{h}}_{\omega,1} \quad \cdots \quad \overline{\mathbf{h}}_{\omega,M}\right]$$

The individual components then become

$$\overline{\mathbf{h}}_{\omega,m} = \overline{\mathbf{J}}'_{ru,m}\,\boldsymbol{\omega}_B \tag{3.2.17}$$

The flexible rotational Coriolis component is of the form

$$\overline{\mathbf{H}}_{\omega u} = \left[\overline{\mathbf{h}}_{\omega u,1} \quad \cdots \quad \overline{\mathbf{h}}_{\omega u,M}\right]$$

where $\overline{\mathbf{h}}_{\omega u,m} = \sum_{p=1}^{M} \eta_p \overline{\mathbf{J}}''_{uu,pm}\boldsymbol{\omega}_B$ (3.2.18)

The nodal forces must undergo a similar transformation, namely,

$$\overline{\mathbf{f}} = \mathbf{S}^T\mathbf{f} \tag{3.2.19}$$

For the case of simple linear elasticity, the stiffness matrix $\mathbf{K}$ is adjusted via

$$\overline{\mathbf{K}} = \mathbf{S}^T\mathbf{K}\mathbf{S} \tag{3.2.20}$$

Lastly the centripetal force term $\mathbf{H}_{\omega}^{T}(\boldsymbol{\omega}_B)$ is transformed by reducing the individual components of $\mathbf{H}_{\omega}^{T}(\boldsymbol{\omega}_B)$. That is,

$$\overline{\mathbf{h}}_{\omega,i} \approx \overline{\mathbf{J}}'_i\boldsymbol{\omega}_B \tag{3.2.21}$$

where

$$\overline{\mathbf{J}}' = \sum_i s_i\mathbf{J}'_i \tag{3.2.22}$$

where s_i's are the scalar components of a shape vector s for the *i*-th degree of freedom.

3.3 Mode Fixity Adjustment

In the current context, the location of the body frame is fixed with respect to the structural model, and thus some adjustments need to be made for any

deformation shape that does not implicitly constrain the flexible deformation of the zeroth node to zero. An example of such a shape might be an unconstrained 'free-free' vibration mode for a given model, where the node corresponding to the body frame origin is arbitrarily deformed. The deformation shape must then be translated and rotated such that the location and orientation of the zeroth node are reset to zero. This adjusted shape may now be used since the deformation at the zeroth node is always zero.

Recall that a shape vector is given in the form

$$\underline{\mathbf{s}} = \begin{bmatrix} \underline{\mathbf{q}}_0 \\ \underline{\mathbf{q}}_1 \\ \vdots \\ \underline{\mathbf{q}}_N \end{bmatrix} \qquad \text{where} \qquad \underline{\mathbf{q}}_k = \begin{bmatrix} \underline{\mathbf{u}}_k \\ \underline{\boldsymbol{\theta}}_k \end{bmatrix}$$

Note that the "underbar" is used here to indicate the *unadjusted* shape vector.

Figure 3.1 breaks down the shape adjustment process to two key steps. **Figure 3.1 a)** depicts an unadjusted rocket body bending deformation shape. For the current figure the body frame origin is assumed to be located at the tip of the fuselage nosecone. **Figure 3.1 b)** shows the translation of the rocket structure to re-position the nose for zero deformation. **Figure 3.1 c)** illustrates the rotation required to eliminate any rotational deformation of the body frame origin.

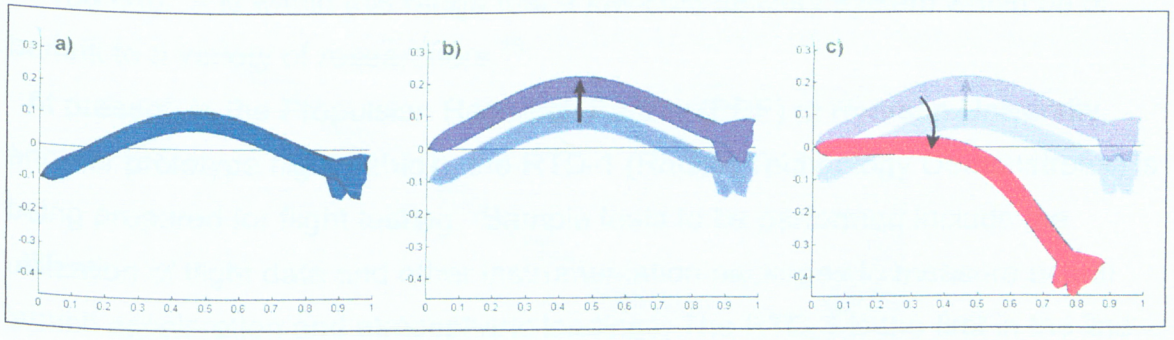

Figure 3.1: Rocket Mode Adjustment

The resulting adjustment to each node may be summarized by the following equation.

$$\begin{bmatrix} \mathbf{u}_k \\ \boldsymbol{\theta}_k \end{bmatrix} = \begin{bmatrix} \left(\mathbf{1}-\boldsymbol{\theta}_0^{\times}\right) & \mathbf{0} \\ \mathbf{0} & \left(\mathbf{1}-\boldsymbol{\theta}_0^{\times}\right) \end{bmatrix} \begin{bmatrix} \underline{\mathbf{u}}_k \\ \underline{\boldsymbol{\theta}}_k \end{bmatrix} - \begin{bmatrix} \mathbf{1} & -\mathbf{r}_k^{\times} \\ \mathbf{0} & \mathbf{1} \end{bmatrix} \begin{bmatrix} \underline{\mathbf{u}}_0 \\ \underline{\boldsymbol{\theta}}_0 \end{bmatrix} \tag{3.3.1}$$

Ignoring the small angle effect in the above equation, one can create a single matrix multiplication to accommodate the entire transformation. That is,

$$\mathbf{s} = \left[\begin{array}{c|ccc} -\mathbf{R}_1 & \mathbf{1} & \mathbf{0} & \cdots & \mathbf{0} \\ -\mathbf{R}_2 & \mathbf{0} & \mathbf{1} & \cdots & \mathbf{0} \\ \vdots & \vdots & \vdots & \ddots & \vdots \\ -\mathbf{R}_N & \mathbf{0} & \mathbf{0} & \cdots & \mathbf{1} \end{array}\right] \underline{\mathbf{s}} \tag{3.3.2}$$

where **Equation (2.5.24)** previously defined the position matrix

$$\mathbf{R}_k = \begin{bmatrix} \mathbf{1} & -\mathbf{r}_k^{\times} \\ \mathbf{0} & \mathbf{1} \end{bmatrix}$$

The transformed deformation shape will not affect the overall functionality of the reduced order set. The transformed shapes will have the same frequencies of vibration as the original unadjusted shapes and thus effectively capture the structural deformation mode.

Chapter 4: 3D Flexible Flight Simulator

The current chapter addresses issues related to the flexible flight simulation program. The program simulates the gross vehicle motions, as well as the flexible response due to the dynamic loadings acting upon the structure. The flight conditions are customizable inputs that may be tailored to suit a variety of configurations. The program was developed for use in the Matlab programming package.[17] The simulation engine also employs the SiMULINK™ suite for the processing and integration of flight dynamic parameters.

4.1 Test Vehicle – SPHADS Rocket

The primary test vehicle for this thesis is the SPHADS-1 rocket, which is currently in development at Ryerson University. The objective of the SPHADS (Small-Payload, High-Altitude Delivery System) program is to provide a relatively low cost delivery system capable of inserting scientific payloads into the upper atmosphere for meteorological, environmental, ionospheric and micro gravity studies. Some additional low-atmospheric test applications are under consideration, including high-g loading tests for payload packages, as well as the investigation of aerodynamic heating effects upon exposed materials. The initial focus of the SPHADS program is to concentrate upon the design of potential prototype variants that would operate in lower segments of the atmosphere (< 100 km). it is within this range that a low-cost delivery system would be of benefit to a variety of researchers.[18]

At present, in the Propulsion Research Facility (PRF) at Ryerson University, another prototype flight vehicle, the RTD-1 (Rocket Technology Demonstrator) is being prepared for flight testing. Sample tests to be performed include the utilization of flight data and other instrumentation packages to measure actual launch acceleration and atmospheric loadings. The RTD-1 is the first in the line of prototype vehicles to be evaluated leading up to the SPHADS vehicle. The six degree of freedom simulations presented here also serve to provide realistic

predictions of expected flight performance and structural deformations for both the SPHADS and RTD-1 flight vehicles.

The SPHADS-1 rocket will employ solid-rocket motor (SRM) technology as its primary means of propulsion. Several SRM variants are under consideration to best meet the desired flight trajectory. Two such examples of a tri-fin SPHADS vehicle are given below in **Figure 4.1**.

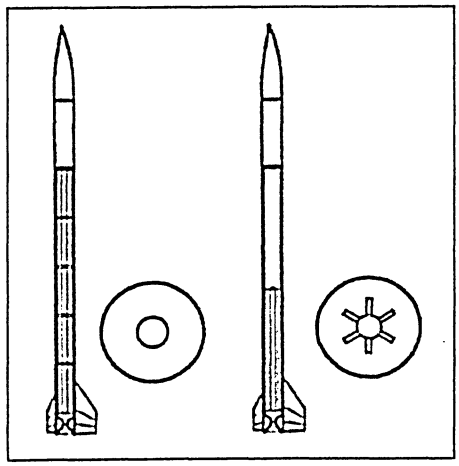

Figure 4.1 SPHADS 1A and 1B prototype vehicles

Two variations on solid rocket propellant grains are depicted, with configuration 1A employing five cylindrical propellant segments with core and end face burning. Configuration 1B employs a twin propellant boost-sustain provided by the combination of star and end burner grain segments.

Figure 4.2 depicts a model representation of quad-fin SPHADS-1 vehicle. In the model representation, the fins are treated as flat plates of constant thickness.

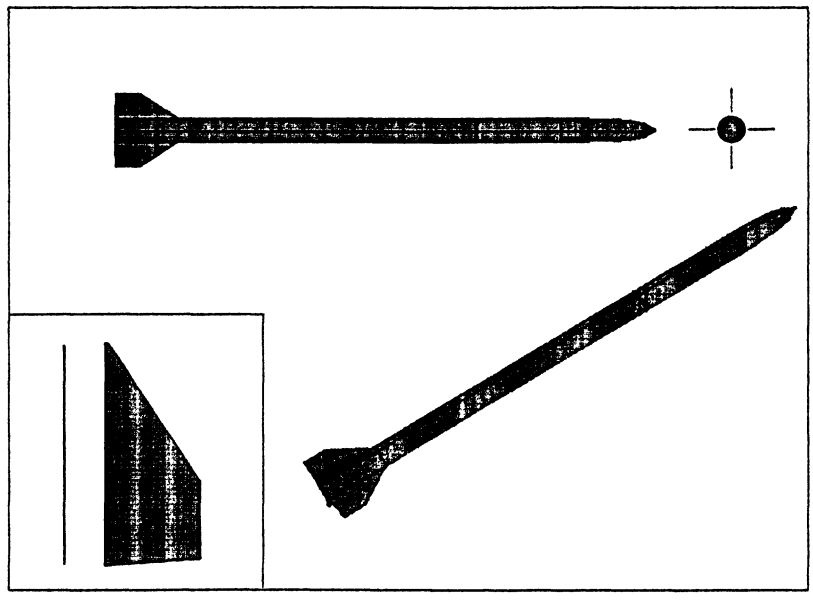

Figure 4.2: SPHADS-1 cruciform variant model

The SPHADS-1 cruciform model is taken as the basis vehicle for all of the simulations contained within this report. Some general dimensional information and characteristics are provided in **Table 4.1.**

Vehicle Length	2.75 m
Fuselage outer diameter (d)	0.127 m
Fin span (b)	0.12723 m
Root chord (c_r)	0.32468 m
Tip chord (c_t)	0.12267 m
Material	aluminum
Young's Modulus	70×10^9
Material density	2710 kg/m^3
Poisson's ratio	0.346

Table 4.1 SPHADS-1 General Properties

4.2 Simulation Capability

At present, the flight simulation engine is configured specifically for the simulation of flexible rocket vehicles. It is constructed in a modular fashion, such that the loads and dynamics are separated into individual blocks, which may be altered, updated or reconfigured as desired. As a result of the modular design, and the generality of the equations of motion presented earlier, this program may conceivably be used to simulate the motions of more complex aerodynamic vehicles such as aircraft or spacecraft. A block diagram summarizing the primary components of the Matlab/SIMULINK derived flexible body simulation model is presented in **Figure 4.3.**

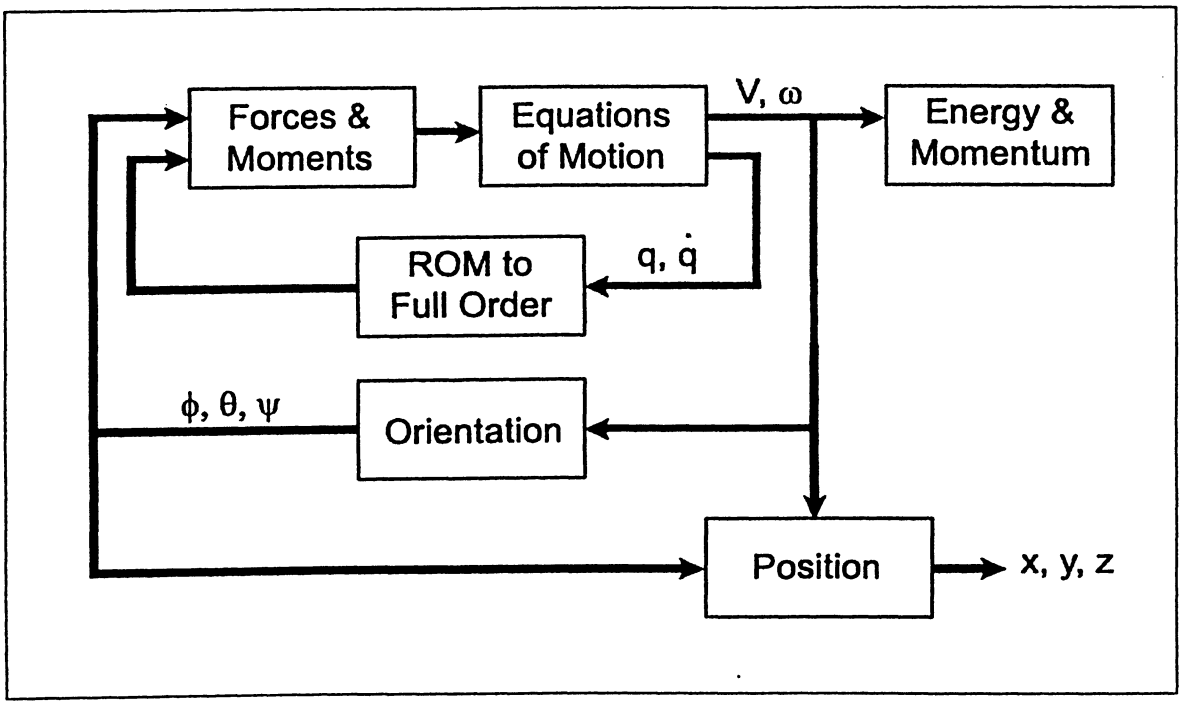

Figure 4.3: Simulation Engine Simplified Block Diagram

In **Chapter 2** the equations for defining the system dynamics were defined in the equations of motion. These equations determine the accelerations acting upon the vehicle in relation to the rigid and flexible degrees of freedom. These accelerations are then integrated to reveal the updated model rates. Referring to **Figure 4.3**, the vehicle rates of change are computed within the subsystem "Equations of Motion". This subsystem then outputs the rigid body translational and rotational velocities (v and ω), as well as the flexible-body degree of freedom rates and displacements ($\dot{q}$ and q). The external forces and torques due to gravity, thrust and aerodynamic loadings are all computed within the "Forces and Moments" subsystem. Additional key subsystems depicted pertain to orientation determination, computation of system energy and momenta, and the conversion between full and reduced order deformations and rates. In all simulations, the SIMULINK™ default integrator was employed for determining all the rigid body and flexible motions.

4.3 Rocket Deformation Shapes

The reduced order modeling method allows for the use of any number of vehicle deformation shapes. The selection of these shapes is left to the judgment of the user. It is imperative to capture the dominant deformation modes and those of particular interest to the study. For the current rocket stability study, the primary deformation shapes considered are those that act to contribute to the overall motion of the rocket fin key-nodes. These rocket key-nodes are used to represent the overall motion of a given structural component by assuming average conditions at a user-selected location. The deformation shapes are derived from the unconstrained natural vibration mode shapes. The first body bending modes are included, as well as the first fin flap and twist modes, as they are seen to have considerable influence on the motion of the fin key nodes.

Samples of these deformation shapes are depicted in **Figures 4.4** to **4.6** below. **Figure 4.4** shows the body deformation of rocket, and **Figures 4.5** and **4.6** show the deformation shapes for a single fin. Identical deformation shapes are also used for each of the remaining fins.

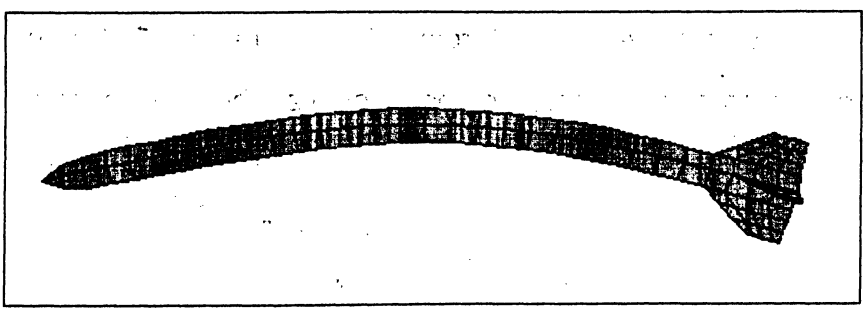

Figure 4.4: First Body Bending Shape

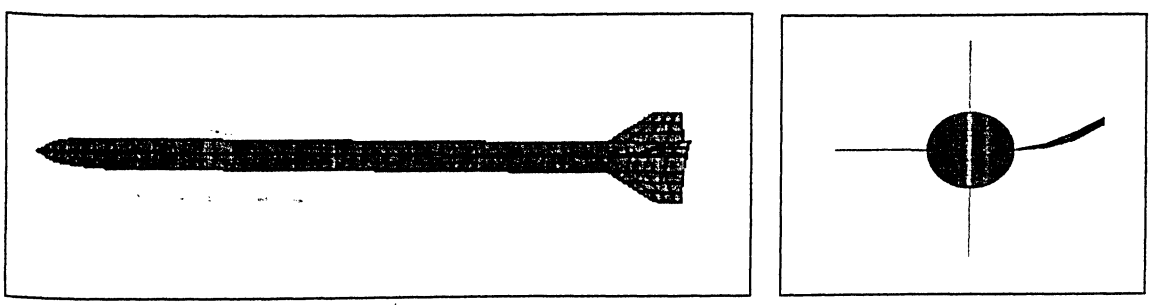

Figure 4.5: Fin Flap Deformation

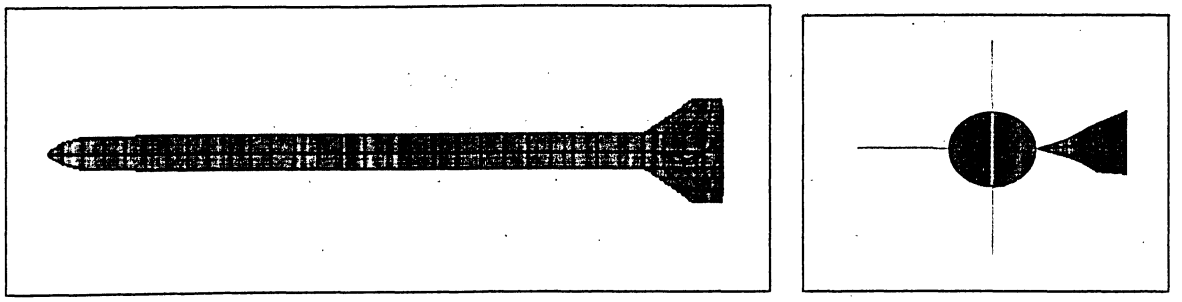

Figure 4.6: Fin Twist Deformation

4.4 Vehicle Orientation

The orientation of the body frame ($\mathcal{F}_B$) is generally defined with respect to an Earth-fixed inertial reference frame ($\mathcal{F}$) commonly located at some point of interest, such as a tracking station on the ground. Note that for long or high altitude rocket flights, the Earth-fixed reference frame is insufficient. For such cases, one might consider a rotating spherical Earth reference frame. The relationship between the inertial and body frames is depicted in **Figure 4.7**.

For the current context, the inertial reference frame is taken with the z-axis directed down towards the centre of the Earth. This is presented in **Figure 4.7**. The inertial position of the rocket is defined by the position vector $\mathbf{r}$. The orientation of the body frame ($\mathcal{F}_B$) with respect to the inertial ($\mathcal{F}$) frame is commonly defined as a set of three angles, known as the Euler angles.

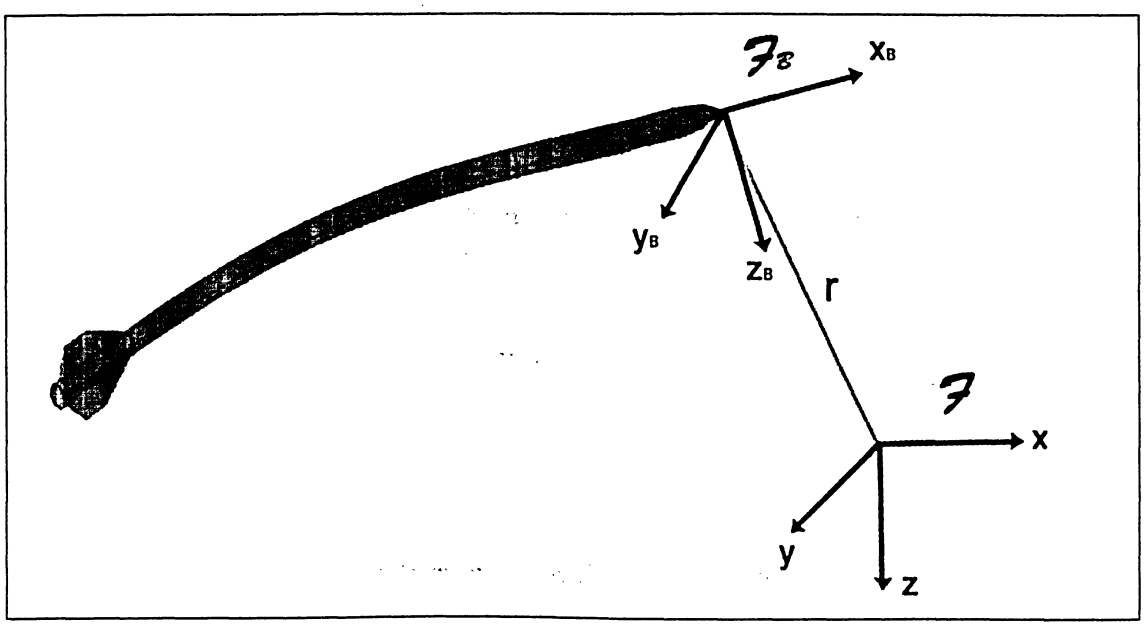

Figure 4.7: Body Frame ($\mathcal{F}_B$) and Inertial Reference Frame ($\mathcal{F}$)

4.4.1 Euler Angles

The body frame can be related to the inertial frame by a series of three rotations about the x, y and z-axes. These orientation angles are commonly referred to as roll (ϕ), pitch (θ) and yaw (ψ) angles respectively, and are a standard convention for aircraft and rockets alike.

The rotation matrices corresponding to the roll, pitch and yaw angles are defined as follows.[19]

For a rotation about the x-axis, (i.e., for a roll angle of ϕ)

$$\mathbf{C}_1(\phi)=\begin{bmatrix}1 & 0 & 0\\ 0 & \cos\phi & -\sin\phi\\ 0 & \sin\phi & \cos\phi\end{bmatrix} \tag{4.4.1}$$

For a rotation about the y-axis, (i.e., for a pitch angle of θ)

$$\mathbf{C}_2(\theta)=\begin{bmatrix}\cos\theta & 0 & -\sin\theta\\ 0 & 1 & 0\\ \sin\theta & 0 & \cos\theta\end{bmatrix} \tag{4.4.2}$$

For a rotation about the z-axis, (i.e., for a yaw angle of ψ)

$$\mathbf{C}_3(\psi)=\begin{bmatrix}\cos\psi & \sin\psi & 0\\ -\sin\psi & \cos\psi & 0\\ 0 & 0 & 1\end{bmatrix} \tag{4.4.3}$$

A general Euler rotation can be expressed as a combination of these angles, such that,

$$\mathbf{C}(\phi,\theta,\psi)=\mathbf{C}_1(\phi)\mathbf{C}_2(\theta)\mathbf{C}_3(\psi) \tag{4.4.4}$$

This can be expressed explicitly as,

$$\mathbf{C}(\phi,\theta,\psi)=\begin{bmatrix}\cos\theta\cos\psi & \cos\theta\sin\psi & -\sin\theta\\ \sin\phi\sin\theta\cos\psi-\cos\phi\sin\psi & \sin\phi\sin\theta\sin\psi+\cos\phi\cos\psi & \sin\phi\cos\theta\\ \cos\phi\sin\theta\cos\psi+\sin\phi\sin\psi & \cos\phi\sin\theta\sin\psi-\sin\phi\cos\psi & \cos\phi\cos\theta\end{bmatrix} \tag{4.4.5}$$

Despite Euler angles being a standard convention, they are not without limitation. A singularity exists such that the exact orientation may not always be uniquely determined for flight at pitch angles of 90°. Euler angles are also

computationally demanding, being defined by a series of sine and cosine angles. Thus for the sake of computational efficiency and accuracy, it is often better to use a set of four orientation parameters known as 'Euler parameters' or 'quaternions', that remove the Euler angle singularity issue, and are much less computationally intensive.

4.4.2 Euler Parameters

Euler's theorem states that a general rotational displacement can be represented by a single rotation (commonly denoted ϕ), about an axis ($\mathbf{a}$). It is from here that the Euler parameters are derived.[19]

A set of four parameters (ε, η) will define the orientation of an object or reference frame. Euler parameters utilize Euler's theorem in a manner that is summarized as follows. The first three Euler parameters are given by ε:

$$\boldsymbol{\varepsilon} = \begin{pmatrix} \varepsilon_1 & \varepsilon_2 & \varepsilon_3 \end{pmatrix}^T = \mathbf{a}\sin\left(\tfrac{1}{2}\phi\right) \tag{4.4.6}$$

The fourth parameter is,

$$\eta = \cos\left(\tfrac{1}{2}\phi\right) \tag{4.4.7}$$

The magnitude of these parameters is equivalent to unity,

$$\boldsymbol{\varepsilon}^T\boldsymbol{\varepsilon} + \eta^2 = \varepsilon_1^2 + \varepsilon_2^2 + \varepsilon_3^2 + \eta^2 = 1 \tag{4.4.8}$$

These parameters are often referred to as quaternions. The rotation matrix relating the orientation in Euler parameters is given as

$$\mathbf{C}(\boldsymbol{\varepsilon},\eta) = \left(\eta^2 - \boldsymbol{\varepsilon}^T\boldsymbol{\varepsilon}\right)\mathbf{1} + 2\boldsymbol{\varepsilon}\boldsymbol{\varepsilon}^T - 2\eta\boldsymbol{\varepsilon}^{\times} \tag{4.4.9}$$

or more explicitly,

$$\mathbf{C}(\boldsymbol{\varepsilon},\eta) = \begin{bmatrix} 1-2\left(\varepsilon_2^2+\varepsilon_3^2\right) & 2\left(\varepsilon_1\varepsilon_2+\varepsilon_3\eta\right) & 2\left(\varepsilon_1\varepsilon_3-\varepsilon_2\eta\right) \\ 2\left(\varepsilon_1\varepsilon_2-\varepsilon_3\eta\right) & 1-2\left(\varepsilon_1^2+\varepsilon_3^2\right) & 2\left(\varepsilon_2\varepsilon_3+\varepsilon_1\eta\right) \\ 2\left(\varepsilon_1\varepsilon_3+\varepsilon_2\eta\right) & 2\left(\varepsilon_2\varepsilon_3-\varepsilon_1\eta\right) & 1-2\left(\varepsilon_1^2+\varepsilon_2^2\right) \end{bmatrix} \tag{4.4.10}$$

This matrix can then be compared to that of **Equation (4.4.5)** to extract the desired roll, pitch and yaw angles, which are much more suitable and easier to visualize for a human observer than quaternions.

4.4.3 Euler Parameter Rates

Differentiating the relations for determining ε and η, gives the following Euler parameter rate terms

$$\dot{\varepsilon} = \tfrac{1}{2}\left(\varepsilon^{\times} + \eta \mathbf{1}\right)\omega \tag{4.4.11}$$

$$\dot{\eta} = -\tfrac{1}{2}\varepsilon^{T}\omega \tag{4.4.12}$$

4.5 Additional Simulation Parameters

Having established the equations of motion and introduced the general framework of the flexible rocket simulator, some additional parameters deserve some consideration. These parameters are critical to the simulation response and are presented in the following sections.

4.5.1 Atmosphere

For the current application, the atmospheric properties are assumed to coincide with the 1976 standard atmosphere convention. However, it is noted that for some situations, it may be desirable to use non-standard conditions. At present, the current simulation model does not explicitly allow for user input of customized atmospheric properties. The atmospheric model is described within a small independent script that may be easily altered and adjusted as desired by the user to meet the requirements of any scenario.

For flight in the troposphere (i.e., for altitudes of less than 11 km), the atmospheric properties are approximated by the following formulae.[20] The absolute temperature ratio is

$$\theta = 1 - 0.0226(h/1000) \tag{4.5.1}$$

where h is given in metres and

$$\theta = \frac{T_{\infty}}{T_{SL}} \tag{4.5.2}$$

where T_{∞} is the temperature at a given altitude, and T_{SL} is the standard atmospheric temperature at sea level ($T_{SL} = 288.16$ K).

The pressure ratio is given by the equation

$$\delta = \theta^{5.256} \tag{4.5.3}$$

where

$$\delta = \frac{p_\infty}{p_{SL}} \tag{4.5.4}$$

where p_∞ is the atmospheric pressure at a given altitude, and p_{SL} is the standard atmospheric pressure at sea level ($p_{SL} = 101.3$ kPa)

The density ratio is given by

$$\sigma = \theta^{4.256} \tag{4.5.5}$$

where

$$\sigma = \frac{\rho_\infty}{\rho_{SL}} \tag{4.5.6}$$

where ρ_∞ is the atmospheric density at a given altitude, and ρ_{SL} is the standard atmospheric density at sea level ($\rho_{SL} = 1.225$ kg/m^3)

For altitudes above 11 km, the atmosphere may be subdivided into several distinct regions. In the upper regions of the troposphere up to an altitude of 23 km, lies a region known as the tropopause, where the atmospheric temperature remains nearly constant.

In this region an approximation for the pressure ratio is defined as,

$$\delta = \delta_c \left[-\frac{g}{RT_c}(h - h_c) \right] \tag{4.5.7}$$

where the subscript "c" is used to denote the conditions at an altitude of 11 km.

The density ratio is found via the following relation:

$$\sigma = \frac{\delta}{\theta_c} \tag{4.5.8}$$

The approximate conditions at 11 km are summarized as follows:

$\delta_c = 0.225$

$\theta_c = 0.752$

$T_c = 216.66$ K

For higher altitudes, the simulation utilizes tabulated 1976 standard atmosphere data, in conjunction with an interpolation technique to determine the atmospheric conditions. The model may be further altered to use any available approximate equations, or any customized configuration that may be chosen by the user.

4.5.2 Stimulus Generation

The focus of this study is to use the flight dynamics simulator to establish the flight characteristics of flexible vehicles. For determining stability, a stimulus generator may be used to excite the structure into oscillation. For the purpose of this study, the primary method for exciting the structure is by means of a gust generator. The gust generator may be customized to act as a random or predetermined vehicle wind velocity change that acts to alter the aerodynamic forces and move the system away from equilibrium. The gust may act for a predetermined fraction of time, or may follow a more continuous and elaborate profile, such as a sinusoid. For stable configurations, the vehicle will flex and induce a short-term oscillation that will persist until the disturbance effects have been dampened out. For unstable configurations, a disturbance will tend to grow until the vehicle experiences either a loss of aerodynamic control or excessively large deformations that result in structural failure.

4.5.3 Energy and Momentum

Energy

To test the overall dynamical integrity of the simulation program, it is necessary to perform certain analyses using defined scenarios for which the outcome may be predicted and expected. Analyzing the energies and momenta for a given model are good indicators as to the overall health of the simulation engine and model description.

For a flexible model that is not subjected to any external forces (such as gravity, thrust, aerodynamics, etc.), it is known that the total energy of the system will remain constant, due to the law of conservation of energy. This is illustrated

below. The kinetic energy of the flexible system is given by the following equation,

$$T = \tfrac{1}{2}\mathbf{v}^T\mathbf{M}_{tot}\mathbf{v} \tag{4.5.9}$$

where $\mathbf{v}$ is the total velocity vector which is comprised of both the rigid and flexible velocity components

$$\mathbf{v} = \begin{bmatrix} \mathbf{v}_B \\ \boldsymbol{\omega}_B \\ \dot{\mathbf{q}} \end{bmatrix}$$

and $\mathbf{M}_{tot}$ is the mass matrix of the system, containing both the rigid properties, as well as the finite element distributed mass matrix and the corresponding momentum coefficients.

In general, $\mathbf{M}_{tot}$ includes the effects of flexible deformation in all of its constituent elements. This mass description was presented in **Equation (2.5.1)**, that is,

$$\mathbf{M}_{tot} = \begin{bmatrix} m\mathbf{1} & -\mathbf{c}_{tot}^{\times} & \mathbf{P} \\ \mathbf{c}_{tot}^{\times} & \mathbf{J}_{tot} & \mathbf{H}_{tot} \\ \mathbf{P}^T & \mathbf{H}_{tot}^T & \mathbf{M} \end{bmatrix}$$

The kinetic energy in general is not expected to be constant. The kinetic energy is continuously being transferred into the structure as deformation potential energy (a.k.a strain energy). The strain energy is given by (assuming simple linear elastic behavior)

$$V_\sigma = \tfrac{1}{2}\mathbf{q}^T\mathbf{K}\mathbf{q} \tag{4.5.10}$$

where $\mathbf{q}$ is the vector of flexible coordinate deformations, and $\mathbf{K}$ is the stiffness matrix corresponding to the flexible degrees of freedom

Gravity may also contribute to the total potential energy. Obviously, for the case in which the rocket is free from all external forces, this component will be ignored. The gravitational potential energy is given by

$$V_g = m_t g h - \mathbf{g}_B^T\mathbf{c} - \mathbf{g}_B^T\mathbf{P}\mathbf{q} \tag{4.5.11}$$

where g is the magnitude of gravitational acceleration, and h is the altitude

Therefore, the total potential energy is simply,

$$V_T = V_\sigma + V_g \tag{4.5.12}$$

The potential energy is similarly in a state of flux as energy is continually transferred between kinetic and potential forms. Thus for a system free from external forces, the total energy will remain constant. That is,

$$E = T + V = \mathbf{const}$$

Momentum

The momentum of the model can also be used as a test for verifying the effectiveness of the overall dynamics. The momentum problem is divided into two parts: translational and angular. The test case of a model free from external forces is again employed here.

Translational Momentum

In the general case, the translational momentum also is dependent on the deformation of the structure. The equation for the total (general) translational momentum in the body frame ($\mathcal{F}_B$) is given below:

$$\mathbf{p}_B = m\mathbf{v}_B - \mathbf{c}_{tot}^{\times}\boldsymbol{\omega}_B + \mathbf{P}\dot{\mathbf{q}} \tag{4.5.13}$$

In the body frame, for the case with no external forces or torques acting on the vehicle, the translational momentum vector is not constant due to the fact that the frame may be rotating. The magnitude of this vector in ($\mathcal{F}_B$) does remain constant, however.

The translational momentum may similarly be evaluated in the inertial frame ($\mathcal{F}$). The conversion is accomplished via the orientation rotation matrix (C) (where $\mathbf{C}_{IB} = \mathbf{C}_{BI}^T$). Thus,

$$\mathbf{p} = \mathbf{C}_{IB}\mathbf{p}_B \tag{4.5.14}$$

In the inertial frame context, again assuming no external forces or torques, both the translational momentum vector and magnitude will be constant.

Angular Momentum

Again considering the situation with no external forces, the angular momentum magnitude in the body frame ($\mathcal{F}_B$) is *not* generally constant. It is constant, however, if the body frame is located at the vehicle mass center. The mass center of the vehicle may be determined from the following equation, which is an adaptation to the standard parallel axis theorem.

$$\mathbf{I}_{tot} = \mathbf{J}_{tot} + \frac{\mathbf{c}_{tot}^{\times}\mathbf{c}_{tot}^{\times}}{m_{tot}} \tag{4.5.15}$$

where $\mathbf{I}_{tot}$ is the inertia about the vehicle mass center, and $\mathbf{J}_{tot}$ is the inertia about the body frame origin.

The body frame first and second mass moments both include their flexible components, which depend on the flexible coordinates $\mathbf{q}$. These terms were defined previously in **Section 2.5.**

The angular momentum in a frame that is parallel to the body frame but situated at the mass center can then be found via

$$\mathbf{h}_{cm,B} = \mathbf{I}_{tot}\boldsymbol{\omega}_B \tag{4.5.16}$$

The angular momentum vector in this frame is generally *not* constant. However, the magnitude at the center of mass does remain constant, provided the vehicle is free from all external forces and torques.

The angular momentum in the inertial frame can be found via the orientation rotation matrix, that is,

$$\mathbf{h}_{cm,I} = \mathbf{C}_{IB}\mathbf{h}_{cm,B} \tag{4.5.15}$$

In this context, both the angular momentum vector and magnitude should remain constant if the vehicle is unaffected by any external aerodynamic, gravitational, or thrust loads.

All of these known configurations may serve as validity checks to verify the correctness of the underlying system equations of motion.

4.6 Procedure for Obtaining Flexible Flight Simulation Data

The steps outlined below indicate the procedure for obtaining simulation results for a generic rocket vehicle model.

1. *Generate a finite element model using the desired rocket dimensions, configurations and material properties.* This may be accomplished with a custom FE generation program or through the use of a commercial software package. For this project, ANSYS™ is used to create the finite element rocket models.
2. *Extract the model properties from the FE generation software.* The software package must provide the full order absolute mass and stiffness matrices, a listing of the location of each node in the global reference, an element list outlining the interconnected nodes defining each element, and any deformation shapes selected to be reduced order degrees of freedom. ANSYS provides the node and element lists and deformation shapes through the Graphical User Interface (GUI). The mass and stiffness matrices may be extracted from the model **.full** file using the '**userprog.exe**' utility.
3. *Create simulation initialization script.* Update a script entitled "initialize variables" by inputting the file addresses for the data collected in step 2. The script automatically processes in the input data and forms all of the required coefficients and matrices required in the flexible flight simulation engine. This script additionally reduces the order of the model in accordance with the number of input deformation shapes to be used with the reduced order model. Initial conditions, such as the flight velocity, orientation and flexible excitation are also included within this script. The node numbers corresponding to the aerodynamic or thrust key-node locations are also input in this file.
4. *Run initialization script, set simulation parameters, and begin simulation.* The SIMULINK™ simulation environment allows for the selection of integration type, simulation length, error tolerances, etc. Simulation is then initiated, important structural and flight data are recorded to output

files that are recorded in the MATLAB workspace. Data such as vehicle velocities, flexible deformations and deformation rates, atmospheric properties, aerodynamic angles, forces, moments, orientation, position, energy, momentum are all recorded for a user selected sample time.

5. *Postprocessing: Simulation Plots.* Run automated plot generating script, which automatically presents important simulation data in a series of figures for quick analysis, and validation.
6. *Postprocessing: Animation.* Run structural animation script, which uses the full order "unreduced" deformation vector to effectively recreate the various deformation shapes experienced by the rocket vehicle model for the duration of the simulation.
7. *Posprocessing: Save File.* Save all important simulation data to file for later use.
8. *Postprocessing: Update Records.* Upon completion of simulation analysis and saving of data to file, a file log is updated, recording the name of the simulation save file, with any important characteristics of flight including initial conditions, flight time, disturbances, etc.

Chapter 5: Forces and Moments

A flexible flight vehicle is subject to a variety of loads. These arise from gravity, aerodynamics, thrust, or a variety of other sources. These forces are discussed and presented in the following sections.

5.1 Gravitational Forces and Moments

The effects of gravitational acceleration on the vehicle motion and deformation are presented below.

5.1.1 Net Gravitational Forces and Moments

The gravity vector is defined to be positive in the inertial z direction. Therefore the gravity acceleration vector in the inertial frame is quantified by,

$$\mathbf{g} = [0 \quad 0 \quad 9.806]^T \tag{5.1.1}$$

However, the magnitude of the acceleration of gravity is known to decrease with increasing altitude. Thus, a small correction factor can adjust the magnitude of the gravity vector accordingly, and is given as follows below,

$$\mathbf{g}(h) = \left(\frac{R_E}{R_E + h}\right)^2 \mathbf{g}_o \tag{5.1.2}$$

where R_E corresponds to the radius of Earth (~ 6378 km), and h corresponds to the altitude of the vehicle above sea level.

The gravity vector is then converted into the body reference frame by the transformation,

$$\mathbf{g}_B = \mathbf{C}_{BI}\mathbf{g} \tag{5.1.3}$$

where $\mathbf{C}_{BI}$ is the rotation matrix for converting elements from the inertial frame to the body frame, as was defined previously.

The total forces resulting from gravity (weight) in the body frame are therefore given by,

$$\mathbf{F}_{G_B} = m_t \mathbf{g}_B \tag{5.1.4}$$

where m_t is the total vehicle mass at a given instant.

If the body reference frame is located arbitrarily (i.e., the frame's origin does not necessarily coincide with the location of the center of gravity of the vehicle) a gravity moment will exist.

The gravity moment will then be of the form,

$$\mathbf{M}_{G_B} = \mathbf{c}^{\times} \mathbf{g}_B \tag{5.1.5}$$

5.1.2 Nodal Gravity Forces and Moments

If the system contains distributed mass with flexibility (as the finite element models to be employed herein will), each node will possess a load due to gravity. These nodal loads can directly affect the flexible motions of the vehicle.

The forces are related through the translational momentum coefficient $\mathbf{P}$ and is given as follows,

$$\mathbf{f} = \mathbf{P}^T \mathbf{g}_B \tag{5.1.6}$$

5.2 Thrust Forces and Moments

In many simulations, thrust force is a predetermined quantity that is often derived from motor performance tables, experiment or theoretical estimates. Therefore, the thrust magnitude is made available to the simulation at any given time (stored versus time in an input array). Ideally, for more complex simulations, the thrust force would be determined from the computation of internal flows. If the vehicle is assumed rigid and the thrust vector is aligned with the vehicle body x-axis, no thrust moments will develop. For the case where the thrust force is perfectly inline with the vehicle body x-axis, the thrust force vector is given by

$$\mathbf{F}_T = \begin{bmatrix} 1 \\ 0 \\ 0 \end{bmatrix} T \tag{5.2.1}$$

where T is the thrust magnitude at a given instant.

In general, the thrust vector is not perfectly inline with the body vehicle axis. Misalignments may arise from a variety of sources, deliberate and unintended. For rocket vehicles, deliberate thrust misalignments are usually the result of active thrust vector control methods that are typically employed to maintain a desired attitude or trajectory. This is accomplished by the redirection of the effective thrust vector from its nominal position. This can be accomplished with gimbaled nozzles or a variety of other methods including jet vanes and cold gas injection, which can vary greatly in cost, complexity and effectiveness.[21,22]

Unintended thrust misalignments are often the result of motor asymmetries and irregularities. Minor manufacturing defects in the nozzle, exhaust flow or vehicle mass asymmetries all can adversely affect the accuracy of the thrust vector in relation to its desired nominal orientation. These unintended thrust misalignments also generate moments which can negatively reflect upon overall vehicle performance. Thus for larger, more complex and costly missions, the thrust misalignment characteristics are typically known parameters and are actively counteracted.

For the current model, the thrust force is assumed to be a point force applied to a node that is pre-selected to represent the effective location of the engine nozzle. It is assumed that the nozzle will be embedded within the rocket casing. Focus is being primarily applied to the deformation of the body as a whole without specific concern at this point in time for the internal nozzle behavior.

Any resulting deformation of the nozzle key-node results in a corresponding deformation in the thrust vector. The thrust vector is permitted to acquire initial deviations from the nominal ideal thrust vector to capture the effects of manufacturing errors and such. These initial deflections of the thrust vector are

represented as a set of translations and rotations, denoted by δ_T and α_T respectively.

The nominally deflected thrust vector is now determined via

$$\mathbf{T}_\alpha = \left(\mathbf{1} + \boldsymbol{\alpha}_T^\times\right)\mathbf{T} \tag{5.2.2}$$

The thrust forces and torques at a user selected node can then be found with

$$\mathbf{f}_T(t) = \begin{bmatrix} \mathbf{C}_T^T(t)\mathbf{T}_\alpha \\ \mathbf{C}_T^T(t)\boldsymbol{\delta}_T^\times \mathbf{T}_\alpha \end{bmatrix} \tag{5.2.3}$$

where the flexible thrust rotation matrix is given by

$$\mathbf{C}_T = \mathbf{1} - \boldsymbol{\theta}_T^\times(t) \tag{5.2.4}$$

This rotation matrix relates the variable flexible rotations acting upon the thrust vector at the nozzle/thrust key-node location. The variable $\boldsymbol{\theta}_T$ represents the vector of flexible rotations at a specified time t.

Net body force and torques are given via

$$\mathbf{F}_T(t) = \mathbf{C}_T^T(t)\mathbf{T}_T \tag{5.2.5}$$

$$\mathbf{G}_T(t) = \left[\mathbf{r}_T^\times \mathbf{C}_T^T(t) + \mathbf{C}_T^T(t)\boldsymbol{\delta}_T^\times\right]\mathbf{T}_T \tag{5.2.6}$$

where $\mathbf{r}_T$ is the fixed nominal location of the nozzle in the body frame.

5.3 Aerodynamics

The aerodynamic modeling is now addressed in detail. As mentioned previously many techniques are available that vary in accuracy and complexity. State of the art techniques such as CFD analysis, while desirable, are unrealistic for the current study due to prohibitory computational requirements and limited development time. Thus, for the sake of the current rocket application, simpler aerodynamic relations are employed to represent the dynamic loadings acting on the vehicle.[22-33]

5.3.1 Fuselage-Body Alone Aerodynamics

The body aerodynamics methodology employed in the following sections is a standard coefficient formulation. In the computation of rocket body aerodynamic loads, it is common to employ a system in which the aerodynamic forces are represented by normal and axial forces with respect to the body axes. This is opposed to the lift and drag convention, more commonly seen with other aerial vehicles such as aircraft, which defines the loads relative to local wind velocity vector. The direction of side force is determined via the right hand rule.

The force conventions are depicted in **Figure 5.1** for the flight of a rocket vehicle in a vertical plane. The normal and axial forces are defined with respect to the body axes regardless of the orientation of the rocket vehicle velocity vector. In contrast, the lift and drag forces are dependent on the body velocity vector and need to be related into the body frame ($\mathcal{F}_B$) for use in the equations of motion.

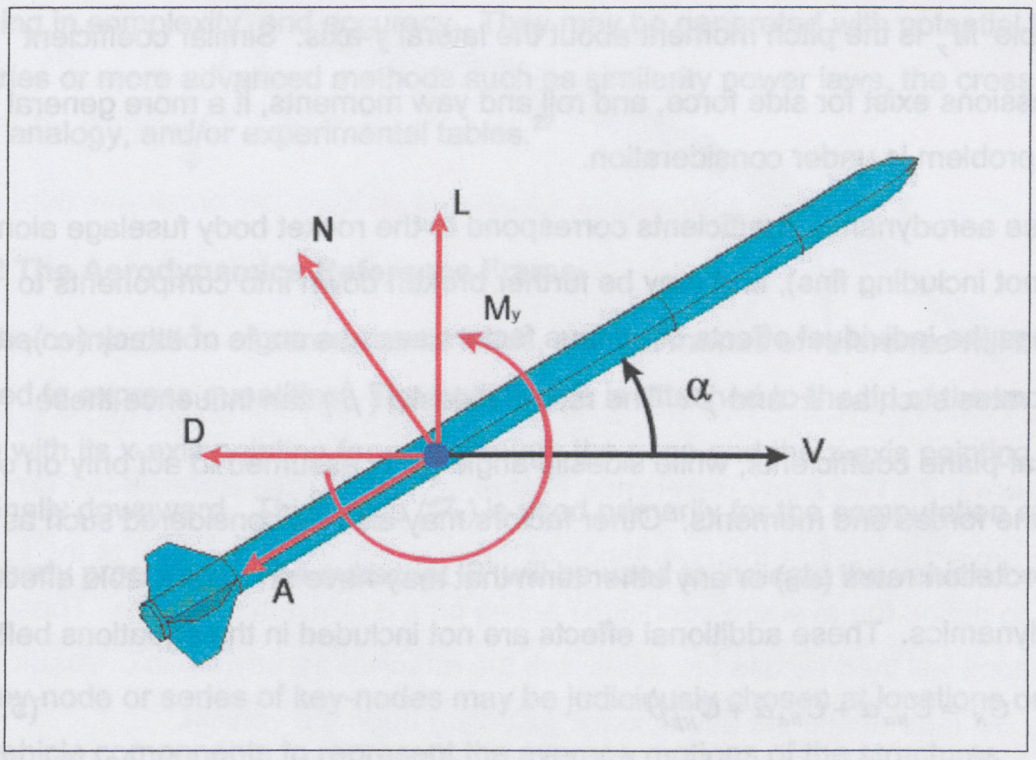

Figure 5.1: Normal Force, Axial Force, Lift and Drag Conventions

The aerodynamic loadings are actually determined via a series of non-dimensional coefficients that are either determined from theoretical or experimental means. The non-dimensionalized aerodynamic coefficients are converted into physical forces and moments via the following equations:

$$N = C_N q_\infty S \tag{5.3.1}$$

$$A = C_A q_\infty S \tag{5.3.2}$$

$$M_y = C_M q_\infty S b_b \tag{5.3.3}$$

where q_∞ is the dynamic pressure, which is given by

$$q_\infty = \tfrac{1}{2}\rho_\infty V^2 \tag{5.3.4}$$

noting ρ_∞ is the density of air for the given altitude, S is the reference area (commonly given as the fuselage cross sectional area for rocket bodies), and b_b is the reference length (commonly given as the fuselage diameter).

Variable M_y is the pitch moment about the lateral y-axis. Similar coefficient expressions exist for side force, and roll and yaw moments, if a more general flight problem is under consideration.

These aerodynamic coefficients correspond to the rocket body fuselage alone (i.e., not including fins), and may be further broken down into components to express the individual effects of various factors such as angle of attack (α), and other rates such as $\dot{\alpha}$ and $\dot{\beta}$. The rate of sideslip ($\dot{\beta}$) can influence these vertical-plane coefficients, while sideslip angle (β) is assumed to act only on out-of-plane forces and moments. Other factors may also be considered such as body rotation rates (ω_B) or any other term that may have an appreciable effect on aerodynamics. These additional effects are not included in the equations below.

$$C_N = C_{N\alpha}\alpha + C_{N\dot{\alpha}}\dot{\alpha} + C_{N\dot{\beta}}\dot{\beta} \tag{5.3.5}$$

$$C_A = C_{Ao} + C_{A\alpha}\alpha + C_{A\dot{\alpha}}\dot{\alpha} + C_{A\dot{\beta}}\dot{\beta} \tag{5.3.6}$$

$$C_M = C_{Mo} + C_{M\alpha}\alpha + C_{M\dot{\alpha}}\dot{\alpha} + C_{M\dot{\beta}}\dot{\beta} \tag{5.3.7}$$

with C_N, C_A and C_M being the normal force, axial force and pitch moment coefficients respectively for the rocket body.

Note: The coefficients that correspond to any angular rate terms (e.g., $\dot{\alpha}$, $\dot{\beta}$ or body rates ω_B, etc.), are non-dimensionalized by the term $\frac{b_b}{2V}$.

For a body of revolution, symmetry implies similar conditions that may be used to reduce the complexity of the model, that is, $C_{N\dot{\alpha}} = C_{N\dot{\beta}}$ and $C_{A\dot{\alpha}} = C_{A\dot{\beta}}$. Thus, the **Equations (5.3.5)** and **(5.3.6)** may be reduced to

$$C_N = C_{N\alpha}\alpha + C_{N\dot{\alpha}}\left(\dot{\alpha} + \dot{\beta}\right) \tag{5.3.8}$$

$$C_A = C_{Ao} + C_{A\alpha}\alpha + C_{A\dot{\alpha}}\left(\dot{\alpha} + \dot{\beta}\right) \tag{5.3.9}$$

These aerodynamic coefficients may be obtained from a variety of methods ranging in complexity, and accuracy. They may be generated with potential flow theories or more advanced methods such as similarity power laws, the cross flow drag analogy, and/or experimental tables.[27]

5.3.2 The Aerodynamics Reference Frame

In the computation of aerodynamic loads, several frames of reference will be utilized to express quantities. The body frame is attached to the tip of the rocket nose with its x-axis pointing forward through the nose and the z-axis pointing nominally downward. This frame ($\mathcal{F}_B$) is used primarily for the computation of the rigid body properties. The subscript 'B' will be used to indicate the vehicle body frame.

A key-node or series of key-nodes may be judiciously chosen at locations on the vehicle components to represent the average motions of the structures themselves. Since the body is flexible, the orientation of the nodal frame will be affected by the local deflections at the key-node location at any given time. For

an undeflected node, the nodal frame ($\mathcal{F}_{bn}$) will be aligned with the body frame ($\mathcal{F}_B$). The resulting nominal rotation matrix for relating these frames is then,

$$\mathbf{C}_{bn0} = \mathbf{1}$$

Note that the subscript 'bn' corresponds to the **b**ody key-**n**ode. The 'b' is used to differentiate from other frames defined at other key-nodes, which may pertain to the fin(s) or other components of the model.

Figure 5.2 depicts the relationship between the two reference frames just discussed: the body frame ($\mathcal{F}_B$) and the body key-node frame ($\mathcal{F}_{bn}$). The location of the body key-node in **Figure 5.2** is placed arbitrarily on the rocket.

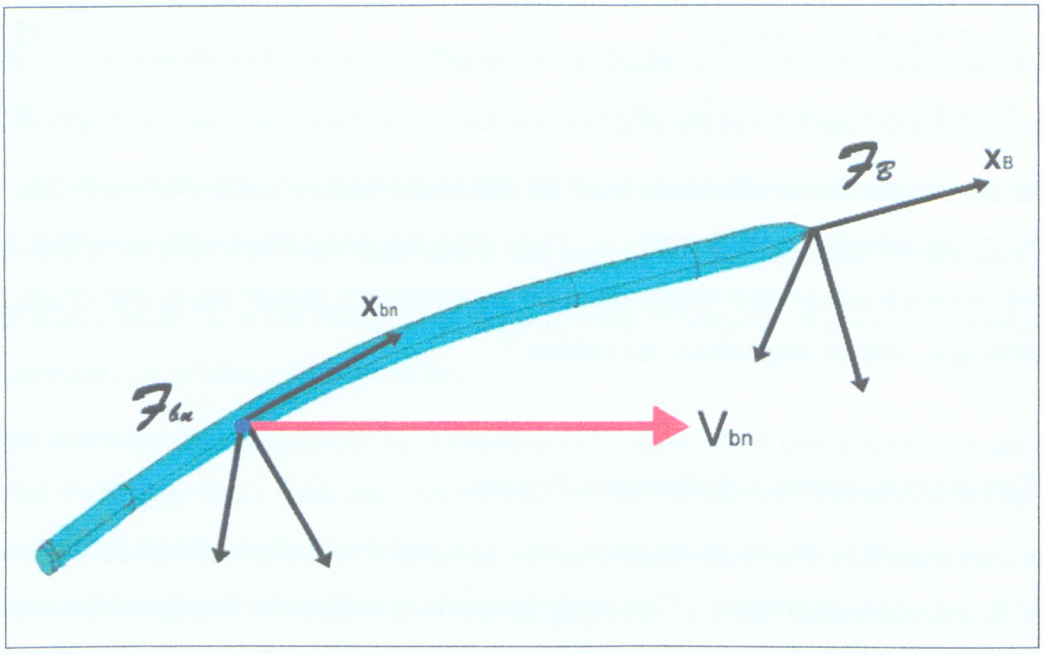

Figure 5.2: The Body Reference Frame and the Nodal Reference Frame

This project will utilize the orientation of the effective velocity vector at the key-node to define the average conditions acting on the relevant structure. These conditions will then be used to determine the effective aerodynamic orientations, which will later define the actual loadings acting upon the vehicle.

Taking into consideration the local angular deformations at the node of concern, and assuming small deformation angles, the rotation matrix becomes

$$\mathbf{C}_{bn,B} = \mathbf{C}_{bn\theta} = \begin{bmatrix} \hat{\mathbf{x}}_{bn}^T \\ \mathbf{y}_{bn}^T \\ \mathbf{z}_{bn}^T \end{bmatrix} \approx \begin{bmatrix} 1 & \theta_{bnz} & -\theta_{bny} \\ -\theta_{bnz} & 1 & \theta_{bnx} \\ \theta_{bny} & -\theta_{bnx} & 1 \end{bmatrix} \tag{5.3.10}$$

or

$$\mathbf{C}_{bn,B} = \mathbf{C}_{bn\theta} = \mathbf{1} - \boldsymbol{\theta}_{bn}^{\times} \tag{5.3.11}$$

where $\boldsymbol{\theta}_{bn}$ is the vector of rotational deformations at the key-node. The velocity of the key-node can be found to be

$$\mathbf{V}_{bn} = \mathbf{V}_B + \boldsymbol{\omega}_B^{\times}\mathbf{r}_{bn} + \dot{\mathbf{u}}_{bn} \tag{5.3.12}$$

where $\mathbf{r}_{bn}$ is the vector relating the distance of the key-node in frame ($\mathcal{F}_B$), and $\dot{\mathbf{u}}_{bn}$ is the vector of flexible translational displacement rates at the key-node location.

If wind is present, then the velocity vector is further adjusted via,

$$\mathbf{V}_{bn} = \mathbf{V}_B + \boldsymbol{\omega}_B^{\times}\mathbf{r}_{bn} + \dot{\mathbf{u}}_{bn} - \mathbf{V}_w \tag{5.3.13}$$

where $\mathbf{V}_w$ is the wind velocity vector

The total angular velocity of the key-node is taken to be the combination of the body rates and local angular rates:

$$\boldsymbol{\omega}_{bn} = \boldsymbol{\omega}_B + \dot{\boldsymbol{\theta}}_{bn} \tag{5.3.14}$$

Next one can define another frame of reference, the aerodynamics frame ($\mathcal{F}_{ba}$). This frame aligns itself with the velocity vector in such a manner so as to eliminate the sideslip angle (β). This is possible due to the fact that the body has an axisymmetric profile and is being considered separately from the fins. Thus, instead of allowing the velocity vector to be defined with respect to the body by two angles of inclination (i.e., angle of attack (α) and sideslip angle (β)), it can be defined by a single angle by rotating the reference frame such that the velocity vector is contained within the x-z plane. Additionally, since the orientation is defined by a single angle, fewer theoretical or experimental coefficients are

required. Refer to **Figure 5.3** for clarity. The origin of the body aerodynamics frame is collocated with the origin of the body key-node frame.

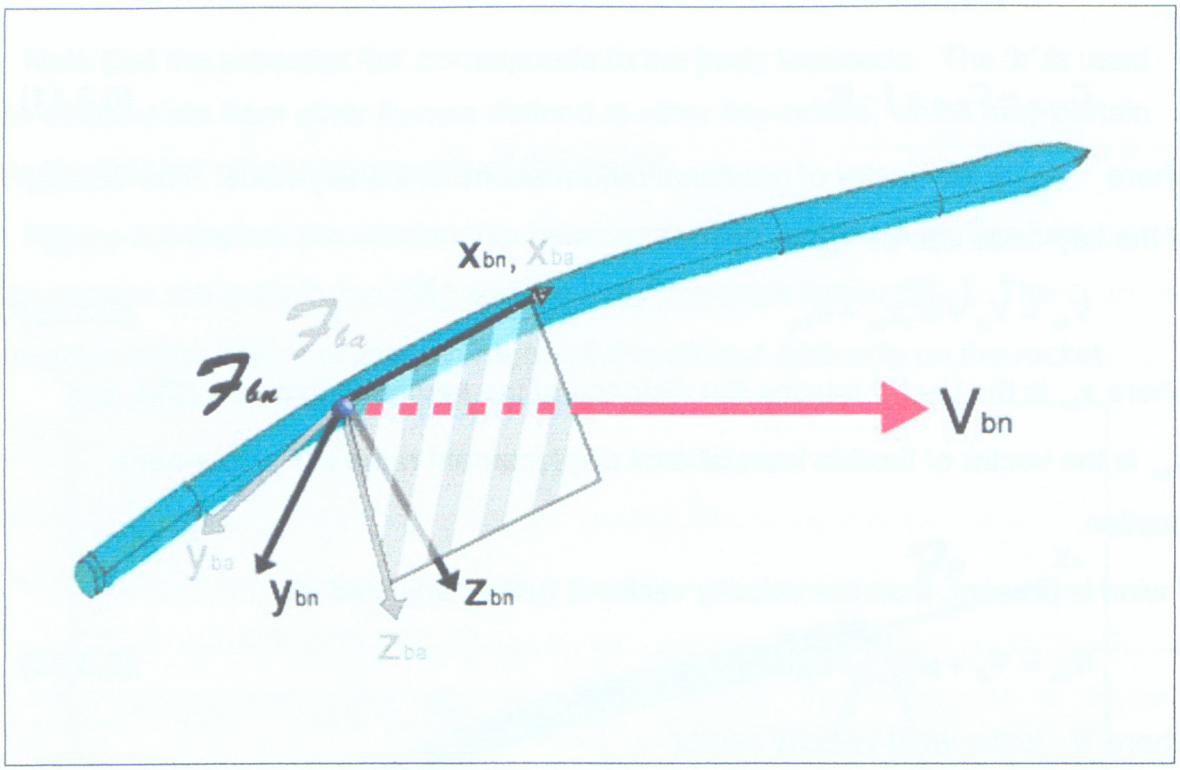

Figure 5.3: Body Key-Node and Aerodynamics Reference Frames

The aerodynamic frame ($\mathcal{F}_{ba}$) x-axis is collinear with the x-axis from the nodal frame ($\mathcal{F}_{bn}$). That is,

$$\hat{\mathbf{x}}_{ba} = \hat{\mathbf{x}}_{bn} \tag{5.3.15}$$

The y-axis is then defined to be perpendicular to the plane that contains both the aerodynamic frame x-axis ($\hat{\mathbf{x}}_{ba}$) and the velocity vector $\hat{\mathbf{V}}_b = \mathbf{V}_b / |\mathbf{V}_b|$. Therefore,

$$\hat{\mathbf{y}}_{ba} = \frac{\mathbf{V}_b^{\times} \hat{\mathbf{x}}_{bn}}{\left| \mathbf{V}_b^{\times} \hat{\mathbf{x}}_{bn} \right|} \qquad \text{or} \qquad \hat{\mathbf{y}}_{ba} = \hat{\mathbf{V}}_b^{\times} \hat{\mathbf{x}}_{bn} \tag{5.3.16}$$

Lastly, the z-axis is found via the cross product of the x and y-axes:

$$\hat{\mathbf{z}}_{ba} = \hat{\mathbf{x}}_{ba}^{\times} \hat{\mathbf{y}}_{ba} \tag{5.3.17}$$

Therefore the rotation matrix $\mathbf{C}_{ba,bn}$ relating the aerodynamic frame ($\mathcal{F}_{ba}$) to the nodal frame ($\mathcal{F}_{bn}$) is given as,

$$\mathbf{C}_{ba,bn} = \begin{bmatrix} \hat{\mathbf{x}}_{ba}^T \\ \mathbf{y}_{ba}^T \\ \mathbf{z}_{ba}^T \end{bmatrix} \tag{5.3.18}$$

Within this frame, the aerodynamic inclination angles are to be determined. The angle of attack is given via the following equation:

$$\sin \alpha_b = \frac{\hat{\mathbf{z}}_{ba}^T \mathbf{V}_b}{V_b} \tag{5.3.19}$$

or, assuming small angles of attack,

$$\alpha_b \approx \frac{\hat{\mathbf{z}}_{ba}^T \mathbf{V}_b}{V_b} \tag{5.3.20}$$

Since the body aerodynamics frame has been rotated to align the velocity vector with the x-z plane, the angle of attack will be strictly positive. By definition, the sideslip angle is also effectively negated, so that

$$\beta_b = 0 \tag{5.3.21}$$

The rate of change of the angle of attack ($\dot{\alpha}_b$) and sideslip ($\dot{\beta}_b$) may be approximated by the following relations through the assumption that the key-node deformation rates and the body angular rates are the primary contributors. Further assuming the persistence of small angles gives,

$$\dot{\alpha}_b = \frac{\dot{\hat{\mathbf{z}}}_{ba}^T \mathbf{V}_b - \hat{\mathbf{z}}_{ba}^T \left(\boldsymbol{\omega}_B^{\times} \mathbf{V}_b \right)}{V_b} \tag{5.3.22}$$

where $\dot{\hat{\mathbf{z}}}_{ba}$ corresponds to the 3rd column vector within the skew symmetric matrix of nodal deformation rates ($\dot{\boldsymbol{\theta}}_{bn}^{\times}$), that is, more explicitly

$$\dot{\hat{\mathbf{z}}}_{ba} = \begin{bmatrix} \dot{\theta}_{by} \\ -\dot{\theta}_{bx} \\ 0 \end{bmatrix} \tag{5.3.23}$$

The rate of change of sideslip ($\dot{\beta}_b$) is similarly computed via

$$\dot{\beta}_b = \frac{\dot{\hat{\mathbf{y}}}_{ba}^T \mathbf{V}_b - \hat{\mathbf{y}}_{ba}^T \left(\boldsymbol{\omega}_B^{\times} \mathbf{V}_b\right)}{V_b} \tag{5.3.24}$$

where $\dot{\hat{\mathbf{y}}}_{ba}$ corresponds to the 2nd column vector within the skew symmetric matrix of nodal deformation rates ($\dot{\boldsymbol{\theta}}_{bn}^{\times}$). More definitively it is given by,

$$\dot{\hat{\mathbf{y}}}_{ba} = \begin{bmatrix} -\dot{\theta}_{bz} \\ 0 \\ \dot{\theta}_{bx} \end{bmatrix} \tag{5.3.25}$$

It is now noted that one additional reference frame is required, which pertains to the computation of the body forces and moments. This frame will be denoted the coefficient frame ($\mathcal{F}_{co}$), and is related to a frame in which the aerodynamic coefficients to be used within the simulation are defined. If the coefficients are extracted from experimental tables, or from software packages, the values will typically be in reference to some fixed location. **Figure 5.4** depicts this scenario, whereby the aerodynamic coefficients are defined with respect to the vehicle centre of gravity.

The coefficient frame is generally set up such that both angle of attack (α) and sideslip (β) angles may be present. However, as was previously stated, the aerodynamic frame is assumed to be inline with the incoming velocity vector, thus reorienting itself to eliminate β. As such, the orientation of the coefficient frame will be closely aligned to the aerodynamics frame so as to take advantage of the same zero sideslip formulation.

Figure 5.4 displays the current orientation of the coefficient frame as used within the simulator. The z-axis of the coefficient frame is parallel to that of the aerodynamic frame, and the x-axis oriented opposite to that of ($\mathcal{F}_{ba}$).

Note that the location of the aerodynamics frame and coefficient frame are selected arbitrarily.

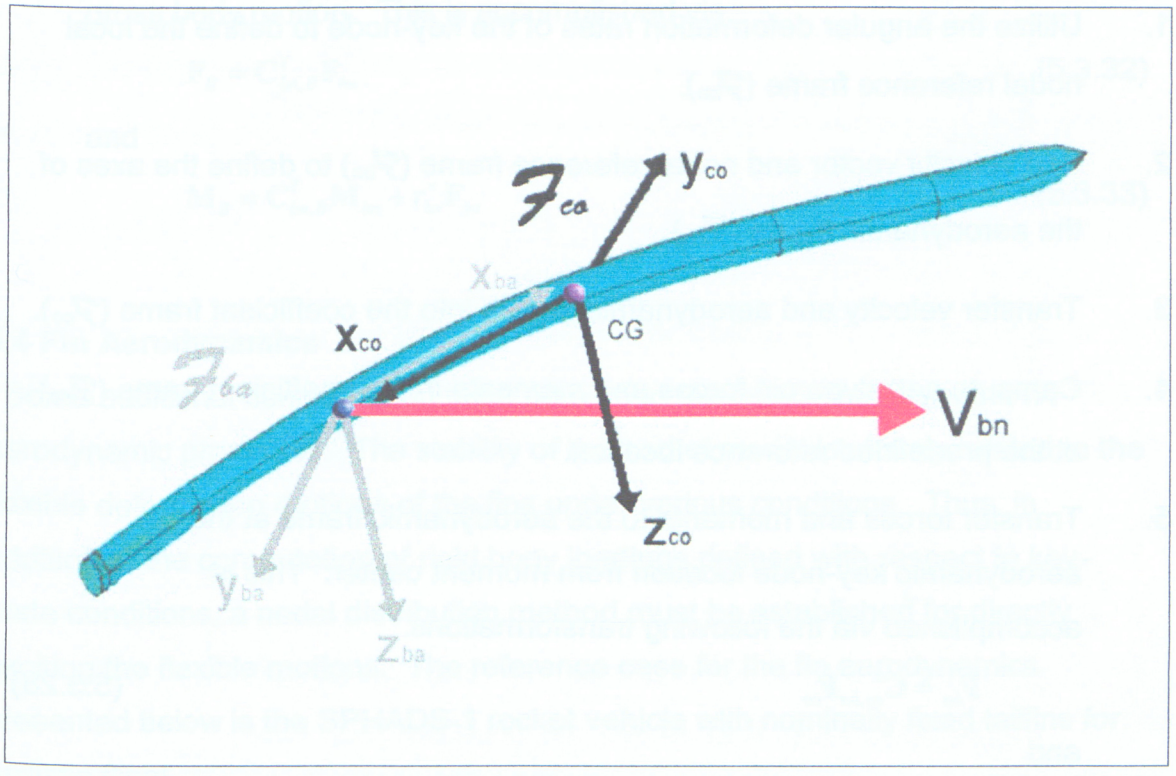

Figure 5.4 Body Aerodynamics and Aerodynamic Coefficient Frames

The rotation matrix is then,

$$\mathbf{C}_{co,ba}(\phi) = \begin{bmatrix} \cos\phi & \sin\phi & 0 \\ -\sin\phi & \cos\phi & 0 \\ 0 & 0 & 1 \end{bmatrix} \tag{5.3.26}$$

The relationship between ($\mathcal{F}_{ba}$) and ($\mathcal{F}_{co}$) for the present rocket application is defined as a fixed rotation of ϕ=180° about the z-axis. Therefore,

$$\mathbf{C}_{co,ba} = \begin{bmatrix} -1 & 0 & 0 \\ 0 & -1 & 0 \\ 0 & 0 & 1 \end{bmatrix} \tag{5.3.27}$$

Once in this frame, the appropriate aerodynamic forces and moments can be finally determined using the available aerodynamic coefficients.

In summary, the general algorithm for computing the aerodynamic loads at any given time, and relating them back to the body frame is presented below.

1. Utilize the angular deformation rates of the key-node to define the local nodal reference frame ($\mathcal{F}_{bn}$).

2. Use velocity vector and nodal reference frame ($\mathcal{F}_{bn}$) to define the axes of the aerodynamic frame ($\mathcal{F}_{ba}$).

3. Transfer velocity and aerodynamic angles into the coefficient frame ($\mathcal{F}_{co}$).

4. Compute aerodynamic forces and moments in the coefficient frame ($\mathcal{F}_{co}$) at the predefined reference location.

5. Transfer forces and moments to the aerodynamic frame at the aerodynamic key-node location from moment center. This is accomplished via the following transformations.

$$\mathbf{F}_{ba} = \mathbf{C}^{T}_{co,ba}\mathbf{F}_{co} \tag{5.3.28}$$

and

$$\mathbf{M}_{ba} = \mathbf{C}^{T}_{co,ba}\mathbf{M}_{co} - \left(\mathbf{r}_{bn} - \mathbf{r}_{cg}\right)^{\times}\mathbf{F}_{co} \tag{5.3.29}$$

where $\left(\mathbf{r}_{bn} - \mathbf{r}_{cg}\right)^{\times}$ is the skew symmetric matrix relating the moment arm between the center of gravity and the location of the key-node.
Note that if the aerodynamic key-node is coincident with the center of pressure, then the aerodynamic moments at the key-node will be zero.

6. Convert loads back to nodal frame ($\mathcal{F}_{bn}$). Note that since both the aerodynamics frame and the nodal frame are situated at the key-node location, there is no moment arm involved in the conversion between frames. The transformation is performed as follows,

$$\mathbf{F}_{bn} = \mathbf{C}^{T}_{ba,bn}\mathbf{F}_{ba} \tag{5.3.30}$$

and

$$\mathbf{M}_{bn} = \mathbf{C}^{T}_{ba,bn}\mathbf{M}_{ba} \tag{5.3.31}$$

7. Lastly, convert the aerodynamic forces and moment back to the body frame ($\mathcal{F}_B$) for use in the equations of motion and for determining the gross body motion. This is accomplished via,

$$\mathbf{F}_B = \mathbf{C}_{bn,B}^T \mathbf{F}_{bn} \tag{5.3.32}$$

and

$$\mathbf{M}_B = \mathbf{C}_{bn,B}^T \mathbf{M}_{bn} + \mathbf{r}_{bn}^{\times} \mathbf{F}_{bn} \tag{5.3.33}$$

5.4 Fin Aerodynamics

Some additional consideration must be paid to the determination of the fin aerodynamic properties. The stability of the rocket model is closely related to the flexible deformation motions of the fins under various conditions. Thus, in addition to the computation of rigid body loadings defined with respect to key-node conditions, a nodal distribution method must be established for directly exciting the flexible motions. The reference case for the fin aerodynamics presented below is the SPHADS-1 rocket vehicle with nominally fixed tailfins for ballistic flight.

5.4.1 Fin Aerodynamic Gross Loading

Each fin is considered to be aerodynamically independent from each other, and from the rocket body. That is, each fin is defined by it's own reference frame, whose origin is placed at a user selected key node located on the fin surface.

In the nominal undeformed state, the rocket fins are typically distributed equally about the circumference of the fuselage. The fin spacing is then determined by the number of fins being used.

The orientation of each fin reference frame is defined such that the x-axis points nominally forward towards the nose of the rocket. The local fin y-axis is aligned such that it extends along the fin span perpendicular to the x-axis. The direction of the z-axis is then defined via the right hand rule. These orientations are summarized in **Figures 5.5** and **5.6.**

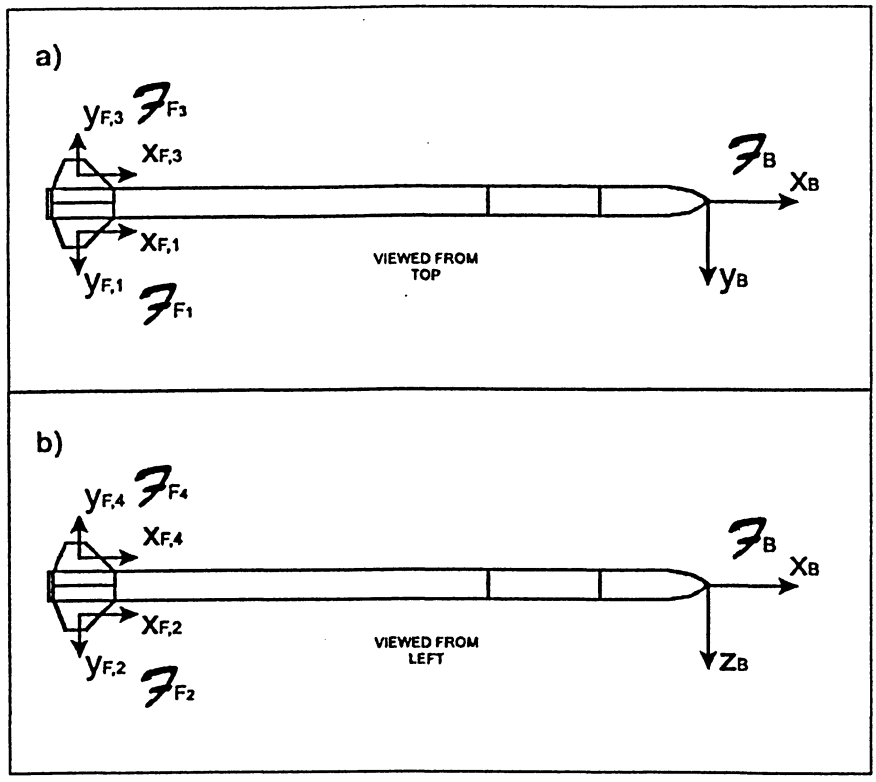

Figure 5.5: Fin Reference Frames (Left and Top view)

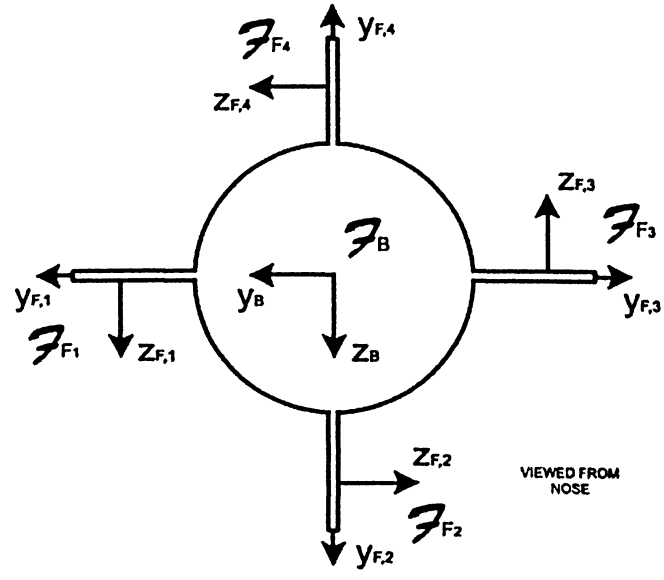

Figure 5.6: Fin Reference Frames (Front View)

The following rotation matrix relates these nominal undeformed fin frames to the body frame, and is defined with respect to a rotation about the body frame x-axis, that is,

$$\mathbf{C}_{f\delta_i} = \begin{bmatrix} 1 & 0 & 0 \\ 0 & \cos\delta_i & \sin\delta_i \\ 0 & -\sin\delta_i & \cos\delta_i \end{bmatrix} \tag{5.4.1}$$

where δ_i is the nominal angular location of the *i*-th fin. For evenly spaced fins, the δ_i's are given by

$$\delta_i = \frac{2\pi(i-1)}{n_{fins}} \qquad \text{where i = 1, 2, ..., } n_{fins} \tag{5.4.2}$$

The rocket model under consideration allows for flexible deformations of both the fuselage and fins. The main focus of this project is to consider the flexibility of the fins and to determine the resulting relationship with respect to flight stability.

Ideally, each fin would determine the instantaneous pressure distribution over the deflected fin surface for every conceivable deformation shape. However, to allow for this capability, advanced CFD modeling would likely be required to capture all of the aerodynamic interference effects induced by the scope of conceivable twisting and bending motions. While CFD techniques are desirable in terms of accuracy, they are unfortunately impractical for this study and thus simplifications must be applied.

To account for the deformation of each fin, an average deflection is assumed using the flexible deformation of the key-node. Therefore, although the fins are allowed to structurally deform to any level of complexity as provided through the degrees of freedom inherent to the model, the flexibility as seen through the aerodynamics is reduced down to a set of three flexible rotations ($\boldsymbol{\theta}_{fi}$). That is, aerodynamically speaking, the rocket fin is represented by a rigid undeformed structure oriented with regard to its nominal state by ($\boldsymbol{\theta}_{fi}$).

The rotation matrix corresponding to the flexible rotations of the key-node is given by,

$$\mathbf{C}_{f\theta_i} = \mathbf{1} - \boldsymbol{\theta}_{fi}^{\times} \tag{5.4.3}$$

Therefore, the rotation matrix relating the body frame ($\mathcal{F}_B$) to the local fin reference frame ($\mathcal{F}_{f,i}$) is

$$\mathbf{C}_{f_i} = \mathbf{C}_{f\delta_i}\mathbf{C}_{f\theta_i} \tag{5.4.4}$$

The fin aerodynamics are simplified in such a manner so as to consider the normal force as the primary component for driving the flexibility. The normal force for the *i*-th fin is given by

$$N_{fi} = C_{N_{fi}} q_{fi} S_f \tag{5.4.5}$$

where the normal force coefficient is

$$C_{N_{fi}} = C_{N\alpha_{fi}} \alpha_{fi} \tag{5.4.6}$$

where $C_{N\alpha_{fi}}$ is the normal force slope of the *i*-th fin, and α_{fi} is the angle of attack of the *i*-th fin.

The relative velocity as seen by the *i*-th fin key-node must be determined for the computation of the nodal forces.

The effective rotational velocity of the *i*-th key-node is given by,

$$\boldsymbol{\omega}_{f_i} = \boldsymbol{\omega}_B + \dot{\boldsymbol{\theta}}_{f_i} \tag{5.4.7}$$

The effective translational velocity of the *i*-th key-node in a frame parallel to the body frame is

$$\mathbf{V}_{Bf_i} = \mathbf{V}_B + \boldsymbol{\omega}^{\times}_{f_i}\mathbf{r}_{f_i} + \dot{\mathbf{u}}_{f_i} \tag{5.4.8}$$

The effective translational velocity in the deformed fin reference frame is given by

$$\mathbf{V}_{f_i} = \mathbf{C}_{f_i}\mathbf{V}_{Bf_i} \tag{5.4.9}$$

where $\mathbf{V}_{f_i} = \begin{bmatrix} V_{fx} \\ V_{fy} \\ V_{fz} \end{bmatrix}_i$

The angle of attack of the fin is then,

$$\alpha_{f_i} = \tan^{-1}\left(\frac{V_{fz_i}}{V_{fx_i}}\right) \tag{5.4.10}$$

The sideslip angle may also be determined via

$$\beta_{f_i} = \tan^{-1}\left(\frac{V_{fy_i}}{\sqrt{V_{fx_i}^2 + V_{fz_i}^2}}\right) \tag{5.4.11}$$

However, this approach does not consider side force in the analysis of the fins, since the focus of the aerodynamic loading is with respect to the normal force. It is generally assumed that the side force will be small in relation to the normal and axial forces for conventional fin configurations.

Thus, it is now possible to determine the aerodynamic forces acting upon each of the fins.

The fin forces are given as

$$\mathbf{F}_{f_i} = \begin{bmatrix} F_{fx} \\ F_{fy} \\ F_{fz} \end{bmatrix}_i$$

where the axial force (F_{fx_i}) is given by

$$F_{fx_i} = -C_{Af_i} q_{f_i} S_f \tag{5.4.12}$$

The side force (F_{fy_i}) is considered to be of secondary importance and is consequentially negated, i.e.,

$$F_{fy_i} = 0 \tag{5.4.13}$$

The normal force (F_{fz_i}) is then

$$F_{fz_i} = -(C_{N\alpha})_{f_i} \alpha_{f_i} q_{f_i} S_f \tag{5.4.14}$$

With respect to the rigid motion of the vehicle, these loads now need to be converted into forces and moments with respect to the body frame. This is accomplished with the following procedure.

The forces are converted back into the body frame by using the previously defined rotation matrix ($\mathbf{C}_{f_i}$):

$$\mathbf{F}_{Bf_i} = \mathbf{C}_{f_i}^T \mathbf{F}_{f_i} \tag{5.4.15}$$

Note that $\mathbf{C}_{f_i}^{-1} = \mathbf{C}_{f_i}^T$. The moments are then

$$\mathbf{M}_{Bf_i} = \mathbf{r}_{f_i}^{\times} \mathbf{F}_{Bf_i} = \mathbf{r}_{f_i}^{\times} \mathbf{C}_{f_i}^T \mathbf{F}_{f_i} \tag{5.4.16}$$

5.4.2 Fin Aerodynamic Distribution

The fin aerodynamic loads not only contribute to the gross body motion of the vehicle, but they also must be considered as local 'nodal' loads, which act to drive the flexible excitation of the structure.

A method for distributing the loads over the fins must be established. In the preceding section, fin loads were defined with respect to the fin key-node orientations. The chosen method of load distribution is accomplished through the use of spanwise and chordwise load factors, given as K_b and K_c respectively.

These factors are dependent upon the load distributions profiles that develop over the fins through various flight regimes. The profiles represent the general shape of the load allocation for combinations of various flight parameters such as angle of attack (α), Mach number (M_∞), altitude (h), and so on.

The fin dimensions are non-dimensionalized such that the spanwise and chordwise positions of each node within a given fin is represented by a number between zero and one.

$$y_b = 0 \rightarrow 1 \qquad \text{and} \qquad x_c = 0 \rightarrow 1$$

More specifically, the spanwise position is given by

$$y_{b_j} = \frac{(y_j - y_{cr})}{b} \tag{5.4.17}$$

where y_{b_j} is the non-dimensionalized spanwise position of node-j, y_j is the spanwise location of node-j from the body frame x-axis, y_{cr} is the spanwise location of the root chord from the body frame x-axis, and b is the total span of the fin.

Note that in this scenario, $y_b = 0$ and $y_b = 1$ correspond to the root and tip chord locations respectively. Similarly, the chordwise position is found via

$$x_{c_j} = \frac{\left(x_j - x_{c_j LE}\right)}{c_j} \tag{5.4.18}$$

where x_{c_j} is the non-dimensionalized chordwise position of node-j, x_j is the chordwise location of node-j along the body frame x-axis, $x_{c_j LE}$ is the location of the local chord leading edge on the body frame x-axis, and c_j is the local chord of the fin.

Note that for this reference $x_c = 0$ and $x_c = 1$ correspond to the leading and trailing edges of the local chord respectively.

The distribution profiles are also non-dimensionalized such that the magnitudes of K_b and K_c range between zero and one. That is,

$$K_b = 0 \rightarrow 1 \qquad \text{and} \qquad K_c = 0 \rightarrow 1$$

The spanwise and chordwise factors are then combined to generate a fractional percentage of the total load. The nodal load for the *j*-th node is then determined via,

$$f_{f_j} = \frac{F_f K_{t_j}}{\sum K_t} \tag{5.4.19}$$

where F_f is the fin force to be distributed, K_{t_j} is the total load factor of node-j,

where $K_{t_j} = K_{b_j} K_{c_j}$ (5.4.20)

These nodal loads must be placed into a full order load vector and subsequently transformed to generate the reduced order load vector:

$$\mathbf{f}_{f_{rom}} = \mathbf{S}^T \mathbf{f}_f \tag{5.4.21}$$

The procedure for generating the load distribution profiles is dependent upon several factors including the Mach number, angle of attack, normal force slope and fin geometry. Subsonic spanwise profiles are handled via a Fourier series expansion.[23,25] The fin distributions for supersonic flow were computed through the use of supersonic wing theory.[28] The methodology for determining these load distribution profiles are presented in **Appendix A**.

5.4.3 Load Distribution Methodology

A sample spanwise load distribution is included below in **Figure 4.7.**

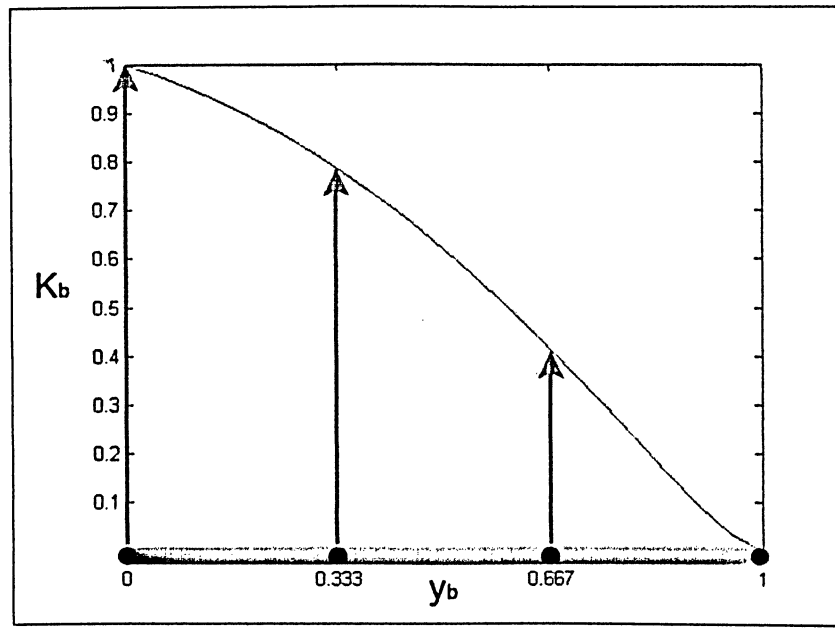

Figure 5.7: Sample Spanwise Load Distribution

The profile above shows that the maximum loading is given at the root of the fin. The load at the tip chord (y_b = 1) is zero. The curved profile shows a computed load distribution for an arbitrarily chosen flight condition. The fin structure is discretized into a finite number of nodes, and as a result, the load is segmented into several nodal loads. For configurations with a coarse spanwise mesh, the resulting effective nodal load representation shown in **Figure 5.7** will not

adequately capture the center of pressure location given by the continuous profile. Thus, a method for adjusting the computation of the load factor is required and is presented.

To retain center of pressure location consistency, the loads must be adjusted using a nodal weighting methodology. For a given spanwise or chordwise section, each node is assumed to carry the loading across a half element edge length (y_{be}) on either side of the node. Thus, all the loading across this segment will be collapsed upon the given node. For nodes at the root or tip in the case of spanwise profiles (or equivalently, leading edge and trailing edge nodes for chordwise profiles), the fin surface exists only on one side and therefore the loading region is ($y_{be}/2$). **Figure 5.8** displays the region of influence for each spanwise node.

The new method for determining the spanwise and chordwise load factors is now found by computing the load at the center of the region of influence and is subsequently weighted by the length of the region of influence, that is,

$$K_{b_i} = K_{bo_i} l_{be} \tag{5.4.22}$$

$$K_{c_i} = K_{co_i} l_{ce} \tag{5.4.23}$$

where K_{bo_i} and K_{co_i} are the loads at the center of the area of influence, and l_{be}, and l_{ce} are the lengths of the areas of influence for the given node.

Note that for meshes with equal element sizing, l_{be} will be equivalent to the element edge length y_{b_e} for central nodes, and $\frac{1}{2} y_{b_e}$ for end nodes. For meshes with variable sized element mapping, the size of each element should be known to determine the appropriate nodal region of influence.

The total load factor (K_t) for each node is then found in the same manner as that described by **Equation (5.4.20)** above.

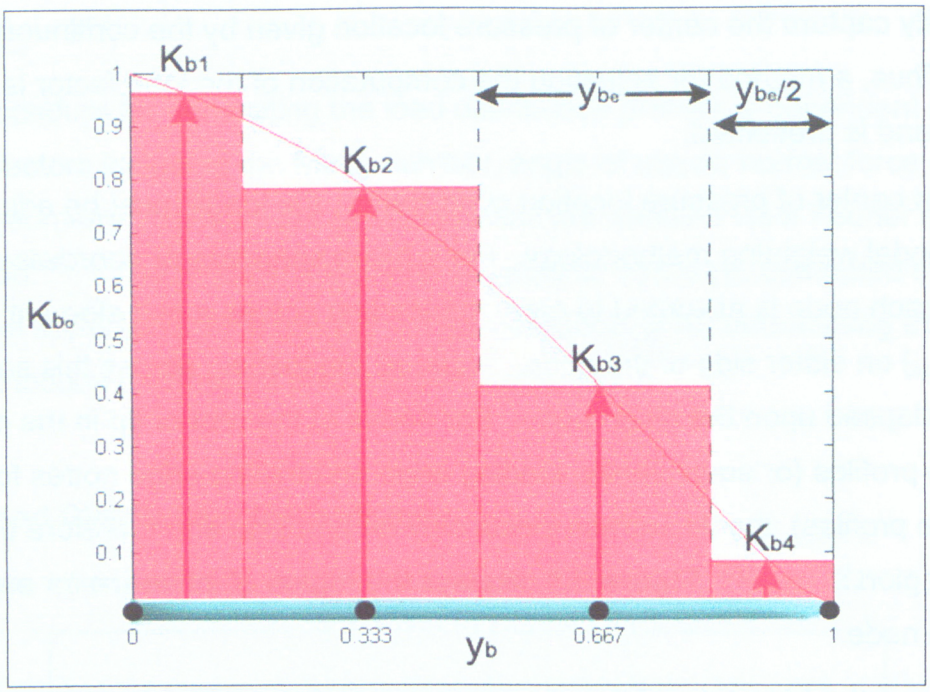

Figure 5.8: Sample Spanwise Load Distribution (Adjusted)

The resulting profile provides much greater consistency with the originally computed center of pressure location, particularly for a coarse fin mesh. For the spanwise case, the tip nodes will carry a small nonzero loading, and the root nodes will have their total load diminished somewhat in relation to the central nodes with larger areas of influence.

The accurate capture of the center of pressure location is critical for the prediction of flexible fin motions. The fin bending motions are strongly influenced by the moment between the fin normal force and the spanwise center of pressure.

A sample load distribution for a fin at an arbitrary flight condition is shown in **Figure 5.9**

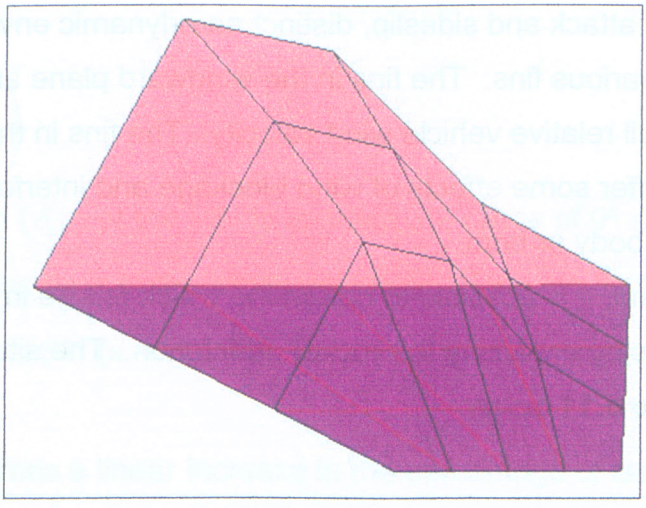

Figure 5.9: Sample Fin Loading

Figure 5.10 shows the resulting adjusted nodal profile, with the resulting nodal loads represented as a series of red dots. Note that for the current profile, all nodes on the fin surface carry a load. This is in contrast to **Figure 5.9**, where the leading edge, trailing edge and tip nodes carried zero loads.

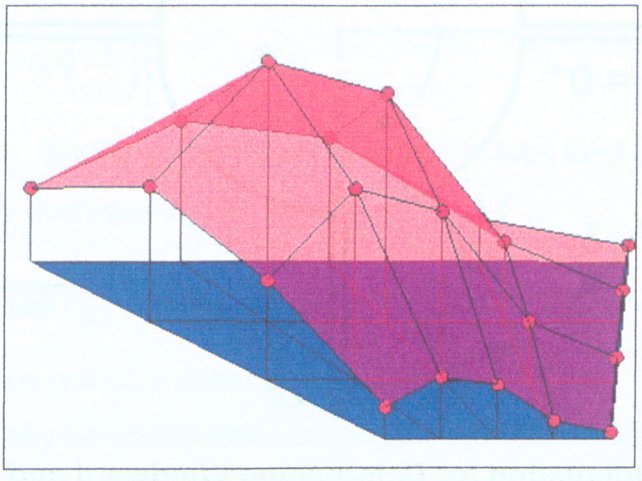

Figure 5.10: Sample Fin Loading (Adjusted)

5.4.4 Leeward Reduction due to Flow Blockage

As the vehicle is rolled, the orientation of the fins changes with respect to the velocity vector. For flight with zero angle of attack, and zero sideslip, the wind velocity experienced by each fin may be assumed to be equivalent. However, at

non-zero angles of attack and sideslip, distinct aerodynamic environments develop upon the various fins. The fins in the windward plane are assumed toexperience the full relative vehicle wind velocity. The fins in the leeward plane are assumed to suffer some effects of wind blockage and interference due to the windward fins, the body or both.

At any given instant, it is possible to determine which fins lie in the windward and leeward planes by analyzing the rocket orientation. The situation is illustrated in **Figure 5.11** below.

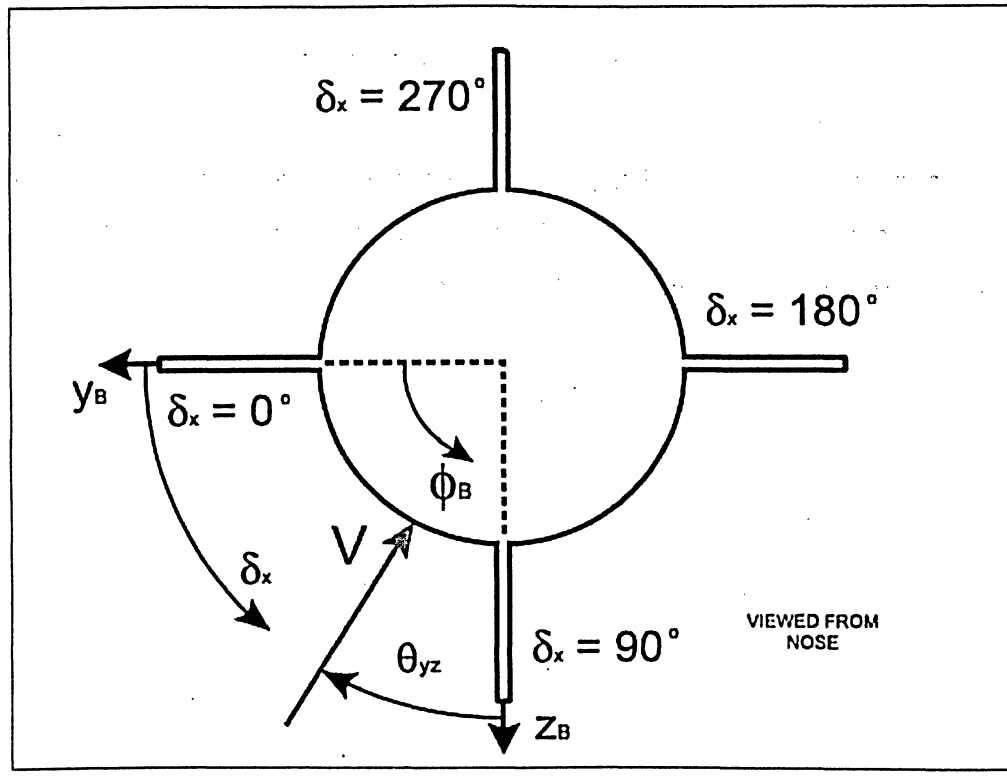

Figure 5.11: Orientation for Determining Windward and Leeward Fins

The angle between the y and z components of the velocity vector (θ_{yz}) and static angular position (δ_x) of each fin are the important factors in determining the whether a fin is in the windward or leeward plane. The net orientation of the *i*-th fin can be determined by

$$\delta_{tot_i} = \delta_{x_i} + \theta_{yz} \tag{5.4.24}$$

where

$$\theta_{yz} = \tan^{-1}\left(\frac{V_{By}}{V_{Bz}}\right) \qquad (5.4.25)$$

If the net orientation (δ_{tot}) of the *i*-th fin is within the range of $0° \leq \delta_{tot} \leq 180°$ ($0 \leq \delta_{tot} \leq \pi$ rad), then the fin is in the windward plane. If the *i*-th fin falls within the range of $180° < \delta_{tot} < 360°$ ($\pi < \delta_{tot} < 2\pi$ rad), then the fin is in the leeward plane.

Reference 31 assumes a linear increase in the percentage of load attributed to the windward fins for increasing angle of attack. The following formula is used to distribute the total fin loads between the windward and leeward planes for a cruciform-tail rocket at a roll angle of $\phi = 45°$ (i.e., the "x" configuration). A maximum leeward loading of 90% is acquired at an angle of attack equivalent to or greater than 65°.

For $\alpha \leq 65°$,

$$(c_n)_{WW} = c_n\left[0.5 + 0.4\left(\frac{\alpha}{65}\right)\right] \qquad (5.4.26)$$

where α is in degrees. Similarly, the percentage of the total load attributed to the leeward fins is linearly decreased. For $\alpha \leq 65°$,

$$(c_n)_{LW} = c_n\left[0.5 - 0.4\left(\frac{\alpha}{65}\right)\right] \qquad (5.4.27)$$

Above $\alpha = 65°$, the ratio remains constant.

The above relation may be extrapolated to include the relative loads carried by fins at any orientation. The method for determining the fin loads in **Reference 31** is different from the one employed here. **Reference 31** computes the total load acting upon the fins, and then attributes a percentage of the total fin load to the windward and leeward fins. However, for this case, the load of each fin is determined separately as outlined in **Section 5.4.2.** Thus, a load reduction factor, hereby introduced as 'f_{LW}', must be determined to represent the effects of flow blockage and interference upon the leeward fins.

It is assumed that the windward fins will receive 100% of their normally calculated load for any flight condition. The minimum condition exists at a relative fin position of $\delta_{tot} = 270°$, where the fin is exactly 180° away from the body velocity wind vector.

Thus, it is known that at $\delta_{tot} = 180°$, f_{LW} = 1. The leeward load reduction factor is also known for the case of $\phi_B = 45°$ (i.e. $\delta_{tot} = 225°$ in the leeward plane), using **Equations (5.4.26)** and **(5.4.27)**. Thus,

$$f_{LW}(225°, \alpha) = \frac{(c_n)_{LW}}{(c_n)_{WW}} = \frac{1-(c_n)_{WW}}{(c_n)_{WW}} \tag{5.4.28}$$

It is assumed that the variation in f_{LW} between $\delta_{tot} = 180°$ and $\delta_{tot} = 270°$ will be exponential. Thus,

$$f_{LW}(\delta_{tot}, \alpha) = e^{-\tau x_\delta} \tag{5.4.29}$$

where τx_δ is the function time-constant, and

$$x_\delta = 1 - \cos(\delta_{tot} - 180°) \tag{5.4.30}$$

The term 'τ' may be extracted from the analysis of the equation at $\delta_{tot} = 225°$. For example,

$$\tau(\alpha) = -\ln[f_{LW}(225°, \alpha) x_\delta(225°)] \tag{5.4.31}$$

The profile is given to be symmetric about $\delta_{tot} = 270°$. The resulting leeward reduction profiles for an arbitrarily oriented fin are presented in **Figure 5.12.** Profiles are shown for up to α = 40°.

The method outlined above is an approximation. In reality, there are many complex interactions, particularly at high velocities, that induce interference effects on the tailfins. For example, for larger Mach numbers, and non zero sideslip angles, asymmetric body vortices will be shed which can drastically affect the relative loadings of certain fins.[33] The flow properties from arbitrarily deformed fins can additionally impose flow variations that are difficult to characterize and predict in general. To achieve such a level of accuracy,

advanced CFD techniques would likely need to be employed to detail the complete interactions between all structures.

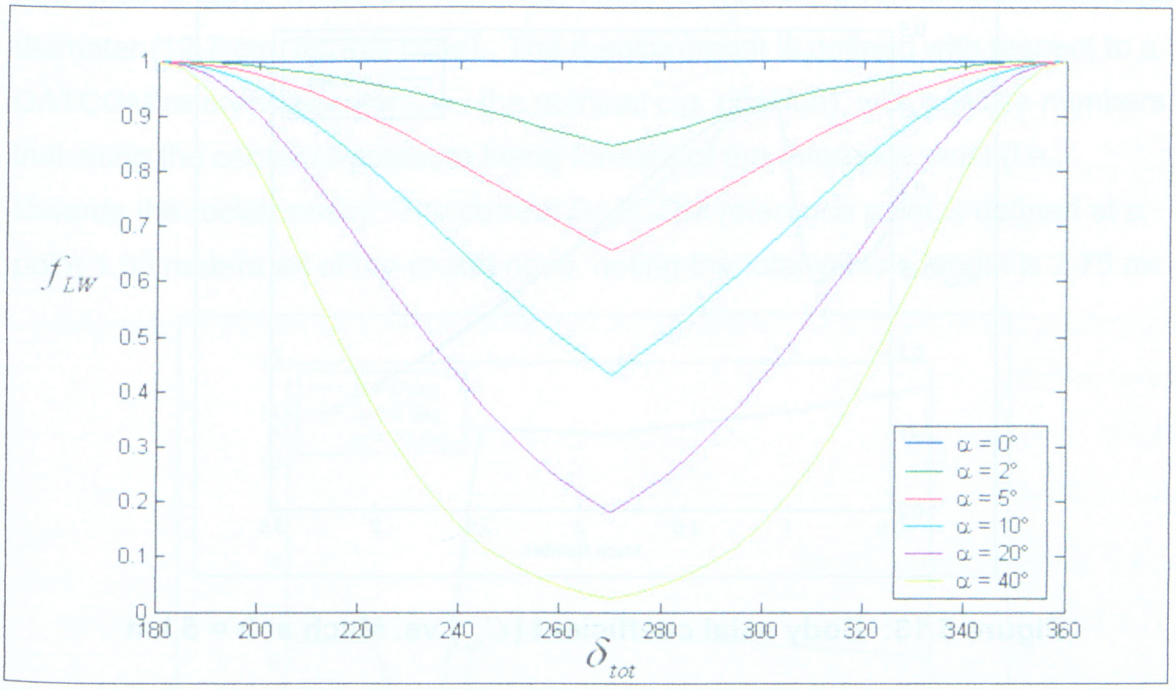

Figure 5.12: Leeward Load Reduction Factor

5.5 Aerodynamic Coefficients

The aerodynamic coefficients used within the flight simulation aerodynamics subsystem have been tabulated from the results given from the program Missile DATCOM.[34] The resulting outputs are specific to a rocket of SPHADS dimensions, with coefficients collected for both the fuselage and fins. The coefficients are defined in the coefficient frame ($\mathcal{F}_{co}$) as was defined in **Figure 5.4**. Results were tabulated for speeds up to Mach 5, and angles of attack up to 20°, for a variety of altitudes. Some sample results are presented in the following figures. The profiles are given for a fixed altitude of 5 km.

Figure 5.13 depicts the axial force coefficient (C_{A_B}) corresponding to the fuselage versus Mach number. A sharp rise is evident when approaching

transonic conditions, as is expected. Profiles are shown for three separate angles of attack.

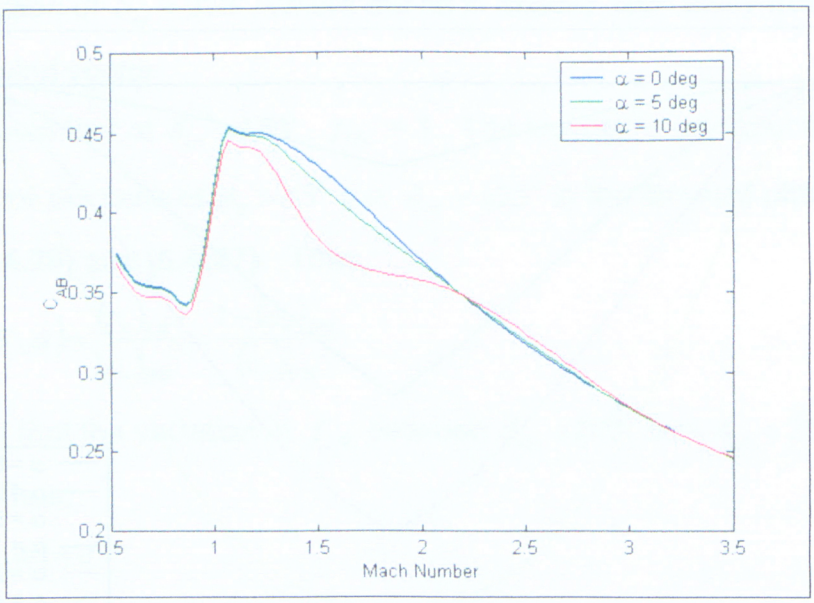

Figure 5.13: Body axial coefficient (C_{A_B}) vs. Mach at h = 5 km

Figure 5.14 shows the fin normal force coefficient with a change in angle of attack ($C_{N\alpha_f}$). For supersonic speeds the coefficients decrease rapidly for each of the three orientations presented.

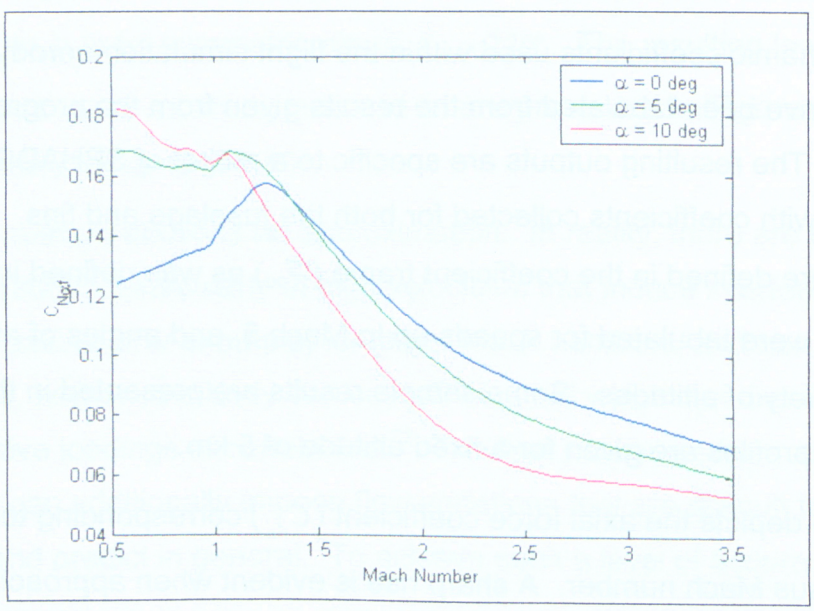

Figure 5.14: Fin normal force slope coefficient ($C_{N\alpha_f}$) vs. Mach at h = 5 km

Some sample results of the location of the fuselage center of pressure are presented in **Figure 5.15**. The values shown are in terms of number of fuselage reference lengths, where the reference length is typically given to be the fuselage diameter (12.7 cm, for this case). The measurement is defined with respect to a DATCOM reference center (i.e., the nominal c.g. position), with positive numbers indicating the center of pressure being forward of the reference point (i.e., towards the rocket nose). The current DATCOM reference point is defined at a point 1.59 meters aft of the rocket nose, noting the total vehicle length is 2.75 m.

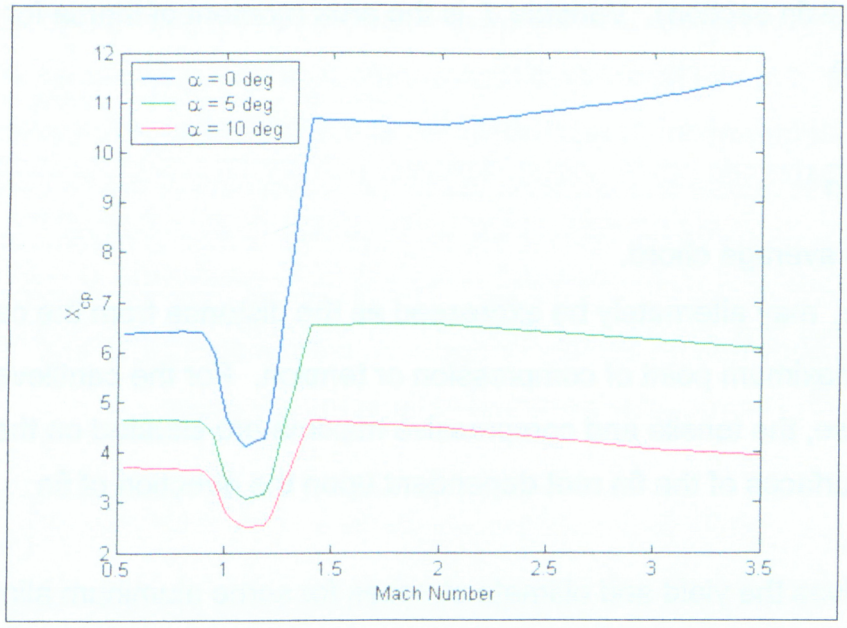

Figure 5.15: Fuselage center of pressure location vs. Mach at h = 5 km in terms of fuselage reference lengths

5.6 Stress Approximation

One facet of the flexural deformation dynamics not modeled explicitly within the simulation engine are the structural limitations of the vehicle material properties. That is, if the loads become large enough, the material strength may be exceeded. The structural component may then deform plastically, and may indeed fail destructively.

In the current project, the primary factor driving the system instability is the fin deformation. An engineering approximation may be made by assuming the fin

structure to be represented by a cantilevered Euler Bernoulli beam. The stress due to bending in the fin may be found with the flexure formula of Euler Bernoulli theory.[35] That is,

$$\sigma = \frac{Mz_c}{I} \tag{5.6.1}$$

where M is the bending moment acting on the fin. In this case, the moment would be derived from the Normal force acting at the center of pressure. Variable z_c is the distance from the centroidal axis (i.e., the centerline of a symmetric tail fin section). Variable I is the area moment of inertia for the given cross section

where

$$I = \tfrac{1}{12}\bar{c}t^3$$

and $\bar{c}$ is the average chord.

The term z_c may alternately be expressed as the distance from the centroidal axis to the maximum point of compression or tension. For the cantilevered beam-fin case, the tensile and compressive maxima are situated on the upper and lower surfaces of the fin root dependent upon the direction of fin deformation.

Table 5.1 gives the yield and ultimate stresses for some aluminum alloys.[35]

Material	σ_y (MPa)	σ_u (MPa)
Aluminum alloy 2014-T6	410	480
Aluminum alloy 6061-T6	275	310

Table 5.1: Aluminum Alloy Properties

The bending moment acting on the fin is assumed to be simply dependent on the fin normal force and the spanwise location of the center of pressure. Thus,

$$M = N_f y_{cp}$$

Assuming the center of pressure is located at the mid-span, the following equation yields the critical value of normal force to reach the yield strength of the given material:

$$\left(N_f\right)_{cr} = \frac{\sigma_y I}{y_{cp} z_c} = \frac{2\sigma_y I}{b z_c} \tag{5.6.2}$$

This current chapter has defined and detailed all of the forces that are deemed most pertinent to the gross and flexible motions of a flexible rocket vehicle. In the next chapter these forces are combined with the equations of motion and the simulator framework as described in **Chapter 4** to present various simulation results.

Chapter 6: Results and Discussion

In the sections to follow, results will be presented for a variety of test scenarios. First, simple representations of the rocket stability problem will be evaluated. Later results from the three dimensional flexible flight simulator will be presented and discussed.

6.1 Planar Pinned Model

Perhaps the simplest stability validation model available considers a rocket pinned at the mass center within a wind-tunnel. The rocket is free to rotate in the pitch plane, and the fin flexibility is represented by a spring as shown in **Figure 6.1**. The fin deformation (δ) represents the scope of flexible deformation permitted in this model and corresponds to the movement of the fin center of pressure in response to the vehicle loading. The fin is free to deform in a direction perpendicular to the fuselage. The distances from the rocket mass center to the body and fin centers of pressure are denoted by 'a' and 'd' respectively.[36] The rocket is assumed to lie in the x-y plane.

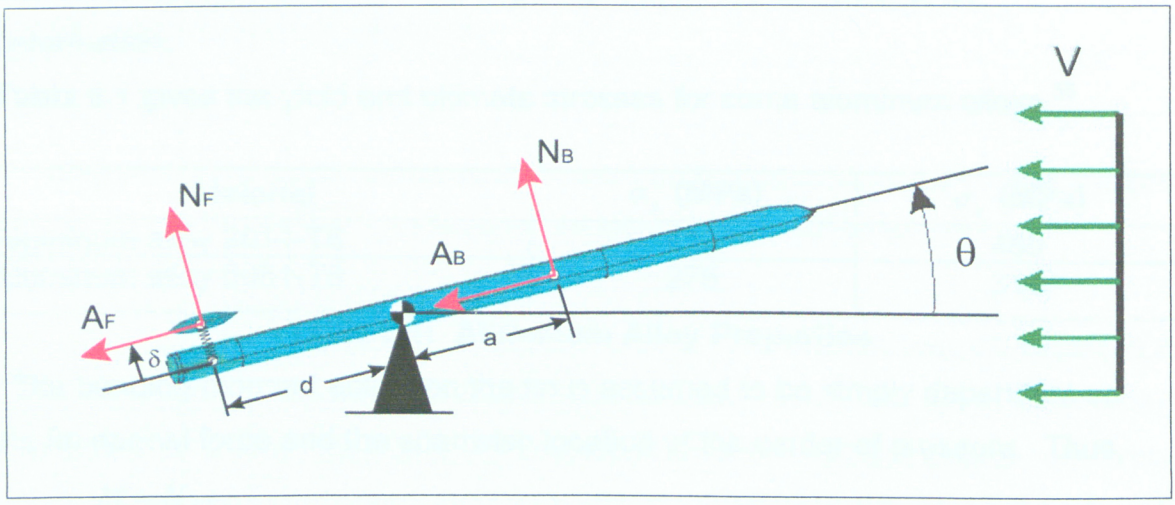

Figure 6.1: Pinned Planar Stability Model

For longitudinal stability to exist the vehicle composite aerodynamic center must lie aft of the vehicle center of gravity.

The equation of motion for this two degree of freedom system is then

$$\begin{bmatrix} J & -m_f d \\ -m_f d & m_f \end{bmatrix} \begin{bmatrix} \ddot{\theta} \\ \ddot{\delta} \end{bmatrix} = \begin{bmatrix} M_B - F_{xf}\delta - F_{yf} d \\ F_{yf} - k\delta \end{bmatrix} \tag{6.1}$$

The vehicles loads are summarized by

$$F_{xf} = -A_f = -qS_f C_{Af} \tag{6.2}$$

$$F_{yf} = N_f = qS_f C_{N\alpha_f} \alpha_f \tag{6.3}$$

where

$$\alpha_f = \theta + \left(\frac{d}{V}\right)\dot{\theta} - \left(\frac{1}{V}\right)\dot{\delta} \tag{6.4}$$

$$M_B = qSaC_{N\alpha_B}\theta + qScC_{M\dot{\alpha}_B}\dot{\theta} + qSaC_{N\dot{\alpha}_B}\dot{\delta} \tag{6.5}$$

The equations of motion reveal that the pitch motion of the pinned vehicle is intrinsically linked to the fin structural deformation through the fin angle of attack term. Substituting **Equations (6.2)-(6.5)** into **Equation (6.1)** and rearranging, gives the equations of motion in the standard mass, damping, and stiffness format:

$$\mathbf{M}\ddot{\mathbf{x}} + \mathbf{C}\dot{\mathbf{x}} + \mathbf{K}\mathbf{x} = \mathbf{0} \tag{6.6}$$

with $\mathbf{x} = \begin{bmatrix} \theta \\ \delta \end{bmatrix}$

where the mass, damping and stiffness matrices are

$$\mathbf{M} = \begin{bmatrix} J & -m_f d \\ -m_f d & m_f \end{bmatrix} \tag{6.7}$$

$$\mathbf{C} = \frac{qS}{V}\begin{bmatrix} -\left(C_{M\dot{\alpha}_B} c + C_{N\dot{\alpha}_B} a\right) + C_{N\alpha f}\left(\frac{S_f}{S}\right)d^2 & -C_{N\alpha f}\left(\frac{S_f}{S}\right)d \\ -C_{N\alpha f}\left(\frac{S_f}{S}\right)d & C_{N\alpha f}\left(\frac{S_f}{S}\right) \end{bmatrix} \tag{6.8}$$

$$\mathbf{K} = qS\begin{bmatrix} -C_{N\alpha_B} a + C_{N\alpha f}\left(\frac{S_f}{S}\right)d & -C_A \\ -C_{N\alpha f}\left(\frac{S_f}{S}\right) & k \end{bmatrix} \tag{6.9}$$

For the purposes of this test, the fin stiffness is assumed to be equivalent to that of a cantilevered beam with a load at a specified location along the span, as seen in **Figure 6.2**. The aerodynamic load is assumed to be located at the midspan location. Thus, from Euler Bernoulli theory, the resulting stiffness becomes

$$k = \frac{24EI}{L^3} \tag{6.10}$$

The bending inertia is then defined as

$$I = \tfrac{1}{12} c t_f^{\,3} \tag{6.11}$$

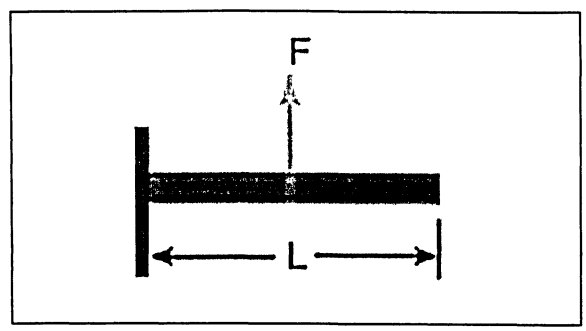

Figure 6.2 Fin Stiffness Load Approximation

The system is then transformed into state space to perform an eigenvalue stability analysis. The general state space form is given by $\dot{\mathbf{X}} = \mathbf{AX}$. Thus, for the present pinned analysis, the following is generated:

$$\begin{bmatrix} \ddot{\mathbf{x}} \\ \dot{\mathbf{x}} \end{bmatrix} = \begin{bmatrix} \mathbf{M} & \mathbf{0} \\ \mathbf{0} & \mathbf{1} \end{bmatrix}^{-1} \begin{bmatrix} -\mathbf{C} & -\mathbf{K} \\ \mathbf{1} & \mathbf{0} \end{bmatrix} \begin{bmatrix} \dot{\mathbf{x}} \\ \mathbf{x} \end{bmatrix} \tag{6.12}$$

where

$$\dot{\mathbf{X}} = \begin{bmatrix} \ddot{\mathbf{x}} \\ \dot{\mathbf{x}} \end{bmatrix}$$

$$\mathbf{A} = \begin{bmatrix} \mathbf{M} & \mathbf{0} \\ \mathbf{0} & \mathbf{1} \end{bmatrix}^{-1} \begin{bmatrix} -\mathbf{C} & -\mathbf{K} \\ \mathbf{1} & \mathbf{0} \end{bmatrix} \tag{6.13}$$

6.1.1 Pinned Rocket Stability Analysis

The rocket model used for the above pinned wind-tunnel analysis, is based upon the SPHADS rocket vehicle as was previously discussed in **Chapter 4**. As the fins decrease in thickness, the stiffness decreases by the third power as seen in **Equation (6.11)**. As the fins decrease in stiffness, they are subject to greater deformations, which in turn reduce the overall effectiveness of the fin. When the fin is no longer able to provide the required restorative forces to return the system to equilibrium the system is unstable.

For a model pinned in a wind tunnel, the system is automatically in equilibrium, provided there are no initial deformations, or deformation rates. The model may be tested for any configuration of fin thickness, velocity and atmospheric density. The atmospheric properties may be altered to simulate the flight at any desired altitude. The aerodynamic coefficients used in the analysis, were generated from a series of Missile DATCOM derived tables.[34] Refer to **Section 5.5** for additional information regarding coefficients.

Figures 6.3 to **6.5** depict the stability boundary plots for the pinned planar rocket model for a variety of altitudes. The contours shown in these plot represent the maximum real eigenvalue component ($\sigma_d = \max(\mathrm{Re}\{\lambda_i\})$). This component ($\sigma_d$) must be negative for stability to exist. The zero contour represents the stability boundary. In this section and in the sections to follow, the term divergence will be used to describe unstable non-oscillating behaviour. The term flutter will be employed to describe any oscillating sinusoidal unstable growth trends. The nature of the instability in the following plots is flutter.

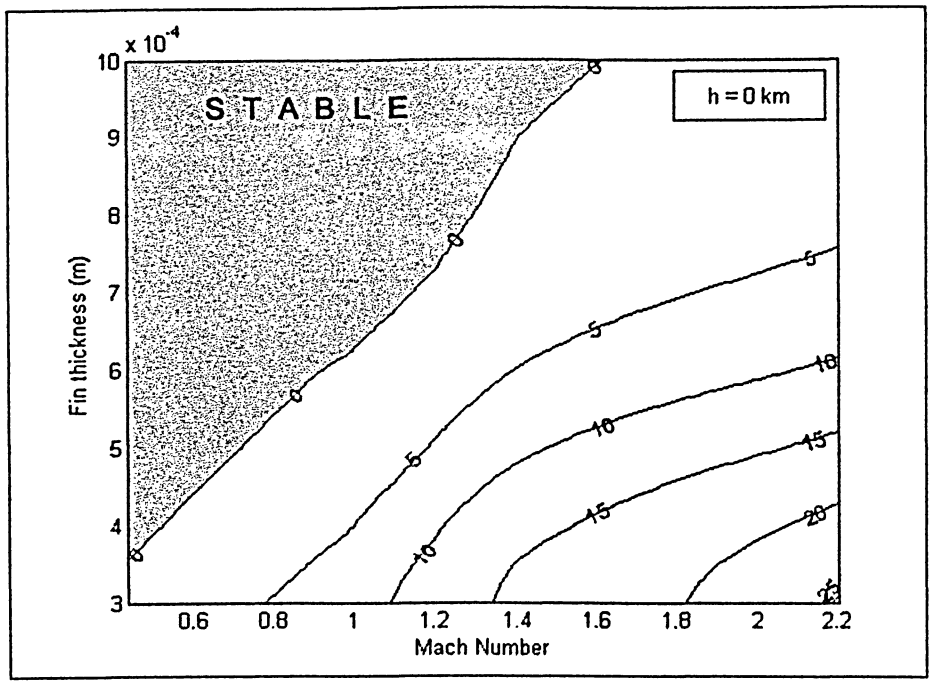

Figure 6.3: Stability Boundary for Pinned Rocket Model (h = 0 km)

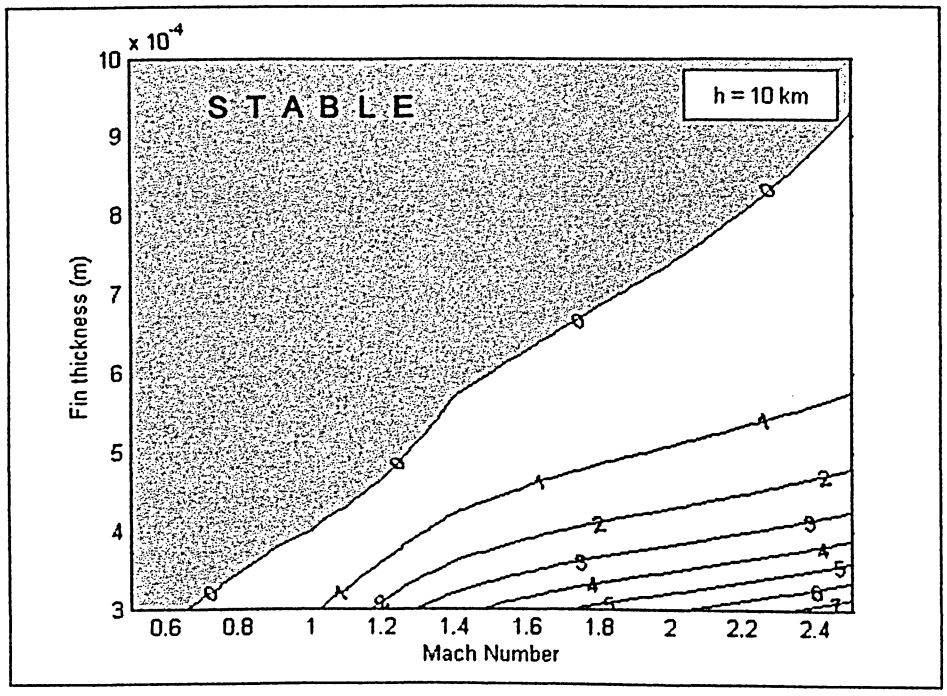

Figure 6.4: Stability Boundary for Pinned Rocket Model (h = 10 km)

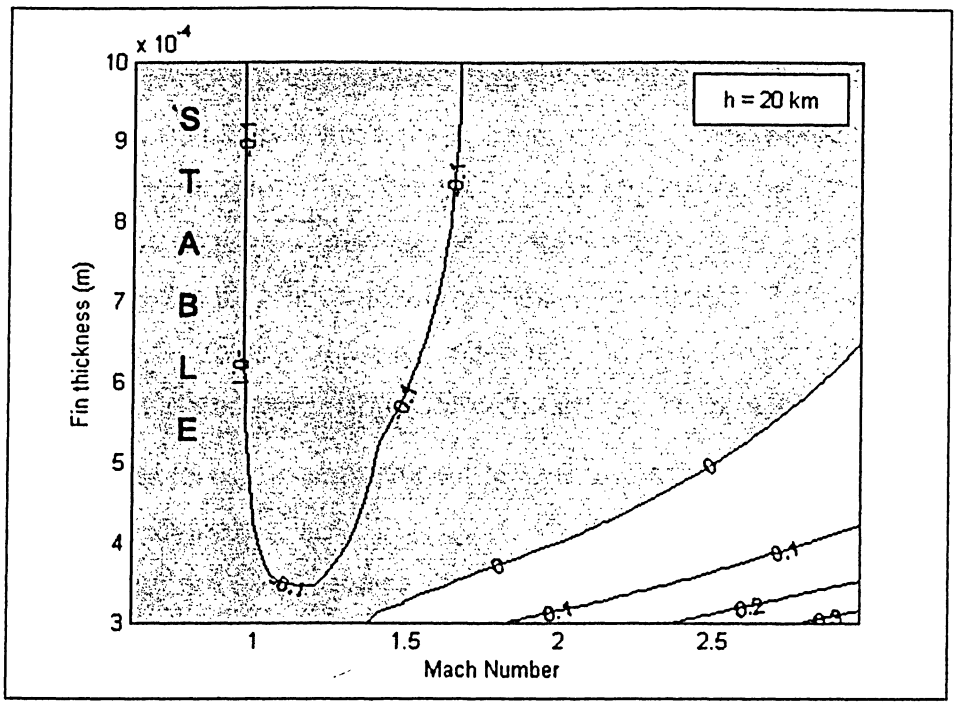

Figure 6.5: Stability Boundary for Pinned Rocket Model (h = 20 km)

Referring to the above figures, it can be seen that increased altitude has the effect of lowering the stability boundary. This result illustrates the decreasing atmospheric density at higher altitudes, which in turn decrease the aerodynamic forces acting on the vehicle. In terms of stability, this effectively means that the configurations are more stable at higher altitudes. Thus, the fin thickness must be decreased to obtain unstable behaviour in comparison to a similar vehicle traveling at the same velocity at a lower altitude.

6.2 Planar Unpinned Model

Another simplified rocket flight model is now considered, with the rocket being removed from the wind-tunnel and free to translate in the x and y-directions. An equilibrium condition must be established to perform the desired perturbation analysis. The simplest free flight equilibrium scenario is the case for which the rocket is directed straight down, traveling at terminal velocity, with axial drag force balancing vehicle weight. For a given model configuration and flight condition the equilibrium may be established through the adjustment of the

atmospheric properties. Equivalently, the altitude may be adjusted (assuming the use of a fixed atmospheric model) until the atmospheric density has sufficiently increased or decreased so as to yield the desired balance of forces.

The scenario is depicted in **Figure 6.6**. As with the pinned model the distances 'a' and 'd' correspond to the distances from the mass center to the body and fin center of pressures respectively. Additionally, the rocket as shown in **Figure 6.6** is situated in the x-y plane. Gravity and weight are now added, along with disturbances 'u' and 'v' which represent velocity disturbances in the body frame x and y directions.[37]

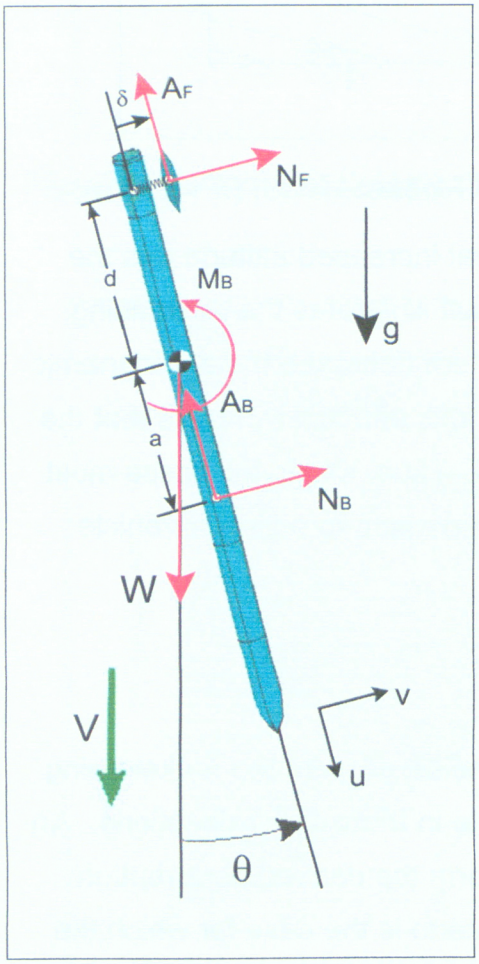

Figure 6.6: Unpinned Planar Stability Model

The conditions required for this equilibrium state to exist are as follows.

$$\sum A_0 = W \qquad N_{B_0} = 0 \qquad N_{f_0} = 0$$

$$f_\delta = 0 \qquad \alpha_{B_0} = 0 \qquad \alpha_{f_0} = 0$$

where f_δ is the net upward force acting on the fin. The initial pitch angle must also be defined as -90°. All equations presented from this point onward refer to the rocket's body frame ($\mathcal{F}_B$).

The velocities at the body frame origin are given as:

$$\begin{aligned} U &= V_0 \cos\theta + u \\ V &= -V_0 \sin\theta + v \end{aligned} \tag{6.14}$$

The velocities at the body center of pressure are then given by (assuming small angles)

$$\begin{aligned} U_B &= U \cong V_0 + u \\ V_B &= V + a\dot{\theta} \cong -V_0\theta + v + a\dot{\theta} \end{aligned} \tag{6.15}$$

Similarly, the local velocities at the fin center of pressure are found to be,

$$\begin{aligned} U_f &= U \cong V_0 + u \\ V_f &= V - d\dot{\theta} + \dot{\delta}_f \cong -V_0\theta + v - d\dot{\theta} + \dot{\delta}_f \end{aligned} \tag{6.16}$$

Referring to **Figure 6.6,** the total net forces and torques acting on the vehicle are,

$$\begin{aligned} \sum F_x &= -(A_B + A_f) + W\cos\theta \\ \sum F_y &= (N_B + N_f) - W\sin\theta \\ \sum M &= M_B + N_B a - N_f d + A_f \delta \end{aligned} \tag{6.17}$$

Now relating the net forces to perturbation forces and considering the fin spring loading yields the following:

$$\begin{aligned} \delta F_x &= -(\delta A_B + \delta A_f) \\ \delta F_y &= (\delta N_B + \delta N_f) - W\theta \\ \delta M &= \delta N_B a - \delta N_f d + \delta M_B + \delta A_f \delta \\ \delta f_\delta &= \delta N_f - k\delta \end{aligned} \tag{6.18}$$

Small angles are assumed in the above set of equations and throughout the remainder of this section. The resulting perturbation equations of motion for this four degree of freedom system are

$$\begin{bmatrix} m & 0 & 0 & 0 \\ 0 & m & c_x & m_f \\ 0 & c_x & I & -m_f d \\ 0 & m_f & -m_f d & m_f \end{bmatrix} \begin{bmatrix} \dot{u} \\ \dot{v} \\ \ddot{\theta} \\ \ddot{\delta} \end{bmatrix} = \begin{bmatrix} \delta F_x \\ \delta F_y \\ \delta M \\ \delta f_\delta \end{bmatrix} \tag{6.19}$$

The perturbation forces in **Equation (6.18)** are now expanded below.

The normal forces are primarily affected by the local angle of attack.

$$\begin{aligned} \delta N_B &= q_0 S C_{N\alpha_B} \alpha_B \\ \delta N_f &= q_0 S_f C_{N\alpha_f} \alpha_f \end{aligned} \tag{6.20}$$

The axial force components may be expanded to consider the perturbation effects of changing dynamic pressure and Mach number as well as angle of

attack. Note that within this section the Mach number is denoted with an overbar '$\bar{}$' to distinguish it and avoid confusion with the moment term. That is,

$$\begin{aligned}\delta A_B &= q_0 S\left[C_{A_{B0}}\delta q + C_{A_{\bar{M}B}}\delta\bar{M} + C_{A\alpha_B}\alpha_B\right]\\ \delta A_f &= q_0 S_f\left[C_{A_{f0}}\delta q + C_{A_{\bar{M}f}}\delta\bar{M} + C_{A\alpha_f}\alpha_f\right]\end{aligned} \tag{6.21}$$

The term δq can be extracted from the expansion of the dynamic pressure term as follows

$$q = \tfrac{1}{2}\rho(V_0+u)^2 = \tfrac{1}{2}\rho\left(V_0^2 + 2V_0u + u^2\right) \approx \tfrac{1}{2}\rho\left(V_0^2 + 2V_0u\right) = q_0 + \delta q$$

Thus,

$$\delta q = \rho V_0 u = \frac{2q_0}{V_0}u \tag{6.22}$$

The Mach number can similarly be expanded, yielding

$$\bar{M} = \frac{(V_0+u)}{\sqrt{\gamma RT}} = \frac{V_0}{\sqrt{\gamma RT}} + \frac{u}{\sqrt{\gamma RT}} = \bar{M} + \delta\bar{M}$$

Thus,

$$\delta\bar{M} = \frac{u}{\sqrt{\gamma RT}} = \frac{\bar{M}}{V_0}u \tag{6.23}$$

The angles of attack can be determined with the expression

$$\alpha = -\frac{V}{U} \qquad \text{(assuming small } \alpha\text{)} \tag{6.24}$$

Recalling **Equations (6.15)** and **(6.16)** relating the velocities at the body and fin center of pressures, the respective angles of attack then become,

$$\begin{aligned}\alpha_B &= \theta - \frac{v + a\dot{\theta}}{V_0}\\ \alpha_f &= \theta - \frac{v - d\dot{\theta} + \dot{\delta}}{V_0}\end{aligned} \tag{6.25}$$

Combining **Equations (6.18)-(6.25)** and following some rearranging, the mass, stiffness and damping matrices can be extracted. The equations of motion are then again of the form,

$$\mathbf{M}\ddot{\mathbf{x}}+\mathbf{C}\dot{\mathbf{x}}+\mathbf{K}\mathbf{x}=\mathbf{0} \tag{6.26}$$

where

$$\mathbf{x}=\begin{bmatrix} x & y & \theta & \delta \end{bmatrix}^T$$

The mass, stiffness and damping matrices for the unpinned planar rocket stability problem are given as follows.

$$\mathbf{M}=\begin{bmatrix} m & 0 & 0 & 0 \\ 0 & m & c_x & m_f \\ 0 & c_x & I & -m_f d \\ 0 & m_f & -m_f d & m_f \end{bmatrix} \tag{6.27}$$

$$\mathbf{K}=q_0 S\begin{bmatrix} 0 & 0 & C_{A\alpha_B}+C_{A\alpha_f}\left(\frac{S_f}{S}\right) & 0 \\ 0 & 0 & -C_{N\alpha_B}-C_{N\alpha_f}\left(\frac{S_f}{S}\right)+\frac{W}{q_0 S} & 0 \\ 0 & 0 & C_{N\alpha_f}\left(\frac{S_f}{S}\right)d-C_{M\alpha_B}c-C_{N\alpha_B}a & 0 \\ 0 & 0 & -C_{N\alpha_f}\left(\frac{S_f}{S}\right) & \frac{k}{q_0 S} \end{bmatrix} \tag{6.28}$$

$$\mathbf{C}=\frac{q_0 S}{V_0}\begin{bmatrix} V_0 C_{Au} & -\left(C_{A\alpha_B}+C_{A\alpha_f}\left(\frac{S_f}{S}\right)\right) & -\left(C_{A\alpha_B}+C_{A\alpha_f}\left(\frac{S_f}{S}\right)\right)a & 0 \\ 0 & C_{N\alpha_B}+C_{N\alpha_f}\left(\frac{S_f}{S}\right) & C_{N\alpha_B}a-C_{N\alpha_f}\left(\frac{S_f}{S}\right)d & C_{N\alpha_f}\left(\frac{S_f}{S}\right) \\ 0 & C_{M\alpha_B}c+C_{N\alpha_B}a-C_{N\alpha_f}\left(\frac{S_f}{S}\right)d & C_{M\alpha_B}ac+C_{N\alpha_B}a^2+C_{N\alpha_f}\left(\frac{S_f}{S}\right)d^2 & -C_{N\alpha_f}\left(\frac{S_f}{S}\right)d \\ 0 & C_{N\alpha_f}\left(\frac{S_f}{S}\right) & -C_{N\alpha_f}\left(\frac{S_f}{S}\right)d & C_{N\alpha_f}\left(\frac{S_f}{S}\right) \end{bmatrix} \tag{6.29}$$

6.2.1 Unpinned Rocket Stability Analysis

As was done for the pinned case, an eigen-analysis as outlined in **Equation (6.13)** was performed for the unpinned case. The stability boundary plot for the unpinned case is showcased in **Figure 6.7.**

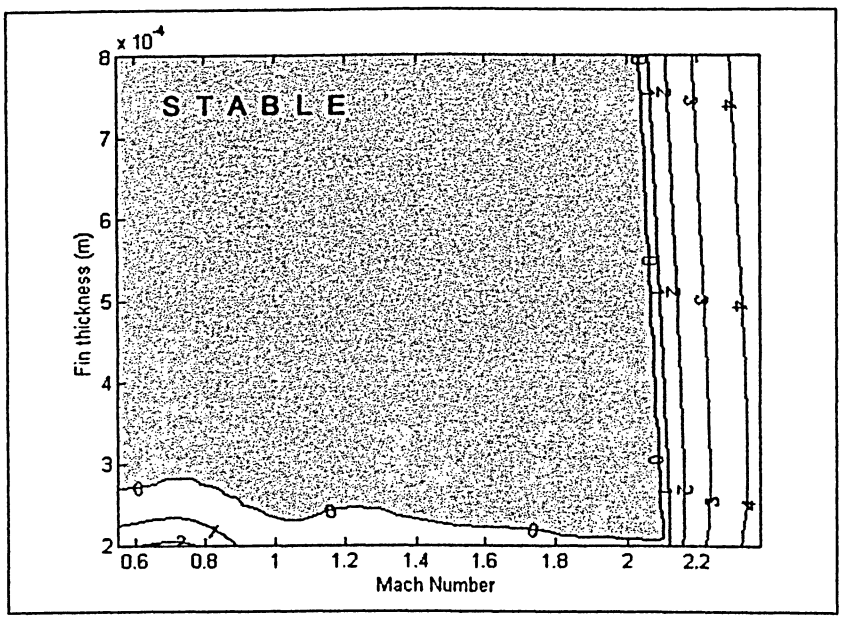

Figure 6.7: Stability Boundary for Unpinned Rocket Model

Referring to **Figure 6.7**, the zeroth contour represents the stability boundary, with the stable region marked by the shaded region. The unshaded regions correspond to configurations that have at least one positive real eigenvalue component, and are therefore unstable. Above Mach 2, there is a sharp rise in the stability boundary contour. This sharp rising trend could be characterized as a wall of instability. Upon analyzing the outputs, the stability study reveal that the instability behaviour in this region is distinct from that of lower Mach numbers. For M <2, the instabililty type is flutter, characterized by an exponential increase in the magnitude of oscillation with time. For configurations, which cross this wall of instability, the unstable behaviour is no longer oscillatory, but is characterized by a divergent exponential growth.

As mentioned previously, the equilibrium condition for the unpinned case involves the flight of a rocket in freefall at terminal velocity. To accommodate

this, the nominal flight altitude has been adjusted for each velocity-thickness pairing, such that the vehicle weight is equivalent to the axial drag force. Consequently, the results presented in this section are not directly comparable with those of the previous section due to the fact that the pinned rocket stability plots (**Figures 6.3-6.5**) assumes constant atmospheric density. For a more direct comparison, the equilibrium altitudes generated for each fin thickness-velocity pair in the unpinned case may be used in the pinned model. The results of this analysis are presented in **Figure 6.8.**

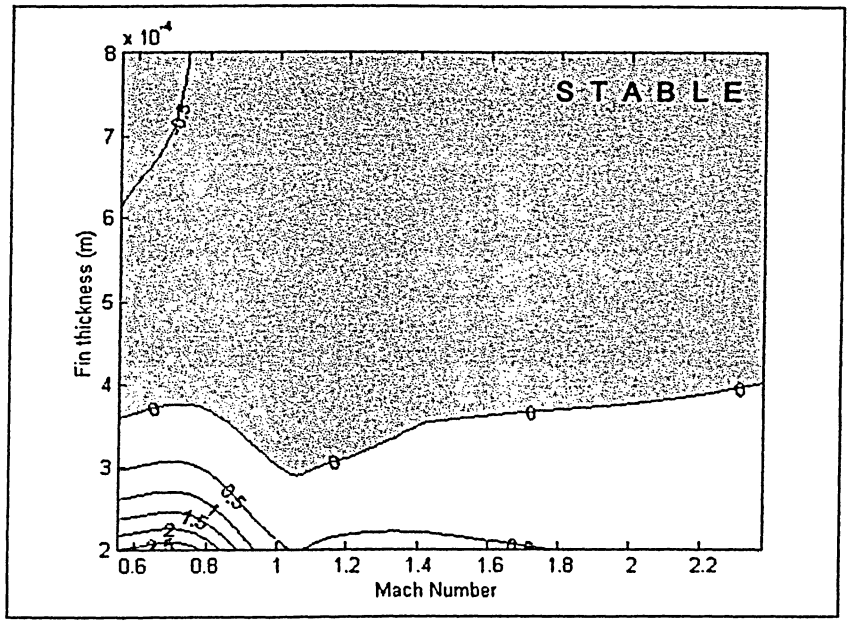

Figure 6.8: Stability Boundary Comparison Pinned Model

The profiles depicted in **Figures 6.7** and **6.8** corresponding to the unpinned and pinned cases respectively share some common trends. The figure show similar stability boundary profiles up to about Mach 1.2, with a peak near Mach 0.8 and a dip just above the sonic line. The stability boundary results for the pinned case are, however, skewed upwards by approximately 0.1 mm with respect to the unpinned model. Above Mach 1.3, the unpinned stability contour begins decreasing, whereas the pinned case continues to increase. Additionally, there is no sharp rise in the stability boundary to indicate a wall of instability for the pinned case as was seen in **Figure 6.7.** Due to the differences in the modeling approaches for these two cases, it is to be expected that the analyses would

generate distinct results. From the examination of these models, it is known that small differences in configuration can greatly affect the overall stability of the rocket, and thus the results presented here are preliminary simplified cases to be used primarily as verification tools for the validation of the full three-dimensional (3D) flight simulator.

6.3 Comparison with Full 3D Flight Simulation Data

The preceding simplified models are to be used as a means of comparison and validation for the full 3D flight computer program. Several test cases were run using the full six-degree of freedom flexible-body flight simulator to contrast with the planar results obtained thus far. The simulation results are presented in the stability boundary diagrams **Figure 6.9** and **6.10**. As before, the zero contour is the calculated stability boundary, with the shaded region indicating stable configurations.

Four simulation test points are highlighted in both **Figure 6.9** and **Figure 6.10.** The rocket model is allowed to reach a terminal velocity equilibrium condition through freefall within the simulator, similar to the method employed for the unpinned planar case. The model is then excited with a small finite gust load, which stimulates the model away from equilibrium point. The resulting decay or growth of the disturbance exhibits the stability of the model configuration. For consistency, the 3D rocket model is limited to body bending and fin flapping motions. No twist deformation modes are included as no twist capability was provided for the planar cases. Each test point is indicated with equivalent second order system response behaviour parameters (σ_d and ω_d). Inset on **Figure 6.10** are angle-of-attack plots, which characterize the relative stability of the system resulting from a finite disturbance. The resulting profile is generally that of an underdamped system.[38] The underdamped response for a second order system is defined as

$$c(t) = Ae^{\sigma_d t}\cos(\omega_d t - \phi) \tag{6.30}$$

where σ_d is the real component of the system pole, and ω_d is the damped natural frequency.

Referring to the diagrams, the 3D simulation data indicates that for a Mach number of approximately 0.62, fin thicknesses of 0.3-0.4 mm yield visibly unstable results. For the case where the fin thickness is 0.5 millimeters, the system also produces a positive real component of a complex root, which renders the system unstable. However, in this instance, σ_d is close to zero, that is, near the stability boundary, and as a result the system exhibits marginally stable behaviour. The slow growth of the angle of attack for this case may be seen in **Figure 6.10.**

The uppermost test case, for a rocket model with fins 0.6 mm thick yields only roots with negative real components. Thus, the system is stable and will return to the equilibrium point after a period of time following the disturbance.

Each of the three methods presented here display similar instability behaviour, for low Mach numbers. The nature of the instability across this speed range is sinusoidal (flutter). It is the flexible deformations of the fins that render them ineffective in maintaining the steady loads required to stabilize the flight vehicle.

The results of the three stability analyses do not perfectly coincide, as one would expect from the vast differences in modeling assumptions and complexity. The simplified models do serve as a reality check in terms of verifying the behaviour of the 3D simulation. The planar models are highly sensitive to small changes in stiffness, and so serve as ballpark estimates for the more complex, and consistent 3D flexible-body flight simulation. The 3D simulation results involve much more complicated and precise loadings over the fin surfaces that vary with time and velocity.

One additional consideration is that, for the planar cases, stability is determined via a state space eigenvalue analysis, which assumes that the aerodynamic coefficients remain strictly constant. For the three-dimensional simulation runs, all of the aerodynamic coefficients become variable. Some coefficients, in particular those pertaining to body and fin normal forces, are strongly influenced by the angle of attack.

In comparing the results, it appears that the critical fin thickness values obtained from the unpinned study are approximately half of those of the 3D simulation. The pinned case similarly underestimates the critical fin thickness by approximately 30%.

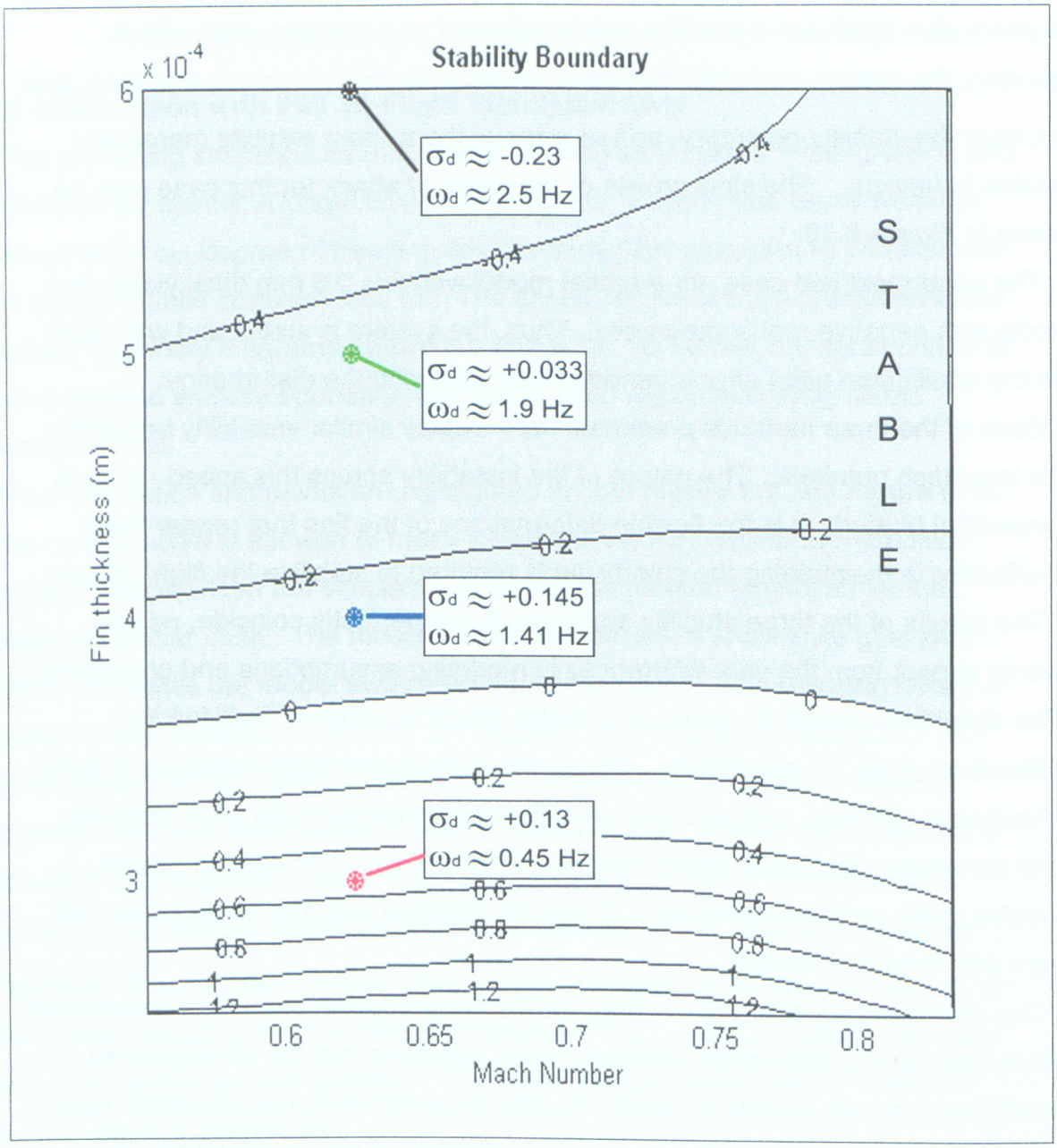

Figure 6.9: 3D Simulation Pinned Stability Boundary Comparison (2D contours of σ_d with 3D simulation test points results superimposed)

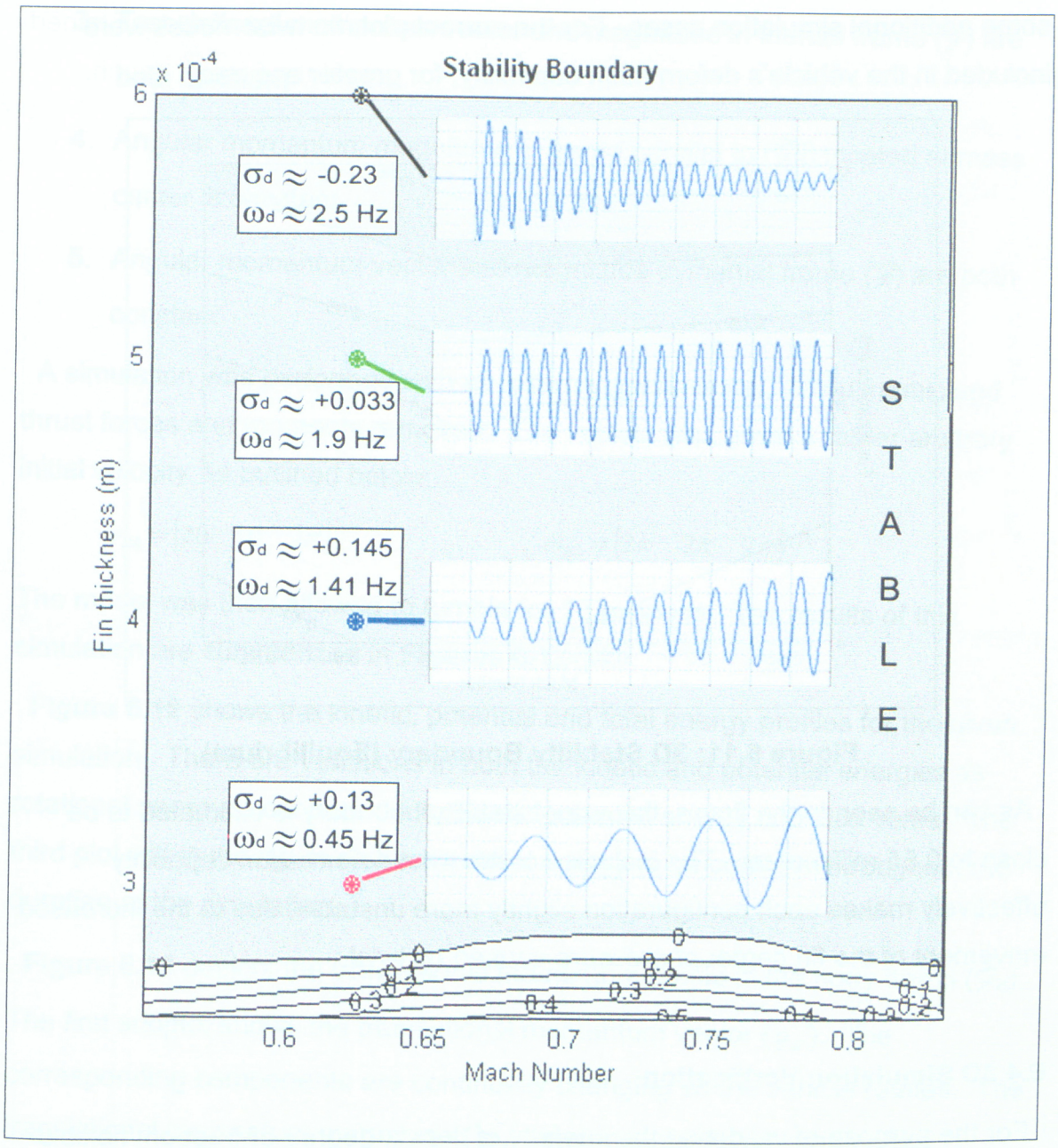

Figure 6.10: 3D Simulation Unpinned Stability Boundary Comparison (α profiles inset)

Figures 6.9 and **6.10** compared the results of the two simplified planar studies with several flight simulator test cases. The 3D simulation cases were forced into equilibrium by setting them into a freefall in which weight and drag were effectively balanced. **Figure 6.11** shows a stability boundary contour diagram for

some additional simulation cases. For the current plot, fin twist modes were included in the vehicle's deformation capability, for greater accuracy.

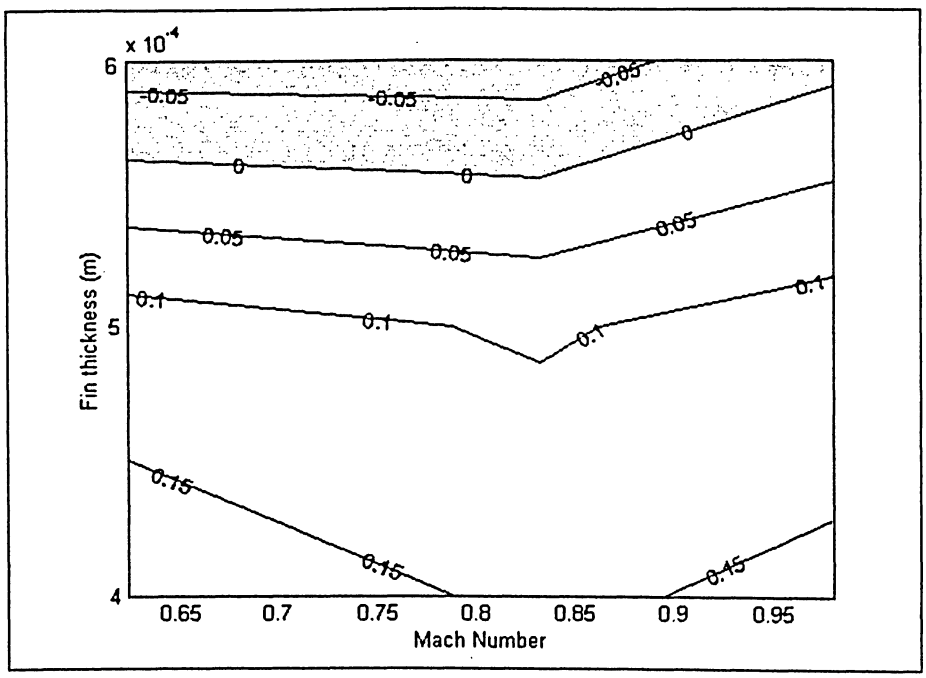

Figure 6.11: 3D Stability Boundary (Equilibrium)

As can be seen in the figure, the actual stability boundary is estimated to be close to 0.55 millimeters. The inclusion of the twist deformation capability effectively makes each configuration slightly more unstable, due to the increased movement of the fin center of pressure caused by twist.

6.4 3D Simulation Verification

For the purpose of validating the integrity of the six-degree-of-freedom flexible-body flight engine, the system energies and momenta provide some useful insight. As outlined in **Section 4.3.3**, for a model released into flight arbitrarily with no external forces, several known results are expected from the laws of conservation of energy and momentum. That is,

1. Total energy is constant (E)
2. Translational momentum magnitude in body frame ($\mathcal{F}_B$) is constant

3. Translational momentum vector and magnitude in inertial frame ($\mathcal{F}$) are both constant
4. Angular momentum magnitude in frame parallel to ($\mathcal{F}_B$) located at mass center is constant
5. Angular momentum vector and magnitude in inertial frame ($\mathcal{F}$) are both constant

A simulation was performed with all external gravitational, aerodynamic and thrust forces and moments removed. The vehicle was given a rather arbitrary initial velocity as outlined below:

$$v_{B0} = [20 \quad 10 \quad 2\pi] \qquad \omega_{B0} = [2\pi \quad 2\pi \quad 2\pi]$$

The model was then allowed to tumble for 10 seconds. The results of this simulation are summarized in **Figures 6.12-14**.

Figure 6.12 shows the kinetic, potential and total energy profiles for the given simulation. There are variations in both the kinetic and potential energies as rotational energy is converted into elastic potential energy and vice versa. The third plot within the figure shows the total energy to be constant throughout the duration of the simulation.

Figure 6.13 depicts the translational momentum profile in the body frame ($\mathcal{F}_B$). The first subplot shows the translational momentum vector ($\mathbf{p}_B$). The corresponding components are continually changing as the vehicle rotates. The translational momentum magnitude ($|\mathbf{p}_B|$) shown in the lower graph does maintain a constant value, as was expected.

Figure 6.14 similarly shows the translational momentum vector ($\mathbf{p}$) and magnitude in the inertial frame ($\mathcal{F}$). Also as expected, the vector components and magnitude are both shown to remain constant for the entire duration of the simulation.

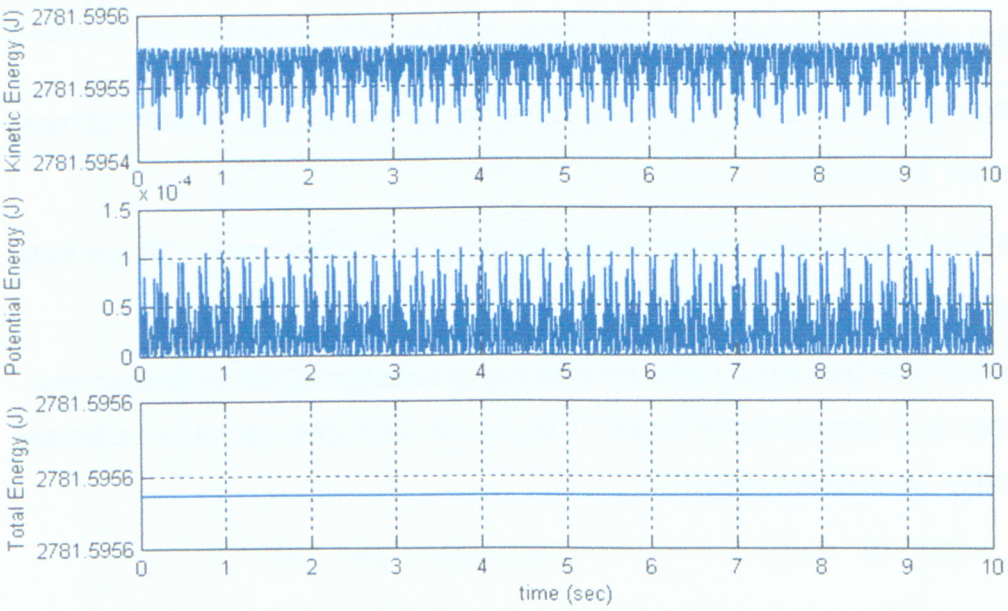

Figure 6.12: Simulation Energy Profiles

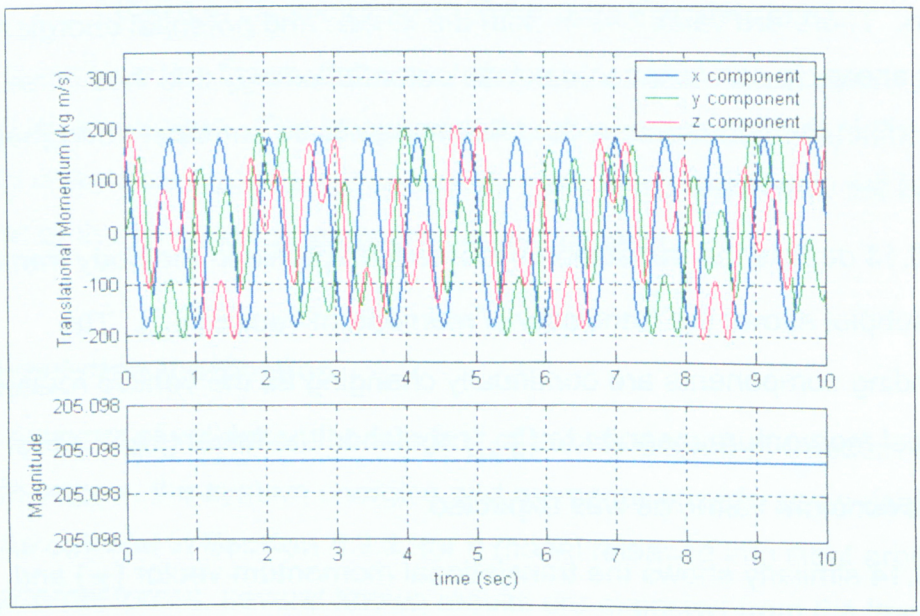

Figure 6.13: Simulation Body Frame ($\mathcal{F}_B$) Translational Momentum Profiles

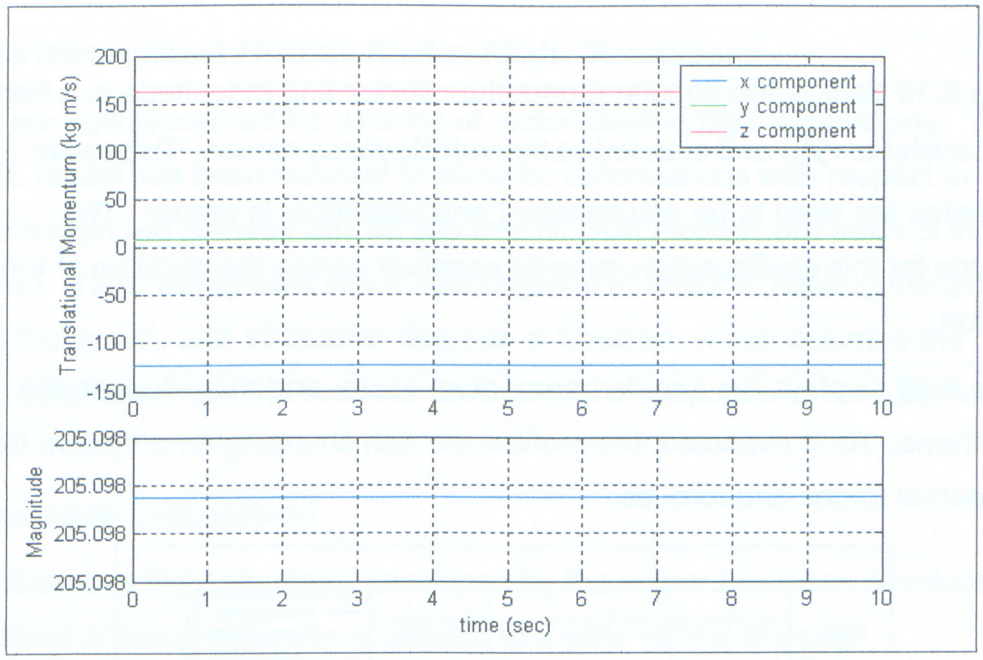

Figure 6.14: Simulation Inertial Frame ($\mathcal{F}$) Translational Momentum Profiles

Figure 6.15 and **6.16** show the angular momentum profiles for the current simulation.

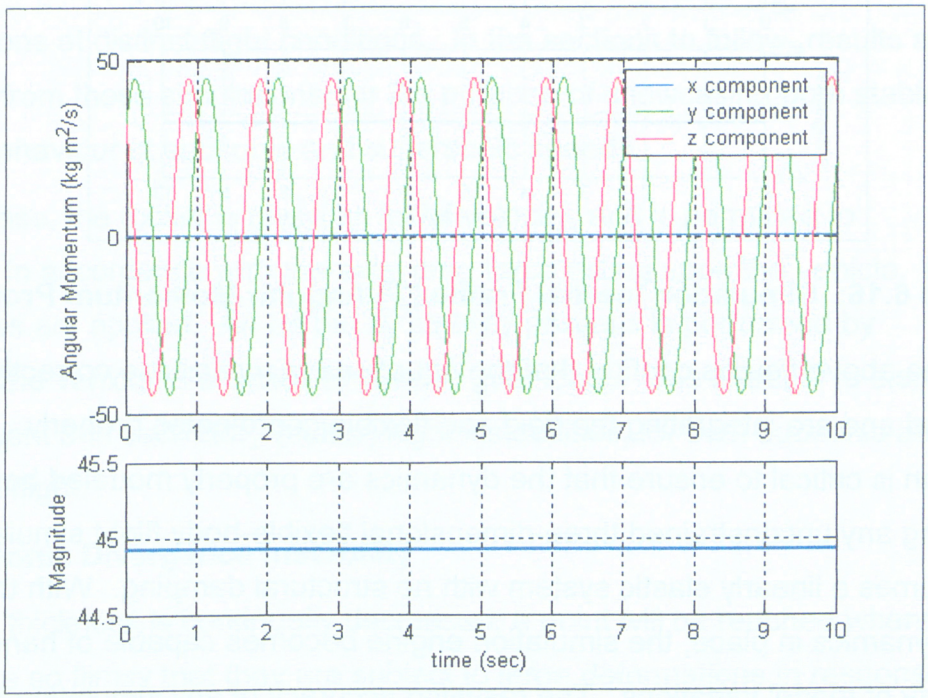

Figure 6.15: Simulation Body Frame ($\mathcal{F}_B$) Angular Momentum Profiles

Figure 6.15 depicts the angular momentum vector and magnitude in a frame that is parallel to ($\mathcal{F}_B$) and situated at the vehicle mass center. The vector components are seen to be non constant and oscillatory in nature. The magnitude for this configuration remains constant across the duration of the simulation.

Figure 6.16 displays the angular momentum vector and magnitude in the inertial frame. As is expected, the profiles are non changing for a system free from external forces and torques.

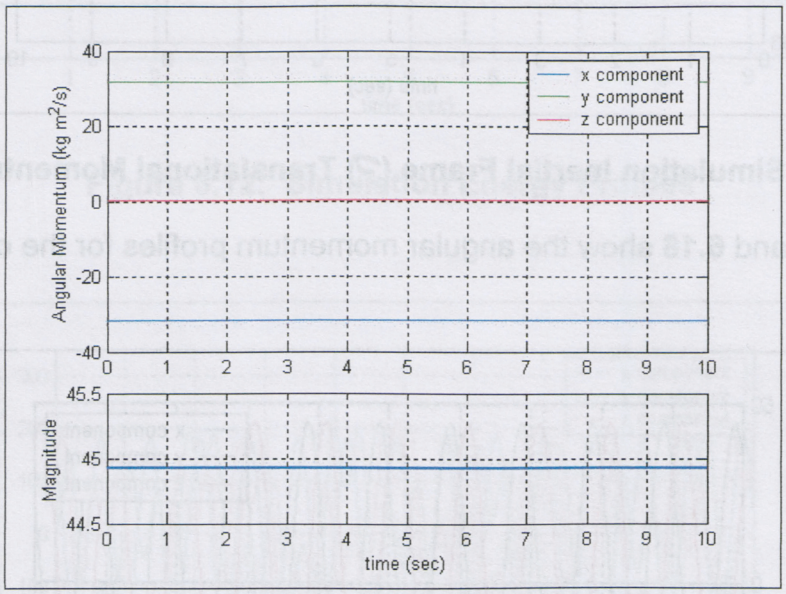

Figure 6.16: Simulation Inertial Frame ($\mathcal{F}$) Angular Momentum Profiles

Thus, the above figures confirm that the equations of motion are correctly formulated and are integrating the rigid and flexible coordinates properly. This verification is critical to ensure that the dynamics are properly modeled before completing any unconstrained three-dimensional flexible-body flight simulations. This assumes a linearly elastic system with no structural damping. With the vehicle dynamics in place, the simulation engine becomes capable of handling any variety of model variations. The resulting accuracy of any simulation then becomes dependent on the relevant description and application of external loadings experienced by the vehicle.

6.5 Three Dimensional Flexible Rocket Flight Simulations

Results are now presented for a series of rocket flexible flight simulations. The vehicle FE model has been reduced to allow for deformations with respect to body bending (in two planes), and fin flap and fin twist motions (for each of the four tailfins). Thus, the system has 6 rigid degrees of freedom relating the gross motion of the vehicle and 10 flexible degrees of freedom, which describe the structural deformations of the reduced order model in response to the external loadings.

6.5.1 Simulation Comparison

The flexible-body flight simulator developed by the author has been developed with the intent of being generally applicable to a wide variety of model configurations and conditions. The current version has been developed to simulate the flight of a flexible rocket vehicle across a wide spectrum of speeds and altitudes.

To exhibit these capabilities, it is intended to examine several rocket configurations at distinct flight conditions. In the sections to follow, results are presented from these simulations, for the purpose of showcasing both stable and unstable behaviour at subsonic and supersonic speeds.

In each case, the rocket is given an initial velocity, and is permitted to decelerate in accordance with the axial drag force acting upon the vehicle. No thrust forces are applied. An on the fly stability analysis is performed by subjecting the vehicle to a series of sudden gust loads. The intent is to display both divergent and oscillatory (flutter) flight instabilities, for both subsonic and supersonic flight.

6.5.2 Subsonic Divergence Instability

As the fin thickness is continually decreased, a point will be reached where the fins become so flimsy that they are subject to large deformations in response to relatively minute loadings. For such a model, the large deformations will most

certainly exceed the material's strength and yield or fail. The resulting behaviour may be summarized as a destructive fin divergence instability.

To exhibit this, a rocket model was developed with a fin thickness value of 0.3 mm. The initial flight conditions are given as follows.

$$\mathbf{V}_{Bo} = [200 \quad 0 \quad 0]^T \text{ m/s} \qquad \boldsymbol{\omega}_{Bo} = [0 \quad 0 \quad 0]^T \text{ rad/s}$$

$$[\phi \quad \theta \quad \psi]^T = [0 \quad 0 \quad 0]^T \qquad h = 5 \text{ km}$$

The rocket is subjected to two 0.1 second duration gusts of 5 m/s at both one and five seconds into the simulation in the body frame z direction. The simulation results are presented in **Figures 6.17 – 6.26.**

The angle of attack contour is shown in **Figure 6.17**. A clear runaway trend is noticeable up to about α = 25°. The simulation was halted shortly after 1.2 seconds due to some aerodynamic parameters exceeding the model design limits. The profile shows that the configuration is inherently unstable, as evidenced by the fact that the runaway trend is clearly defined before the interaction with the gust load one second into the simulation. Thus, even in the absence of any gust disturbances, the unstable rocket behaviour quickly develops.

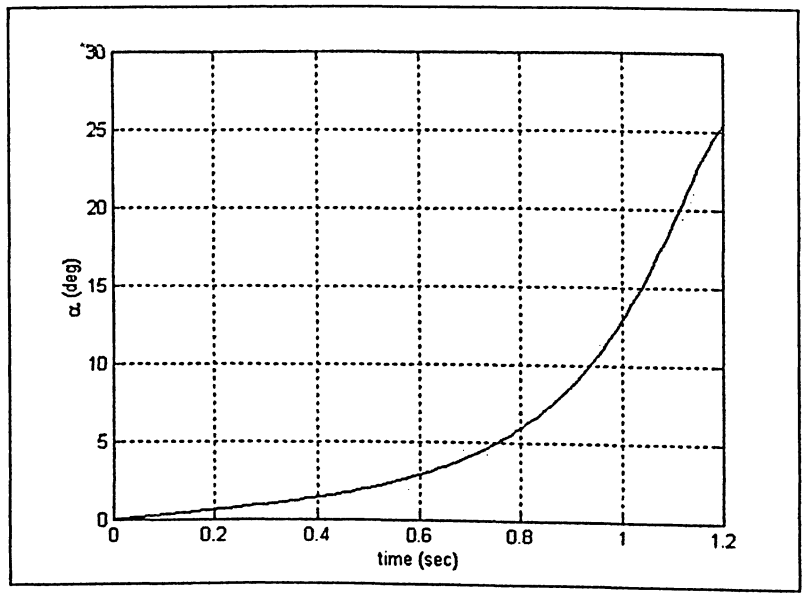

Figure 6.17: Angle of Attack Profile for Subsonic Divergence

The reduced order fin flapping deformation coordinates are presented next. It can be seen from the following figure, which depicts the deformations of each of the four rocket fins, that a clear divergence trend is discernable. At a 1.2 seconds into the simulation, the deformation of these fins has grown to be quite considerable. The fin flap deformation magnitudes shown in **Figure 6.18** are in relation to the user selected deformation shapes that were employed as reduced order model degrees of freedom. The profile magnitudes are unitless, being scale factors with respect to the original deformation shape vectors.

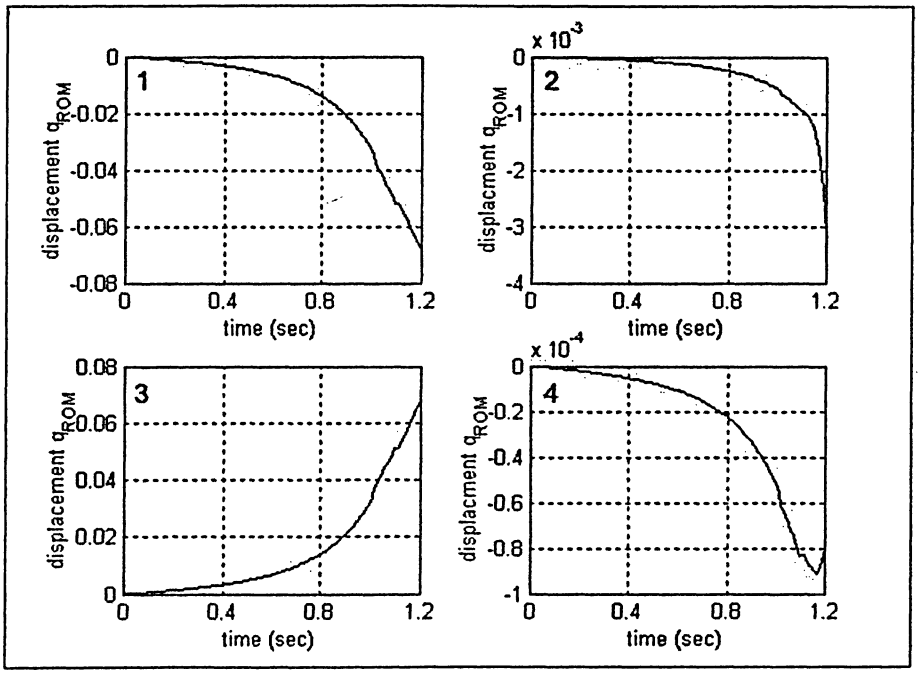

Figure 6.18: Fin Flap Deformation Profiles for Subsonic Divergence

The vehicle body frame velocities are included in **Figures 6.19-6.20.** The translational velocities show the deceleration of the vehicle in the x-direction as a result of the axial drag forces as well as the rapid increase angle of attack, which transfers some of the vehicle velocity into the z-direction. This trend is visible within the z-velocity component as well.

The body frame angular velocities show a large unbalanced increase in the pitch rate (ω_y). By the end of the simulation, the instability begins to creep into the other rates, as the remaining windward fin (plot number two in **Figure 6.18**)

begins to deflect. This deformation also explains the translational y-velocity contour in **Figure 6.19.**

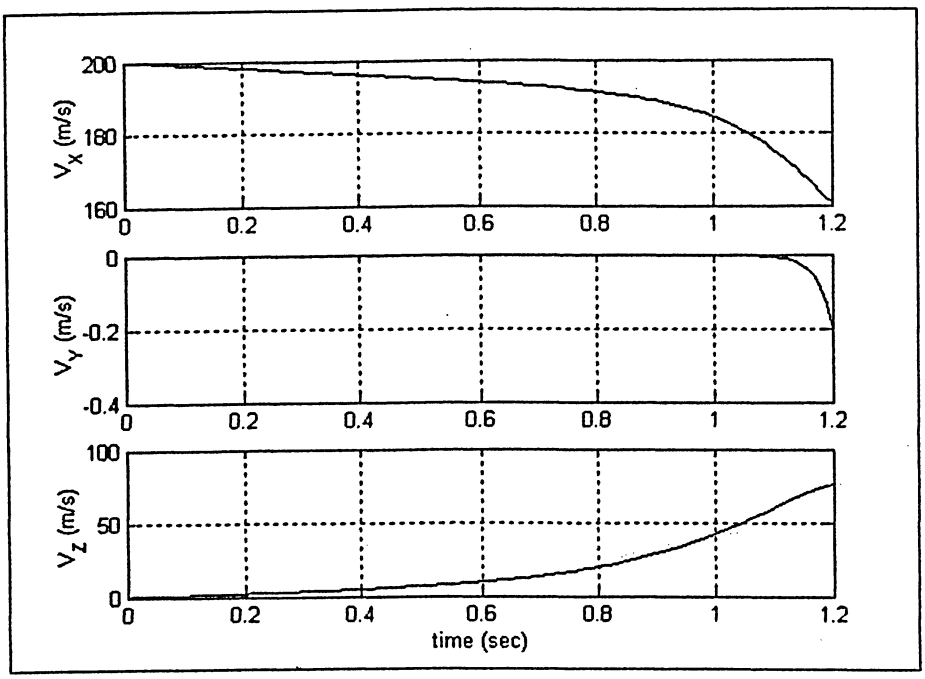

Figure 6.19: Translational Velocity Profiles for Subsonic Divergence

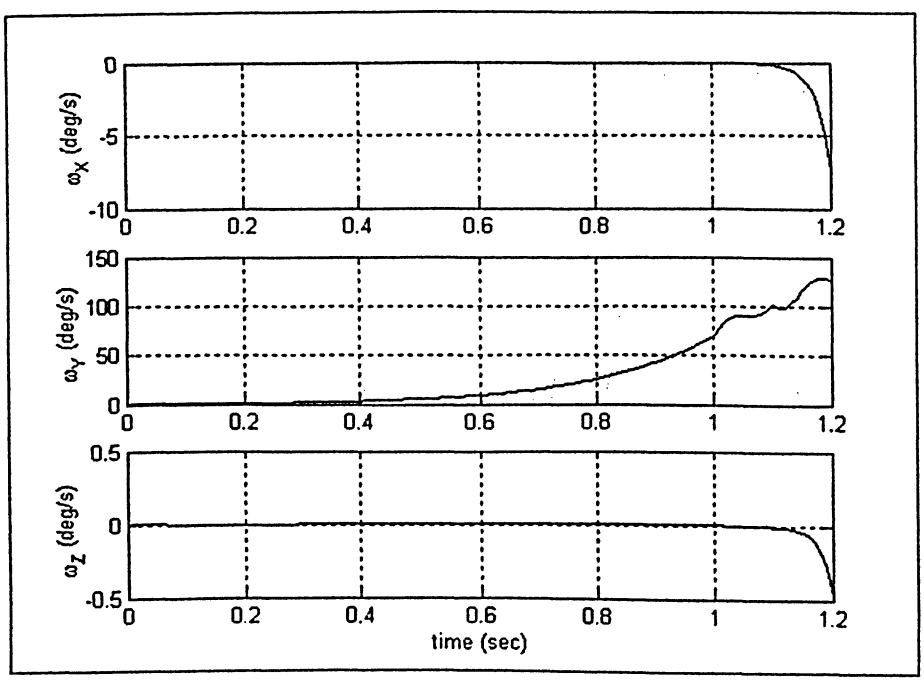

Figure 6.20: Translational Velocity Profiles for Subsonic Divergence

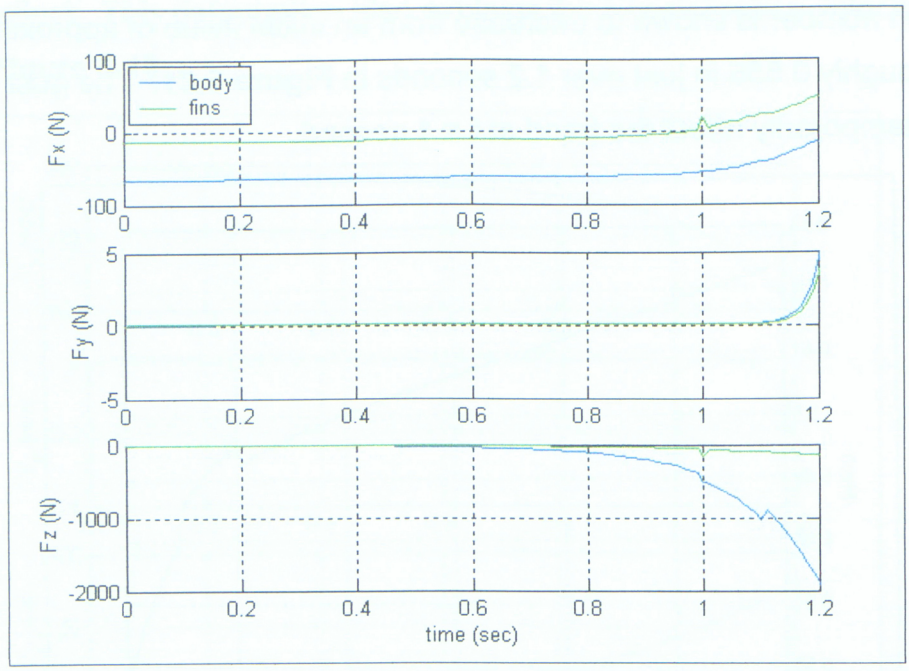

Figure 6.22: ($\mathcal{F}_B$) Aerodynamic Force Profiles for Subsonic Divergence

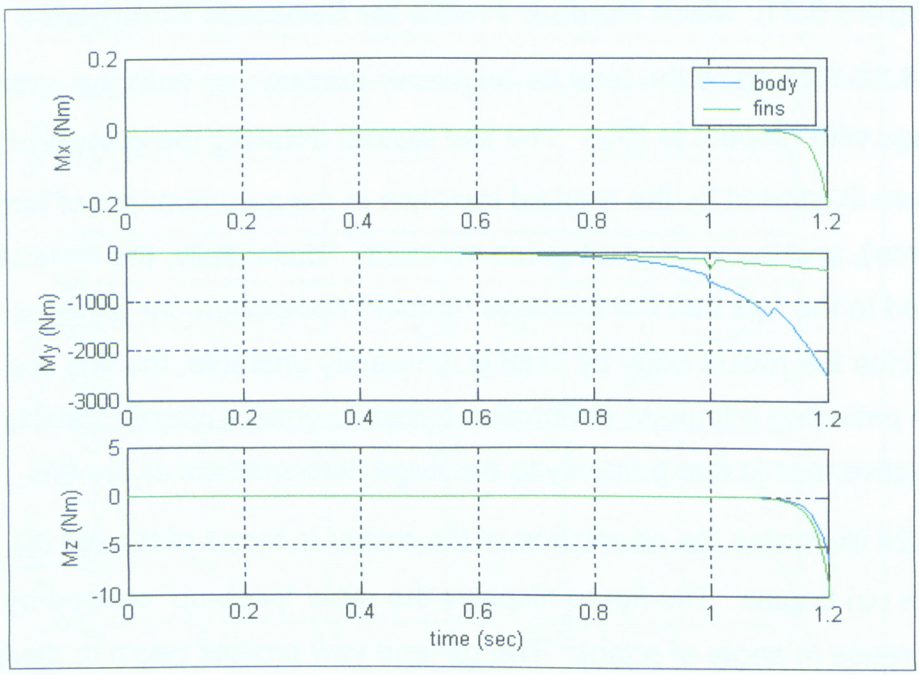

Figure 6.23: ($\mathcal{F}_B$) Aerodynamic Moment Profiles for Subsonic Divergence

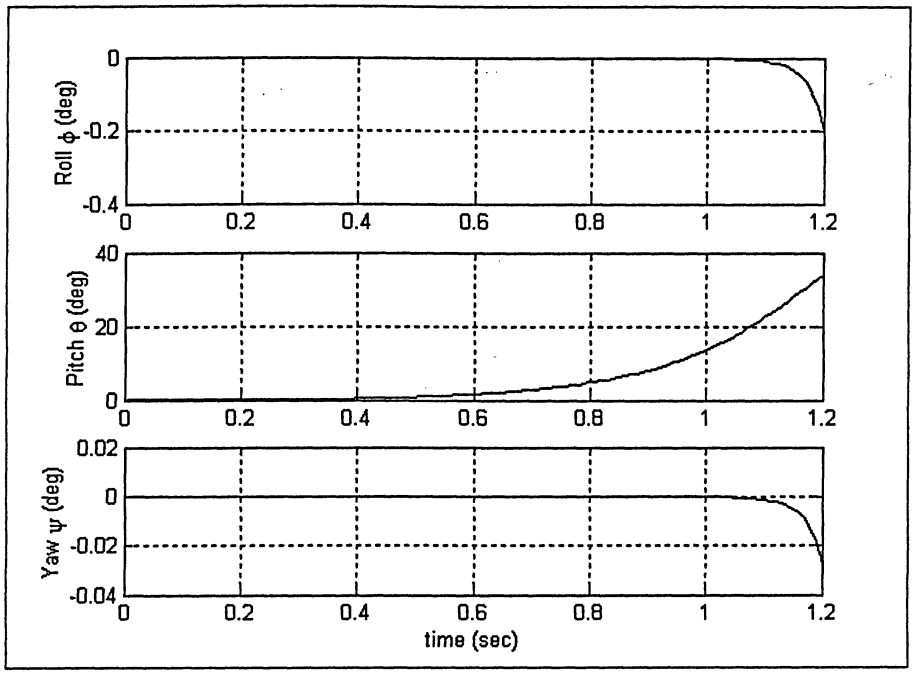

Figure 6.24: Roll, Pitch and Yaw Profiles for Subsonic Divergence

The divergent behaviour of the rocket model with 0.3 mm thick fins, is perhaps most effectively displayed with some animation still frames. Below in **Figure 6.25**, the rocket deformation is presented in three images at 0.4, 0.8 and 1.2 seconds. The rocket is viewed from the front, that is, looking towards the nose.

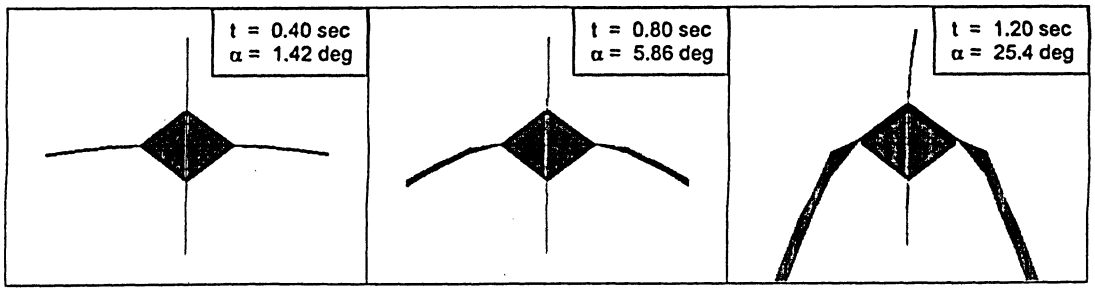

Figure 6.25: Rocket Deformation (Front) for Subsonic Divergence

The fins are seen to deflect rapidly and to a considerable degree. The yield strength would surely be exceeded within the fins for any realistic material (aluminum being used here) undergoing such large deformations. The last frame shows the upper fin beginning to deflect. This deflection would then initiate the roll and yawing motions seen previously. An alternate view of the rocket is presented for these three animation frames in **Figure 6.26**.

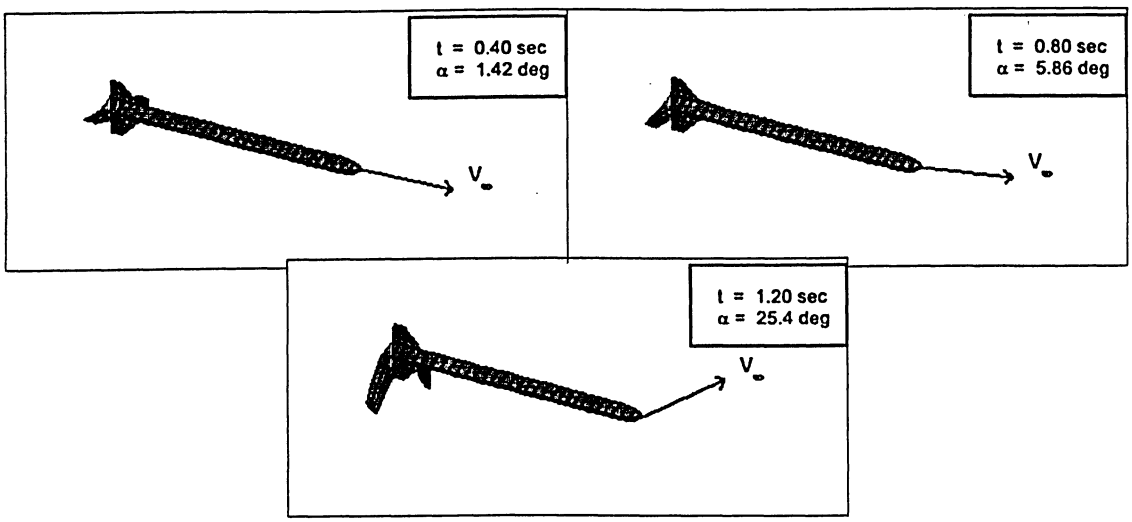

Figure 6.26: Rocket Deformation (3D) for Subsonic Divergence

A three dimensional view of the rocket is now presented. The velocity vector is additionally represented by the arrow in **Figure 6.26**. The fins again are shown to deflect considerably under the loads applied to them. Note that the 3D images shown in **Figure 6.26** are not precisely to scale as the rocket body frame y and z-axis scales have been enhanced to aid visibility.

Thus, it can be concluded that the rocket model, derived from the SPHADS-1 vehicle, with fins of 0.3 mm nominal thickness is inherently unstable at subsonic speeds above Mach 0.55. The nature of this instability is divergence.

6.5.3 Subsonic Oscillatory Instability

The simulation was again run with initial conditions for a rocket model whose fins have a constant thickness of 0.4 mm. That is, the initial conditions are identical to those presented for the previous case.

The rocket is once again subjected to two gusts of 5 m/s each lasting a duration of 0.1 seconds at t = 1 and t = 5 seconds in the body frame z direction.

The angle of attack profile is shown in **Figure 6.27** . The profile can be divided up into three distinct regions. The first region pertains to the flight prior to any disturbance (gust) loads acting upon the vehicle. There are small order oscillations in α present as a result of the acceleration due to gravity, which is initially perpendicular to the direction of flight. At t = 1 second, the first gust

drives the vehicle into a sinusoidal oscillation. This oscillation is increasing in amplitude and is therefore unstable. The vehicle interacts with another gust five seconds into the simulation. The unstable growth trend continues indefinitely. **Figure 6.28** shows the displacements of the rocket fin flap reduced order coordinates (i.e., the fin flap degrees of freedom). The unstable trend is clearly visible. The fins continue to deform to a greater extent with each oscillation. This vibration is undesirable and may lead to an undesireable trajectory or a more severe structural failure as the fins are torn away from the fuselage.

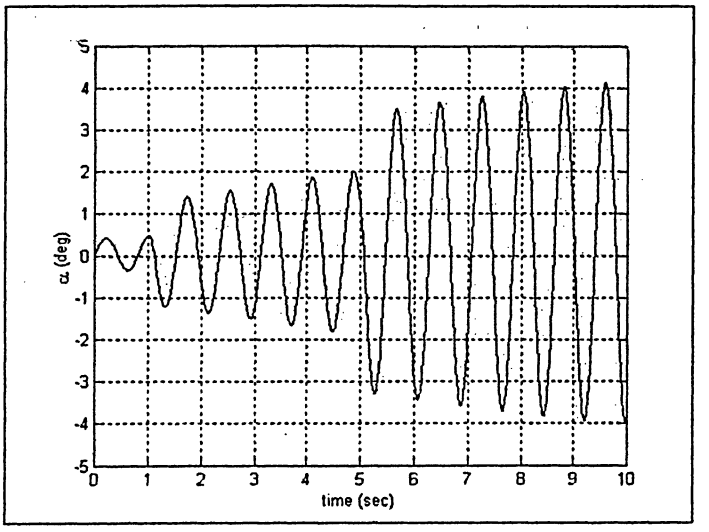

Figure 6.27: Angle of Attack Profile for Subsonic Flutter Instability

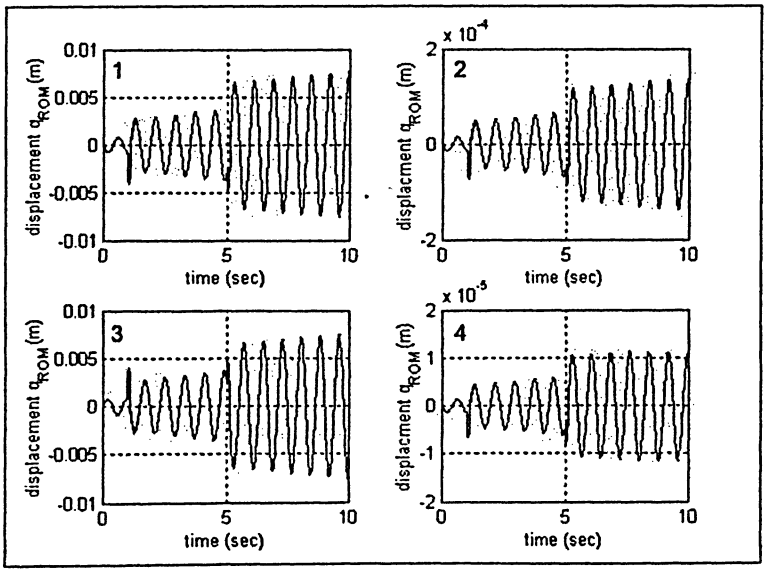

Figure 6.28: Fin Flap Deformation Profiles for Subsonic Flutter Instability

The body frame velocity profiles are depicted in **Figures 6.29-6.30.** The translational velocities **(Fig 6.29),** shows the vehicle velocity in the x-direction decreasing due to the axial drag force acting on the body. The body frame z-direction velocity profile shows the growing unstable sinusoidal trend. The same unstable behaviour is captured by the pitch rate (ω_y) velocity component in **Figure 6.30.**

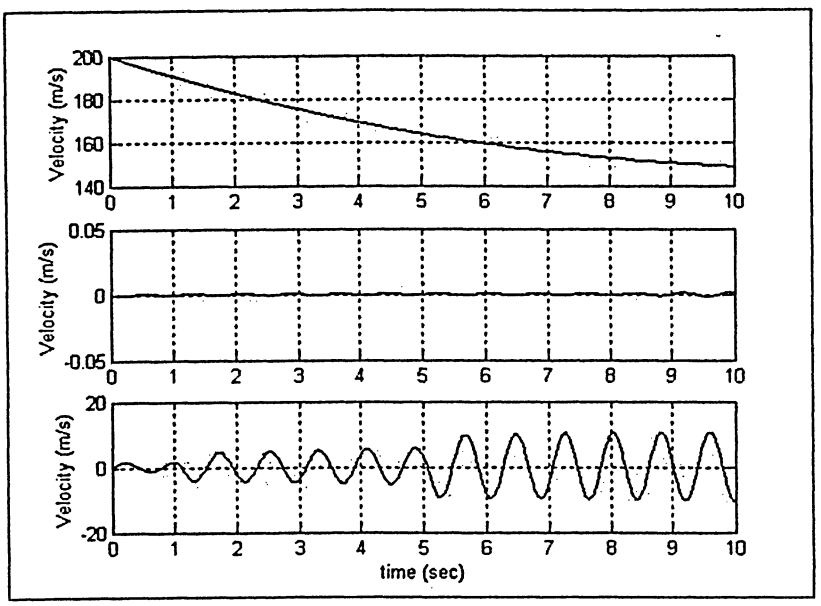

Figure 6.29: Translational Velocity Profiles for Subsonic Flutter Instability

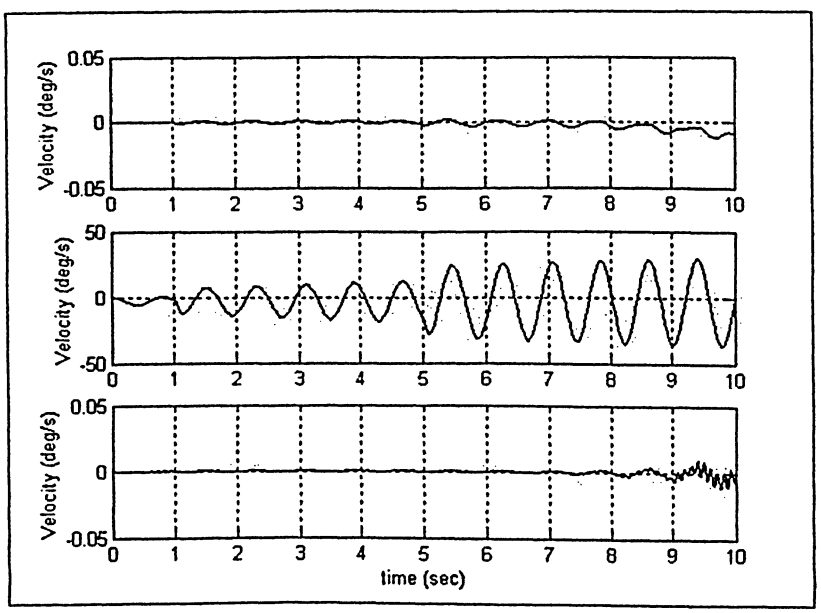

Figure 6.30: Angular Velocity Profiles for Subsonic Flutter Instability

The Mach number profile is shown in **Figure 6.31**. It is important to note that the exponential growth trends showcased above in the angle of attack and flexible coordinate deformations are being continuously moderated by the effect of the decrease in vehicle speed with time. That is, as the vehicle slows down, and the Mach number decreases, the aerodynamic loadings are steadily decreasing due to decreasing dynamic pressure. It is conceivable then, that if the vehicle is permitted to decelerate further, a point may be reached where the system reverts to a stable configuration. If this should occur, the vehicle will have effectively traversed the stability boundary for the given flight condition. As seen by **Figures 6.27, 6.28** and **6.31**, the current configuration remains unstable throughout the duration of the simulation run, and through the speed range of Mach 0.46 through 0.62.

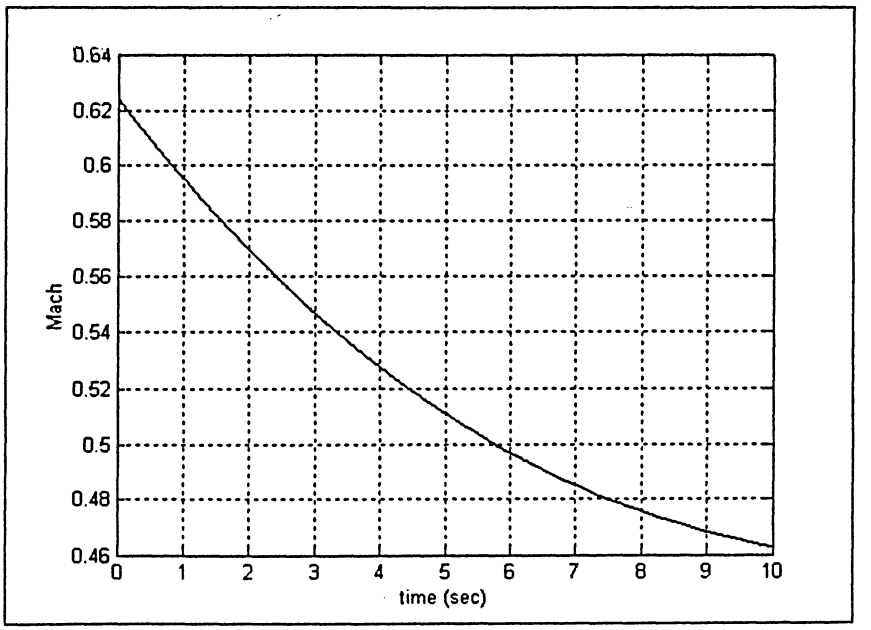

Figure 6.31: Mach Number Profile for Subsonic Flutter Instability

The body frame total aerodynamic forces and moments are depicted in **Figures 6.32** and **6.33**. The total aerodynamic loads are divided into both body and fin components. The forces in the x-direction (axial) are decreasing due to the overall deceleration of the vehicle. The z-direction forces again depict the growth behaviour resulting from the two disturbances. This may also be seen in **Figure 6.33** in the second subplot corresponding to the pitch moment.

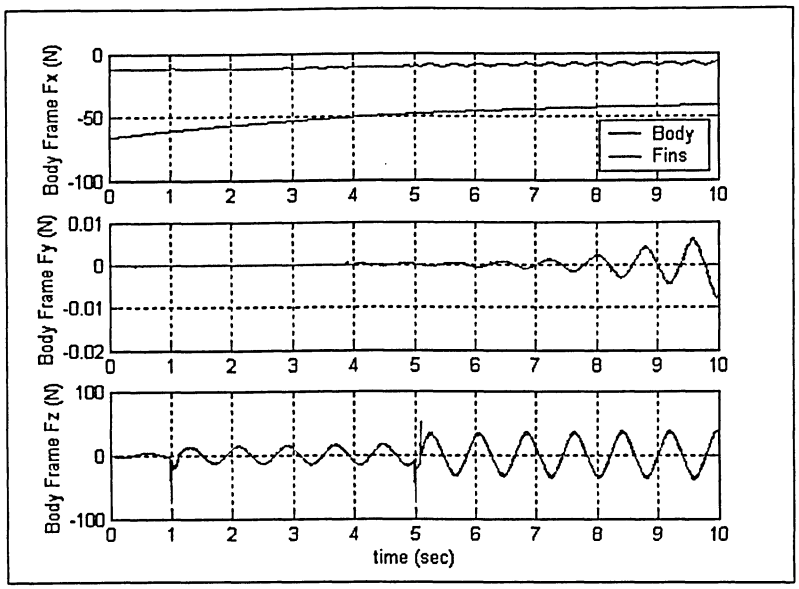

Figure 6.32: ($\mathcal{F}_B$) Aero Force Profiles for Subsonic Flutter Instability

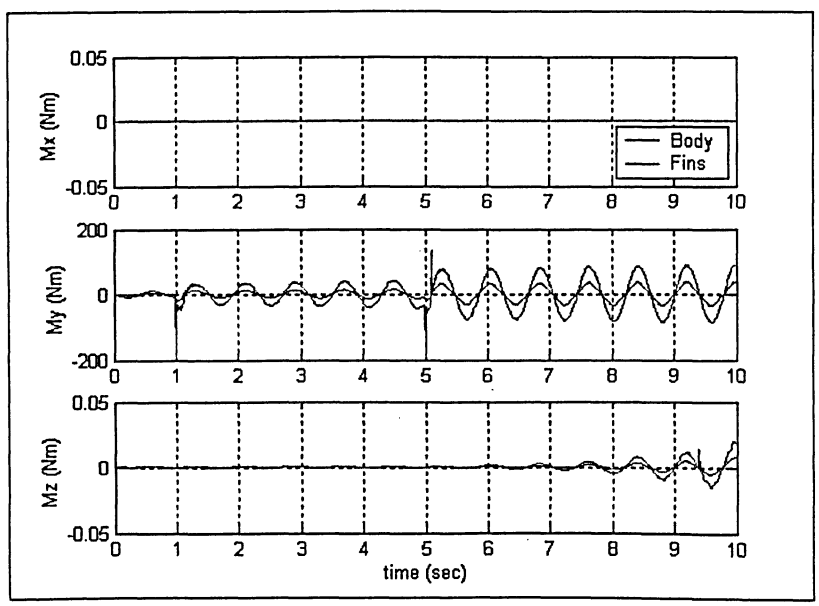

Figure 6.33: ($\mathcal{F}_B$) Aero Moment Profiles for Subsonic Flutter Instability

Figure 6.34 shows the orientation data for the current simulation. The roll, pitch and yaw angles are presented in the following subplots. While the roll (ϕ) and yaw (ψ) angles remain approximately zero, the pitch (θ) angle oscillates under the combined effects of the Earth's gravitational acceleration, which initiates a "gravity turn", and the gust load disturbances. The oscillations within the profile

are a result of the increasingly unstable flight of the rocket, which is driven by the deformation of the fins.

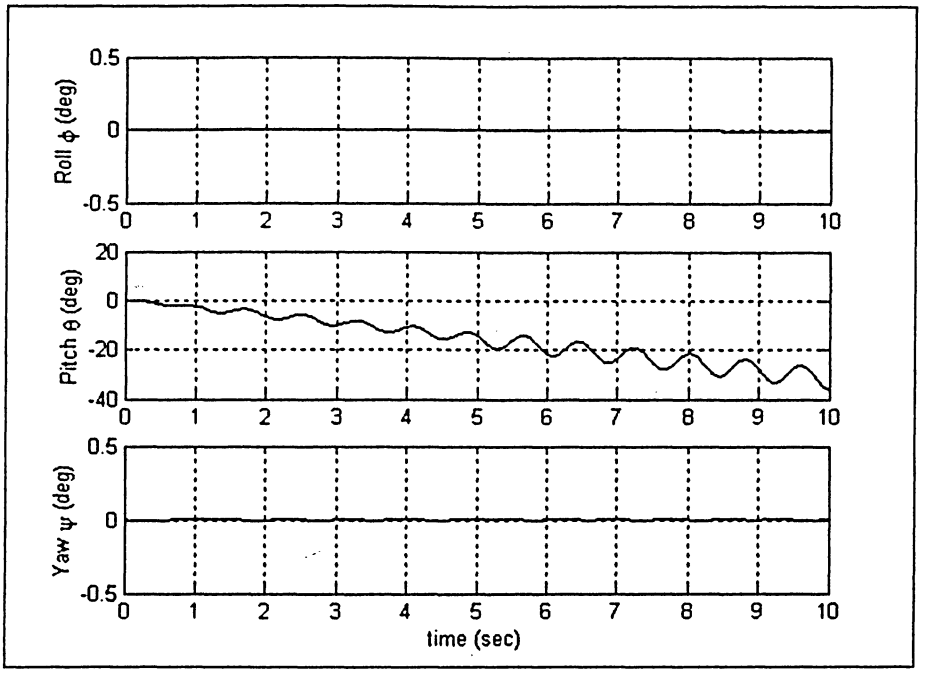

Figure 6.34: Roll, Pitch and Yaw Profiles for Subsonic Flutter Instability

The results presented above provide numerical representations of the flight instability for a rocket vehicle flying supersonically with fins 0.4 mm thick. The figures below depict the unbounded growth of deformation with some flight animation still frames. **Figure 6.35** shows the front view of the rocket (looking down at the nose), and **Figure 6.36** depicts a 3D representation of the rocket. The orientation of the velocity vector is also shown. Actual deformations have been magnified by a factor of two for clarity.

The first frame in both animation sets corresponds to the maximum deformation just prior to the initiation of the second gust load. Frame two depicts the first maximum deformation following the first gust load. Frames three and four represent further samples of oscillating deformation maxima, up to the simulation stop time of 10 seconds. Examining these images, a growth trend may be observed. Fin twist motions may also be observed in **Figure 6.35**, as evidenced by the apparent thickening of the fin cross section. The fuselage does exhibit

some deformation behaviour as well; however, it is of a smaller magnitude than that of the fins, and is not discernable in the structural animation stills below.

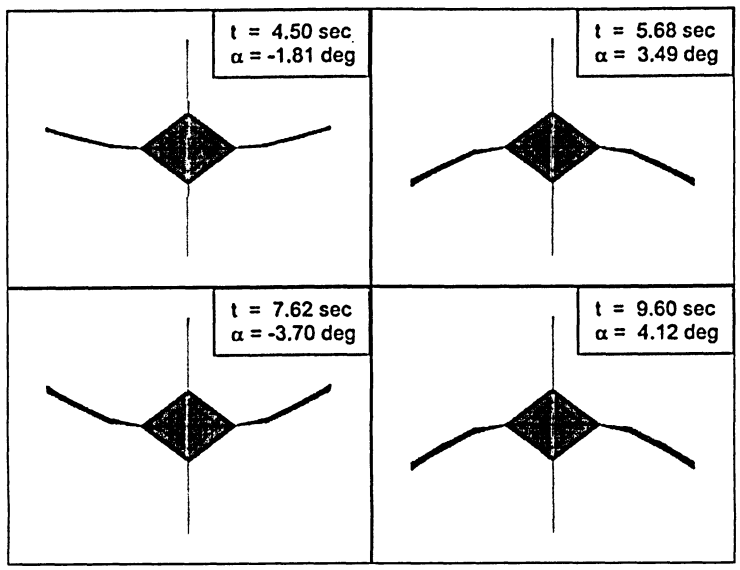

Figure 6.35: Rocket Deformation (Front) for Subsonic Flutter Instability

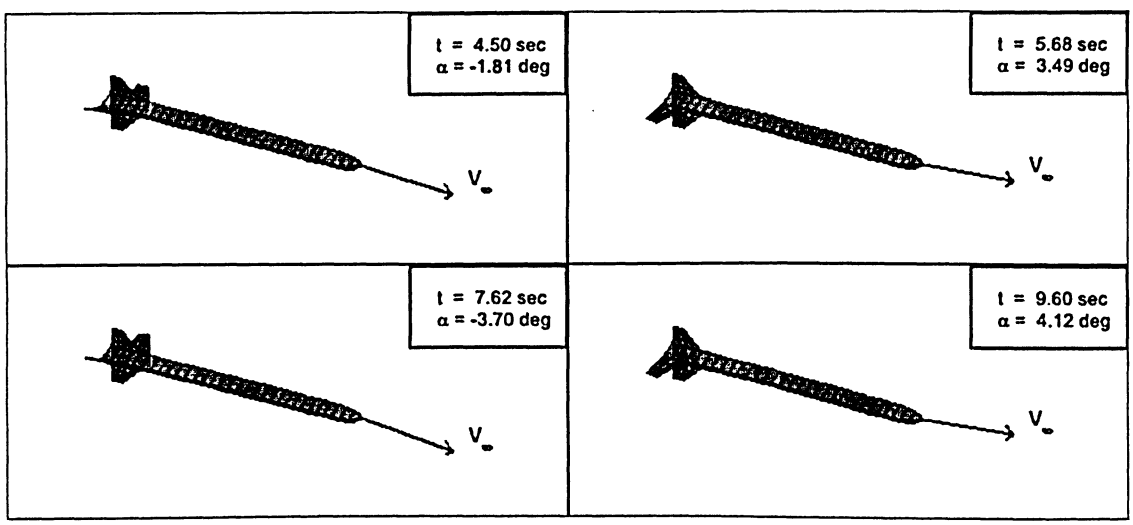

Figure 6.36: Rocket Deformation (3D) for Subsonic Flutter Instability

6.5.4 Subsonic Stability

The simulation was again run with initial conditions for a rocket model whose fins have a constant thickness of 0.6 mm. The initial conditions are identical to

those of the previous two cases. As before, the rocket is also subjected to two 0.1 second duration gusts of 5 m/s at both t = 1 and t = 5 seconds in the body frame z direction.

The angle of attack profile for this configuration is showcased in **Figure 6.37.** An initial α oscillation is present simply due to the effect of the gravitational acceleration vector being perpendicular to the initial velocity vector. The disturbance gusts quickly induce higher magnitude oscillations, which appear to decrease exponentially. This decay pattern indicates that the longitudinal flight stability is maintained for the duration of the test scenario.

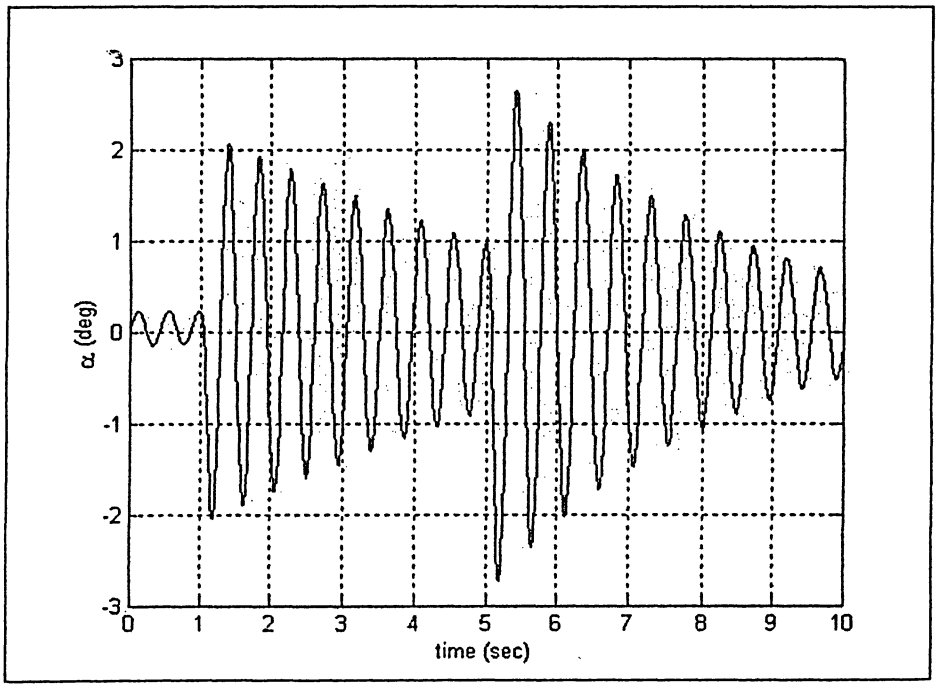

Figure 6.37: Angle of Attack Profile for Subsonic Stability

Figures 6.38-6.39 show the various reduced order coordinate displacements for both the fins. **Figure 6.38** represents the deformations of the fin flapping coordinates. Fins one and three lie in the body frame x-y plane and provide the required restorative forces. All four fins show similar decay patterns, although the deformations experienced by fins two and four are of a lesser magnitude. **Figure 6.39** shows the fins twist motions, where fins one and three show a

similar decreasing sinusoidal profile. Fins two and four are essentially inactive with respect to the twist deformation. For the current simulation, there is no significant body bending motion, and thus the coordinates corresponding to these motions are not presented.

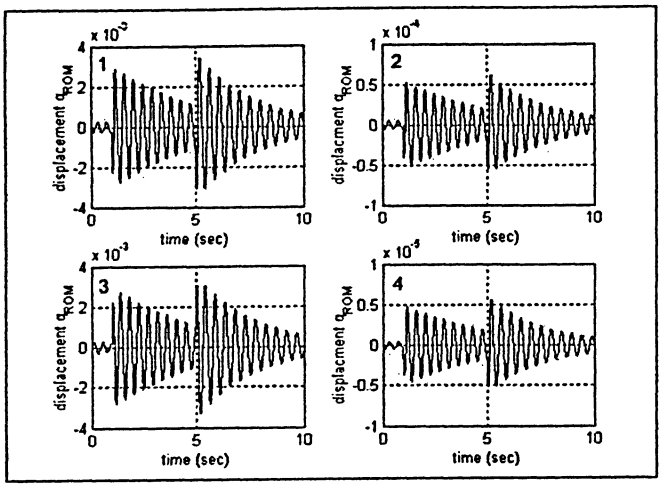

Figure 6.38: Fin Flap Deformation Profiles for Subsonic Stability

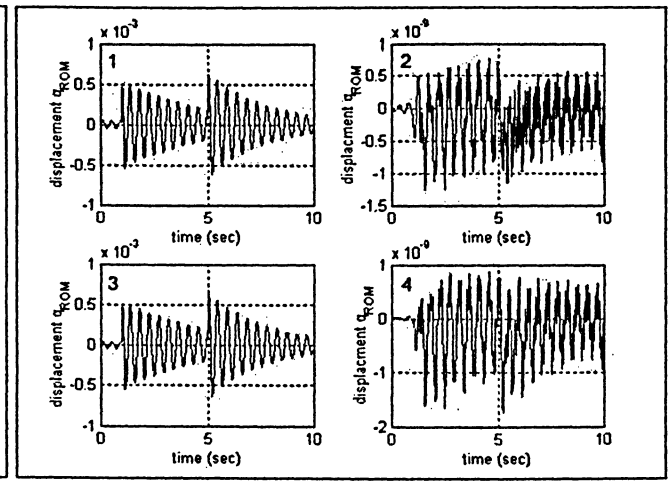

Figure 6.39: Fin Twist Deformation Profiles for Subsonic Stability

The decreasing sinusoidal trend is similarly observed in the vehicle rigid body velocities. **Figure 6.40** displays the rocket translational velocities and **Figure 6.41** presents the angular velocity trends with respect to the body frame axes. **Figure 6.40** shows the rapid decrease of the velocity in the x-direction. The value begins to level off towards the end of the simulation as the vehicle is approaching the terminal velocity condition, where the vehicle weight is effectively balanced by drag. This fact may also be observed by referring to the Mach number profile given in **Figure 6.42**. Examination of the z component of translational velocity (V_Z), and the pitch velocity (ω_Y) reveals stable bounded behaviour for the bounded disturbances applied to the vehicle.

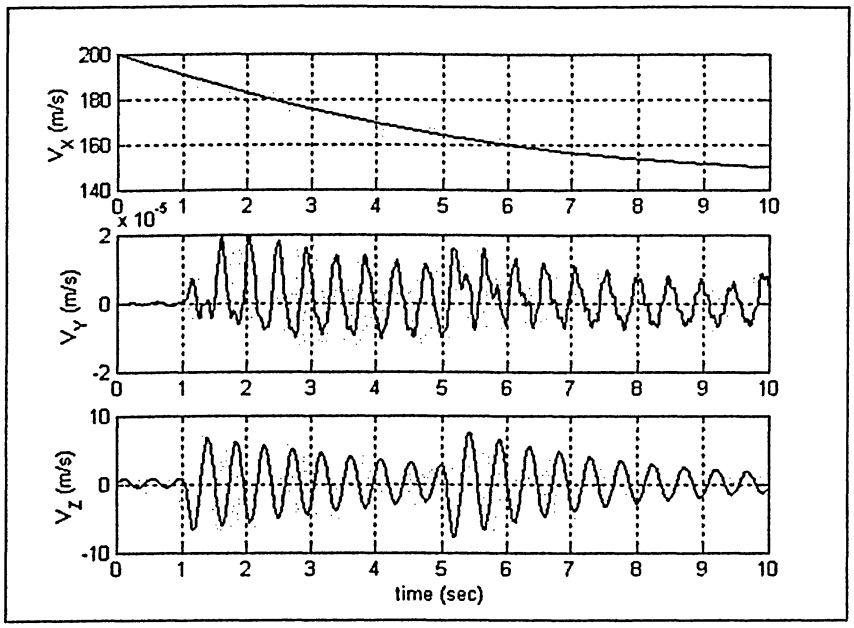

Figure 6.40: Translational Velocity Profiles for Subsonic Stability

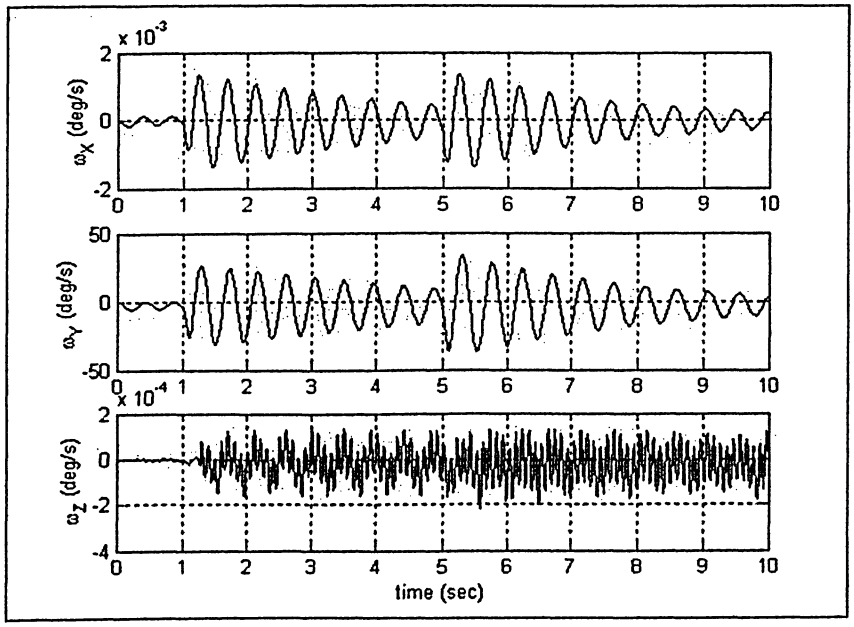

Figure 6.41: Angular Velocity Profiles for Subsonic Stability

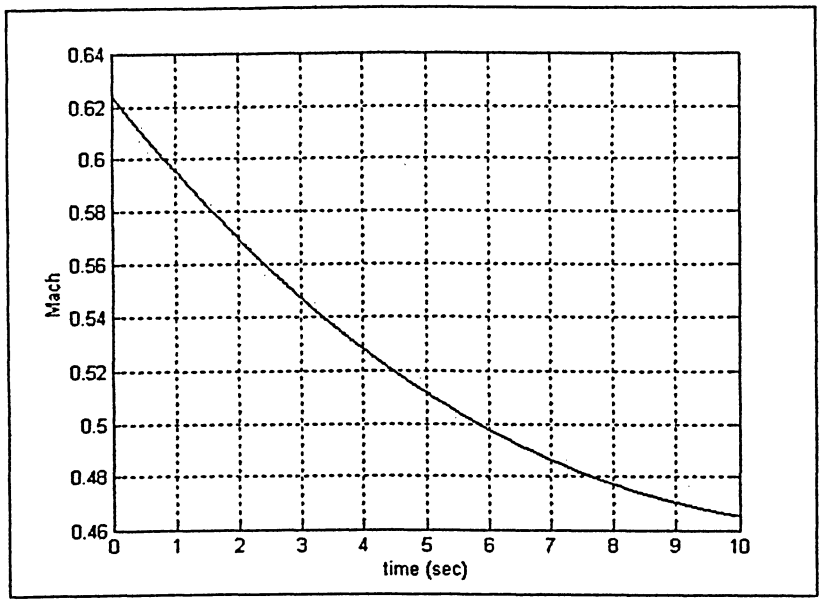

Figure 6.42: Mach Number Profile for Subsonic Stability

Figures 6.43 and **6.44** depict the aerodynamic loads acting on both the fuselage and fins throughout the simulation. Unlike the previous cases, it can be seen from the pitching moment plot (M_Y) in **Figure 6.44**, the fin moment always exceeds that of the fuselage. This in itself does not always guarantee stability, since the location of the body frame may be arbitrarily located, and these aerodynamic moments are defined with respect to ($\mathcal{F}_B$). However, in the present context with the body frame affixed at the rocket nose, it has been shown in previous plots (angle of attack, pitch rate, V_Z, etc.) that the forces acting on the fins, and the resulting moments, are sufficient to ensure longitudinal stability. The diminishing sinusoidal profile is replicated both in normal force (F_Z) and pitch moment (M_Y), which both drive the vehicle recovery following the onset of the gust load disturbances.

The vehicle orientation history is summarized in **Figure 6.45**. The pitch contour shows a gradual pitch downward, as a result of the effect of gravity. In response to the sudden gust loads, oscillations develop within the pitch profile. However, these oscillations begin to quickly dampen out as the magnitude of the angle of attack oscillations is rapidly reduced.

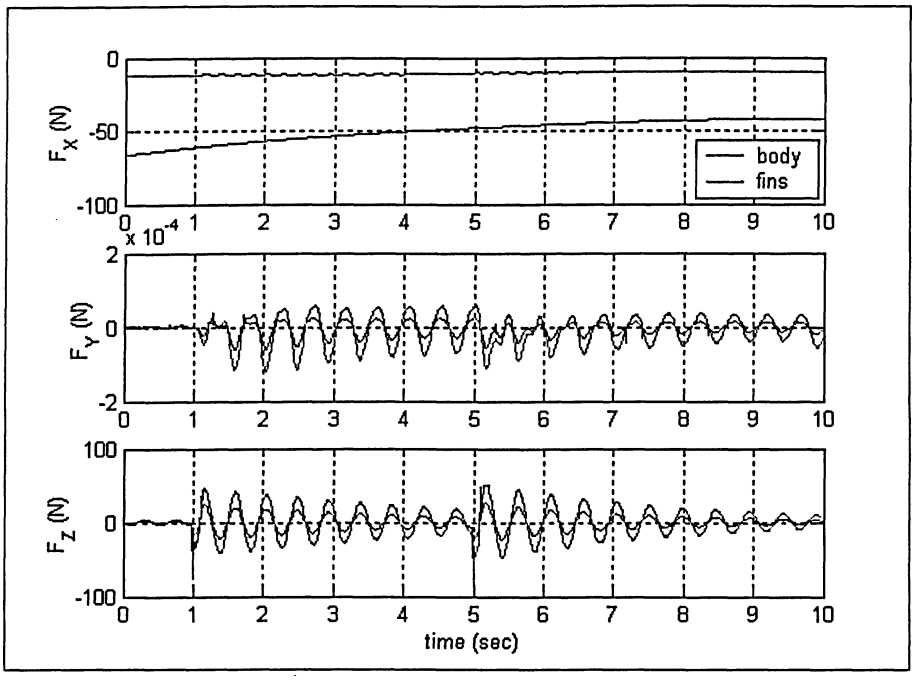

Figure 6.43: ($\mathcal{F}_B$) Aerodynamic Force Profiles for Subsonic Stability

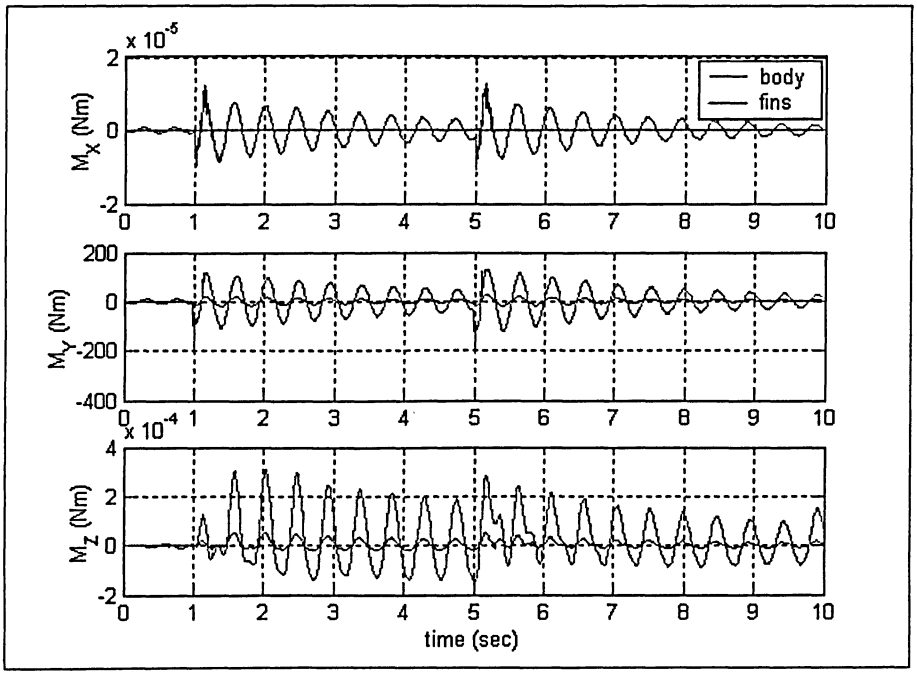

Figure 6.44: ($\mathcal{F}_B$) Aerodynamic Moment Profiles for Subsonic Stability

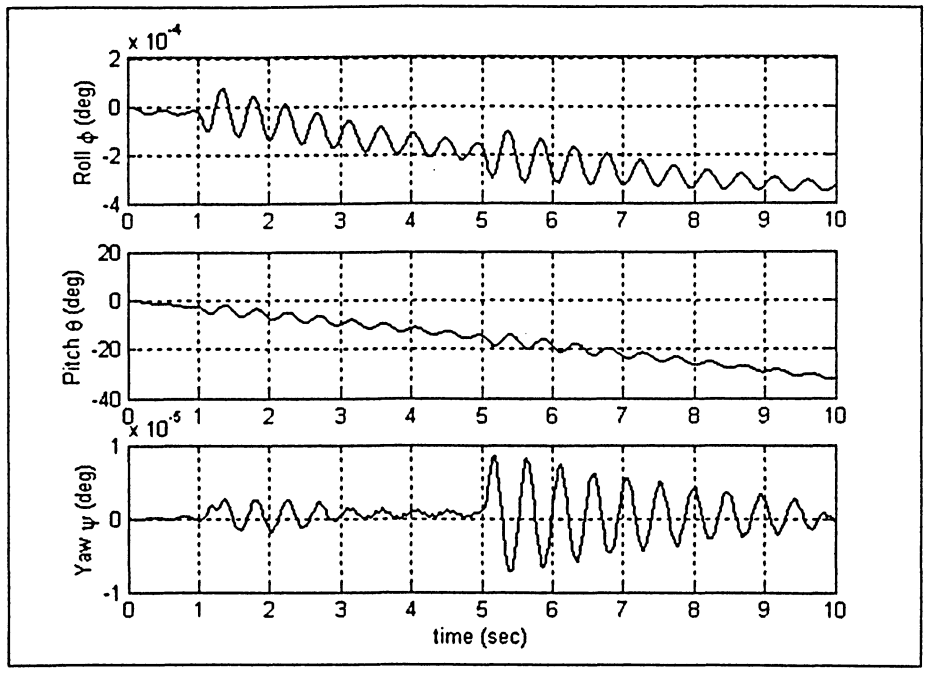

Figure 6.45: Roll, Pitch and Yaw Profiles for Subsonic Stability

The final step is to analyze the actual physical deflections of the rocket vehicle with respect to time. **Figures 6.46 and 6.47** illustrate the deformation of the rocket at four distinct instances within the simulation test. The first frame in each figure corresponds to the maximum deformation resulting from the first gust load. Frame two depicts the new local maximum deformation at a time just prior to the initiation of the second gust load. That is, this frame represents the extent to which the fin deformation magnitude has decreased following the first flight disturbance. The third frame shows the maximum deformation immediately after the completion of the second gust load. The fourth and final frame again depicts the last local maximum deflection just prior to the completion of the simulation.

All deformations have been enhanced by a factor of two for illustrative purposes. It can be clearly seen that the fin deformation is decreasing with respect to time. **Figure 6.47** presents a three dimensional view of the rocket and additionally relates the orientation of the velocity vector which in turn illustrates a visual reference of the instantaneous of angle of attack.

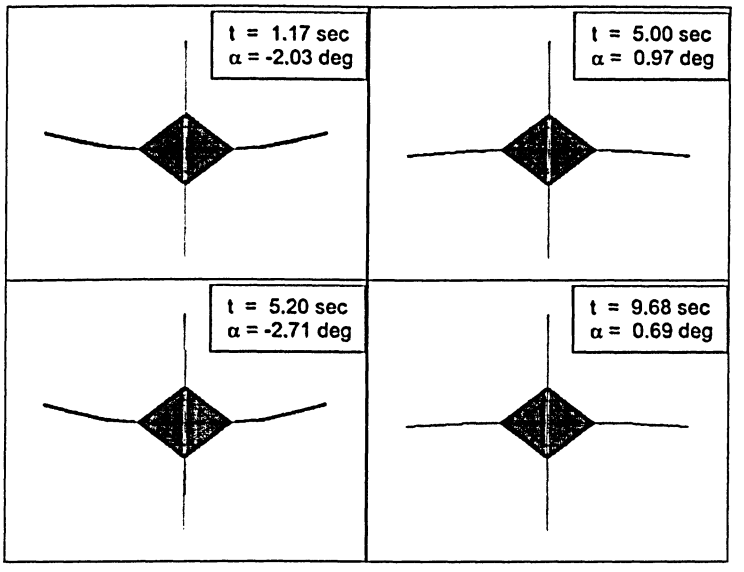

Figure 6.46: Rocket Deformation (Front) for Subsonic Stability

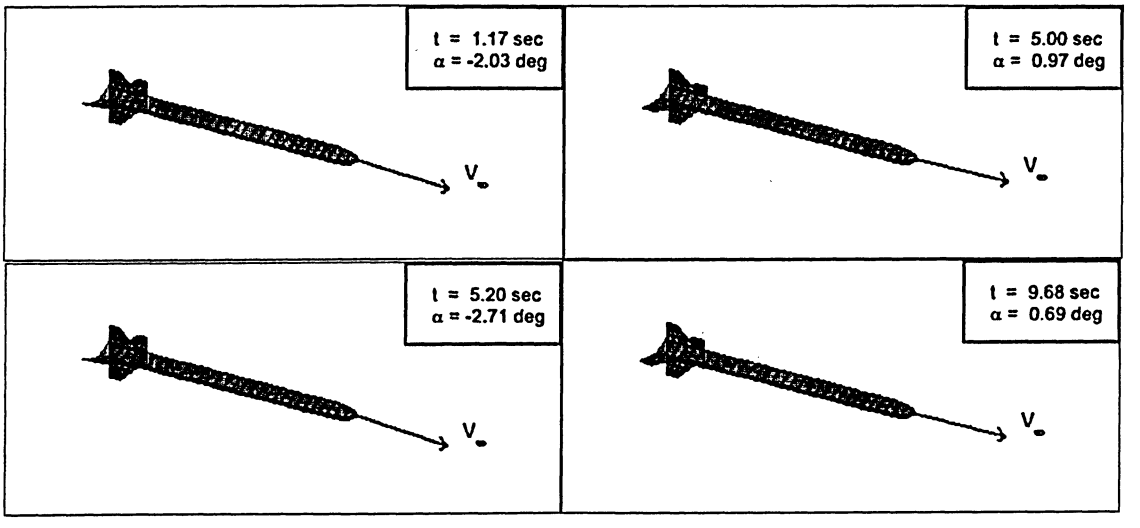

Figure 6.47: Rocket Deformation (3D) for Subsonic Stability

6.5.5 Supersonic Divergence Instability

The focus is now shifted to examining the behaviour of various rocket models at supersonic speeds. The increased velocities correspond to higher dynamic pressures, which typically lead to higher loadings on the various aerodynamic bodies. Thus, it is presumable that a rocket operating in the supersonic regime will require thicker fins to maintain stability than that established for subsonic speeds.

A flight simulation was performed for a rocket model whose fins have a constant thickness of 0.6 mm. The initial conditions for this scenario are

$$\mathbf{V}_{Bo} = [700 \quad 0 \quad 0]^T \text{ m/s} \qquad \boldsymbol{\omega}_{Bo} = [0 \quad 0 \quad 0]^T \text{ rad/s}$$

$$[\phi \quad \theta \quad \psi]^T = [0 \quad 0 \quad 0]^T \qquad h = 10 \text{ km}$$

The results of this simulation are presented in **Figures 6.48-6.58**

The angle of attack (α) profile is shown below. Similar to the subsonic divergence case, a clear exponential growth is evident. However, for this case, the growth is considerably quicker given that the simulation reaches the modeling limits before the first gust load is be initiated at t = 1 second.

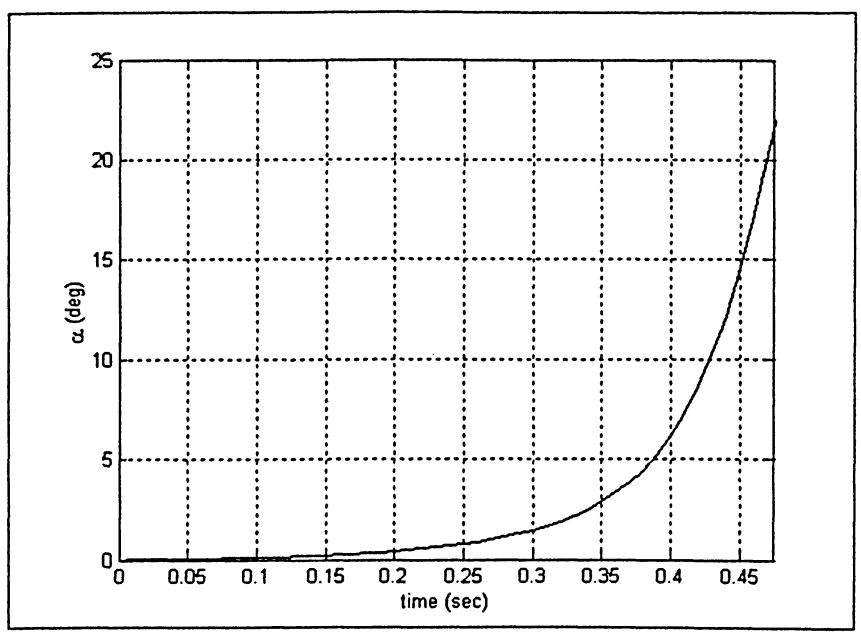

Figure 6.48: Angle of Attack Profile for Supersonic Divergence

Figures 6.49-6.50 show the fin flap and body bending reduced order coordinate deformations. The fin displacements show the divergence trend in fins one and three. Fins two and four are initially in plane with the velocity vector, with fin two being in the windward plane and fin four in the leeward plane.

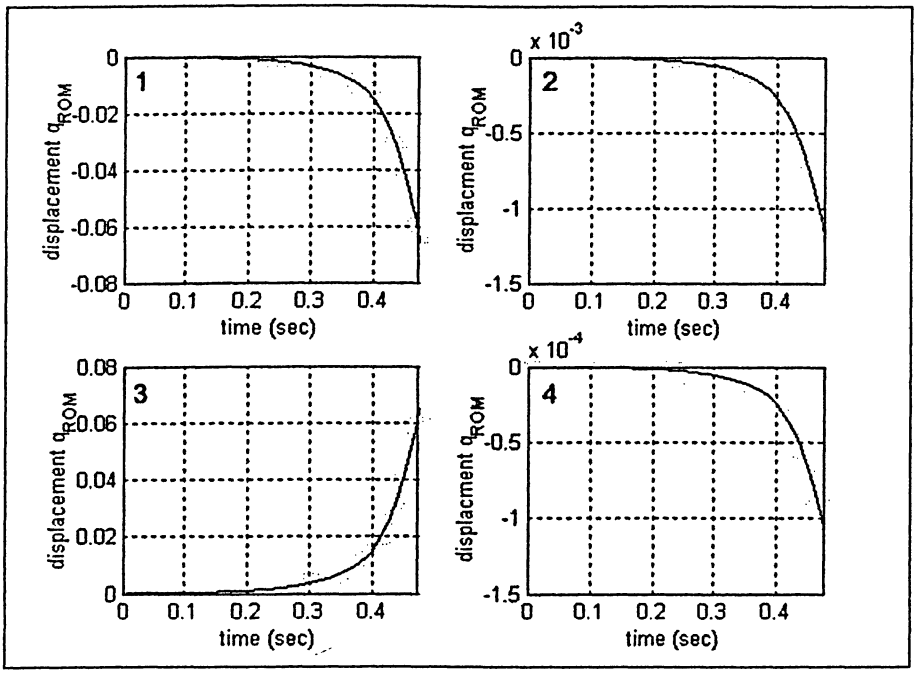

Figure 6.49: Fin Flap Deformation Profiles for Supersonic Divergence

The body deformation coordinates are additionally shown in **Figure 6.50** due to the fact that some body (bending) deformation becomes evident as the flight instability develops. The profiles are identical due to the fact that the shape vectors used to define the body bending degrees of freedom were defined at angles to the body frame x-y and x-z planes. Therefore, the identical deformation values indicate motion in the body frame x-z plane (pitch plane).

Several of the following figures present contours that closely mirror the trends presented for the subsonic divergence case. Translational and angular velocities in the body frame are given in **Figures 6.51** and **6.52.** Divergence trends are predominantly evident in the translational z-velocity component and the angular (pitch) y-velocity component. The vehicle is also decelerating across the short duration of the simulation. This is illustrated somewhat by the x-velocity profile in **Figure 6.51**, and more definitively by the Mach number contour displayed in **Figure 6.53.**

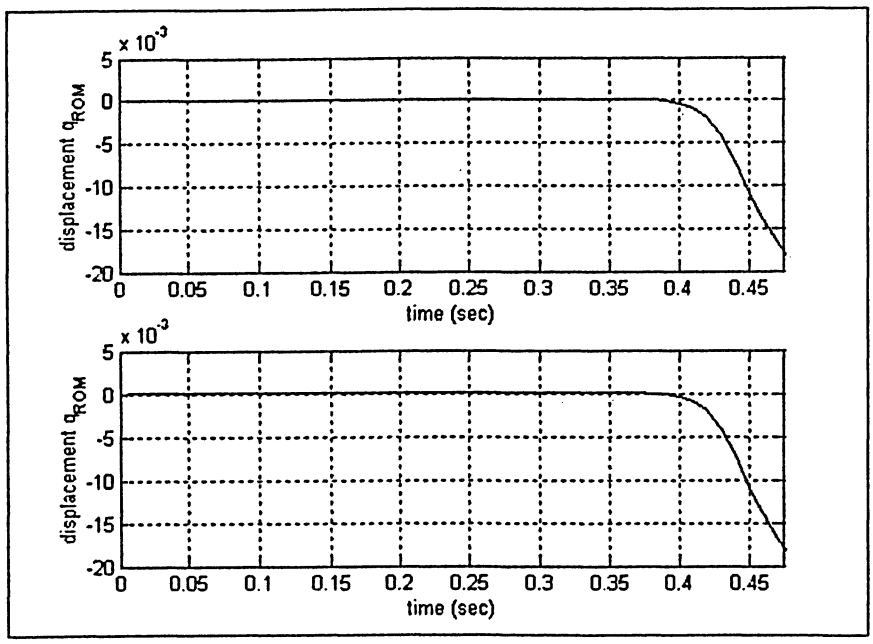

Figure 6.50: Body Deformation Profiles for Supersonic Divergence

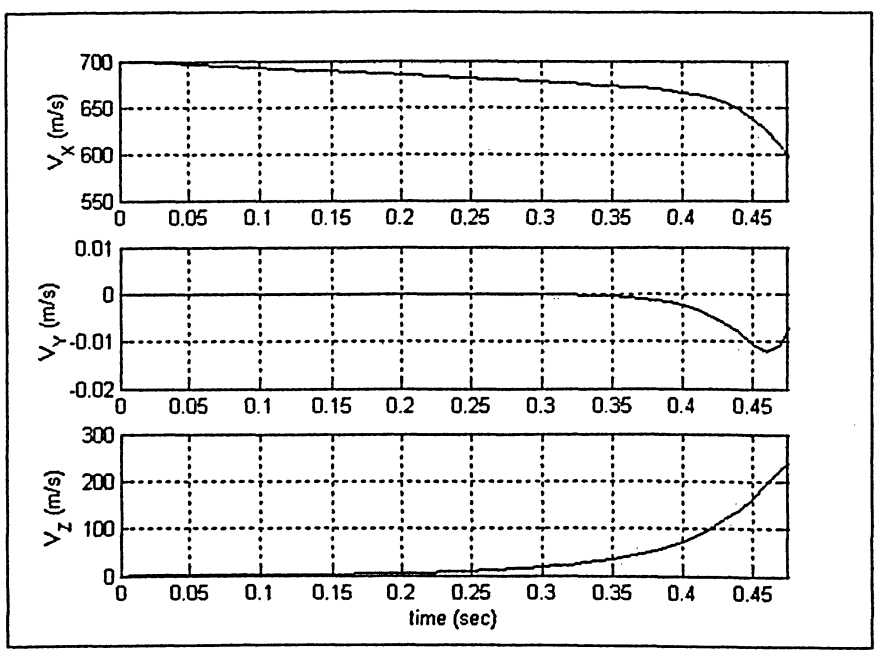

Figure 6.51: Translational Velocity Profiles for Supersonic Divergence

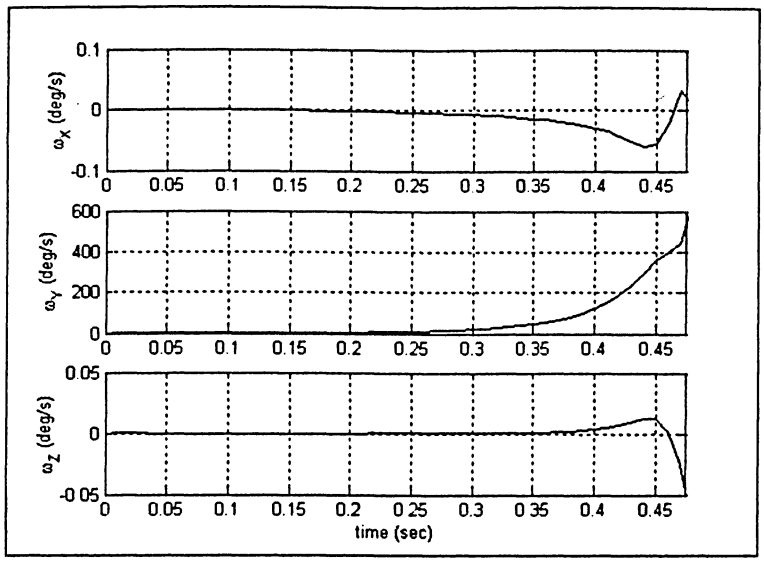

Figure 6.52: Angular Velocity Profiles for Supersonic Divergence

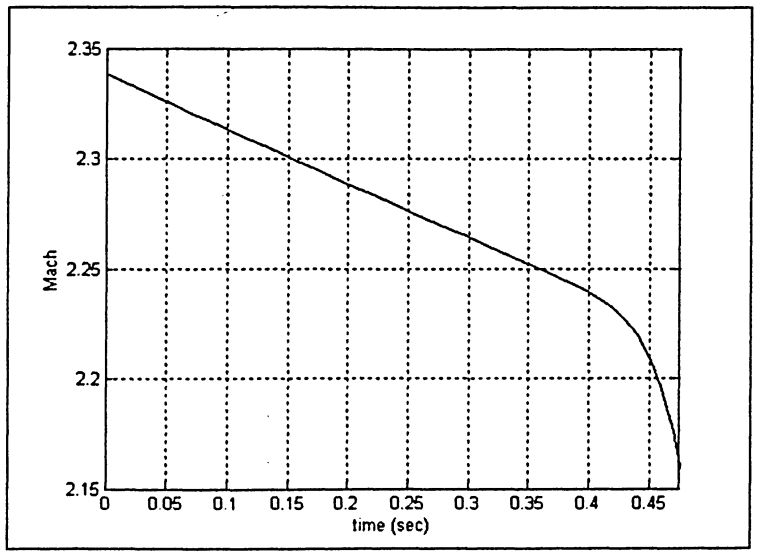

Figure 6.53: Mach Number Profile for Supersonic Divergence

The total aerodynamic loads for both the fuselage and fins are presented in **Figures 6.54** and **6.55**. Similar to the subsonic case, exponential growth trends are present for the normal forces (force z-component), and the pitch moment (moment y-component). The fins are incapable of providing the needed forces to establish longitudinal stability. As a result, the rocket motion is dominated by the aerodynamic effects of the fuselage and is subsequently unstable. As the instability progresses, other rigid body motions begin to develop as seen by the

growth of the roll and yaw rates in **Figure 6.55**, and the side force (y-component) in **Figure 6.54**. The roll and yaw motion progression is also evidenced in **Figure 6.56**, which presents the orientation data for the current simulation.

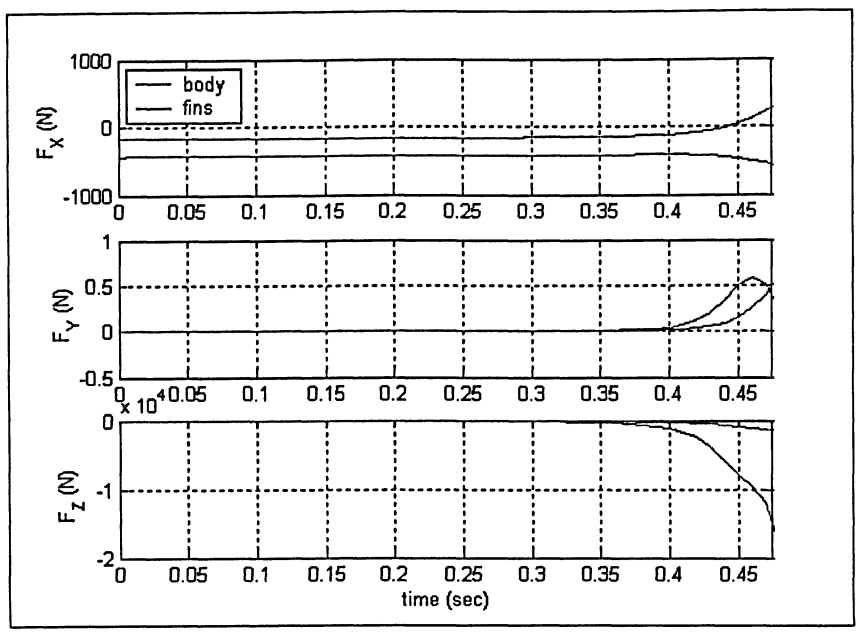

Figure 6.54: ($\mathcal{F}_B$) Aerodynamic Force Profiles for Supersonic Divergence

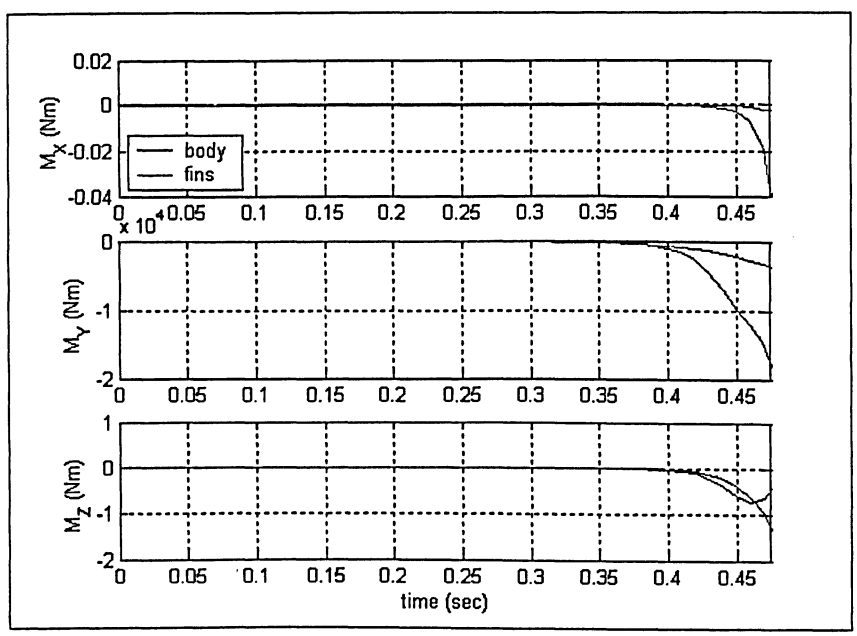

Figure 6.55: ($\mathcal{F}_B$) Aerodynamic Moment Profiles for Supersonic Divergence

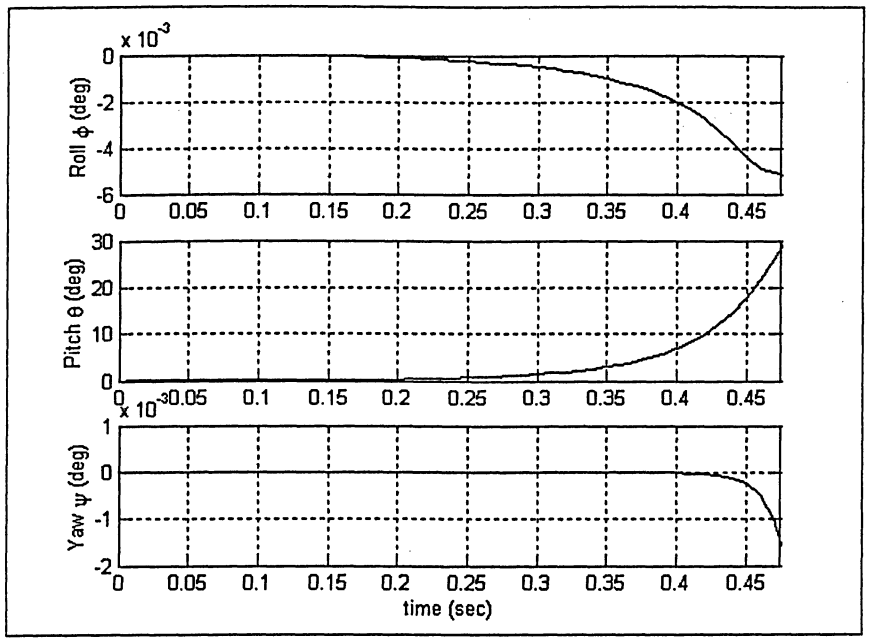

Figure 6.56: Roll, Pitch and Yaw Profiles for Supersonic Divergence

The progression of the divergence instability is summarized in the following animation frames. The rocket is depicted 0.15, 0.3 and 0.467 seconds into the simulation. The rapid and large-scale deformation of the fins is evidenced in **Figures 6.57** and **6.58**. **Figure 6.57**, shows the front view (looking down at the rocket nose). Some body bending motion is visible in the third and final animation frame. **Figure 6.58** displays a three-dimensional view of these same simulation images along with the current orientation of the velocity vector. The large deformation of the fins would again most likely exceed the yield strength of the rocket fin material (aluminum), resulting in destructive fin failure.

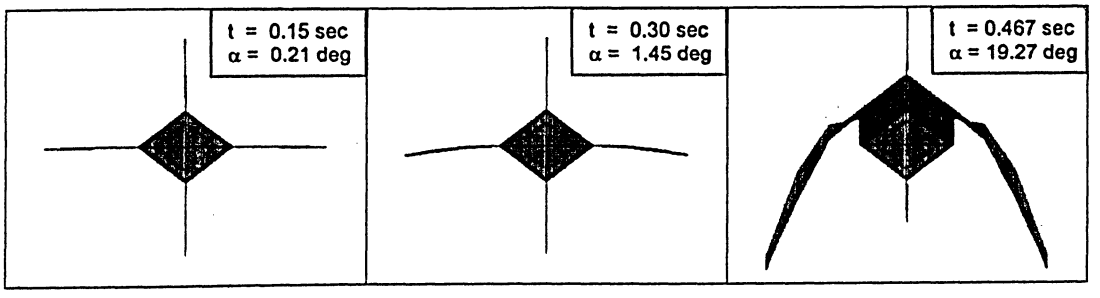

Figure 6.57: Rocket Deformation (Front) for Supersonic Divergence

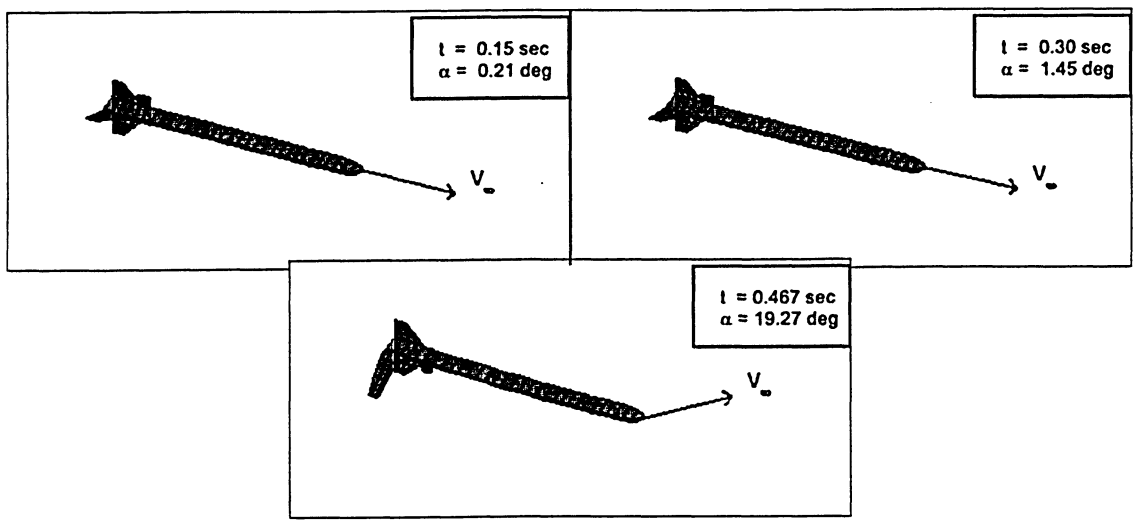

Figure 6.58: Rocket Deformation (3D) for Supersonic Divergence

6.5.6 Supersonic Oscillatory Instability

A flight simulation was performed for a rocket model whose fins have a constant thickness of 0.7 mm. The initial flight conditions are identical to those of the previous supersonic case. The simulation results are presented in **Figures 6.59-6.70.**

The angle of attack contour for the present simulation is shown in **Figure 6.59.** Several distinct trends are discernable from this graph. Initially, there is a slight oscillation, driven by the gravitational acceleration as was evident in the previous cases. This continues until t = 1 second when the rocket is disturbed by the first 5 m/s gust. This gust initiates an increasing oscillatory trend indicating that the current rocket configuration is unstable.

As in all the previous simulation cases, the rocket is given an initial velocity and permitted to follow the trajectory that is dictated by the forces acting upon it. As a result, the vehicle decelerates across a wide spectrum of velocities throughout the simulation. This fact is illustrated in **Figure 6.60**, which depicts the Mach number variation experienced by the rocket. The Mach number decreases significantly from an initial value of approximately 2.3 to subsonic speeds at the simulation end time.

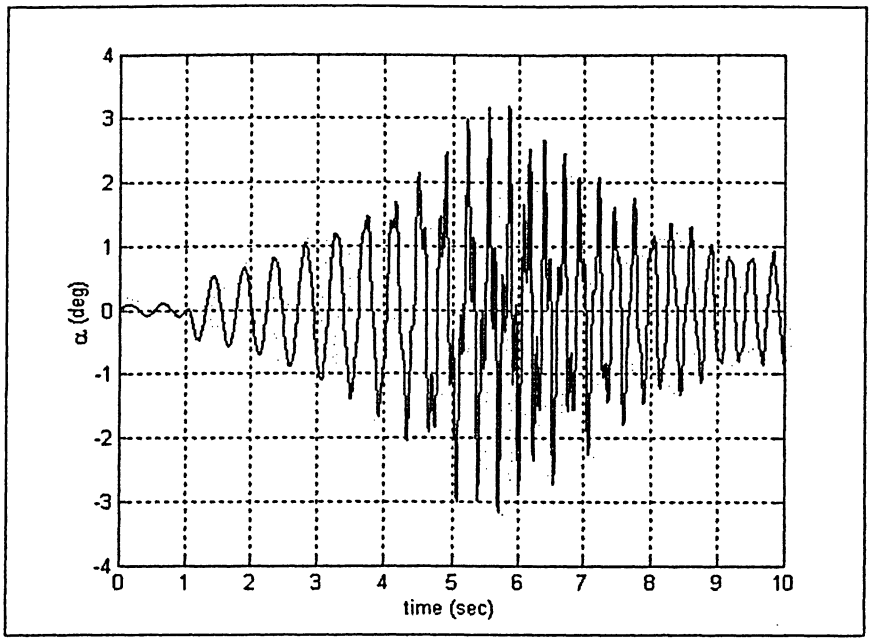

Figure 6.59: Angle of Attack Profile for Supersonic Flutter Instability

Referring back to **Figure 6.59**, the sinusoidal instability trend is reversed shortly following the second gust load. This trend nicely illustrates the vehicle crossing the stability boundary in transitioning from unstable to stable flight. This boundary crossing is effected by the rapid deceleration of the vehicle. Referring to the Mach number plot, it can be seen that at the time of maximum α magnitude, the rocket is traveling at a speed of roughly Mach 1.3. Thus, it may be inferred that the current rocket configuration with fins that are 0.7 mm thick, at an altitude of about 10 kilometers will be stable if the freestream Mach number is less than about 1.3. Speeds in excess of that value will tend to quickly develop unstable flight behaviour.

Figures 6.61 and **6.62** showcase the fin deformation coordinates for the current test case. **Figure 6.61** shows the fin flap coordinates for each of the four fins, and **Figure 6.62** depicts the fin twist motion coordinates. The fin flap coordinates show a clearly unstable, sinusoidal growth trend across the first half of the simulation. The return to stability is also indicated following the completion of the second gust load. Twist motions are rather small across the first half of the

simulation, but quickly increase as the vehicle decelerates from roughly Mach 1.5 to Mach 1.1.

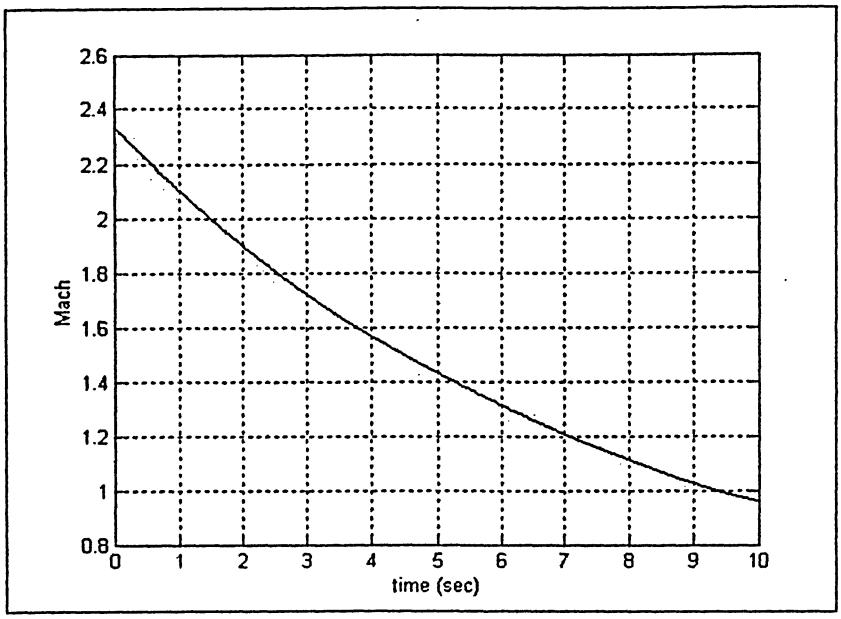

Figure 6.60: Mach Number Profile for Supersonic Flutter Instability

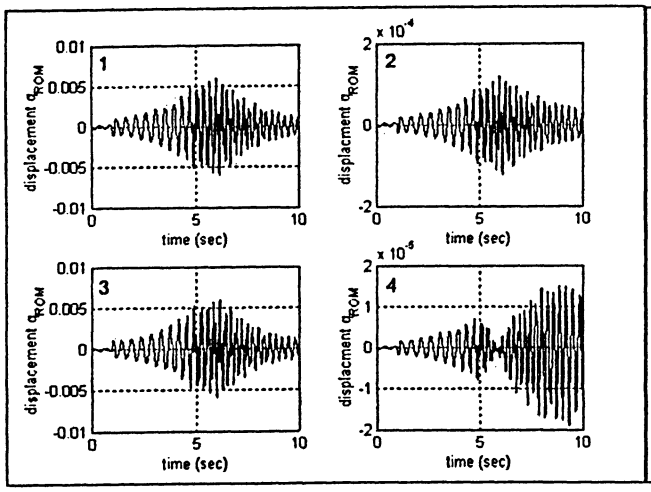

Figure 6.61: Fin Flap Deformation Profiles for Subsonic Flutter

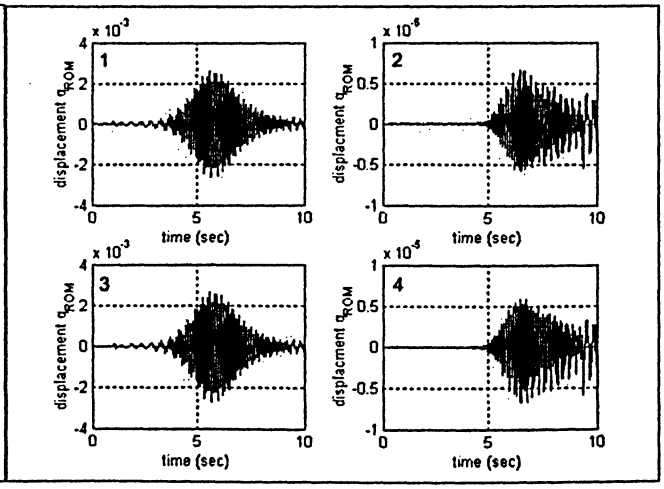

Figure 6.62: Fin Twist Deformation Profiles for Subsonic Flutter

Coincidentally, the body bending deformations are active across the same Mach spectrum as the fin twist motions. The profiles are displayed in **Figure 6.63.** This is due to the fact that for the current model, the natural frequencies for both the body bending and fin twist motions are approximately equal (~90 Hz). This is also

evidenced by the higher frequency oscillations observable across this Mach range in the angle of attack profile. The combination of body bending and fin twist motions alter the previously smooth sinusoid contour.

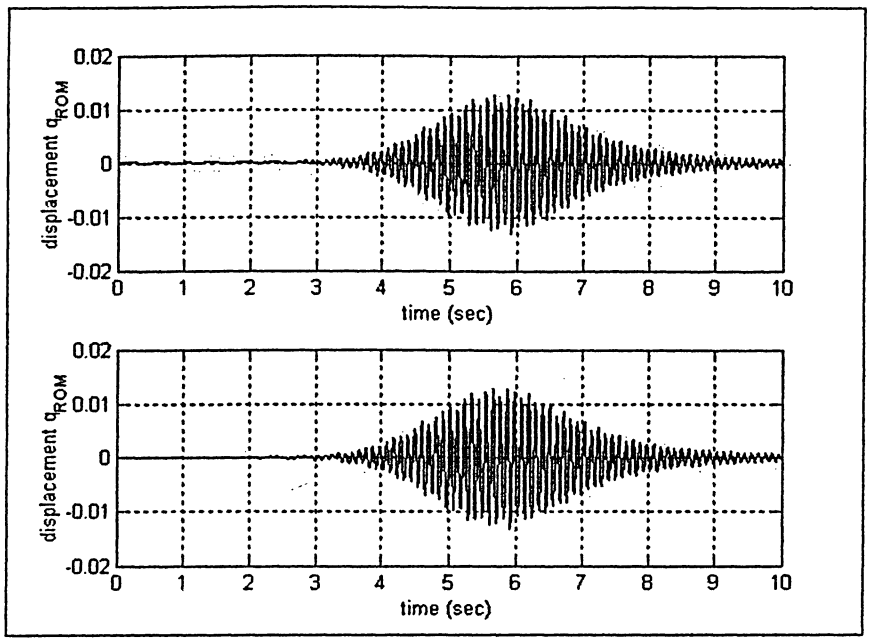

Figure 6.63: Body Deformation Profiles for Supersonic Flutter Instability

The body frame translational and angular velocity profiles are shown in **Figures 6.64** and **6.65** respectively. The sinusoidal growth and recovery trend is captured again in the translational z-velocity component and the angular y-velocity component (pitch rate). Higher frequency effects may be observed in the jagged V_Z profile across the range where the body bending and fin twist motions are most active. The pitch rates are also seen to be of quite large in magnitude for this duration.

The total aerodynamic forces and moments for both the fuselage and fins are presented in **Figures 6.66** and **6.67**. As expected, the normal force (F_Z) and pitch moment (M_Y) components both exhibit the unstable oscillating magnitude growth across the first half of the simulation followed by a stable oscillatory recovery. Higher order effects induced by the body motions show a rough jittery profile beginning around 4 seconds and extending through the next four seconds of simulation time.

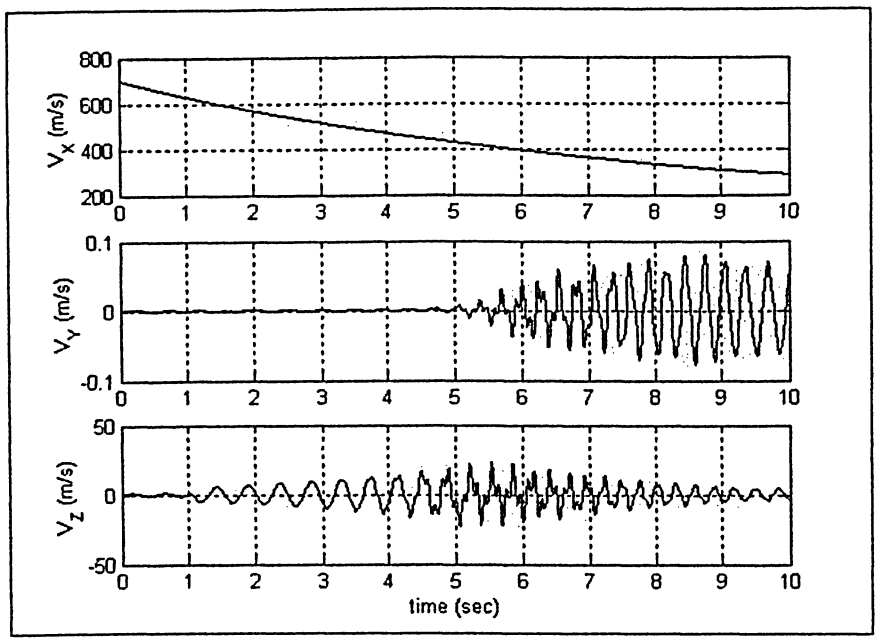

Figure 6.64: Translational Velocity Profiles for Supersonic Flutter

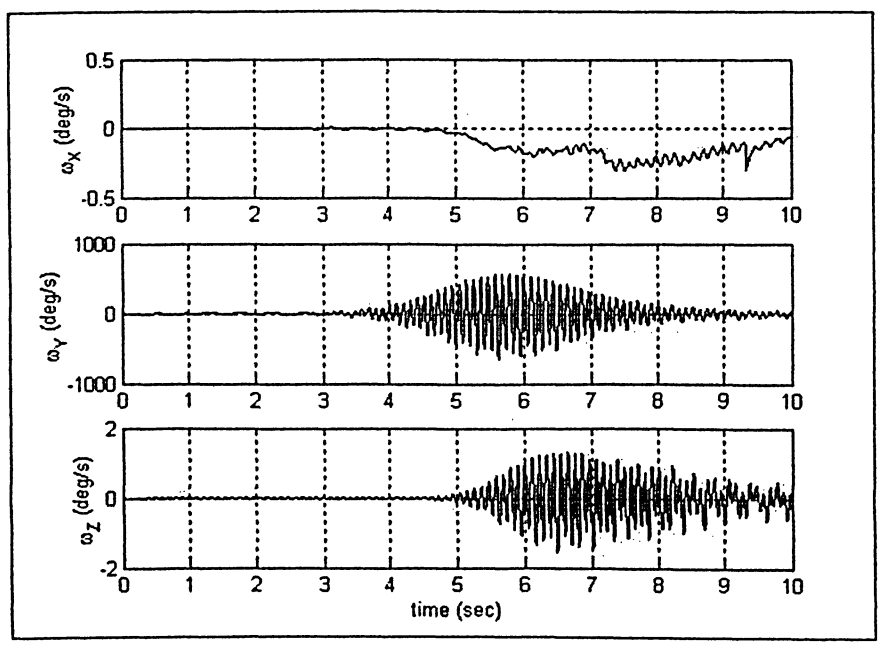

Figure 6.65: Angular Velocity Profiles for Supersonic Flutter

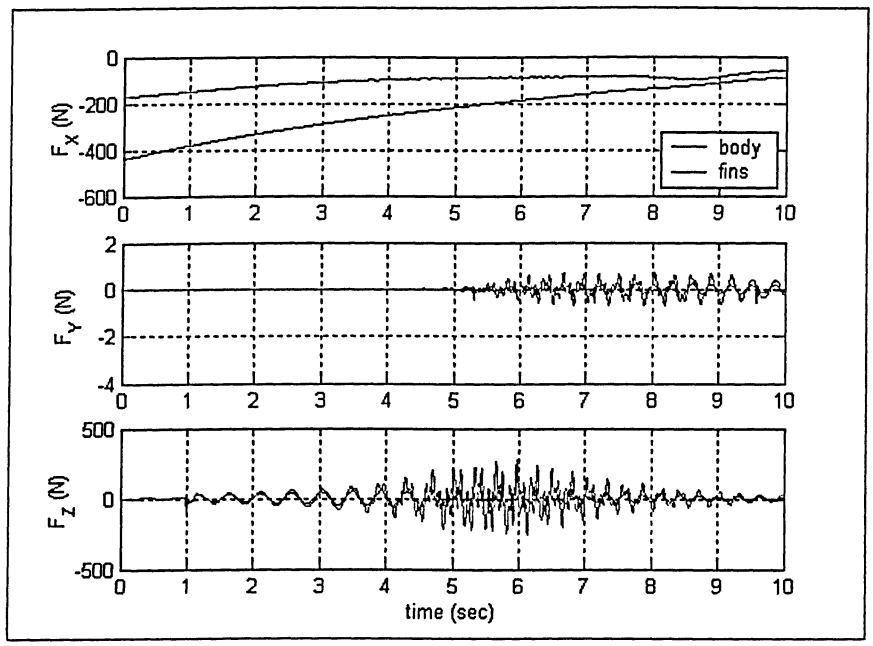

Figure 6.66: ($\mathcal{F}_B$) Aerodynamic Force Profiles for Supersonic Flutter

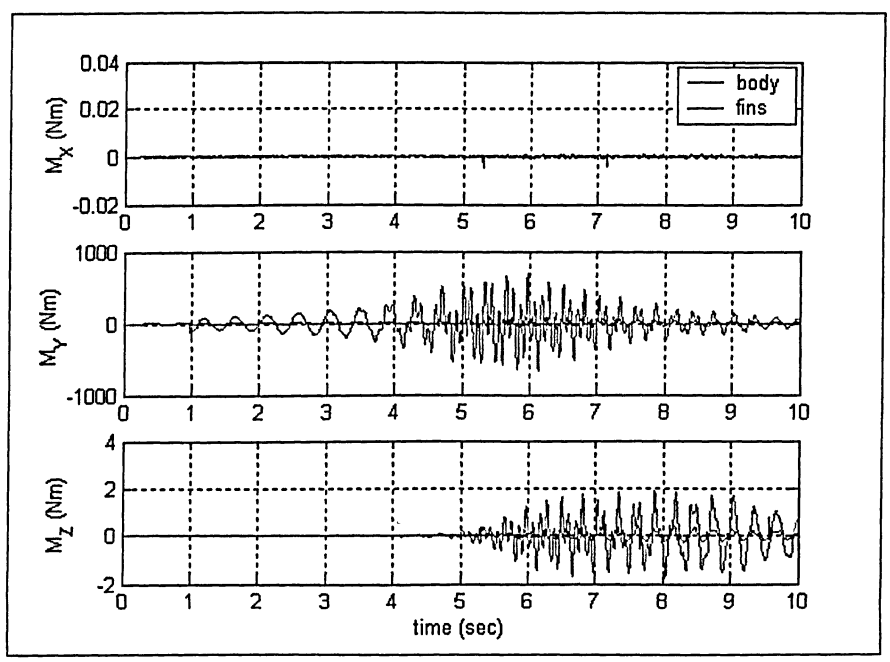

Figure 6.67: ($\mathcal{F}_B$) Aerodynamic Moment Profiles for Supersonic Flutter

Next, the orientation data are presented through plots of the rocket roll, pitch and yaw angles against time. The pitch angle (θ) begins its standard gradual pitchover due to the effects of gravity. The gust loads then initiate some oscillations into what would otherwise be a smooth profile. The oscillations

initially grow then suddenly begin to decrease as the vehicle decelerates and crosses the stability boundary, which results in a sudden dampening of the disturbance effects.

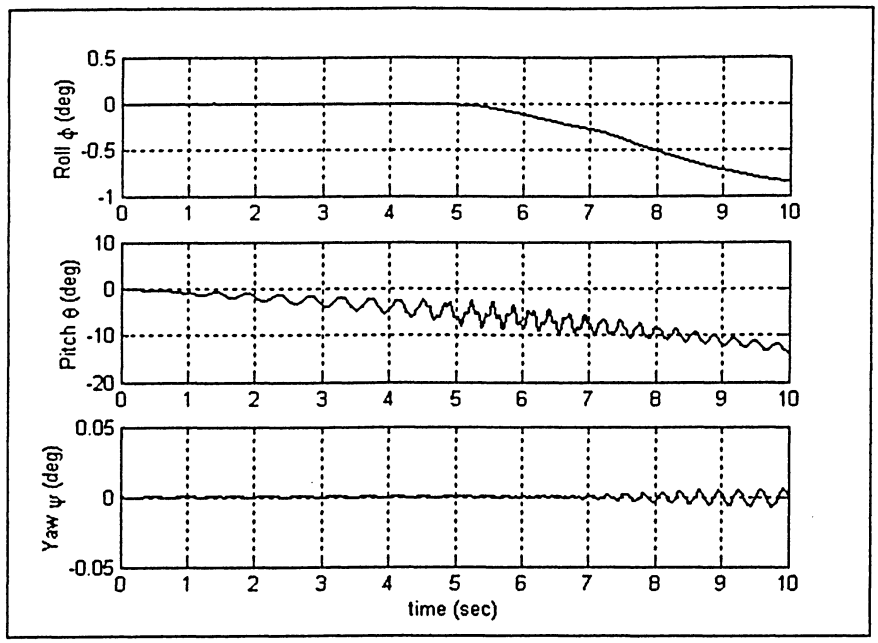

Figure 6.68: Roll, Pitch and Yaw Profiles for Supersonic Flutter

It has already been established that the rocket model employing fins with a thickness of 0.7 mm, shows a mix of stable and unstable behaviour as the rocket traverses the supersonic flight regime. The information is now presented with several animation frames depicting the rocket deformations with respect to time. **Figures 6.69** and **6.70** show four distinct instances of time from two different perspectives. All deformations have been enhanced by a factor of two to aid and highlight the flexible motions. **Figure 6.69** shows a front view of the rocket, with **Figure 6.70** illustrating a three-dimensional view.

The first frame shows a local maximum of deformation approximately one quarter into the simulation. At this point, the dominant motion is the flapping deformation of the fins. This frame is in the unstable, exponentially increasing segment of flight. The second frame shows the instance of maximum body deflection. The image in **Figure 6.67** is somewhat misleading as the deformation is still rather small. It is important to recall that the rocket body is 2.75 meters (9

feet) in length, and thus the deformation appears significant from the front perspective. **Figure 6.70** gives a clearer perspective regarding the extent of body deformation. The fins in this frame are also seen to have a considerable amount of twist. This is to be expected given that the fin twist and body deformation shapes have approximately the same natural frequencies. Frame three shows the point of maximum α, which follows closely after the maximum body deformation. The fourth and final frame shows how the rocket has recovered from unstable growth and has returned to smaller deformations dominated by the fin flapping motion.

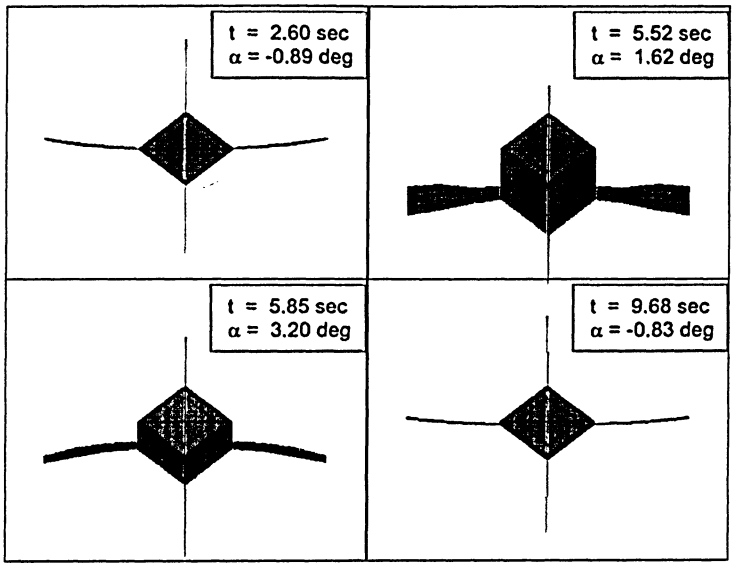

Figure 6.69: Rocket Deformation (Front) for Supersonic Flutter

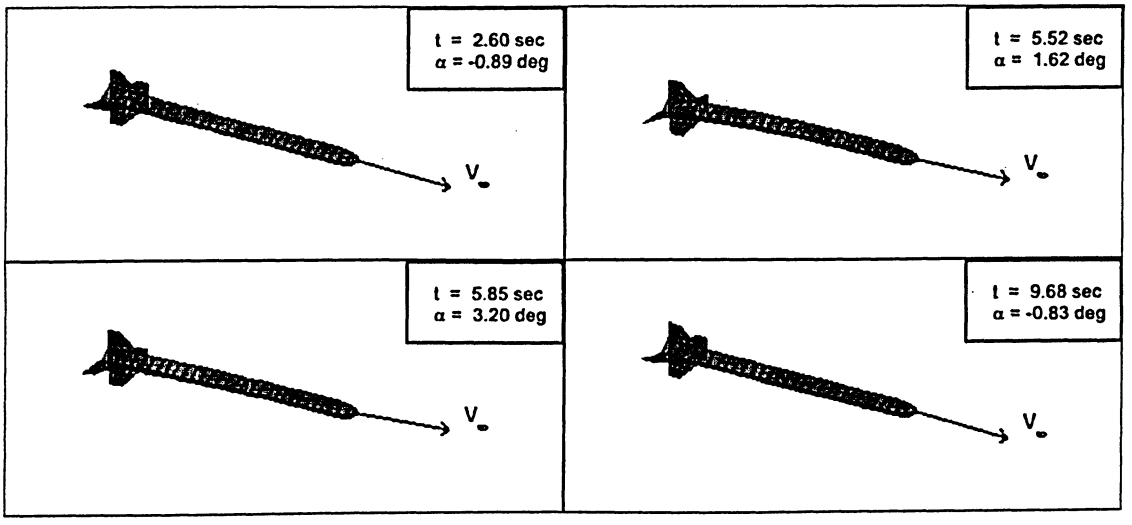

Figure 6.70: Rocket Deformation (3D) for Supersonic Flutter

6.5.7 Supersonic Stability

A final simulation was performed utilizing a rocket model that has fins of a constant thickness of 1 mm. The initial flight conditions are identical to that of the previous two supersonic cases. Additionally, the gust loads are identical to those explained in the previous cases. The simulation results are presented in **Figures 6.71-6.80.**

The angle of attack profile is depicted in **Figure 6.71.** The contour shows a definite decreasing sinusoidal trend in response to the gust loads at one and five seconds. This indicates that the current configuration is indeed stable across the entire velocity range.

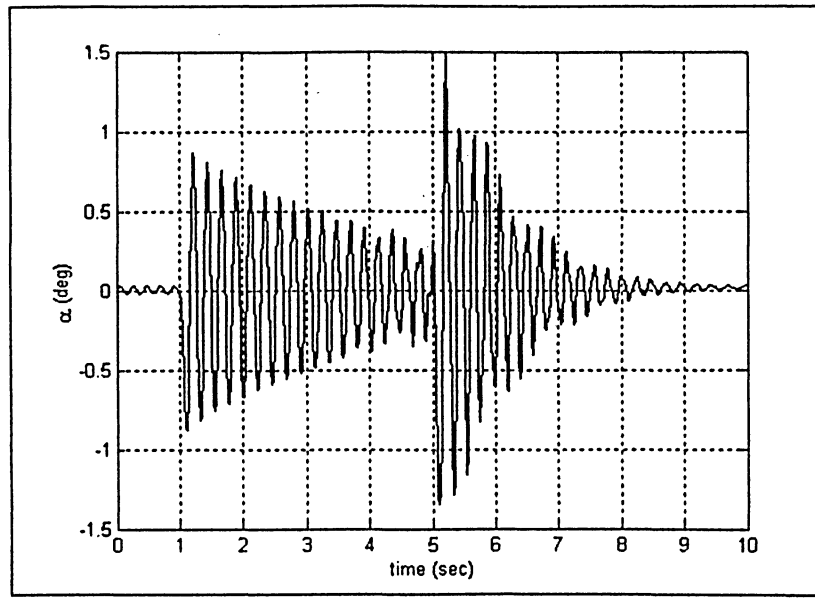

Figure 6.71: Angle of Attack Profile for Supersonic Stability

The Mach number profile for this case is virtually identical to that of the previous, supersonic flutter instability case. The Mach number decreases from roughly 2.3 to 0.95 in 10 seconds. The profile was shown in **Figure 6.60.**

The deformation profiles for the fins and body are shown in **Figures 6.72-6.74.** The deformations that develop following the gust loads rapidly decrease as seen with respect to the fin deformation coordinates. As was the case with the flutter instability simulation, the body deformation is excited across the same time and

Mach range. This is due to the fact that the only thing changing from model variations is the fin thickness. The natural frequencies for the body bending motions remain fixed at ~90 Hz.

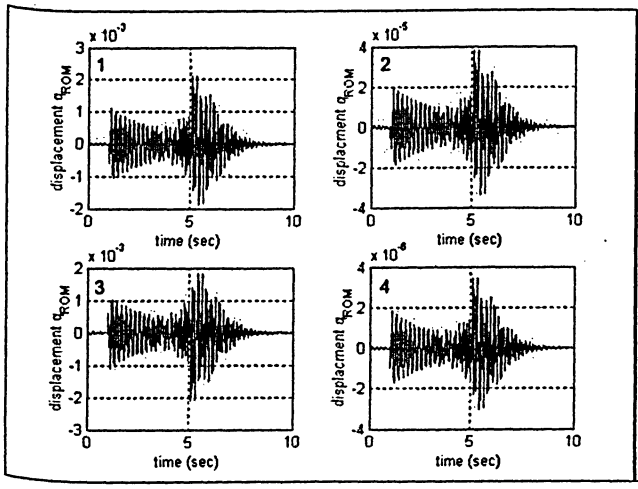

Figure 6.72: Fin Flap Deformation Profiles for Subsonic Stability

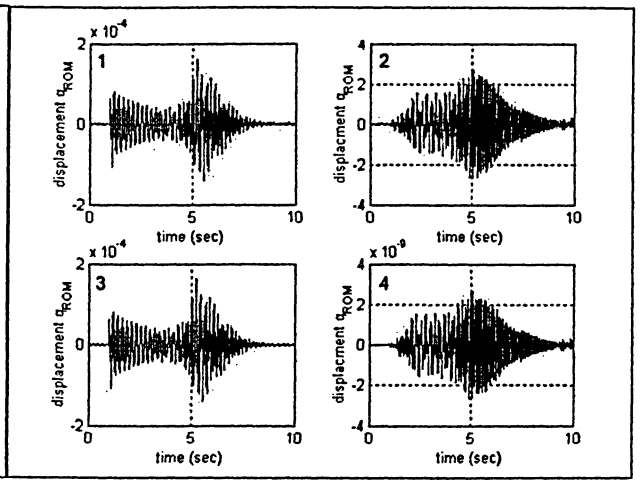

Figure 6.73: Fin Twist Deformation Profiles for Subsonic Stability

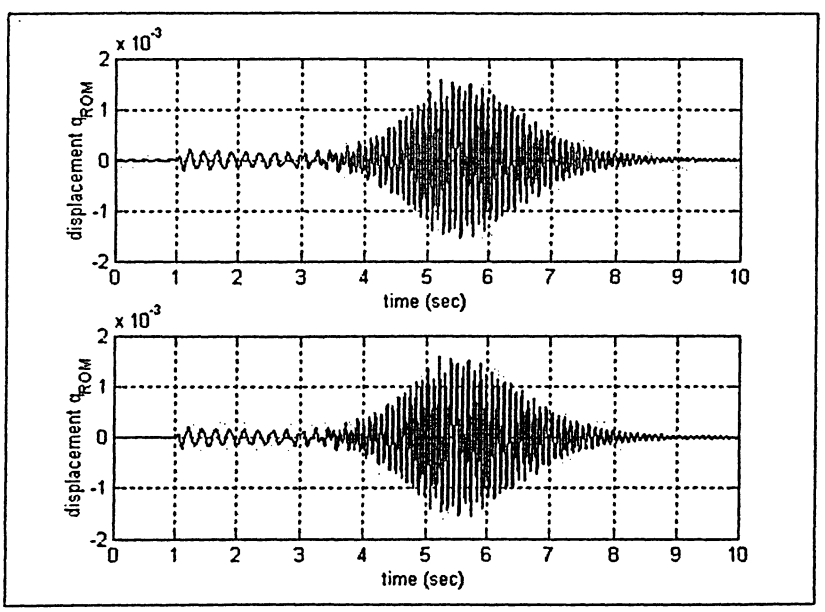

Figure 6.74: Body Deformation Profiles for Supersonic Stability

The rigid body translational and angular velocities are displayed in **Figures 6.75** and **6.76** respectively. As is expected, the stable exponential decrease is evident in the z-velocity (V_Z) and the y-angular velocities (ω_Y).

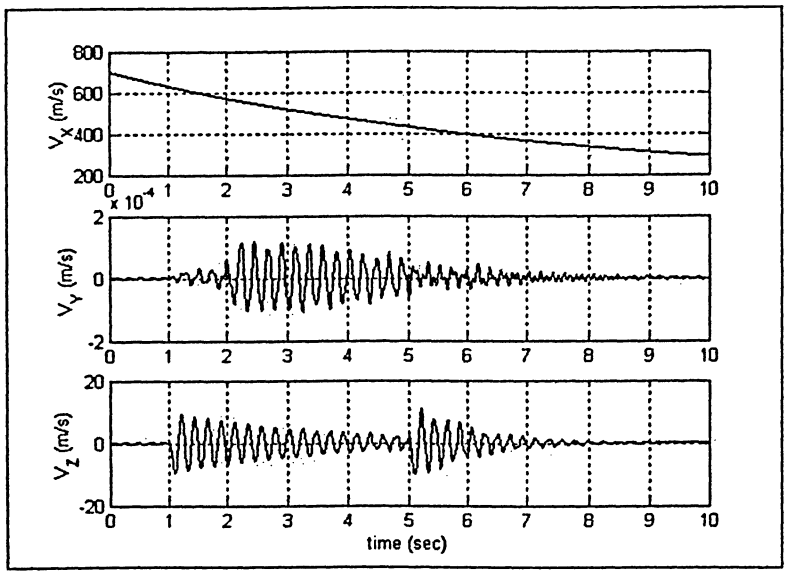

Figure 6.75: Translational Velocity Profiles for Supersonic Stability

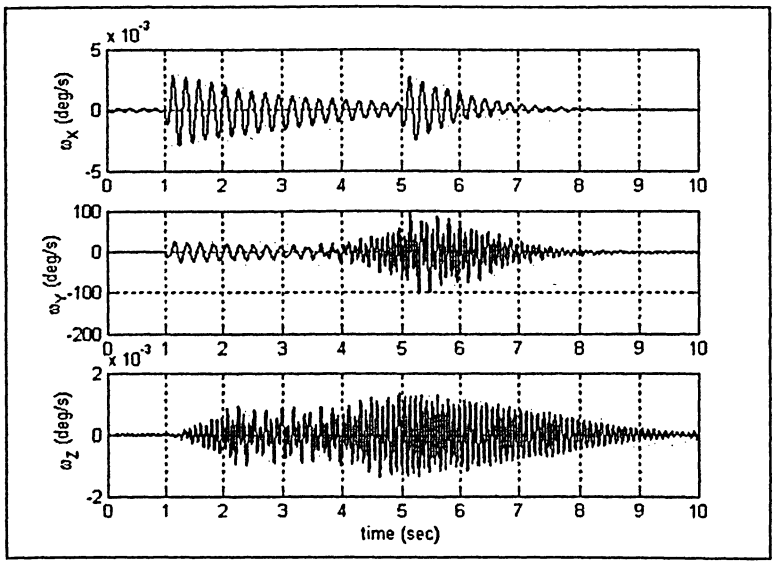

Figure 6.76: Angular Velocity Profiles for Supersonic Stability

The total body frame aerodynamic loads are shown in **Figures 6.76** and **6.77**. The results once again confirm that the current model configuration is stable for the entire velocity range experienced by the rocket.

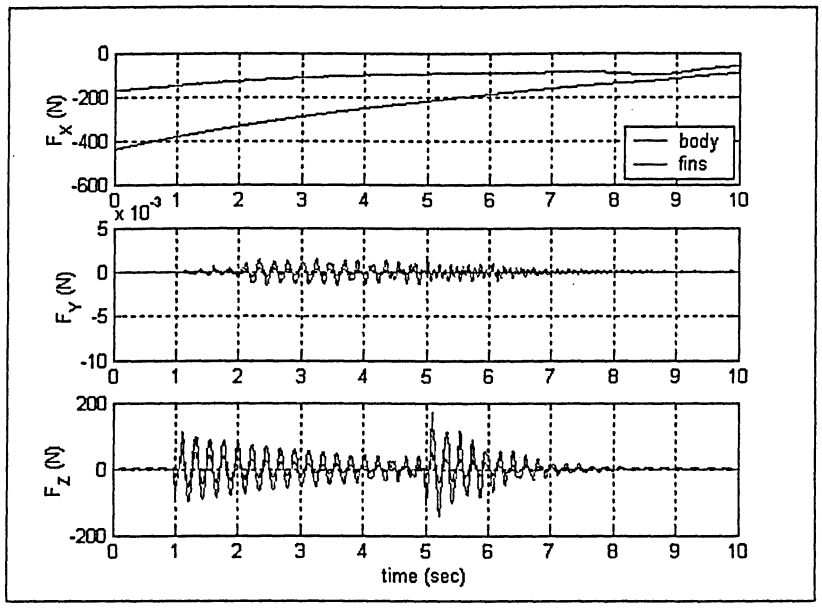

Figure 6.77: ($\mathcal{F}_B$) Aerodynamic Force Profiles for Supersonic Stability

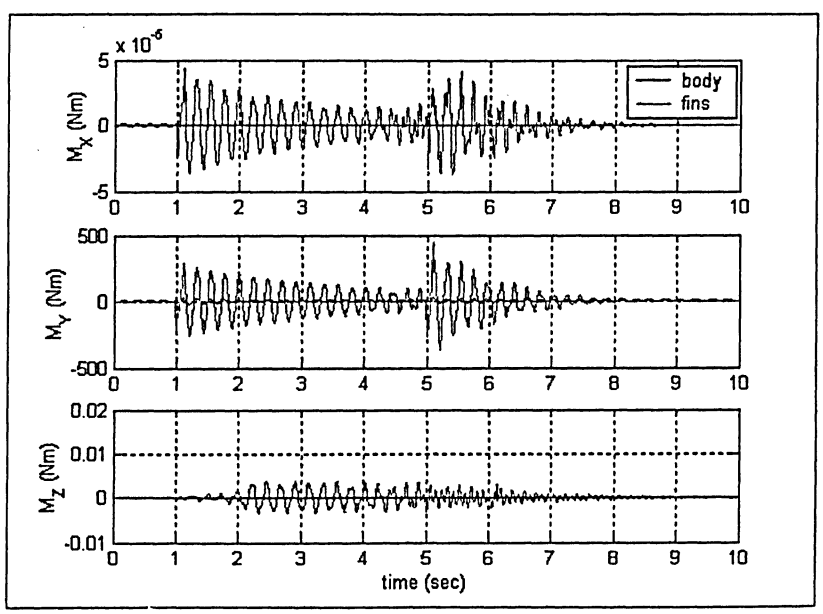

Figure 6.78: ($\mathcal{F}_B$) Aerodynamic Moment Profiles for Supersonic Stability

The roll, pitch and yaw profiles for the current stable simulation are presented in **Figure 6.79**. The dominant motion is with respect to the pitch angle, which experiences a gentle gravity turn effect. This profile is disturbed by the gust loads which initiate an oscillatory pitch response as detailed in the figure.

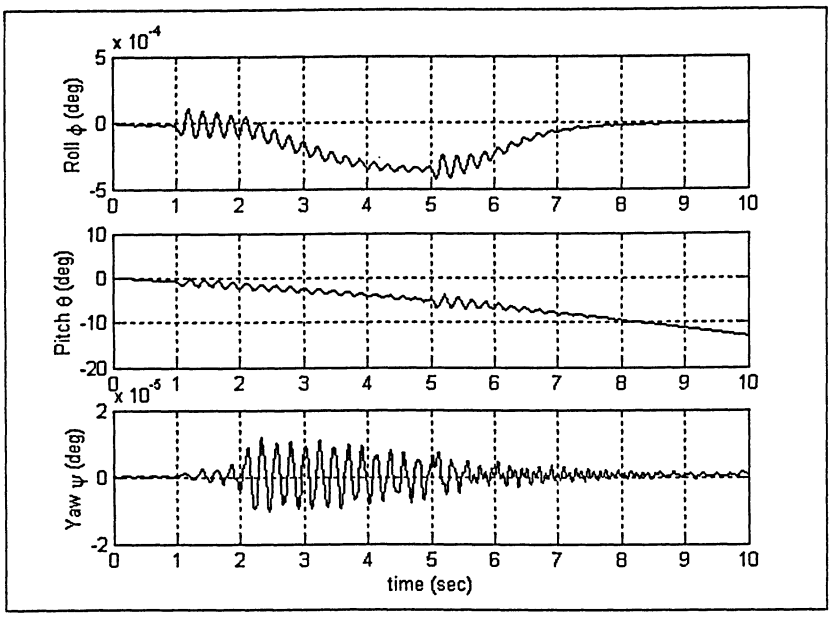

Figure 6.79: Roll, Pitch and Yaw Profiles for Supersonic Flutter

Lastly, the physical deformation of the rocket vehicle is shown in **Figure 6.80**. The deformation is viewed from the front, that is, looking down at the nosecone section. Deformations have been enhanced by a factor of four to aid in visibility. The first frame shown below corresponds to the instance of maximum angle of attack experienced by the vehicle shortly after the removal of the second gust load. Frames two and three then correspond to the deformation of the rocket one and two seconds later. In the third frame at approximately 7.2 seconds, the fin deformation has nearly ceased entirely. A slight bending effect is noticeable in the second image. The three-dimensional view of the rocket is not depicted since even at 4X magnification the results are not easily discernable.

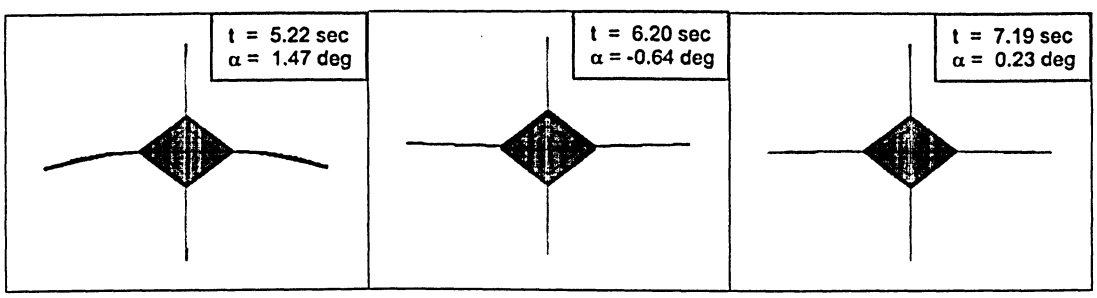

Figure 6.80: Rocket Deformation (Front) for Supersonic Stability

6.5.8 Results Summary

The preceding sections presented the detailed simulation data from a variety of rocket model configurations for both subsonic and supersonic flows. The results from these 3D flexible body flight simulations are summarized in the two tables below. The equivalent 2nd order system response parameters are given in the columns corresponding to the behaviour immediately following the two gust loads. The σ_d term corresponds to the eigenvalue (i.e., the dominant system pole), which describes the resulting growth or decay of the flight parameters. The frequency of oscillation is also shown by the term ω_d. In each case, the vehicle is decelerating, which explains the changing system response characteristics following the gust loads at t = 1 and t = 5 seconds.

The first rows in **Tables 6.1** and **6.2** show the divergence cases, where no oscillatory motion can be observed. The second row of data presents the case which shows oscillatory exponential growth trend. **Table 6.2** also shows the rocket reverting into stability following the second gust load as illustrated by the negative σ_d term. The final row in both tables correspond to two completely stable configurations. The degree of stability can also be seen to increase towards the end of the simulation as the vehicle continues to decelerate. This is again evidenced by the eigenvalue becoming more negative for the second gust case. Another trend that becomes evident is that thicker fins result in higher frequencies of oscillation.

SUBSONIC		GUST 1		GUST 2	
V_o (m/s)	t_f (mm)	σ_d	ω_d (Hz)	σ_d	ω_d (Hz)
200	0.3	4.2594	--	--	--
200	0.4	0.1233	1.2658	0.0481	1.2658
200	0.6	-0.1908	2.2472	-0.3273	2.1505

Table 6.1: Subsonic Simulation Summary

SUPERSONIC		GUST 1		GUST 2	
V_o (m/s)	t_f (mm)	σ_d	ω_d (Hz)	σ_d	ω_d (Hz)
700	0.6	13.5013	--	--	--
700	0.7	0.4547	2.1277	-0.2483	3.4188
700	1.0	-0.2921	4.4444	-0.8964	4.6512

Table 6.2: Supersonic Simulation Summary

Chapter 7: Conclusions

This thesis project has been developed with several goals in mind. The first was to develop a versatile flight simulation engine that is capable of accurately capturing the dynamic system responses for a wide array of sophisticated, non-simplified structural models. Special attention has been paid to the validation of the underlying equations of motion, so as to ensure that all relevant motions are being accounted for and considered.

Finite element modeling is an advanced technique that is employed for accurately modeling the dynamics of complex structures worldwide. By utilizing this FE capability, the resulting structural models maintain their applicability and realistic scope of behaviour. This is contrasted with an oft-used technique of using simple reduced structural elements to represent more complex models. The reduced order modeling techniques showcased within this report provide a means for balancing the desire for a large-scale sophisticated structural model with the constraints of computational efficiency. By selecting appropriate modes of deformation to represent the realm of vehicle flexibility, accurate responses may be acquired for a fraction of the processing power that would otherwise be necessary.

The software has been developed in a modular fashion, such that all components are standalone functional blocks that are easily customizable to meet the needs of any test scenario. For the purposes of this thesis report, the flexible vehicle simulator has been configured to simulate the flight of a flexible rocket.

The second principal goal of this project is to demonstrate the capabilities of the flight simulation engine by performing a parametric study with respect to a prototype rocket vehicle being developed at Ryerson University, the SPHADS-1 rocket. The simulator was used to evaluate the flight stability of a rocket model matching the SPHADS-1 dimensions for various flight conditions and model variations.

The simulation dynamics were verified for the case of an arbitrary velocity rocket tumbling in the absence of any external forces, by tracking the system energies and momenta. The three-dimensional flight simulator was additionally compared to some simplified planar flight models. It was shown that the planar tests tend to underestimate the values of critical fin thickness for a given flight configuration.

Results from the flight simulation program demonstrate the various flight instabilities that can develop in response to sudden gust loadings. The flexible motions of the aluminum fins were determined to be the critical factors in establishing and maintaining the rocket flight stability. Therefore to exploit this notion, several model variations were produced that maintained identical dimensions, with the exception of the rocket fin thickness. With the fin thickness as a variable, several flight tests were performed at both subsonic and supersonic speeds.

For both of these flight regimes, results were obtained that spanned the boundary between unstable and stable behaviour. For fin thicknesses as small as 0.3 mm, unstable divergent responses were exhibited for speeds as low as Mach 0.5, although it is believed that the instability for this configuration would be present for even lower velocities. The divergent behaviour is evidenced by large fin deformations, which in a physical setting would most likely result in the destructive failure the fins. As the fin thickness is increased, a sinusoidal unstable growth trend becomes evident in the simulation parameters. Certain vehicle velocities, fin deformations, forces, and moments all exhibit the characteristic growth, as deformations become increasing large in magnitude as time progresses. Finally, by increasing the fin thickness to a larger, more reasonable value, flight stability is retained across wide velocity ranges due to the increased rigidity of the fin structure.

The SPHADS-1 vehicle is expected to experience high Mach numbers in excess of Mach 2 during the launch phase.[18] As a result, it would be recommended that the vehicle maintain a minimum of 1 mm thick fins to ensure

adequate stability across the entire flight envelope. However it is noted that in reality, the fins would likely have a thickness in excess of 1 mm, as determined by the material strength and the dynamic stress profile seen at the fin root.

7.1 Recommendations for Future Work

Several recommendations can be made for future studies. While the modeling capability and the flexible body equations of motion are adequately sophisticated, the modeling and distribution of the external forces can be improved rather extensively.

In terms of aerodynamics, lower level CFD techniques such as strip or panel theory can be applied to the aerodynamic surfaces to establish a more comprehensive distribution of dynamic pressure (and corresponding loadings) with time. In particular, a model that could reasonably predict the flow distortion and interference effects for the scope of bent and twisted fins could greatly enhance the accuracy of the aerodynamic loadings. This could be accomplished via an on-the-fly computation, which may or may not be completely viable with respect to simulation efficiency constraints for the application. Alternatively, this data could be precompiled into a series of tables or functions that are relative to the instantaneous flight condition parameters and relative degree of deformation.

The current model does not permit variable mass applications, which would include the burning of propellant. This is of particular interest for aerial vehicles, with rockets in particular. While the current model is capable of looking at relative instantaneous (quasi-steady mass) flight instabilities, it would be beneficial to emulate the entire flight envelope of a rocket from launch to apogee.

Another interesting proposition would be to consider the flight of other vehicles such as aircraft, or spacecraft. While some modifications would surely be required with respect to the application of the external forces and moments, the underlying dynamics should be quite capable of processing such FE-derived models.

References

1. Bisplinghoff, R.L, "Principles of Aeroelasticity" Dover Publications, Inc., New York, 1975.
2. Schuster, D. M., Liu, D. D. and Huttsell, L. J., "Computational Aeroelasticity: Success, Progress, Challenge", AIAA/ASME/ASCE/AHS Structures, Structural Dynamics and Materials Conference, AIAA 2003-1725, April 2003.
3. Meirovitch, L. and Tuzcu, I., "Integrated Approach to the Dynamics and Control of Maneuvering Flexible Aircraft", Virginia Polytechnic Institute and State University, Blacksburg, Virginia, NASA/CR-2003-211748, June 2003.
4. Logan, D. L., "A First Course in the Finite Element Method", 2nd Ed., PWS Publishing, Boston, 1992.
5. Rao, S.S., "The Finite Element Method in Engineering", 2nd Ed., Pergamon Press, Toronto, 1989. pgs 377-387.
6. Krishnamoorthy, C.S, "Finite Element Analysis – Theory and Programming", 2nd Ed., Tata McGraw-Hill Publishing Company Ltd., New Delhi, 1995.
7. Bathe, Klaus-Jurgen, "Finite Element Procedures", Prentice Hall, New Jersey, 1996.
8. "ANSYS Workbook; Release 5.3", ANSYS Inc, Houston, PA, 1997.
9. Malcom, D. J., Laird, D. L., "Modeling of blades as equivalent beams for aeroelastic analysis" AIAA Reno, January 2003, #0870.
10. Ohshima, Tsukasa, and Sugiyama, Yoshihiko, "On Simplified Mechanical Models for Rocket-Body Divergence and Flutter", AIAA/ASME/ASCE/AHS Structures, Structural Dynamics and Materials Conference, AIAA 2003-1945, April 2003.
11. Lahidjani, M.H. Sadr, Ovesy, H.R., Shams, Sh., "Aeroelastic and Flutter Analysis of a Flexible Wing", AIAA/ASME/ASCE/AHS Structures, Structural Dynamics and Materials Conference, AIAA 2003-1492, April 2003.
12. McTavish, D.J, Davidson, K. and Greatrix, D.R., "Modeling of an Unconstrained Flexible Flight Vehicle", CSME Forum, London, Ontario, June 2004.
13. McTavish, D.J., "Full and Reduced Order Models for Flexible Body Motion: A Comprehensive Consistent-Mass Finite-Element Based Procedure," submitted to AIAA Journal of Guidance, Control and Dynamics, October 2004.
14. Raveh, D. E., "Identification of CFD-Based Unsteady Aerodynamic Models for Aeroelastic Analysis", AIAA/ASME/ASCE/AHS Structures, Structural Dynamics and Materials Conference, AIAA 2003-1407, April 2003.
15. Davidson, K., McTavish D.J., and Greatrix D.R., "High Detail Modeling of an Unconstrained Flexible Rocket Vehicle for Flight and Stability Analysis", submitted to Canadian Aeronautics and Space Institute (CASI) Journal, February 2005.

16. Riley, W. F. and Sturges, L. D., "Engineering Mechanics Dynamics", 2nd Ed., John Wiley & Sons, Toronto, 1996.
17. Matlab Documentation, http://www.mathworks.com/access/helpdesk/help/techdoc/matlab.html
18. Greatrix, D.R. and Karpynczyk, J. "Rocket Vehicle Design for High-Altitude Payload Delivery", CSME Forum, Toronto, May 1998.
19. Hughes, P.C., "Spacecraft Attitude Dynamics", John Wiley & Sons, Toronto, 1986. pgs. 7-31.
20. McCormick, B. W., "Aerodynamics, Aeronautics and Flight Mechanics", 2nd Edition, John Wiley & Sons, Toronto, 1995.
21. Sutton, G. P. and Biblarz, O., "Rocket Propulsion Elements", 7th Edition, John Wiley & Sons, New York, 2001.
22. Archer R. D. and Saarlas, M., "An Introduction to Aerospace Propulsion", Prentice Hall, New Jersey, 1996.
23. Houghton, E.L. and Carpenter, P.W., "Aerodynamics for engineering students" 5th Ed., Elsevier Science, Boston, 2003.
24. Bertin, John, J., "Aerodynamics for Engineers", 4th Ed., Prentice Hall, NJ, 2002.
25. Anderson, J. D., "Fundamentals of Aerodynamics", 2nd Ed., McGraw-Hill, Toronto, 1991.
26. Chin, S. S., "Missile Configuration Design", McGraw-Hill Book Company, New York, 1961.
27. Mendenhall, M., "Tactical Missile Aerodynamics: Prediction Methodology" Progress in Astronautics and Aeronautics, Vol 142, AIAA, Washington, 1992.
28. Nielsen, J.N., Missile Aerodynamics, McGraw-Hill, New York, 1960.
29. Glauert, H., "The Elements of Aerofoil and Airscrew Theory", 2nd Ed., University Press, Cambridge, 1948.
30. Pitts, W. C., Nielsen, J. N. and Kaattari, G. E., "Lift and Center of Pressure of Wing-Body-Tail Combinations at Subsonic, Transonic, and Supersonic Speeds" NACA Report 1307, Jan 1957.
31. McInville, R. M., Moore, F. G. and Housh, C., "Nonlinear Structural Load Distribution Methodology for the Aeroprediction Code", Naval Surface Warfare Center, Dahlgren Div Va, NSWCDD/TR-96/133, 1996.
32. Moore, F.G., McInville, R.M. and Hymer, T., "The 1998 Version of the NSWC Aeroprediction Code: Part I – Summary of New Theoretical Methodology", Naval Surface Warface Center, Dahlgren Div, Va, NSWCDD/TR-98/1, 1998.
33. Le Beau, R., "The Effect of Angle of Attack on Induced Rolling Moment for a Low Aspect Ratio Missile", Naval Ship Research & Development Center, AGARD Conference Proceedings on Aerodynamic Interference, Washington.
34. Blake, W. B., "Missile DATCOM, User's Manual – 1997 Fortran 90 Revision", Air Force Research Laboratory, Wright-Patterson Air Force Base, Ohio, 1998. Report No. AFRL-BA-WP-TR-1998-3009.
35. Craig, R. R., "Mechanics of Materials", John Wiley & Sons, Toronto, 1996.

36. Davidson, K., Greatrix, D. R., McTavish, D. J. "Stability Analysis of a Flexible Rocket", presented at the 13th Propulsion Symposium, Canadian Aeronautics and Space Institute (CASI) 50th Annual General Meeting, Montreal, QC, May 2003.
37. McTavish D.J., Greatrix D.R., Davidson K., "Unconstrained Flight and Stability Analysis of a Flexible Rocket Using a Detailed Finite-Element Based Procedure" (submitted to Computational Ballistics Conference, Cordoba, Spain, 2005).
38. Nise, N. S., "Control Systems Engineering" 3rd Ed., John Wiley & Sons, New York, 2000.
39. Riley, W. F. and Sturges, L. D., "Engineering Mechanics Statics", 2nd Ed., John Wiley & Sons, Toronto, 1996.
40. Serway, R. A., "Physics: for Scientists and Engineers with Modern Physics", 4th Ed., Saunders College Publishing, Chicago, 1996.
41. Schildt, H., "C: The Complete Reference", 4th Ed., Osborne/McGraw Hill, California, 2000.
42. Anderson, P.K., Bjedov, G. and Scarbrough, M.G., "Essential C: An Introduction for Scientists and Engineers", Saunders College Publishing, Florida, 1995.
43. Van Loan, C. F., "Introduction to Scientific Computing: A Matrix-Vector Approach Using MATLAB", 2nd Ed., Prentice Hall, NJ, 1999.

Appendix A: Fin Load Distributions

The load distribution techniques used to allocate nodal loads over the fin structure may be customized to match any level of desired complexity as is deemed reasonable or available. In the current context, the direct computation of the pressure distribution over the fin is avoided for the sake of simplicity across the range of allowable Mach numbers and non-linear aerodynamics. In contrast, simpler equations are employed, or tabulated experimental results may additionally be used if available.

As discussed in **Section 5.3**, the aerodynamic loads are determined through the use of tabulated aerodynamic coefficients for a wide range of Mach numbers, angles-of-attack and altitude.

A.1 Subsonic Aerodynamic Load Distribution

Many factors influence the load distribution over an aerodynamic surface such as a fin. Interference from adjacent bodies, disturbances from geometric protuberances, orientation of the velocity vector, normal or oblique shocks, all may serve to affect the loading.[30-33] For low velocity applications, the distribution profiles may be approximated with some simple relations. Complex shock interference interactions may be present for high velocity subsonic (i.e., transonic) cases as regions of supersonic flow may arise over the fin surfaces for a given cross sectional profile. These interactions are highly dependent on the vehicle configuration and thus it might be beneficial to use more accurate experimental or theoretical profiles for improved accuracy within this transonic region.

A.1.1 Fourier Sine Series Fin Distribution Method

Spanwise Distribution

A simple method for acquiring a load distribution over an arbitrary finite wing or fin is to represent the loading with a Fourier sine series expansion.[23,25]

Thus, Prandtl's integral equation for the circulation (Γ) at any section along the span using a Fourier expansion in terms of airfoil parameters is given by

$$\Gamma = 4sV_\infty \sum A_n \sin n\theta \tag{A1.1}$$

where s is the span of a single fin (semispan)

Examples of the first four Fourier expansion terms are presented in **Figure A1** below. Once the Fourier coefficients (A_n's) have been determined the terms are summed to reveal the load distribution.

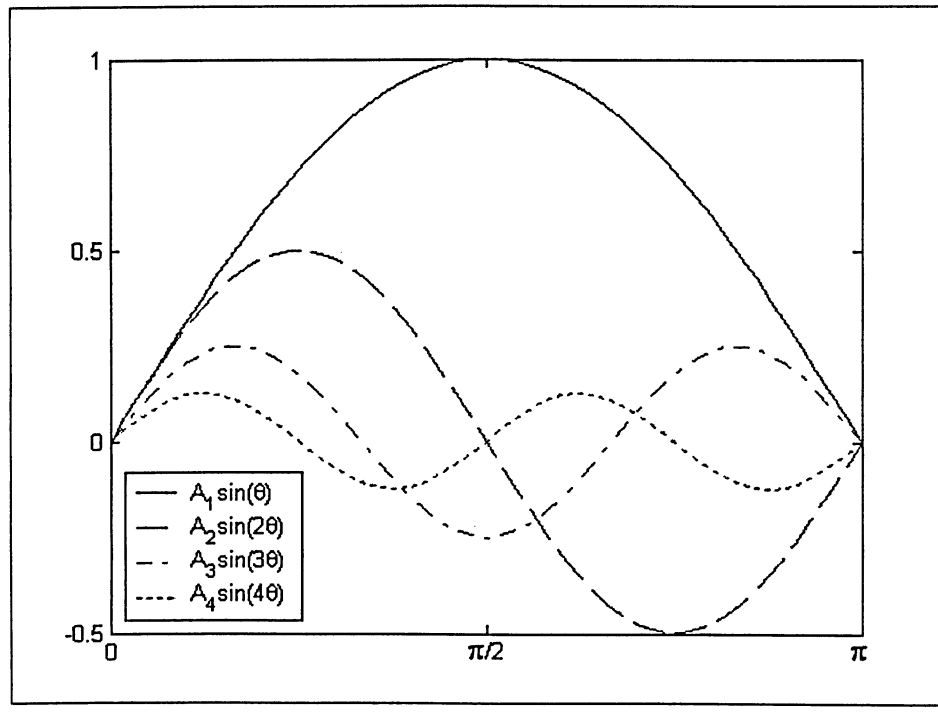

Figure A1: Fourier Coefficient Expansion

The first Fourier coefficient can be extracted from the flight characteristics including the normal force slope ($C_{N\alpha}$) and angle of attack (α), as follows,

$$A_1 = \frac{C_N}{\pi AR} = \frac{C_{N\alpha}\alpha}{\pi AR} \tag{A1.2}$$

Define the Fourier series as

$$\mu(\alpha - \alpha_0) = \sum A_n \sin n\theta \left(1 + \frac{\mu n}{\sin\theta}\right) \tag{A1.3}$$

Rearranging and given α_0 = 0, yields

$$\mu\alpha \sin\theta = \sum A_n \sin n\theta (\sin\theta + \mu n) \tag{A1.4}$$

where

$$\mu = \frac{c_\theta a_\infty}{8s} = \frac{c_\theta C_{N\alpha}}{8s} \tag{A1.5}$$

where c_θ is the local chord at the span location θ, and

$$c_\theta = c_r(1-\lambda)\cos\theta + c_r$$

and λ is the taper ratio

$$\lambda = {}^{c_t}\!/_{c_r}$$

The spanwise location (θ) can be related to fin parameters via

$$z = -s\cos\theta \tag{A1.6}$$

Referring to **Equation (A1.1)**, it is evident that all the terms are known except for the Fourier coefficients (A_n's). Typically four coefficients are used to provide an adequate spanwise distribution. Odd numbered coefficients are used if a symmetric profile is desired (e.g., A_1, A_3, A_5, A_7), whereas a sequential numbering is used if an unsymmetric profile is preferred (e.g., A_1, A_2, A_3, A_4). Spanwise loads are assumed to have a symmetric profile for subsonic flows. Thus, the Fourier expansion would appear as follows

$$\mu\alpha\sin\theta = A_1\sin\theta(\sin\theta+\mu) + A_3\sin 3\theta(\sin\theta+3\mu) + A_5\sin 5\theta(\sin\theta+5\mu) + A_7\sin 7\theta(\sin\theta+7\mu) \tag{A1.7}$$

Equation (A1.7) is a single equation with four unknowns. The coefficients may be determined by evaluating this equation at four distinct spanwise locations. The angular spanwise locations that are commonly used are

$$\theta = \tfrac{\pi}{8}, \tfrac{\pi}{4}, \tfrac{3\pi}{8}, \tfrac{\pi}{2}.$$

The system can be solved by placing it in standard form

$$[\mathbf{A}]\{\mathbf{x}\} = [\mathbf{B}] \tag{A1.8}$$

or more explicitly,

$$\begin{bmatrix} \sin\theta_1(\sin\theta_1+\mu) & \sin 3\theta_1(\sin\theta_1+3\mu) & \sin 5\theta_1(\sin\theta_1+5\mu) & \sin 7\theta_1(\sin\theta_1+7\mu) \\ \sin\theta_2(\sin\theta_2+\mu) & \sin 3\theta_2(\sin\theta_2+3\mu) & \sin 5\theta_2(\sin\theta_2+5\mu) & \sin 7\theta_2(\sin\theta_2+7\mu) \\ \sin\theta_3(\sin\theta_3+\mu) & \sin 3\theta_3(\sin\theta_3+3\mu) & \sin 5\theta_3(\sin\theta_3+5\mu) & \sin 7\theta_3(\sin\theta_3+7\mu) \\ \sin\theta_4(\sin\theta_4+\mu) & \sin 3\theta_4(\sin\theta_4+3\mu) & \sin 5\theta_4(\sin\theta_4+5\mu) & \sin 7\theta_4(\sin\theta_4+7\mu) \end{bmatrix} \begin{Bmatrix} A_1 \\ A_2 \\ A_3 \\ A_4 \end{Bmatrix} = \begin{bmatrix} \mu\alpha\sin\theta_1 \\ \mu\alpha\sin\theta_2 \\ \mu\alpha\sin\theta_3 \\ \mu\alpha\sin\theta_4 \end{bmatrix} \tag{A1.9}$$

The coefficients are obtained by performing the following operation

$$\{x\} = [A]^{-1}[B] \tag{A1.10}$$

Examples of symmetric and unsymmetric Fourier coefficient load distributions are given in **Figures A2** and **A3** respectively.

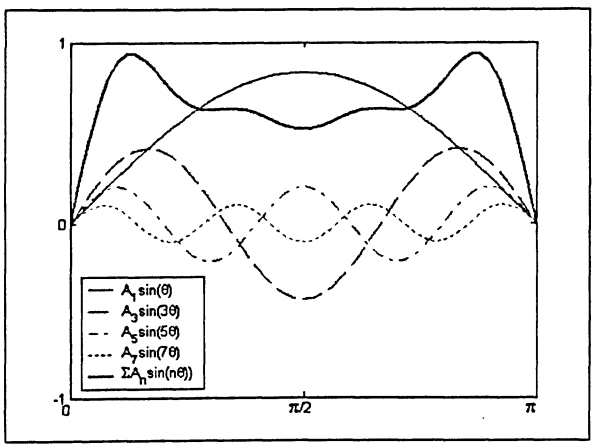

Figure A2: Symmetric Profile

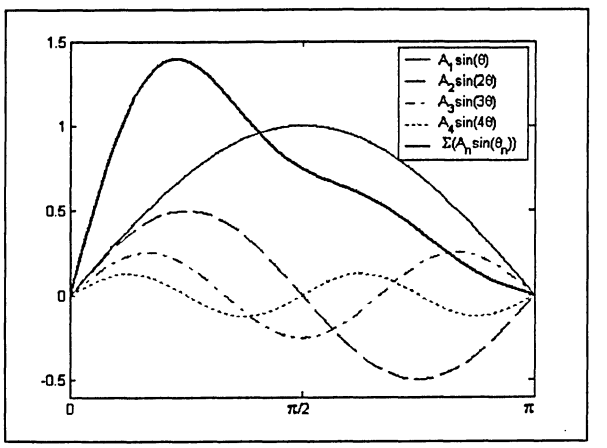

Figure A3: Asymmetric Profile

Chordwise distribution

The chordwise distribution is determined using a Fourier coefficient expansion method as was described in the previous section. The chordwise distribution is assumed to be asymmetric and thus the even Fourier coefficients (harmonics) are included. The actual profile used in the simulation is an adjusted Fourier coefficient distribution that maintains the center of pressure about the quarter chord line.

A.2 Supersonic Aerodynamic Load Distribution

For supersonic flows, shock waves inherently develop over the vehicle surface. The interactions of these shocks as they impinge on aerodynamic components can significantly alter the load distribution profiles. To capture precise distributions, CFD methods would likely need to be employed, particularly for cases with complicated structures experiencing high-speed flows. An approximate method is presented below that does include consideration for shock interaction over the fin surface.

A.2.1 Supersonic Aerodynamic Distribution from Supersonic Wing Theory

The following method is used to compute the span-wise load distribution profiles for a rocket fin in supersonic flow. Methods are presented for span loading distributions for both triangular and rectangular airfoils. The two cases are then combined to present results for a general wing with leading edge sweep (Λ) and taper ratio (λ) for a variety of relevant Mach number regions.[28]

In supersonic flow, any disturbances can only propagate downstream. At any point in a specified supersonic velocity flow field, the region subject to disturbances or flow irregularities emanating from that point will be bounded by an imaginary conical contour. This boundary line is known as a *Mach line*, and is defined with a Mach angle (μ) that is inclined with respect to the flow. The Mach angle is related to the Mach number and is determined via the following equation.

$$\mu = \sin^{-1}\left(\frac{1}{M_\infty}\right) = \tan^{-1}\left(\frac{1}{\beta}\right) \tag{A2.1}$$

where

$$\beta = \sqrt{M_\infty^2 - 1} \tag{A2.2}$$

The section lift coefficient is given by the integration of the pressure distribution ΔP over the upper and lower surfaces of the airfoil, that is,

$$c_l = \frac{1}{c}\int_{le}^{te} \Delta P dx \tag{A2.3}$$

The span-wise load distribution is given by the product of the section lift coefficient and the local chord (cc_l). This will form the basis for determining the distribution profiles at a variety of supersonic speeds.

A.2.2 Triangular Wings in Supersonic Flow

The flow over a triangular wing in supersonic flow can be divided into two categories. For lower supersonic Mach numbers, the Mach angle will be greater than the semiapex (ω) angle of the triangular wing. Therefore, the Mach line will lie forward of the wing surface leading edge as seen in **Figure A4 (a)**. Thus, the fin will have subsonic leading edges. For larger Mach numbers, the Mach angle

will become smaller than the wing semiapex angle, and the leading edges of will then become supersonic. This can be seen in **Figure A4 (b)**.

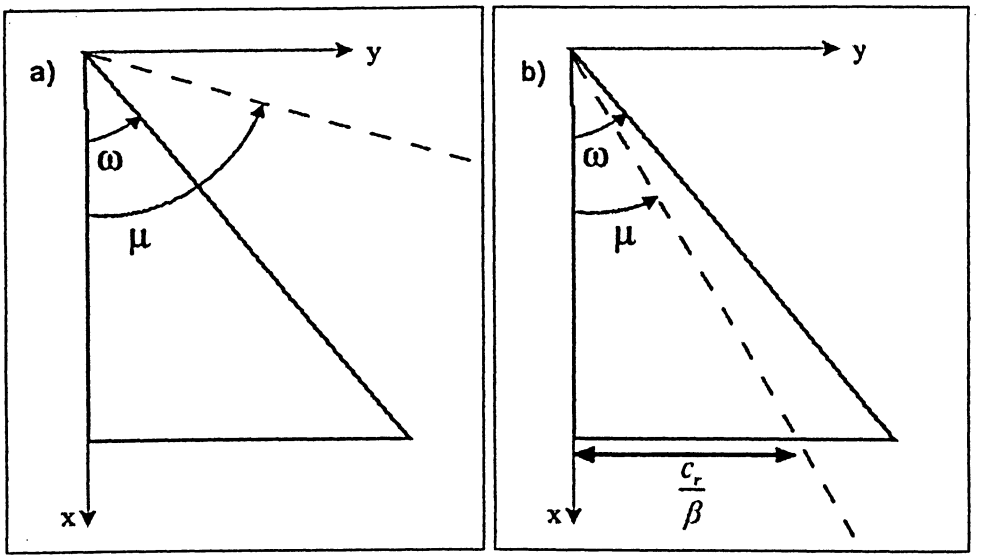

Figure A4: Flow Regimes over a Triangular Wing

Note that c_r in **Figure A4** corresponds to the root chord of the triangular fin.

A.2.3 Triangular Wing with Subsonic Leading Edges

For this case, the pressure distribution is constant along radial lines emanating from the fin apex. The pressure distribution is then,

$$\Delta P = \frac{4\alpha \tan\omega}{\sqrt{1-\frac{\tan^2\nu}{\tan^2\omega}E}} \qquad \text{(A2.4)}$$

where α is the angle of attack, ω is the semiapex angle, ν is the radial angle given by $\nu = \tan^{-1}\left(y/x\right)$, and E is the complete elliptic integral of the second kind.

Elliptic Integral

There are several forms of elliptic integral;[17,28] however, only the second kind is used and presented here. The second kind of elliptic integral is generally

dependent on two factors, the amplitude (ϕ) and modulus (m). The amplitude is typically within the range $0 \leq \phi \leq \frac{\pi}{2}$:

$$E(m,\phi) = \int_0^{\phi} \sqrt{1 - m\sin^2\theta}\, d\theta \tag{A2.5}$$

The integral E is considered to be complete when $\phi = \frac{\pi}{2}$. Note that the modulus is sometimes represented as the variable 'k' instead of 'm', where $k^2 = m$.

The flow over a triangular wing with subsonic leading edges generates an elliptical load distribution. Combining **Equation (A2.3)** and **(A2.4)**, the load distribution can then be found. The resulting span load profile is,

$$cc_l = (cc_l)_0 \sqrt{1 - \frac{\tan^2\nu}{\tan^2\omega}} \tag{A2.6}$$

where $(cc_l)_0$ is the span loading at the root chord, and is found via

$$(cc_l)_0 = \frac{4\alpha c_r \tan\omega}{E} \tag{A2.7}$$

A.2.4 Triangular Wing with Supersonic Leading Edges

For the case where the leading edges experience supersonic flow, the loading is no longer elliptical due to the effect of local supersonic regions over the wing. The load distribution for this case can be divided into two segments. The innermost region extends from the root chord to the point at which the Mach line intersects the trailing edge. The load distribution for this region is given by

$$cc_l = \frac{4\alpha}{\sqrt{\beta^2\tan^2\omega - 1}}\left[b + \frac{(b-y)}{\pi}\sin^{-1}\left(\frac{y\beta^2\tan^2\omega - b}{(b-y)\beta\tan\omega}\right) - \frac{(b+y)}{\pi}\sin^{-1}\left(\frac{y\beta^2\tan^2\omega + b}{(b+y)\beta\tan\omega}\right)\right] \tag{A2.8}$$

This equation is relevant for the regions on the fin bounded by $0 \leq y \leq \frac{c_r}{\beta}$.

The remaining outermost region lies forward of the Mach line and thus the flow over this section of the wing is completely supersonic. The variation here is linear, and is given by

$$cc_l = \frac{4\alpha(b-y)\cot\omega}{\sqrt{\beta^2 - \cot^2\omega}} \tag{A2.9}$$

over the region corresponding to $\frac{c_r}{\beta} \le y \le b$.

A.2.5 Rectangular Wings

For rectangular wings the dominant characteristic that affects the profile is the interaction between the Mach lines emanating from the wing tips. Several flow configurations are possible for a given fin geometry at various Mach numbers. These are summarized in **Figure A5** below.

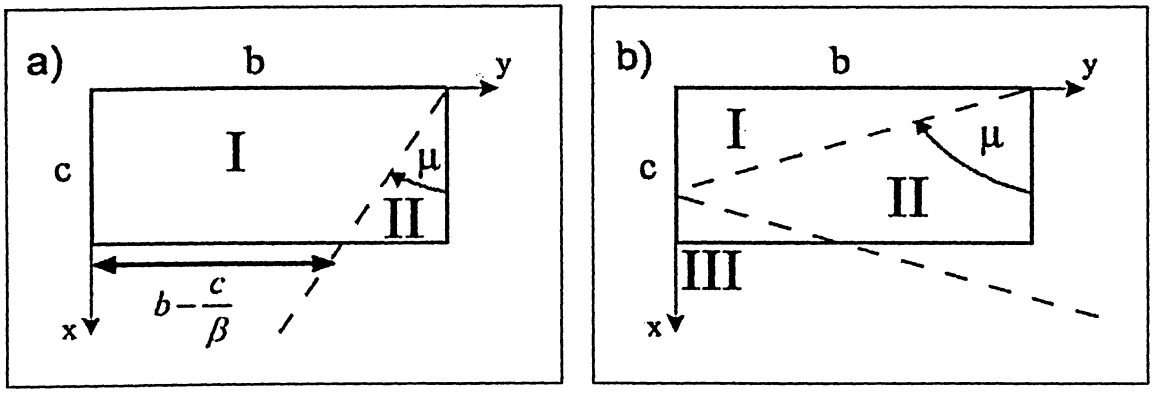

Figure A5: Flow Regimes over a Rectangular Wing

Note that in **Figure A5**, a rectangular half wing is shown, and that the x-axis may be seen as a plane of symmetry. Case (a) depicts the situation when the wing tip Mach line does not intersect any other Mach line on the surface of the wing. That is, the velocity is large enough such that the Mach lines emanating from the two tips do not cross anywhere over the wing. Case (b) illustrates the situation where the two Mach lines do intersect on the wing surface. For the half wing shown here, the intersected Mach line may be equivalently expressed as a reflection from an unseen solid surface.

Three distinct regions are depicted in **Figure A5**. Area I, corresponds to the portion of the wing that does not receive any influence of the disturbed flow from the tip chord. For this region the pressure distribution is given simply by,

$$\Delta P_I = \frac{4\alpha}{\beta} \qquad \text{(A2.10)}$$

The span load distribution is then

$$cc_l = \frac{4\alpha c_r}{\beta} \tag{A2.11}$$

Within area II, the Mach lines streaming from the tip chord affect the flow over the fin surface. The resulting change in pressure within this region can be calculated and subtracted from the otherwise nominal pressure distribution ΔP_I. That is, the pressure distribution within area II is given by

$$\Delta P_{II} = \frac{4\alpha}{\beta}\left\{1-\left[1-\tfrac{1}{\pi}\cos^{-1}\left(1-2\beta\tan\theta\right)\right]\right\} \tag{A2.12}$$

or

$$\Delta P_{II} = \Delta P_I - \Delta P_{tips} \tag{A2.13}$$

The resulting span-wise load distribution is given via

$$cc_l = \frac{4\alpha c_r}{\beta}\left\{\frac{1}{\pi}\cos^{-1}\left(1-\frac{2\beta(b-y)}{c}\right)+\frac{2}{\pi}\sqrt{\frac{\beta(b-y)}{c}-\frac{\beta^2(b-y)^2}{c^2}}\right\} \tag{A2.14}$$

Lastly, for area III, the Mach lines intersect and produce a region where the flow and resulting pressure distribution is affected from two sources. Conceptually this may also be represented as the nominal distribution being influenced by two separate disturbances.

$$\Delta P_{III} = \frac{4\alpha}{\beta}\left\{1-\left[1-\tfrac{1}{\pi}\cos^{-1}\left(1-2\beta\tan\theta_1\right)\right]-\left[1-\tfrac{1}{\pi}\cos^{-1}\left(1-2\beta\tan\theta_2\right)\right]\right\} \tag{A2.15}$$

or

$$\Delta P_{III} = \Delta P_I - \Delta P_{tip1} - \Delta P_{tip2} \tag{A2.16}$$

The resulting load distribution is given by

$$cc_l = \frac{4\alpha c_r}{\beta}\left\{\frac{1}{\pi}\cos^{-1}\left(1-\frac{2\beta(b-y)}{c}\right)+\frac{2}{\pi}\sqrt{\frac{\beta(b-y)}{c}-\frac{\beta^2(b-y)^2}{c^2}}+\frac{1}{\pi}\cos^{-1}\left(1-\frac{2\beta(b+y)}{c}\right)+\frac{2}{\pi}\sqrt{\frac{\beta(b+y)}{c}-\frac{\beta^2(b+y)^2}{c^2}}-1\right\} \tag{A2.17}$$

A.2.6 Arbitrary Fin with Leading Edge Sweep and Taper Ratio

The preceding equations for both triangular and rectangular fins in supersonic flow will serve as the basic building blocks for developing a method for determining the load distributions over a conventional tailfin.

Figures A6 and **A7** show the construction of a generic tailfin with leading edge sweep (Λ) and taper ratio (λ). The fin presented here has no trailing edge sweep for simplicity.

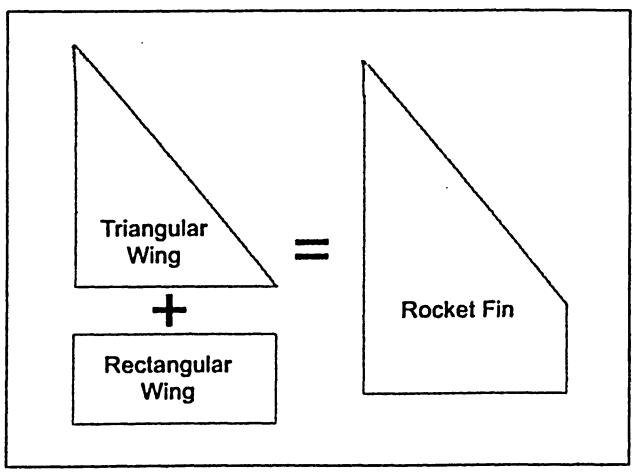

Figure A6: Rocket Fin Construction

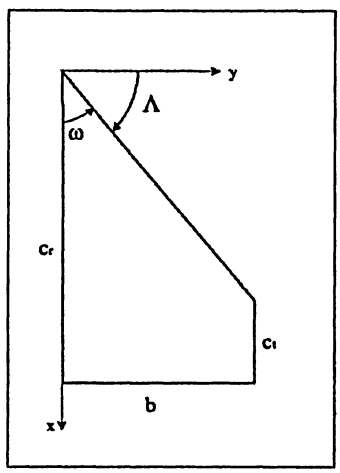

Figure A7: Fin Geometry

Next the loading conditions for a tapered fin will be constructed from the basic building blocks of the rectangular and triangular wings.

Figure A8 presents four loading scenarios for the given fin configuration, which will be used to derive the span load distribution data for any supersonic Mach number.

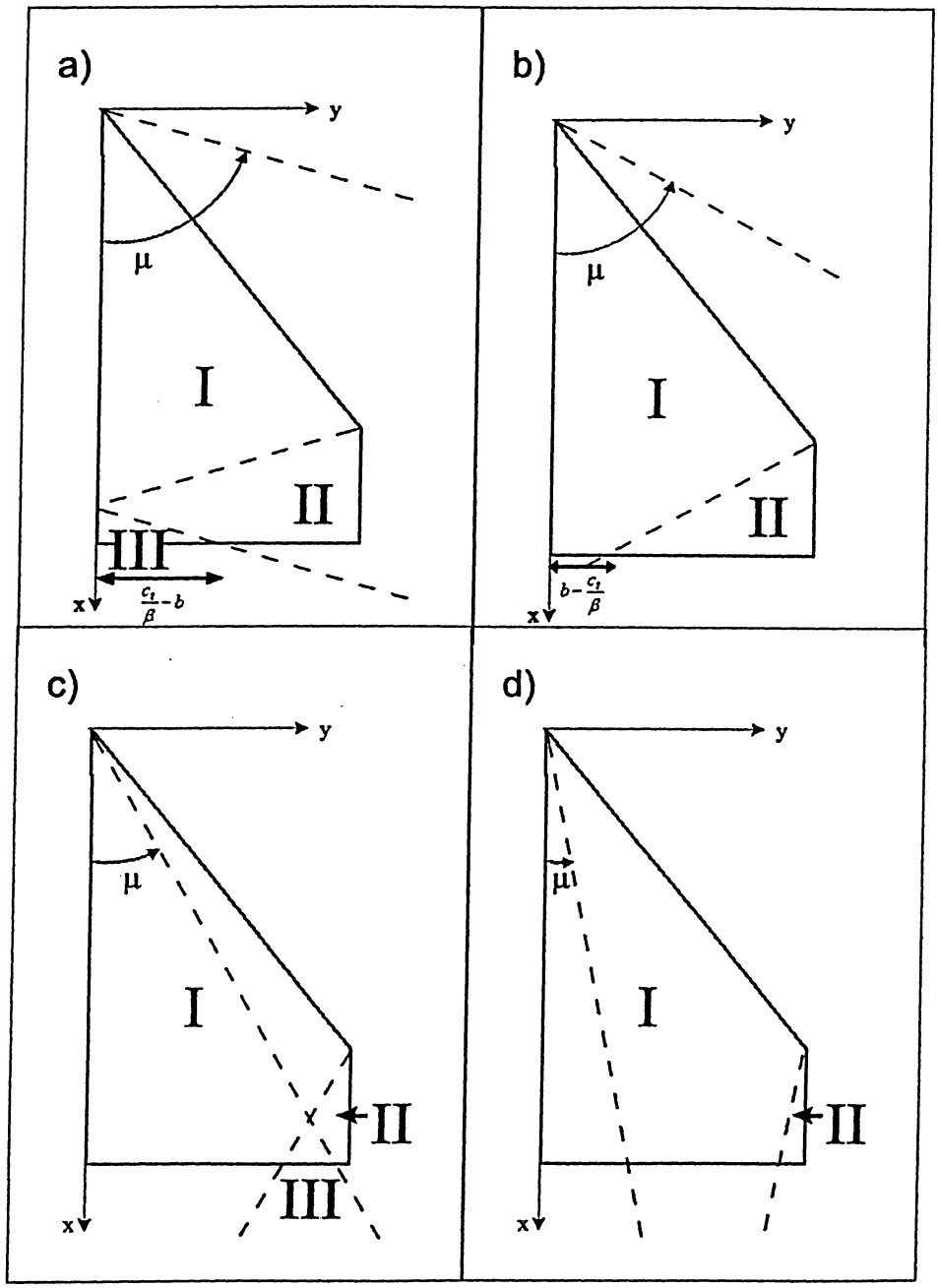

Figure A8: Flow Regimes over a Swept, Tapered Rocket Fin

(a) Subsonic leading edges with body reflection (b) subsonic leading edges with no reflection (c) supersonic leading edges with Mach line intersection (d) supersonic leading edges with no intersection

Figure A8 (a) depicts the scenario in which the leading edge of the fin is subsonic, and the Mach number is sufficiently small to allow for the Mach line to

become incident upon the root chord. It is assumed here that the fuselage is represented by a solid wall oriented perpendicular to the root chord. Thus, a region of doubly mixed flow will exist aft of the reflected tip Mach line. The reflected Mach line is conceptually equivalent to the Mach line that would originate from the tip of an identical fin reflected in the y-z plane in the absence of the fuselage. The innermost region bordered from the root to the point at which the reflected Mach line touches the trailing edge is affected by two disturbances.

An important observation to make before jumping to any load distribution conclusions is that unlike the case for the rectangular wing, the local chord c at any given spanwise location is not constant. For a rectangular wing, the percentage of chord affected by the tips decreases linearly since the chord is constant across the span. However, for a standard linearly tapered fin ($\lambda < 1$), the local chord increases in size towards the root, and therefore the overall percentage of local chord affected by the disturbed flow imparted by the tips decreases nonlinearly.

Therefore, a correction factor must be applied to pressure and load distributions that were presented in **Section A2.3** for the rectangular wings. The correction factor utilizes the percentage of local chord affected by the tips in relation to that of a rectangular wing, that is,

$$f_{tip} = \frac{r_{tip}}{(r_{tip})_{rect}} \tag{A2.18}$$

where $r_{tip} = \frac{x_{c,tip}}{c_t}$ is the ratio of chord affected by the tips to the local chord, and

$(r_{tip})_{rect} = \frac{x_{c,tip}}{c_t}$ is the ratio of chord affected by the tips for a rectangular fin of $c = c_t$.

This correction factor allows for the same interference pressure change equations presented for the rectangular wing to be used for a tapered wing. Thus, the total spanwise loading is dependent upon the relative percentage of the chord being affected by Mach line effects.

For **Figure A8 (a)**, the following load distributions equations are applicable over the indicated segments of the fin.

For the Mach range from M = 1 to the point at which the Mach line from the tip strikes the trailing edge of the root chord the region III will exist.

The Mach angle corresponding to this condition is given by

$$\mu_{uA} = \tan^{-1}\left(\frac{b}{c_t}\right) \tag{A2.19}$$

The upper Mach limit for this scenario is then determined via

$$M_{uA} = \frac{1}{\sin \mu_{uA}} \tag{A2.20}$$

where the subscript 'u' is used to indicate the properties defining the upper Mach limit.

For area I, the section is dominated by the triangular wing with subsonic leading edges formulae. The region is defined for $0 \le y \le b$:

$$cc_l = (cc_l)_{tri-sub}\left\{1 - f_{tip}\left[1 - \frac{1}{\pi}\cos^{-1}\left(1 - \frac{2\beta(b-y)}{c_t}\right) + \frac{2}{\pi}\sqrt{\frac{\beta(b-y)}{c_t} - \frac{\beta^2(b-y)^2}{c_t^2}}\right]\right\} \tag{A2.21}$$

where $(cc_l)_{tri-sub}$ corresponds to the load distribution for a triangular wing with subsonic leading edges. This was given previously by **Equation (A2.6).**

The span load distribution of the entire fin may be solved using this single equation. The reflected Mach line deflecting off the body may be accounted for by adjusting the relative area of influence for the overlapping segment through the fin area correction factor f_{tip}. That is, for the region that is affected by both the incident and reflected Mach lines, the total disturbance can be summed to give an effective affected region, which may be handled directly by the f_{tip} term.

For case (b), as seen in **Figure A8**, the Mach number has increased such that the Mach line now intersects with the trailing edge, eliminating any reflections from the body. Two distinct regions for calculation are present for this scenario.

The Mach range corresponding to case b) is bounded from the upper limit of case A up to the point at which the Mach line from the fin apex becomes collinear with the leading edge. That is, when the Mach angle (μ) equals the semiapex angle (ω),

$$\mu_{uB} = \omega$$

which will occur at a freestream Mach number

$$M_{uB} = \frac{1}{\sin \mu_{uB}}$$

Thus,

For $0 \le y \le \left(b - \frac{c_t}{\beta}\right)$,

$$cc_l = (cc_l)_{tri-sub} = (cc_l)_0 \sqrt{1 - \frac{\tan^2 \nu}{\tan^2 \omega}} \qquad \text{(A2.22)}$$

where $(cc_l)_{tri-sub}$ was stated previously.

For the region, $\left(b - \frac{c_t}{\beta}\right) \le y \le b$, the spanwise loading is given by,

$$cc_l = (cc_l)_{tri-sub} \left\{ 1 - f_{tip} \left[1 - \frac{1}{\pi} \cos^{-1}\left(1 - \frac{2\beta(b-y)}{c_t}\right) + \frac{2}{\pi} \sqrt{\frac{\beta(b-y)}{c_t} - \frac{\beta^2 (b-y)^2}{c_t^2}} \right] \right\} \qquad \text{(A2.23)}$$

In **Figure A8 (c)**, the Mach number has now increased to the point at which the leading edges have become supersonic. The Mach lines from the tip and the apex intersect on the body surface, creating a region of flow affected from two sources.

The upper bound for this case is found when the two Mach lines intersect on the trailing edge of the fin. This occurs when

$$\mu_{uC} = \tan^{-1}\left(\frac{b}{c_r + c_t}\right) \qquad \text{and} \qquad M_{uC} = \frac{1}{\sin \mu_{uC}}$$

If the Mach line originating from the fin apex intersects with the tip chord, then there will be two analysis regions for the case: a region affected only by flow of a triangular wing with supersonic edges and a region that is disturbed due to tip

effects. If the apex Mach line intersects with the trailing edge, there will be three distinct analysis regions. The two innermost regions will be identical to those just described with a third region consisting of the linearized component of supersonic flow also affected by tip disturbances as mentioned in **Section A2.3.**

The innermost region, affected only by supersonic flow over a triangular wing is given by **Equation (A2.8).**

For $0 \le y \le \left(b - \frac{c_t}{\beta}\right)$, the loading is thus restated,

$$cc_l = (cc_l)_{tri-sup} = \frac{4\alpha}{\sqrt{\beta^2 \tan^2 \omega - 1}}\left[b + \frac{(b-y)}{\pi}\sin^{-1}\left(\frac{y\beta^2 \tan^2 \omega - b}{(b-y)\beta \tan \omega}\right) - \frac{(b+y)}{\pi}\sin^{-1}\left(\frac{y\beta^2 \tan^2 \omega + b}{(b+y)\beta \tan \omega}\right)\right]$$

If the apex Mach line intersects the tip chord, the next region will be bounded by the limit $\left(b - \frac{c_t}{\beta}\right) \le y \le b$. Should the apex Mach line intersect the trailing edge, then the second of three analysis regions will be bound by $\left(b - \frac{c_t}{\beta}\right) \le y \le \frac{c_r}{\beta}$.

The load distribution will then be,

$$cc_l = (cc_l)_{tri-sup}\left\{1 - f_{tip}\left[1 - \frac{1}{\pi}\cos^{-1}\left(1 - \frac{2\beta(b-y)}{c_t}\right) + \frac{2}{\pi}\sqrt{\frac{\beta(b-y)}{c_t} - \frac{\beta^2(b-y)^2}{c_t^2}}\right]\right\} \quad \text{(A2.24)}$$

The third computation region (if in existence) will then be bounded by $\frac{c_r}{\beta} \le y \le b$.

The load distribution is determined via,

$$cc_l = (cc_l)_{sup-lin}\left\{1 - f_{tip}\left[1 - \frac{1}{\pi}\cos^{-1}\left(1 - \frac{2\beta(b-y)}{c_t}\right) + \frac{2}{\pi}\sqrt{\frac{\beta(b-y)}{c_t} - \frac{\beta^2(b-y)^2}{c_t^2}}\right]\right\} \quad \text{(A2.25)}$$

where $(cc_l)_{sup-lin}$ is the outermost linearized portion of supersonic flow over a triangular wing, as was stated previously in **Equation (A2.9)**:

$$(cc_l)_{sup-lin} = \frac{4\alpha(b-y)\cot\omega}{\sqrt{\beta^2 - \cot^2\omega}}$$

Lastly, **Figure A8 (d)** depicts the situation where the Mach number has increased to the point at which the Mach lines propagating from the fin apex and tip no longer intersect over the fin surface. Thus, there is no region of doubly affected flow for a given fin geometry.

There is no upper bound for this region as further increases in Mach number will only cause the Mach angle to decrease in size, and no further Mach line interactions will take place over the surface of the fin.

The fin surface may be divided into three distinct analysis regions. The first and innermost region is governed by the supersonic flow over a triangular wing. Thus for $0 \le y \le \frac{c_r}{\beta}$, the loading is given by

$$cc_l = (cc_l)_{tri-sup}$$

The next region is characterized by the linear component of supersonic flow over triangular wings.

That is, for $\frac{c_r}{\beta} \le y \le \left(b - \frac{c_t}{\beta}\right)$, the loading is determined via

$$cc_l = (cc_l)_{sup-lin}$$

The third and final region includes the linearized component of supersonic flow over triangular wings diminished in accordance with the disturbance propagating from the tip leading edge. This region is bounded by $\left(b - \frac{c_t}{\beta}\right) \le y \le b$.

The loading is stated as,

$$cc_l = (cc_l)_{sup-lin}\left\{1 - f_{tip}\left[1 - \frac{1}{\pi}\cos^{-1}\left(1 - \frac{2\beta(b-y)}{c_t}\right) + \frac{2}{\pi}\sqrt{\frac{\beta(b-y)}{c_t} - \frac{\beta^2(b-y)^2}{c_t^2}}\right]\right\} \quad \text{(A2.26)}$$

Supersonic Chordwise Distribution

The chordwise distribution is determined by integrating the spanwise distributions just outlined over the local chord for a given fin geometry. The resulting effect is a sloping effect over the tapered sections of the local chord, with a constant loading for the untapered regions.

A.3 Aerodynamic Load Distribution Notes

The method presented in this Appendix provides the methods necessary to determine a general span-load distribution profile for any range of Mach number for a specified fin geometry. It is understood and admitted freely that the preceding method is not without limitations and obvious simplifications. To accurately capture and determine the flow characteristics over the fins at high speed, a much more sophisticated method should be employed, such as a computational fluid dynamics (CFD) technique.

The goal of this section is not to accurately determine the actual loadings for the fin at each given flight condition, but to capture the normalized load profiles. As outlined elsewhere in this report, the actual aerodynamic loads are determined via a series of interpolated aerodynamic coefficients. The profiles generated here are used to distribute these loads over a finite element mesh representation of a fin for a given flight condition. One particular shortcoming of this method is that the present context does not allow for any interference effects imparted on the flow over the fin by the fuselage. For increased accuracy, any number of techniques may be employed to improve the aerodynamic load profile. However, for the current context, the above method will suffice.